Methodological Reduction of Magnetically Induced Noise in Magnetic Multilayers for Sensor Applications

Dissertation

for obtaining the academic degree of Doctor of Engineering (Dr.-Eng.)

zur Erlangung des akademischen Grades Doktor der Ingenieurwissenschaften (Dr.-Ing.)

Matic Jovičević Klug

2019

I hereby declare that I wrote my dissertation Methodological Reduction of Magnetically Induced Noise in Magnetic Multilayers for Sensor Applications, to the best of my knowledge and with the help of none but the indicated sources. I declare that this dissertation has not been submitted beforehand to any examination authority, institute or university. Furthermore, I declare that the research work in this dissertation is presented within the rules of good scientific practice of the German Research Foundation.

Matic Jovičević Klug
Christian-Albrechts-Universität zu Kiel

Date: **Signature:**

Reviewers:

Prof. Dr.-Ing. Jeffrey McCord

Prof. Dr.-Ing. Eckhard Quandt

Dr. habil. Klaus Rätzke, apl. Prof.

Date for the oral exam: 12.09.2019

The beauty of a researcher's work at the heart lies,

where curiosity and passion towards his research resides.

But, if the heart strong is to stay,

the love and support of people around him is what fuels it day by day.

Matic Jovičević Klug

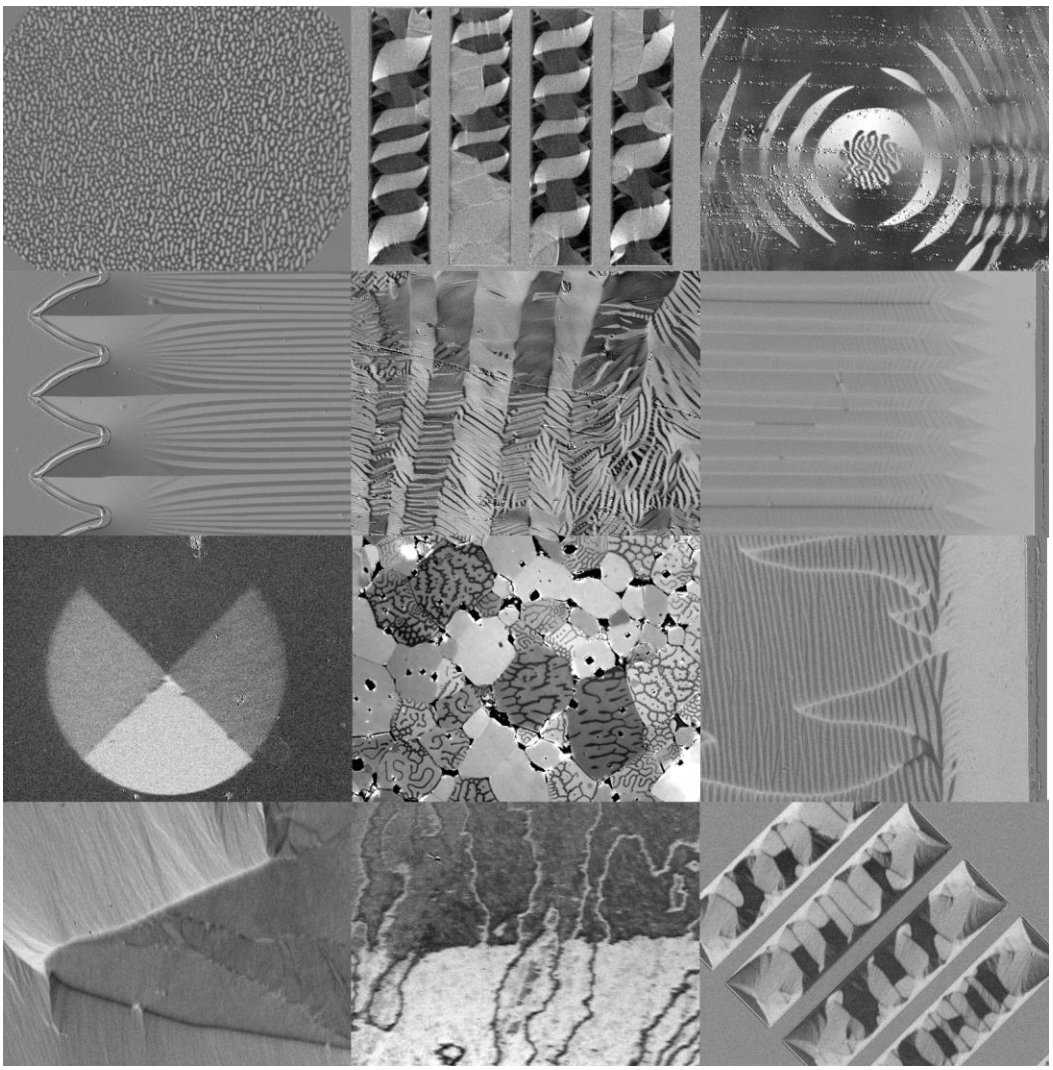

Acknowledgements

Firstly, I would like to thank my mentor Jeffrey McCord, for his continuous support, great discussions and pushing me to understand deeply my research. His guidance and mentorship have sculpted a great part of my professional persona by teaching me to be more concise, critical-thinking and attentive to details. I thank Jeffrey also for giving me the chance to work in his work group and providing me the opportunity to immerse myself in the mesmerizing world of magnetism, which has grown to be one of my favorite research fields. I would also like to thank my second mentor Dirk Meyners, who also taught me many things in relation to material preparation and characterization. His critical reasoning and discussions gave me the chance to question my results and allowed me to refine and improve my work to a significantly higher quality. Many thanks also go to my former and current colleagues of the Nanoscale Magnetic Materials group. Thanks go to my predecessor Necdet Onur Urs, who showed and trained me in all the various techniques and gave me the basics to start my work. Thanks also go to Enno Lage, who besides his nice and interesting discussions gave valuable input on improving the presentation of my scientific data. Special thanks go also to my officemates Cai Müller, Rasmus B. Holländer, Finn Klingbeil and Simon Jarausch for their amusing and interesting discussions and for simply giving me a friendly and comfortable working environment, where the time flew fast by. For nice conversations about various topics I thank also Umer Sajad and Farzaneh Karmiran that made my days in the office that much more interesting. I specifically also thank Umer for taking the time to read thoroughly my work and providing invaluable input to it. For all the scientific support in the lab and in the office, I thank all before mentioned and also Findan Block, Malte Römer-Stumm and Babak Mozooni. Special thanks also go to our secretary Ellen Riemer, who helped me all these years with various bureaucratic things at which she always did it with a smile and accompanying pleasant words. Thanks also go to visiting researchers Fasheng Qiu and Oh-Youl Kwon with whom I had the pleasure to collaborate and learn about electrical steels and their characterization.

Another collection of thanks goes to the massive group of the CRC 1261: Magnetoelectric Sensors: From Composite Materials to Biomagnetic Diagnostics. A more specific thanks goes to members I worked closely with and have provided in various ways input to my

work: Eckhard Quandt, Reinhard Knöchel, Michael Höft, Fabian Lofink, Jeffrey McCord, Dirk Meyners, Phillip Durdaut, Eric Elzenheimer, Patrick Hayes, Christine Kirchhof, Anne Kittmann, Viktor Schell, Matthias Krantz, Rahel Kruppe, Nils Lukat, Mona Mintken, Volker Röbisch, Lars Thormählen, Sebastian Toxværd, Alexander Teplyuk, Sebastian Zabel, Benjamin Spetzler and Erdem Yarar. I specifically want to thank Lars Thormählen, Volker Röbisch, Sebastian Toxværd, Patrick Hayes and Rahel Kruppe for the preparation of various samples, sensors and measurements of them, that were needed for the successful outcome of this work. Even more special thanks go to Lars for his fantastic positive energy and comradeship that gave the project A1 a more unique and strong character, making the work that much more pleasant and fruitful.

Grateful thanks also go to the German Research Foundation DFG for funding the CRC, giving us the chance to realize our ideas into models, measurements, results and finally sensors, which will drive the research of biomagnetic sensing forward.

I am also grateful to Stefania Pizzini and her impressive team at the Institute Néel for taking me as a visiting researcher and making me feel as one of their own. Thanks also go to Laurent Vila and Toshiki Gushi for giving me the chance to be a part of the very interesting work that was done during my research stay. Thanks also go to Marlio Bonfirm who gave me some insight into electronics and coil designs and helping me with wire bonding of samples. Thank you all in Grenoble for teaching me so many new things about magnetism and spintronics.

Additional thanks go to my Bachelor and Master students Jakob Horn, Mona Mintken and James Nwafor for their valuable research input to this work. Thanks also go to our technician Sandra Robien as well as workshop leaders Berndt Neumann, Matthias Burmeister and their team for creating various designs and parts that were much needed for many conducted experiments. Small thanks also go to Mr. Dragon for his input and corrections on my writing of this work.

Finally, my gratitude goes also to my family and my wonderful wife Patricia, who has supported me and stood by my side even at the most difficult moments. Her energy and passion as a researcher have inspired me to go further and deeper into my work resulting in several important breakthroughs to occur in my work. Thank you, Patricia, for seeing in me the best and filling my heart with joy and love, which enriched my life these many years and gave me the essence to become the person I am today.

Abbreviations

ME	**Magnetoelectric**
LOD	**Limit of detection**
MOKE	**Magneto-optical Kerr effect**
MO	**Magneto-optical**
FM	**Ferromagnet**
AFM	**Antiferromagnet**
t_{FM}	**Ferromagnetic thickness**
M_S	**Saturation magnetization**
K_u	**Uniaxial magnetic anisotropy**
K_σ	**Stress induced anisotropy**
H_k	**Anisotropy field**
H_{dem}	**Demagnetization field**
H_{str}	**Stray field**
EB	**Exchange bias**
PEB	**Parallel exchange bias**
APEB	**Antiparallel exchange bias**
H_{EB}	**Exchange bias field**

Abstract

Current composite magnetoelectric (ME) sensors of cantilever design have shown promising properties and positive tendencies toward sensor applications in biomagnetic sensing. Despite great signal performance, the sensors have limitations, resulting from noise generated by the magnetic phase. The magnetically induced noise dominates the sensors performance even further when low frequency signals are probed, using magnetic frequency conversion (MFC). The work orients around this specific impediment and provides various techniques to suppress the noise sources, originating from the magnetic phase.

In the beginning, the work reviews the effectiveness of multilayer exchange bias (EB) systems that were used to reduce magnetic noise. An improvement of the system is introduced that allowed increased signal yield. However, the noise response could not be improved. For this reason, a new magnetic multilayer system dubbed antiparallel exchange bias (APEB) is introduced, which is formed with a specialized post-production heating scheme.

The developed coupling allows formation of a stable magnetic configuration, leading to a significant reduction of the magnetic noise. Incorporated into the ME sensors, the APEB yields improvement in their limit of detection (LOD) and reproducibility of their sensing properties. The sensors were characterized electrically as well as magnetically using magneto-optical Kerr effect microscopy. In their finalized form, the sensors exhibit a significantly decreased noise behavior, demonstrating a voltage noise threshold below 10^{-7} V/Hz$^{1/2}$ at optimal working parameters at 10 Hz during MFC operation. The sensors demonstrate more than two orders of magnitude and one order of magnitude lower noise level in comparison to conventional single layer sensors and multilayer exchange biased sensors respectively. The sensors demonstrate noise limitations only by the thermo-mechanical noise level with application of MFC.

Thickness increase of individual ferromagnetic layers and variation of anisotropy alignment was performed to counteract the reduction of the signal output, whilst

upholding the low noise behavior. The new sensors with a total ferromagnetic thickness of 4 µm provided an LOD of 50 pT/Hz$^{1/2}$ at 10 Hz.

Within this work also MOKE analysis of sensor behavior during electrical excitation was performed. The effect and mechanism of the electrical excitation on the domain construct is investigated for single layer as well as multilayer (AP)EB systems. Preliminary measurements of such sensors already indicated an LOD of 30 pT/Hz$^{1/2}$ at 10 Hz.

The final part of the dissertation revolves around the minimization of edge effects that plague the sensor designs and form a major noise source in the magnetic phase. To circumvent this effect, an investigation of various patterned edges was employed in order to induce the stress effect complementary to the desired magnetic anisotropy direction.

In conclusion, this work provides significant research in the field of magnetic domain manipulation and magnetic domain stabilization that is not limited in applicability to ME sensors. It spans also to other sensors that utilize magnetic layers for the sensing of magnetic fields. Furthermore, the newly developed concepts could be implemented into other devices utilizing magnetic thin film components such as energy harvesters, magnetic shielding and magnetic recordings.

Key words: magnetoelectric sensors, magnetometers, biomagnetic sensing, magnetic noise, magnetic domains, magneto-optical Kerr effect, multilayer magnetic thin films, exchange bias, antiparallel exchange bias, thin film edge patterning

Zusammenfassung

Gegenwärtige magnetoelektrische (ME) Kompositsensoren, die auf einem Biegebalkendesign beruhen, besitzen vielversprechende Eigenschaften bezüglich der Anwendung als Magnetfeldsensor zur Detektion biomagnetischer Signale. Trotz der hohen Signalamplitude weisen diese Sensoren Einschränkungen auf, die auf von der ferromagnetischen Phase erzeugten Rauschbeiträgen beruhen. Diese magnetisch induzierten Rauschbeiträge dominieren die Sensorleistung, insbesondere wenn Niederfrequenzsignale mit der sogenannten magnetischen Frequenzumwandlung (MFC) abgetastet werden. Der Fokus der Arbeit liegt daher auf diesem spezifischen Problem, und es werden verschiedene Techniken aufgezeigt, um die von der magnetischen Phase herrührenden Rauschquellen zu unterdrücken.

Zu Beginn der Arbeit wurde die Wirksamkeit von mehrschichtigen Exchange-Bias (EB) Systemen untersucht, die bereits zur Reduktion des magnetischen Rauschens eingesetzt werden. Durch eine Verbesserung des Systems konnte eine erhöhte Signalausbeute ermöglicht, jedoch das Rauschverhalten nicht verbessert werden. Aus diesem Grund wurde ein magnetisches Mehrschichtsystem, "Antiparallel Exchange Bias" (APEB), eingeführt. Das neue System wird mittels einer speziellen Temperaturnachbehandlung hergestellt.

Das neu entwickelte Kopplungsschema ermöglicht die Bildung einer stabilen magnetischen Konfiguration, welche zu einer signifikanten Reduzierung des magnetischen Rauschens führt. Zusätzlich verbessert das APEB die Nachweisgrenze (LOD) und die Reproduzierbarkeit der Sensoreigenschaften. Die Charakterisierung der Sensoren wurden sowohl elektrisch als auch magnetisch mittels magnetooptischer Kerr-Effekt (MOKE) Mikroskopie durchgeführt. In ihrer endgültigen Form zeigen die Sensoren ein signifikant verringertes Rauschverhalten unter 10^{-7} V/Hz$^{1/2}$ bei 10 Hz bei optimalen Arbeitsparametern während der Anwendung von MFC. Die Sensoren weisen damit einen mehr als zwei Größenordnungen bzw. eine Größenordnung niedrigeren Rauschpegel im Vergleich zu herkömmlichen Einzelschichtsensoren bzw. herkömmlichen

mehrschichtigen EB Sensoren auf. Die Performance der Sensoren ist damit auch bei der Verwendung von MFC nur durch das thermomechanische Rauschen begrenzt.

Eine Erhöhung der Schichtdicke der einzelnen ferromagnetischen Schichten sowie eine Variation der magnetischen Anisotropieausrichtung wurden durchgeführt, um der einhergehenden Verringerung der Signalamplitude entgegenzuwirken und dabei trotzdem das rauscharme Verhalten beizubehalten. Die Sensoren mit einer ferromagnetischen Gesamtdicke von 4 µm und angeregt mit MFC lieferten ein LOD von 50 pT/Hz$^{1/2}$ bei 10 Hz.

Im Rahmen dieser Arbeit wurden zusätzliche MOKE-Analysen des Sensorverhaltens während elektrischer Modulation durchgeführt. Der Effekt und Mechanismus der elektrischen Anregung auf das Domänenverhalten wurden sowohl für Einzelschicht-systeme als auch für mehrschichtige EB-Systeme untersucht. Für diese Anregungsmethode wurden auch spezielle APEB Sensoren entwickelt. Vorläufige Messungen der Sensoren zeigten bereits ein LOD von 30 pT/Hz$^{1/2}$ bei 10 Hz.

Der letzte Teil der Dissertation befasst sich mit der Minimierung von Randeffekten, die die Hauptstörquellen in der magnetischen Phase bilden. Um diese Effekte zu umgehen, wurde eine Untersuchung verschiedener Kantenstrukturen zur Induktion des Spannungseffektes komplementär zur gewünschten Anisotropieausrichtung durchgeführt.

Zusammenfassend liefert diese Arbeit einen bedeutenden Fortschritt auf dem Gebiet der magnetischen Domänenmanipulation und Domänenstabilisierung, die nicht nur auf ME-Sensoren anwendbar ist, sondern auch auf andere Sensortypen, die Magnetschichten zum Erfassen von Magnetfeldern verwenden. Darüber hinaus könnten die neu entwickelten Konzepte in andere Gebieten implementiert werden, die magnetische Dünnschichtkomponenten verwenden. Dazu gehören sogenannte Energy Harvester, magnetische Abschirmungen und magnetische Datenspeicher.

Schlüsselwörter: **magnetoelektrische Sensoren, Magnetometer, biomagnetische Abtastung, magnetisches Rauschen, magnetische Domänen, magneto-optischer Kerreffekt, mehrschichtige magnetische Dünnschichten, Exchange Bias, antiparalleles Exchange Bias, Dünnschichtkantenstrukturierung**

Contents

Chapter 1

Introduction and basics

1.1 Introduction

Magnetically induced noise has induced persistent limitations in various applications, from electrical components such as transformers [1] down to filters [2], magnetic shielding [3] [4] and sensors [5] [6]. Magnetic noise originates from irreversible and spontaneous magnetization changes such as Barkhausen jumps [7] and magnetization switching [8]. In the past, the development of such noise has been omitted by selecting harder magnetic materials that allowed stable domain configuration to form. However, for applications such as magnetic field sensors, the magnetic component has to be soft as to allow sensitivity of low magnetic fields into ranges below μT. For this reason specialized shaping [9]–[11], biasing [12] [13] and construct of multilayered magnetic materials [14] [15] were performed on very soft magnetic materials to attain low-noise magnetic properties. The resulting effect for all solutions is the need of balancing or tradeoff between sensitivity and noise performance. In this work, this specific problematic is challenged, basing the research on magnetoelectric (ME) sensors, which sustain similar noise limitations as other magnetic field sensors. The goal of the research is to develop novel techniques that support high-sensitive, low-noise magnetic layer systems for integration into composite ME sensors.

Current composite ME sensors of thin film cantilever design have shown promising properties and shown positive tendencies toward sensor applications in biomagnetic sensing [16]. Due to various methods and sensor subtypes, they provide high versatility, from usage at room temperature to flexible form and arrangement in arrays. They deliver also very high spatial resolution due to the possibility of miniaturization and integration into chip designs [17] [18]. They exert also the possibility to be tunable and easier to handle than other sensors for biomagnetic sensing [19]. Current research has delivered sensors reaching limit of detection (LOD) as low as 400 fT/Hz at resonance frequency [20]. However, their relatively low sensitivity (range of 10 nT [20]) in the low frequency regime (1-100 Hz) reduces their functionality for low signal biomagnetic measurements, such as brain monitoring. For this reason, several concepts (exact sensor subtypes are explained in section 2.1) have been developed to make the sensors capable of sensing low frequency, low amplitude magnetic signals.

The best sensors before this work provide a LOD of 300 pT/Hz$^{1/2}$ at 1 Hz [21]–[23]. However, such LOD is still insufficient for measurement of biomagnetic signals exerted by the human body. This current drawback has been extensively researched [13] [21], [24] [25] and latest research has shown that the insufficient sensitivity of these sensors is due to high magnetically induced noise exerted by the magnetostrictive part of the composite sensor [24] [25]. This has been determined and measured by Kerr effect microscopy with support of electrical measurements and noise characterization [24]. This also confirmed the correlation between domain wall motion and domain switching with signal to noise ratio of the sensors [24]. In order to reduce such noise formations, a more stable and controllable domain configuration must be incorporated into the magnetostrictive phase of the sensor. Composite thin film ME sensors have the possibility to be flexibly manipulated in terms of their magnetic phase as they are prepared with sputtering technique [21]. With it, integration of multilayer structures with various magnetic coupling mechanisms as well as specialized shape structuring with lithographic processes is possible. All these points are also the main topic of this research and they are discussed individually in detail more in further chapters. With the new concepts described in this work a new generation of ME sensors was developed with substantially better noise performance, resulting in improved sensitivity and quality of the sensors. With the establishment of these new sensors, this research provides a new stepping-stone towards ultra-low noise ME sensor applications.

To give the reader an overview of the theory behind the experiments, the basic magnetic quantities and effects are discussed further on. Since the core of this work is devoted to attaining better performance of ME sensors, the current progress of these sensors as well as certain competing magnetic field sensors are presented and described separately in Chapter 2. Additionally, at the end of that chapter a comparison is given between the ME sensors developed within the Collaborative Research Center (CRC) 1261 and the competing sensor concepts developed for biomagnetic sensing applications. The subsequent chapter is devoted to the experimental and modeling techniques used within this research. From there onwards, the work dives into the topic of magnetically induced noise and providing examples of various noise sources and their specifics in basic model structures. In Chapter 5 the first research topic of parallel exchange bias is covered followed by the main topic antiparallel exchange bias in the next chapter. The possibilities of modifying the antiparallel exchange bias system are presented in Chapter 7. In Chapter 8, domain analysis of sensors utilized for electrical modulation technique is presented. In this chapter, an insight is given on the domain behavior and noise mechanisms. In the last chapter, the effects of edge structuring are described and analyzed. The work concludes with a short synopsis and conclusions of the whole work, indicating also the possibilities for future work on the researched topics. Appended to this work is also the so-called B-side of research. It is intended to act as a repository of data, which is not directly connected with the topic at hand, but is of high scientific value and potential to be further researched.

1.2 Basic magnetic quantities and their interplay

As the whole work is devoted to magnetic properties of magnetic thin films, the basic quantities that drive magnetism in a ferromagnetic material are explained.

Static magnetism and domain formation in a ferromagnetic material can be described by a series of energy terms that contribute to the overall energy of a magnetic material. In this part, each individual energy term and its effect on the total energy term are shortly described. The total magnetic energy consists of the following energies:

$$E_{total} = E_{exch} + E_{Zee} + E_{str} + E_{aniso} + E_{si} + E_{ms} \qquad \textbf{(1.1)}$$

Where E_{exch} is the exchange energy, E_{Zee} is the Zeeman energy, E_{str} is the stray field energy, E_{aniso} is the total anisotropy energy, E_{si} is the stress-induced anisotropy energy and E_{ms} is the magnetostrictive energy [26].

1.2.1 Exchange energy

The exchange energy term is determined by the interaction of localized electron magnetic moments within a material. Due to the two possible spin orientations of the electrons, the interaction is limited by the outcome of the spins being either parallel or antiparallel to each other due to the Pauli Exclusion Principle. The first possibility results in formation of ferromagnetism, for which the parallel coupled spins form spontaneous magnetization in the material. The second outcome induces the antiferromagnetic coupling, which results in a zero net magnetization as the antiparallel magnetization moments cancel each other out. The following equation describes such interaction and gives the exchange energy in a certain volume:

$$E_{exch} = \int -2J_{ex}(S_a \cdot S_b)dV \qquad (1.2)$$

J_{ex} is the exchange constant, which determines the magnitude and type of exchange, whereas S_a and S_b indicate the local spins of two neighboring atoms [26]. The exchange energy term can be used for a multitude of materials as well as at the interface, when two different magnetic materials physically meet. This applicability is especially important for the determination of interlayer exchange coupling and exchange bias coupling which are discussed in subchapters 1.2.4.3 and 1.2.4.4 respectively. It is important to mention that the ordering resulting from the exchange interaction dissipates with increasing temperature. This dependency is formed due to a swiveling motion of the two neighboring spins from the minimal energy state. The motion causes the angle between the spins to change temporally and with enough thermal energy the spins behave decoupled leading to a paramagnetic behavior of the magnetic material. Temperature at which this transition occurs is named the Curie temperature T_C and Néel temperature T_N for a ferromagnetic (FM) and antiferromagnetic (AFM) material respectively. Since the J_{ex} is a quantum mechanical term, it is relatively hard to determine it precisely from experimental

results. For this reason, the equation (1.2) can be modified into another form when the material is isotropic and consists of one atom type:

$$E_{exch} = A \int (grad\ m)^2 dV\ , \tag{1.3}$$

where

$$A = \frac{J_{ex} \cdot S^2}{a} \tag{1.4}$$

***A* is the exchange stiffness and *m* is the local magnetization. In equation (1.4), *a* represents the lattice parameter for a cubic structured material [26] and *S* is the local spin. The exchange stiffness is an important parameter as it encompasses all the quantum related quantities, making it much easier to extract from experimental measurements compared to J_{ex}. With the final equation (1.3) it can be understood that any variation of the magnetization from the minimal energy state will result in an increase of the total energy E_{total} .**

1.2.2 Zeeman energy

The Zeeman, also known as external magnetic field energy determines the magnetization *M* response to an externally applied magnetic field H_{ext}. The relation is given by the scalar product in equation (1.5)

$$E_{Zee} = -\int \left[\mu_0\, \vec{H}_{ext} \cdot \vec{M}\ \right] dV = -\int \left[\mu_0\, H_{ext}\, M\ cos(\beta)\right] dV\ , \tag{1.5}$$

where μ_0 is the magnetic permeability of vacuum and β is the angle between H_{ext} and *M*. This equation explains that the energy is reduced when *M* lies closer to the axis of *H* and becomes largest when the two vectors are antiparallel [26]. This energy term in principle also explains the resulting torque exerted on the magnetization by the applied field.

1.2.3 Stray field energy

A magnetic material without any externally applied field will generate a magnetic field originating from its internal magnetization configuration. The formation of such a field comes directly from the Maxwell's equation, stating the divergence of magnetic flux *B* equals: $div\ \boldsymbol{B} = div(\mu_0 \boldsymbol{H} + \boldsymbol{M}) = 0$. Because of the equivalence, the material forms closed loops of magnetic field correspondingly to the formed magnetization within the material. Since $div\ \boldsymbol{B} = 0$, the flux forms two sets of magnetic fields of equal magnitude, but in opposite sign (Figure 1(a)). One is generated outside of the material, denoted as stray field H_{str} and the other is generated inside the material, named as demagnetizing field H_{dem}. The energy exerted by either of these fields can be expressed as:

$$E_{str} = \frac{1}{2}\mu_0 \int_{all\ space} H_{str}^2\ dV = \frac{1}{2}\mu_0 \int_{sample} H_{str}\ M\ dV\ ;\ H_{str} = -H_{dem} \qquad (1.6)$$

The H_{str} is proportional to the saturation magnetization M_S, at which the exact shape of the loops also depends on the magnetization alignment. The shape dependency can be expressed for individual coordinate directions with the so-called demagnetization factor N_i. The sum of the demagnetization factors of all principle axes must always equal unity. For an ellipsoid shaped material, the general formulation presented in equation (1.7) can be applied [26] [27]:

$$H_{str,i} = N_i M_s \qquad (1.7)$$

Since this work emphasizes on thin film magnetic materials, only the formulations for an extended magnetic film is discussed further on. When an infinitely extended magnetic film is magnetized along its thickness, then the *N* along that dimension is unity, whereas the other two axes exhibit *N* equal to zero. The final equation of E_{str} is then:

$$E_{str} = \int \frac{1}{2}\mu_0\ M_s^2\ dV \qquad (1.8)$$

The final equation however is limited in applicability, as produced magnetic films have finite lateral dimensions and the equation only provides the overall demagnetization effects. In fact *N* is a function of position and the local magnetization [28].

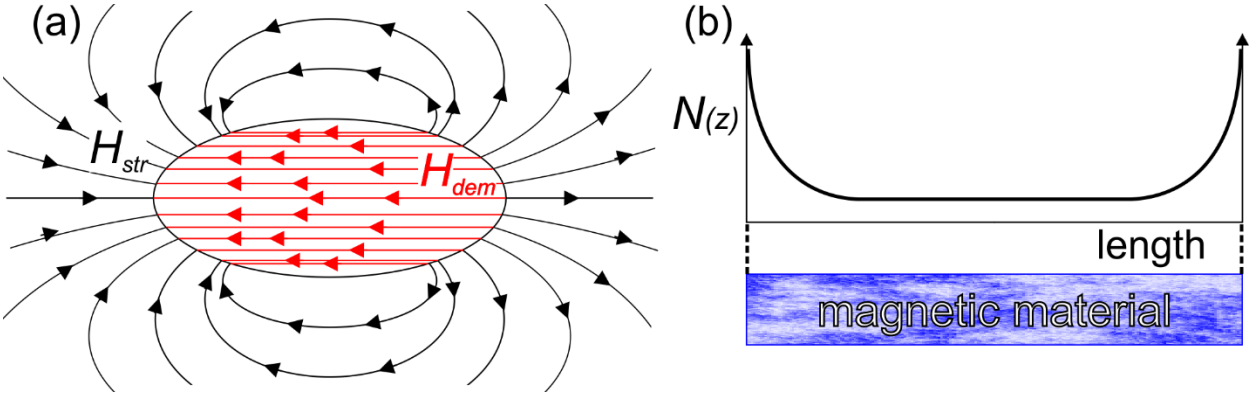

Figure 1: **(a)** Schematic of the resulting stray field H_{str} and demagnetization field H_{dem} generated in an ellipsoid. **(b)** Schematic plot of the local demagnetization factor $N(z)$ independent of material thickness over the length of the material. Adapted from [29].

Through the work of Aharoni [29], this is especially visible for structures with edges and corners, as the demagnetization effects increase towards infinity from middle to the edge of the structure (Figure 1(b)). The exact calculation of demagnetization factors for a finite thin film is further discussed in section 3.2.

1.2.4 Anisotropy energy

The anisotropy energy term is constructed by the sum of individual anisotropy terms, which are discussed individually further in this subchapter.

1.2.4.1 Magnetocrystalline anisotropy

The most basic anisotropy is the magnetocrystalline anisotropy. It originates from the spin-orbit coupling and the lattice-orbit coupling. This means, when a magnetic material has a crystalline structure, the electron orbits become quenched and deformed by the lattice structure. This leads to a formation of energetically more favorable coupling axes that can be distinguished when an external magnetic field is applied to the material. For a cubic crystal structure, an expression is given for the total magnetocrystalline anisotropy energy E_{mca}:

$$E_{mca} = \int K_1\left(m_x^2 m_y^2 + m_y^2 m_z^2 + m_x^2 m_z^2\right) + K_2(m_x^2 m_y^2 m_z^2) \qquad (1.9)$$

The parameters m_x, m_y and m_z represent the directional cosines in the noted axes, whereas K_1 and K_2 represent the temperature dependent anisotropy constants. Depending on the material and its structure, the values of anisotropy constants change appropriately and can therefore lead to different energy character of individual directions. As a typical example, the family of directions <100> is determined as easy axis for Fe (BCC), whereas for Ni (FCC) it is deemed as the hard axis [26]. It should be clear that the above equation explains only the E_{mca} of an individual crystallite. This means, that in order to get the overall anisotropy behavior of a polycrystalline material a projection of the energy states needs to be done in the selected Cartesian space.

1.2.4.2 Magnetization induced anisotropy

In order to gain an anisotropy effect in a magnetic material, it is also possible to form a short-range ordering of the spins. The modified ordering forms a uniaxial anisotropy K_u in the material [30]. This is mostly applied on amorphous and polycrystalline materials. In practice it is possible to induce the anisotropy during material deposition or by means of heating the material in an external magnetic field to a temperature, where the diffusion is sufficient for alignment of atoms along the field direction [31]. To form a uniform anisotropy inside the whole material, the field has to be sufficiently high to saturate it. It is also important to keep the temperature under Curie temperature T_c, otherwise the diffusion cannot be influenced by the directional effective field exerted by the magnetization, resulting in an unordered state. For a uniformly aligned anisotropy, the energy E_{mia} can be expressed as:

$$E_{mia} = \int K_u sin^2\theta \; dV \qquad (1.10)$$

The θ is the angle between the magnetization and K_u. The K_u can be approximately determined from the magnetization loops measured along the easy and hard axis. As depicted in Figure 2(a), the differential area between the two curves gives the anisotropy energy equal to K_u: Another characteristic value of such anisotropy is the anisotropy field H_k which can be determined as the field at which the linear slope from the middle part of

the hard axis meets the easy axis loop (Figure 2(a)). Using this parameter K_u can be mathematically determined:

$$K_u = \frac{1}{2} H_k M_s \tag{1.11}$$

However, this is only possible when only the field-induced anisotropy is present and the shape of the material has equal effect on the loops (for instance circular shaped thin film samples).

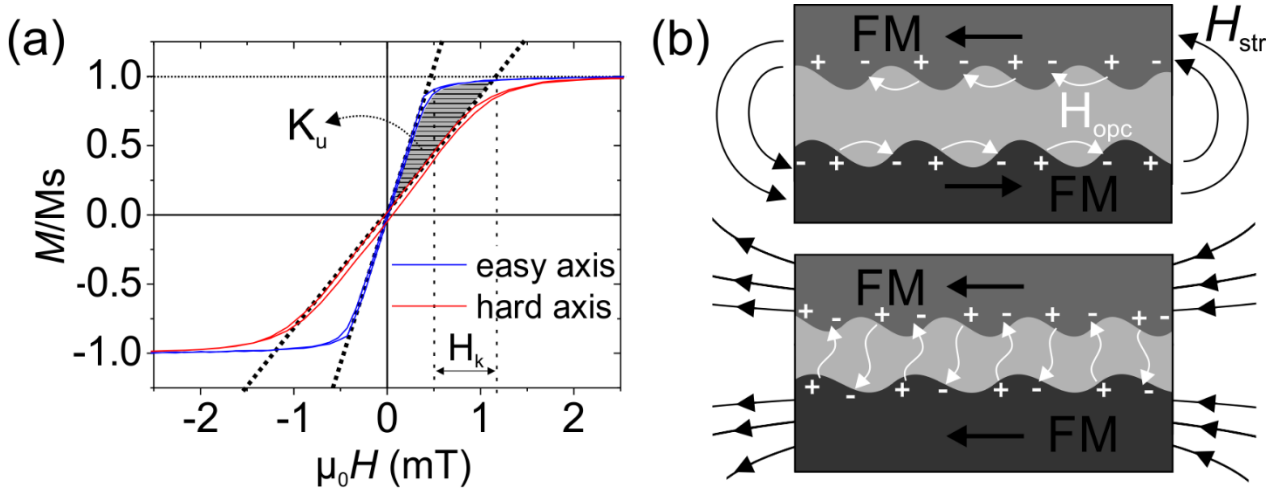

Figure 2: **(a)** Diagram with easy and hard axis magnetization loops. The grayed area represents the uniaxial anisotropy K_u and the corresponding anisotropy field H_k is marked. **(b)** Representation of orange-peel coupling for both possible cases. In the sketch above the FM layers are antiparallel to each other as the coupling is insufficient to overcome the stray field coupling of the layers. Below the opposite case is sketched, where the internal flux closure formed by orange-peel coupling compensates the increased state of Zeeman energy generated by the larger flux closure of the stray field H_{str}.

1.2.4.3 Interlayer and interface exchange coupling

Anisotropy formation is not limited to only one material. The interaction of multiple magnetic materials coupled directly or indirectly through a so-called spacer layer can also generate an anisotropy effect. In the simplest example, two different FM materials can be formed by having a common structural interface (for instance two thin films deposited one over the other). To simplify the explanation, one of the FM is magnetically softer (meaning smaller intrinsic coercivity) than the other. Their mutual interaction leads to local coupling of the spins of the two materials, which creates a lag in the rotation of the spins from the magnetically softer material when an external magnetic field is

applied. As a result an offset in the magnetization response occurs for the soft FM along the field axis [28]. The resulting unidirectional FM - FM coupling anisotropy K_{FF} forms the following energy term E_{FF}, where θ is the angle between the magnetization of the soft FM and the anisotropy direction (bound to magnetization direction of the hard FM):

$$E_{FF} = -\int K_{FF} \cos\theta \, dV \tag{1.12}$$

Another coupling possibility is to contact the two FM materials with a non-magnetic layer (named also spacer layer) made of rare-earth transition metal. In this case the resulting coupling of the two layers varies depending on the thickness of the spacer layer, which can result in either FM (parallel) or AFM (antiparallel) coupling. A model named Ruderman-Kittel-Kasuya-Yoshida (RKKY) model was established to predict the variation of the coupling strength and coupling type with varying spacer thickness [32] [33].

A completely different setting of anisotropy can be achieved due to magnetostatic interaction of multilayers separated by nonmagnetic spacer layers. Such coupling is formed as the H_{str} of neighboring FM layers couple into a closed flux in order to reduce the Zeeman energy. As a result, the layers are aligned antiparallel. Additionally, compared to the previous two coupling mechanisms, the stray field coupling is not homogeneous throughout the interface. Instead, the coupling is only homogeneous in the middle and near the structural edges of the layers, where the coupling is enhanced. The coupling however does not necessarily have to be parallel. In the case of roughness at the interfaces of the FM and spacer layer charging of the surfaces occur. The charging can then form internally generated H_{str}, which can couple the dimples and hills of the rough surfaces of neighboring layers. The effect is called orange-peel or Néel coupling [34]. A sketch of such coupling is presented in Figure 2(b). The resulting coupling can have antiparallel or parallel coupling effects, depending on several parameters of the interface. In equation (1.13) developed by Néel the resulting energy term of orange-peel coupling is given [35]:

$$E_{OPC} = -\frac{\pi^2 \mu_0 h^2 M_s M_s'}{\sqrt{2}\lambda} e^{-\left(\frac{2\pi t\sqrt{2}}{\lambda}\right)} \tag{1.13}$$

The energy term and the coupling depend on the thickness of the spacer layer *h*, the saturation magnetization of both layers M_s, M_s' and the wavelength of the roughness λ.

1.2.4.4 Exchange bias

An even more specific, but often used coupling is the so-called exchange bias (EB) coupling, where a FM is in direct contact with an AFM. The effect in the simplest form creates a shift in the magnetization curve of the FM. The shift is experimentally characterized by reading the corresponding exchange bias field H_{EB}, which is a macroscopic evaluation of the EB coupling and its strength (Figure 3(a)). In practice, to achieve reasonable EB effect, the AFM has to have a directional structure by having a preferred growth direction (polycrystalline material). This allows the restructuring of the AFM moments in the same fashion during its deposition on a saturated FM material or with a heating step while applying, for the FM, saturating magnetic fields (known as field cooling). For proper EB alignment, the temperature has to be in a specific range determined by the materials. The temperature should not be below the blocking temperature T_B of the AFM. Above this temperature, the magnetic moments of the AFM become loosely coupled, which allows diffusional reorientation of the spins in the direction of the neighboring FM spins. For thin films T_B scales with the AFM thickness t_{AFM} until it reaches the value of T_N. However, the T_B is not straightforward to determine for the whole AFM, as it depends on the individual crystal size as well as on the magnetocrystalline energy of each crystal. In regards to the scaling of the EB strength i.e. magnitude of H_{EB}, it is inversely proportional to the thickness of the FM t_{FM}, whereas it increases with the t_{AFM}, but only to a critical value and then it either stagnates or decreases further on [36]. With keeping the t_{AFM} constant, the resulting H_{EB} can be calculated:

$$H_{EB} = \frac{J_{EB}}{M_S \cdot t_{FM} \cdot \mu_0}, \qquad (1.14)$$

where J_{EB} is the exchange energy constant of the interface between FM and AFM. In order to understand the exact meaning of J_{EB}, a microscopic view of the interface has to be considered.

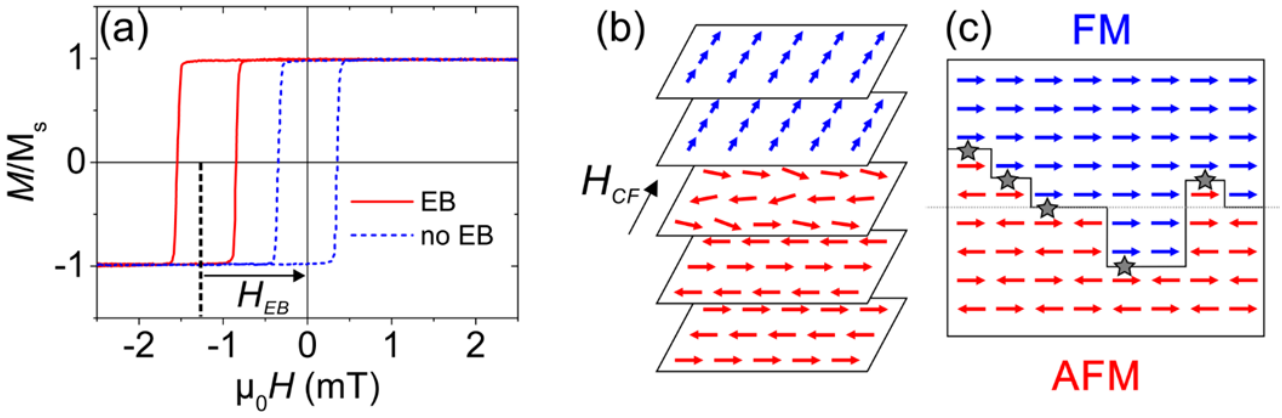

Figure 3: **(a)** An exemplary plot of a magnetization loop with and without EB coupling. The dark arrow indicates the corresponding shift of the loop due to EB. The newly formed middle position of the loop is marked by the dashed line, which also marks the value of the H_{EB}. On right hand side, models of EB coupling of **(b)** orthogonal magnetic lattices and **(c)** random interface model are sketched. The red and blue arrows represent individual AFM and FM spins respectively. In (b) the sections represent the individual monolayers of each material close to the interface. The cooling field H_{CF} direction is marked with an arrow. In **(c)** the dark full line denotes the randomized rough interface. The dashed line represents the mean interface level. The stars indicate the frustrated positions formed at the interface. Note: the model examples yield opposite EB effects, **(b)** positive EB, **(c)** negative EB. **(b)** and **(c)** adapted from [37].

Although EB has been discovered already in 1956 by Meiklejohn and Bean [38] the exact mechanism of the coupling on the microscopic scale is still not completely understood and several theories have been proposed to explain the origin of this effect. Here only the model of Schulthess and Butler [39] [40] is discussed further on, as it provides a comprehensible explanation of the effect. The model is constructed out of two separate models developed beforehand and then adjoined and adapted by the previously mentioned authors. First model determines that the ground state of magnetic moments of the AFM is perpendicularly aligned to the FM moments. In addition, it also determines that the AFM moments are canted in the region of the interface by a small angle relative to the easy axis of the FM opposite to the cooling field (Figure 3(b)) [41]. This was an important step as this theory can explain the interface structure of the local spins with compensated structure and explain why positive EB [42] [43] can form with the application of high cooling fields. However, this model is insufficient to explain the effective H_{EB} as the canted spins cannot create a reasonable directionality and with it unidirectional anisotropy. The other model explains the generated H_{EB} by means of variation of the interface in terms of defects. This means that uneven number of spins is formed, which creates uncompensated segments at the interface (Figure 3(c)). This

leads to generation of random magnetic fields that influence the local spins at the interface, which henceforth yield a unidirectional anisotropy. The resulting state generates H_{EB} equal to values obtained experimentally [44]. The drawback of this model is the dependency of the system to inherent defects and their number at the interface, which makes the model rather vague in terms of experimental analysis and results. Despite such shortcomings of both models, the conjoining of the orthogonal arrangement with defect induced random magnetic field and canted magnetic moments of the AFM at the interface yields significantly better results and comprehension of the mechanism. The devised dipolar energy term, defined by the conjoined model, is given in equation (1.15) [40]:

$$E_D = \sum_{i \neq j} \frac{[\,\vec{\mu}_i \cdot \vec{\mu}_j - 3(\vec{\mu}_i \cdot \hat{n}_{ij})(\vec{\mu}_j \cdot \hat{n}_{ij})]}{\left|\vec{R}_i - \vec{R}_j\right|^3} = J_{EB} \qquad (1.15)$$

The $\vec{\mu}_i$ and $\vec{\mu}_j$ represent the local magnetic moment configurations, $\hat{n}_{ij}$ the unit vector pointing parallel to the resulting vector of the difference of positional vectors $\vec{R}_i$ and $\vec{R}_j$.

1.2.5 Stress-induced anisotropy energy

When a magnetic material is exposed to an external applied stress σ_{ext}, the material deforms due to its elasticity. In response to the newly reshaped volume, the magnetic energy rearranges to incorporate the additional anisotropy term induced by the stress. The microscopic explanation is the spin-orbit coupling, because of which the joint rotation of several spins causes a reshaping of the orbits, leading to a lattice displacement and dimensional change of the magnetic material. The reaction of the material is designated as magnetostriction and is characterized by the magnetostrictive tensor λ_s, which can become complex depending on the crystal structure and pre-given anisotropies of a material. The λ_s can be either positive or negative in sign, which gives the name to the magnetostriction in a specific axis correspondingly. However, for an isotropic material λ_s collapses to a single coefficient λ_{si}, which applies to all axes. The resulting energy term induced by σ_{ext}, which is applied at an angle θ to the magnetization, is given in equation (1.16) [26]:

$$E_{si} = -\int \frac{3}{2}\lambda_{si}\sigma_{ext}[\sin^2\theta]dV \qquad (1.16)$$

However, it needs to be considered, that the magnetostriction coefficient is dependent on temperature as well as on the stress state of the material [45]. The last dependency is discussed more in details in the next energy term.

1.2.6 Magnetostrictive self-energy

A magnetic material can also generate internal strains due to the previous mentioned magnetostriction without any externally applied stress. To compensate the increase of energy, the material rearranges the local magnetization by means of increasing the magneto-elastic energy E_{ME}. With the moderate increase in E_{ME} and the reduction of the flux , the E_{str} can be significantly decreased. The difficulty of calculating such behavior is not arbitrary as λ_s depends on the internal strain ε of the material. The change of λ_s with strain is given in equation (1.17) [46]:

$$\lambda_s(\varepsilon) = \lambda_s(0) + \frac{d\lambda_s}{d\varepsilon}\varepsilon\,, \qquad (1.17)$$

Where $\lambda_s(0)$ is the λ_s in a state with zero strain. Since it is known that the stress state is related to the resulting configuration of all local magnetizations, the equation (1.17) can be reformed to express the magnetization change dependency. In the simplest calculation, an ideal demagnetized state is firstly taken as it behaves magnetostrictively isotropic. Now, since the integral of the formula above gives a linear form, only the ending state, which is chosen as a random partial magnetized state, is needed for the calculation of final magnetostriction λ. As a result λ measured at an angle θ to the local magnetizations can be calculated with equation (1.18) [27]:

$$\lambda = \frac{3}{2}\lambda_{si}\left(\langle\cos^2\theta\rangle - \frac{1}{3}\right) \qquad (1.18)$$

The angled brackets indicate the average value of $\cos^2(\theta)$ over all magnetic moments. When the initial state is a saturated state, is a special case where all the magnetization

vectors M_s are pointing perpendicular to the observed magnetostriction axis. When comparing it with the ending random partial magnetized state the magnetization vectors M can be described as $M=M_S \cos(\theta)$. If put in equation (1.18) an interesting relation is revealed:

$$\lambda = \frac{3}{2}\lambda_{si}\left(\frac{M}{M_s}\right)^2 \qquad (1.19)$$

From equation (1.19), it is clear, that λ is proportional to M^2. This means, that antiparallel aligned magnetizations yield the same magnetostriction. This dependency, as it will be seen later in section 2.1 is a crucial property of the basic functional principle of ME sensors. From the dependency it is also clear that λ is not a constant, but changes with the hysterics of the material, leading to a formation of a nonlinear magnetostrictive response with H_{ext}. The evolution of the λ from a typical magnetic magnetization loop is given in Figure 4.

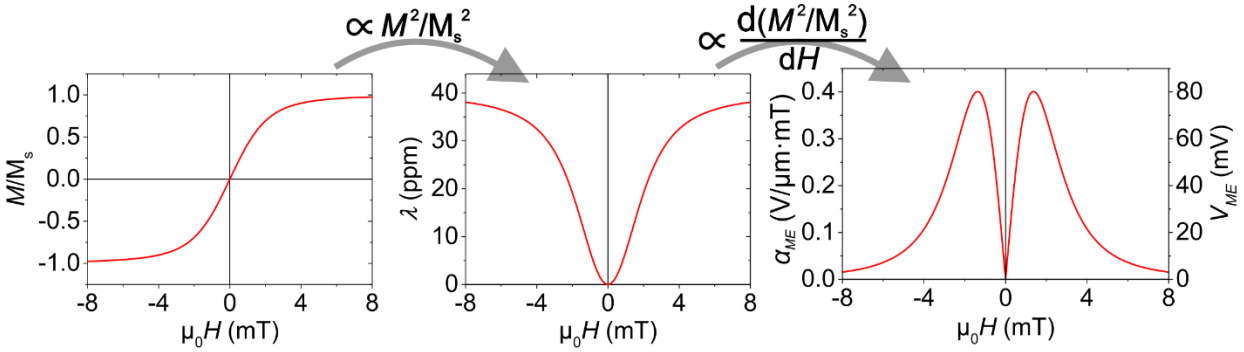

Figure 4: The transposition from a typical magnetization response with H_{ext} (left) to a magnetostriction response curve (middle) which is proportional to the square of M. From the derivative of the magnetostriction curve over field, the ME response can be obtained (right). The latter is also usually named as a bias curve of the ME response. The ME response is plotted with voltage response V_{ME} as well as with the ME coefficient α_{ME}. The last diagram shows, that the maximum ME response is achievable only with a certain bias field in either positive or negative direction. To note: arbitrary coefficients were given to allow both conversions to attain proper units by assuming that the coefficients are constants and the non-linear behavior is induced only by M.

Since the change of magnetostriction is directly proportional to the magneto-elastic energy density change, the magnetostrictive self-energy for an isotropic material can be described easily by the volume integral in equation (1.18):

$$E_{ms} = -\int \frac{3}{2}\lambda_{si}\left(\langle\cos^2\theta\rangle - \frac{1}{3}\right)dV \quad (1.20)$$

1.3 Magnetoelectric effect

Some magnetic materials can exhibit a very special effect named magnetoelectric (ME) effect. It dictates that a change in the dielectric polarization ***P*** of a material will occur when exposed to an external magnetic field H_{ext}. Conversely, when such a material is exposed to an electrical field E_{ext}, the magnetization ***M*** inside the material will change correspondingly based on the value of the ME tensor α of the material. For the material to exhibit ME effect, it needs to have the absence of time-reversal symmetry and space-inversion symmetry, which can be set by ferromagnetism and ferroelectricity respectively. The ME effect can be described by the following equations [47]:

$$P_i = \alpha_{ij} \cdot H_j \quad (1.21)$$

$$M_i = \alpha_{ji} \cdot E_j \quad (1.22)$$

It should be mentioned, that the above equations only describe the linear ME effect. Despite the relative complexity of having a 3x3 tensor for the ME effect, it can be easily decomposed to a single effective coefficient when the directions of the applied quantity and measured quantity are set. By converting the polarization into an electrical field response of the material, the equation (1.21) can be restated as a differential equation:

$$dE = \varepsilon_0\ \varepsilon_r\ \alpha\ dH_{ext} \quad (1.23)$$

The ε_0 is the electrical permittivity of space and ε_r is the relative permittivity of the material. By combining the permittivities and α, the most important figure of merit for ME materials is formed, named the ME voltage coefficient α_{ME}:

$$\alpha_{ME} = \varepsilon_0\ \varepsilon_r\ \alpha \quad (1.24)$$

This coefficient is very useful as it gives the direct relation of the exerted electrical field (or voltage V_{ME}) with the amount of externally applied magnetic field. The most commonly

used units for this coefficient is kV/(cm·Oe), however in order to comply with SI unit standard, V/(μm·mT) is used in this work. The units of V/A could also be used, however due to the indirectivity with the variables of the system, this form is not used. The α_{ME} behavior can be also explained in terms of magnetic susceptibility χ^m and electric susceptibility χ^e, at which the following relation is constructed:

$$\alpha_{ij} \leq \sqrt{\chi_{ii}^{m} \chi_{jj}^{e}} \tag{1.25}$$

Out of this dependency, the constraint of the system is visible, that the ME effect cannot be large in a single-phase material. The reason is that the two quantities are inversely bound due to structural dependencies of the two effects [48]. Nevertheless, this limitation can be eluded by forming a composite by conjoining a piezoelectric material with a magnetostrictive material. At which the piezoelectric material is a material that changes its dimension with E_{ext} and inversely, it generates a change of P with the application of σ_{ext}. The composite allows the transient ME effect, which means that the magnetic and electric quantities exchange from one to the other by a transformation through the stiffness and compliance matrix of both materials. By this, a new mathematical construct for α_{ME} is created by assembling the individual coefficients [48] [49]:

$$\alpha_{ME} = q_{ij,m} k_c d_{kl,p} = \frac{\partial \lambda}{\partial H_{ext}} \frac{\partial \sigma}{\partial \lambda} \frac{\partial E}{\partial \sigma} \tag{1.26}$$

Where $q_{ij,m}$, k_c and $d_{kl,p}$ are the piezomagnetic coefficient, interface coupling coefficient and piezoelectric coefficient respectively. The relations covered by individual coefficients are given on the right hand side of equation (1.26). The effective evolution of the ME response from a magnetic hysteresis by assuming the piezoelectric part as a constant is presented in Figure 4. With the composite ME effect a new opportunity opened up for the development of new devices such as energy harvesters, logic devices, tunable emitters as well as sensors [50].

Chapter 2

Magnetic field sensors

2.1 Composite ME field sensors

With the composite ME effect described in previous section, the development of new type of magnetic field sensors became a possibility. At the beginning the simplest example of a composite ME sensor was done by combining an amorphous Fe-B-Si magnetic ribbon adhered with a viscous medium to a piezoelectric PZT (lead zirconate titanate) plate. Such a bulk-type sensor (63.5 x 15.9 x 0.625 mm^3) could already demonstrate a minimum detectable field of 8.7 $pT/Hz^{1/2}$ at 1 Hz [51]. In later time newly developed bulk composite ME sensors utilizing PMN-PT (lead-based perovskite: $0.7{\cdot}Pb(Mg_{1/3}Nb_{2/3})O_3{-}0.3{\cdot}PbTiO_3$) for the piezoelectric phase, have reached the lowest detectable field of 5.1 $pT/Hz^{1/2}$ at 1 Hz [52]. However, due to their sturdy design the sensors provide poor spatial resolution and directional sensitivity. In contrast to them, sensors developed by wafer based thin film preparation can be processed in significantly smaller dimensions. The processing is done by depositing a piezoelectric material on one side of a substrate and the magnetostrictive layer on the opposite surface. Despite better spatial resolution and flexibility in terms of forming arrays, they have shown to detect magnetic fields only down to some 100 $pT/Hz^{1/2}$ at 1 Hz [21]–[23]. The reason is not in the magnetic component, as the thin film preparation allows higher control and tailoring of magnetic properties in

comparison to melt spinning with which the magnetic ribbon is produced for the bulk ME sensors [51] [52]. This allows the compensation of lower output due to lower thickness (range of 1 µm) with the much lower noise output. Instead, the reason is the severely lower piezoelectric output of the AlN, which is commonly used in thin film preparation. For an exemplar comparison the piezoelectric coefficient d_{31} is -3.53 pm/V [53] and -1231 pm/V [54] for AlN (0.5 – 2 µm thick) and PMN-PT (682 µm thick) respectively. Comparison shows the dominance of PMN-PT in its piezoelectric response, however, the drawback is in the material's hysteretic behavior and higher dielectric losses as well as the gradual decaying of its properties with time and temperature [55] [56]. The AlN is therefore used as it provides high thermal and temporal stability of its properties as well as a broad linear response with low losses and large signal to noise ratio [54]. Consequently, such material is purposely used for integration in the wafer designed ME sensors, which aim for a long lifetime and stable measurement output in various ambient conditions.

A possibility of how to use such a sensor is to design it in a cantilever form at which it is mechanically fixed from one side by either gluing, clamping or substrate shaping as a hanging structure. A sketch of such a sensor is given in Figure 5(a) with its layer structure presented in Figure 5(b). The sensor is then exposed to a magnetic field. Due to the magnetostrictive effect (see section 1.2.6), the magnetic layer either contracts or expands forming a bending motion. It is important to prepare the magnetic phase with an induced anisotropy perpendicular to the sensing axis of the sensor. This allows preferential domain formation with their magnetization set along the short axis. Such configuration allows gradual rotation of magnetization to occur with an applied magnetic field resulting from the Zeeman energy along the long axis (perpendicular to the K_u). Additionally, the configuration maximizes the sensors signal output as most of the beginning magnetizations lie in the same axis perpendicular to the applied field (see section 1.2.6). The displacement due to magnetostriction leads to a stress generated at the interface with the substrate and is mechanically transferred to the piezoelectric phase. In response, a polarization forms in the piezoelectric (see section 1.3) that can be read out as generated potential on the electrodes encompassing the piezoelectric phase. Now in most cases the response of the sensor is week due to low thickness of both phases, leading to a LOD of 1µT/Hz$^{1/2}$ at 1 Hz [57]. However, the response can be enhanced when the sensor is operated under certain conditions. In the next sections

selected methods of operation of the sensor developed within the CRC 1261 and used in this work, are shortly presented.

2.1.1 Direct mechanical resonance enhancement

The basis of all the methods of operation used in this work is improvement of the ME effect in a sensor by mechanical resonance enhancement. This results in an amplified bending motion of the cantilever, leading to an improved response of the sensor. With just setting the external excitation field to the resonance frequency f_{res}, the sensor's LoD improves from 1μT/Hz$^{1/2}$ at 1 Hz to 7.1 pT/Hz$^{1/2}$ at 669 Hz [57]. The sensors then also exert a high ME coefficient reaching a value of up to 7 kV/cmOe. The increased signal response of the sensor with frequencies close to the resonance is presented in Figure 5(c). With further improvement of the sensor's components and geometry a very good LoD of 400 fT/Hz at 876 Hz was achieved at the latest [20].

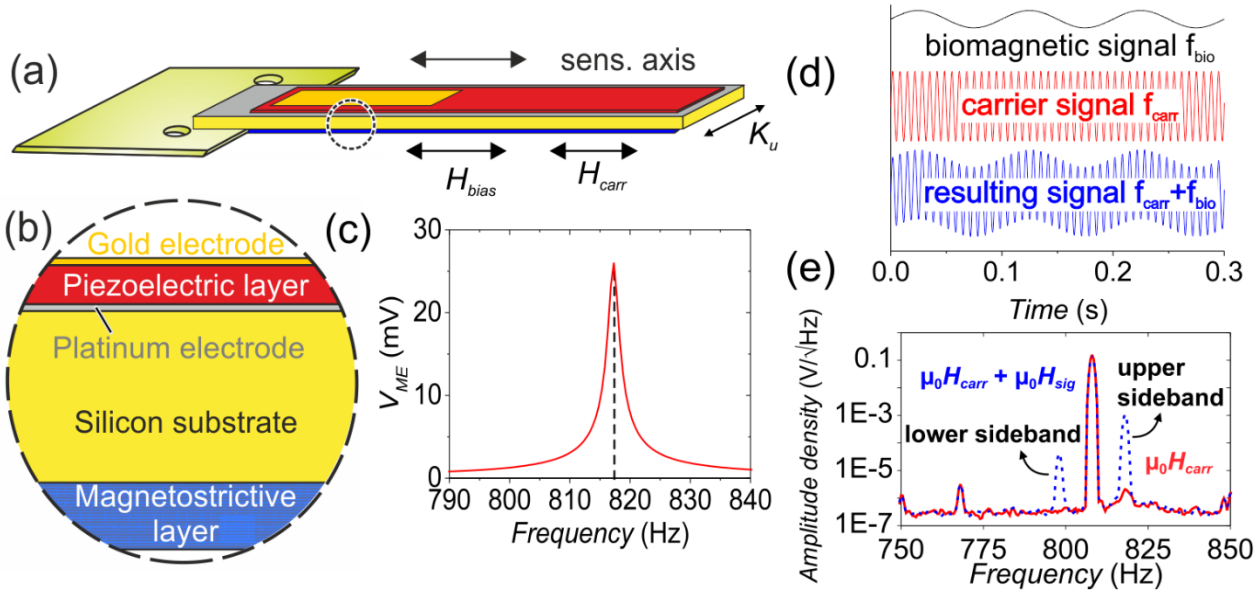

Figure 5: **(a)** Schematic of a ME sensor with corresponding denoted anisotropy K_u, applied fields (H_{bias}, H_{carr}) and sensing axis. **(b)** Inset marked in the sensor schematic, where the layered structure of the sensor is indicated. **(c)** A ME response in dependency of frequency around the resonance frequency of the sensor. The maximum amplitude of the response is positioned at the resonance frequency (marked by dashed line). **(d)** Schematic representation of mixing a low frequency signal (biomagnetic signal) with a high frequency signal (carrier signal) which due to frequency mixing forms a resulting signal with frequency of the sum of frequencies of the other two signals (the difference is not presented). **(e)** Typical frequency spectrums formed with MFC with (blue dashed curve) and without (red curve) the biomagnetic signal. The two sidebands are indicated. Schematics **(a)** and **(b)** are adapted from [58].

It should be mentioned, that such values were achieved with an applied DC magnetic bias field along the sensing axis as to achieve the maximal magnetostriction response of the magnetic material (see Figure 4). Despite such high enhancement, this technique is weak in terms of frequency selectivity and narrow bandwidth of only some Hz. The resonance scheme is bounded to the sensor geometry which determines the resonance frequency and with it the quality factor *Q*. This factor is the ratio between f_{res} of the cantilever and the bandwidth Δf of the oscillation. The Δf is determined as the width of the resonance curve at -3 dB of the maximum amplitude. This is an important parameter as it conveys the ratio between the energy stored and the energy loss of a cantilever. As such *Q* is inversely proportional to the damping of the oscillation, which results from several mechanism. The two loss mechanism with the strongest contribution are the viscous damping exerted by the surrounding air and the support damping originating from elastic energy radiation to the mechanical support of the cantilever. The resulting *Q* of viscous and support damping can be described by equations (2.1) and (2.2) respectively:

$$Q_{vis} = \frac{4\rho HW f_{res}}{6\eta + 3B\sqrt{\frac{M}{RT_0}\eta\pi f_{res}\rho}} \tag{2.1}$$

$$Q_{supp} = \kappa\left(\frac{L}{H}\right)^3 \tag{2.2}$$

at which, ρ is the average density of the cantilever material, *H, L* and *W* are the thickness, length and width of the cantilever respectively. *R* is the gas constant, T_0 is the absolute temperature and η and *M* are the viscosity and molar mass of air respectively. κ is a calculated constant determined by the material and design of the support. In order to achieve higher Q, the cantilever has to be of small dimensions in order to reduce the viscous contribution, leading to high resonance frequencies (several kHz) and larger bandwidths.

However, to measure in the low frequency regimes expected for biological signals, the sensor would need to be in a slender elongated form that would reduce the f_{res}. Such geometry does lead to an additional problem as the lower frequencies are more exposed to acoustic distortions and increased 1/f noise [59]. Due to these drawbacks, the

magnetic frequency conversion technique was developed to omit these weaknesses and allow higher flexibility of the sensors.

2.1.2 Magnetic frequency conversion (MFC)

This technique utilizes the same named principle of mixing radio signals (also called heterodyning) to shift the frequency f_{carr} of a primary signal (called carrier) to another range by mixing it with another signal (called modulating signal) of different frequency f_{mod} (Figure 5(d)). The mixing produces the sum $f_{carr} + f_{mod}$ and the difference $f_{carr} - f_{mod}$ of the two signals that can be seen in a frequency spectrum in Figure 5(e) as upper and lower sidebands respectively. One of the sidebands is then utilized as the new signal, whereas the other one is usually filtered out. The same now applies to the magnetic frequency conversion (MFC) [57], where the signals are magnetic. The carrier signal is set at a frequency $f_{res} – f_{bio}$ at which the f_{bio} is the frequency of the biomagnetic signal that is aimed to be measured with the resonance enhancement. The upper sideband then coincides with the resonance frequency allowing not only the resonance enhancement, but also sensing the biomagnetic field with much lower 1/f noise. For this reason, also the upper side band is larger in amplitude compared to the lower sideband due to the resonance enhancement of the conversed signal. The drawback of such a system is the need of the additional magnetic signal, which needs an additional set of coils that increases the overall size and energy consumption of the sensor system. Furthermore, the carrier needs to have much higher amplitude compared to the biomagnetic signal, in order to attain a good response of the sensor (the higher the carrier amplitude, the higher the magnetostrictive response). This can lead to leakage of the carrier into the upper sideband, which increases the signal noise. However, the main drawback of this method is the excitation of the magnetic domains with the carrier, which in turn produces an increased noise output of the magnetic phase.

To characterize the sensor's noise, only the carrier signal is applied to the sensor. The frequency spectrum then provides the noise behavior of the sensor (shown in Figure 5(e) by red curve). The magnetic noise dominates the other noise contributions [60], leading to a deteriorated sensitivity and best LoD of 180 pT/Hz$^{1/2}$ at 10 Hz [21] that could be reached before this research. For the signal behavior, it needs to be clear, that the signal response is highly influenced by the symmetry and linearity of the bias curve from the

zero-field point. This can be understood by the mixing terms of the MFC, which are of a square character. If the symmetry is perfect of the negative and positive side of the bias curve and both are linear, then the mixing energy will completely translate to the upper sideband. However, if there is any asymmetry and/or non-linearity, then the energy will translate to higher order terms, which are not directly detectable and are considered as a loss. This means, that the conversion loss can be greater than 2, which is the optimal conversion loss (half amplitude of the whole conversion as two sidebands are formed) [60].

2.1.3 Electrical modulation

Instead of magnetically exciting the magnetostrictive phase of the composite, electrical modulation (EM) technique is used, at which the piezoelectric phase is excited with an alternating voltage signal. In this case the converse magnetoelectric effect is used, at which the flexing motion excited by the piezoelectric phase imposes stress on the magnetic phase, which leads to a magnetization change. In order to readout the sensor's response, either a second piezoelectric layer is used or a coil encompassing the sensor is used to inductively pick up the change in magnetization. The working principle is then analogous to that of the MFC technique, with shifting the biomagnetic signal to the resonance frequency of the sensor using the excitation voltage as carrier signal. It is advantageous to use EM as it allows applying signals with higher frequencies with lower energy consumption compared to MFC. The EM also allows excitement of higher oscillation modes with much smaller power input compared to MFC. Additionally, the design can be miniaturized to smaller sizes, as there is no need for additional coils for the introduction of the magnetic carrier signal, making it more convenient for the production of sensor arrays. However, the readout coil can still provide limitations in that respect. Despite the application of EM on micromachined bulk cantilevers is not yet well researched compared to MFC, the EM has shown already promising results reaching an LOD of 1.2 nT/Hz$^{1/2}$ at 200 mHz [61] and 70 pT/ Hz$^{1/2}$ at 10 Hz [62], which is possible by utilizing more complex mechanical resonance modes existing in the range of 500 kHz (modes U1 and U2) [61].

2.1.4 ΔE effect

The final method discussed in this work is the ΔE effect, where the change of the elastic modulus *E* due to magnetostriction effect is utilized. The so-called ΔE effect originates from the change of the stress-strain state (due to spin-orbit coupling, see section 1.2.6) due to magnetization changes, leading to a non-linear modification of *E* with the magnetostrictive susceptibility [27]. As a result, the mechanical frequency of the ME sensor changes, which forms a detuning effect on sensor's oscillation at previous resonance frequency. In order to operate such a sensor, a sinusoidal voltage (the electrical carrier signal) is applied to the piezoelectric phase at the sensor's resonance frequency. A generated current from the same electrodes used for the oscillation is read out. The readout signal has a different form and it has a resonance-antiresonance curve, which is denoted as the electromechanical resonance. Nevertheless, the shift occurs proportionally as for the mechanical resonance, when an external magnetic field is applied. With this, the small biomagnetic signal modulates the current signal, giving the possibility to measure the change of admittance and with it the amplitude of the biomagnetic signal due to the resonance change/elastic modulus change [63]. The advantage of such a readout scheme is the larger bandwidth compared to MFC and the possibility to utilize higher bending and oscillating modes. Additionally, the excitation, similar as for the EM, is electrical, therefore does not need to rely on additional magnetic coils or similar and is energetically much more efficient, especially when considering the excitation of higher oscillation modes. The current challenges are the problem of small scaling of sensors leading to higher noise effects originating from the magnetic phase, which is challenged in this work. Furthermore, the sensors have to have a much thinner substrates compared to the other techniques in order to achieve high ΔE values, which requires much more complex handling and production of sensors. The latest sensors have provided the best LoD of 140 pT/Hz at 10 Hz [63].

2.2 Current progress of magnetic field sensors

2.2.1 SQUID magnetometers

Magnetic sensing applications have been developing as early as from beginning of 20th century and several sensor concepts have been developed. In this section, the discussion is focused on the magnetic field sensors that are applicable for biomagnetic signal sensing. One of the most famous sensor designs is the SQUID (superconducting quantum interference device) sensors. These sensors work on the principle of quantum current change with externally applied field within a superconducting loop inhabiting two parallel Josephson junctions. During the operation of the sensor, a continuous current is sent through the loop splitting the current equally through both junctions, when no magnetic field is applied. This driving current or also called bias current has to exceed the critical current of the Josephson junctions (depends on superconducting materials and linking material) in order to attain a voltage output. When the device interacts with an external magnetic field, a so-called screening current forms that runs around the loop in order to compensate the applied magnetic field with opposing magnetic field generated by the current (Meissner effect induced phenomena). For geometrical reasons the screening current runs opposite to the bias current in one of the junctions, whereas in the other one the screening current runs parallel. The newly developed difference in the currents form a new voltage generated at the end of the loop. With varying magnetic field, the voltage shows an oscillating behavior, which is related to the phase difference of the two junctions. The periodicity of the oscillations is determined as the quantum of the magnetic flux and gives the resolution limit of the sensor. Since the sensor is based on superconducting properties, it needs to be continuously cooled with liquid helium for optimal operation. With cooling, the sensors yield a LOD of a few fT/Hz$^{1/2}$ at 1 Hz with a bandwidth in the range of 100 MHz [64]. The main drawback of the SQUID design is the cooling, as it highly increases the operation costs and brings limitations to applicability and measurement flexibility. For these reasons, other sensors have been developed, which can be operated without the need for cooling.

2.2.2 Magnetoresistance sensors

One broad group of magnetic field sensors is the magnetoresistive sensors, at which all work on the same basic principle. The idea is to measure the changes of resistance of the material with respect to the change of magnetic state of their magnetic sensing layer/layers with an externally applied magnetic field. The first magnetoresistive sensor type to be developed is the anisotropic magnetoresistance (AMR) sensors. The AMRs can be constructed from a single layer of a magnetic material with an inherent magnetic anisotropy. During operation, a current is pushed through the magnetic material and the conduction of current depends on the magnetization direction of the material. Magnetization lying perpendicular to the direction of the current will yield the lowest impact, whereas magnetization lying in the axis of the field will generate the highest influence in conduction. This also means the change is only axially dependent due to the symmetry of this effect. The reason for resistance change with magnetization state is related to the spin-orbit coupling. It in turn induces changes of the scattering probability of conducting electrons with the electron cloud of the magnetic lattice, which reforms proportionally to the magnetization change. The AMRs are sensitive to the magnetic structure of the magnetic layers as any incoherent and irreversible magnetization changes lead to noisy output. For this reason, the magnetic state is preferred to be in a single domain state and the magnetization changes with coherent rotation of the magnetization. A possibility to gain such behavior is to use a magnetic material shaped in a strip with induced magnetic anisotropy along the long axis and using a special 45° barber pole configuration that reduces the need for large magnetization turning [9]. Despite their relatively low maximum change in resistance of about 3%, the AMR sensors have shown a LOD of 40 pT/ $Hz^{1/2}$ at 1 Hz [65], which is sufficient for some limited biomagnetic sensing applications.

Much more sensitive sensors can be produced by utilizing a multilayer stack consisting of in the simplest case two FM layers separated by a conductive (giant magnetoresistance - GMR) and insulating (tunneling magnetoresistance - TMR) layer lacking ordered magnetism. For GMR sensors, the working principle is the difference in spin dependent scattering of spin-up and spin-down electrons of a current with the d and f orbital electrons of the two FM layers. Electrons with spin parallel to the magnetization scatter more strongly than the electrons with spin antiparallel to the magnetization. The

border cases are that the FM layers are aligned parallel or antiparallel with their magnetizations. In the case of the parallel alignment the scattering of spin-up and spin-down electrons have two times bigger ending difference in scattering, whereas in the antiparallel alignment of the layers, the two types of electrons scatter equally (when assuming both FM materials are the same). Now, if the scattering is interpreted as resistance, it is clear, that the parallel case yields lower resistance than the antiparallel case. The scattering effect is schematically shown in Figure 6(a). In the latest GMRs, one layer is fixed using biasing schemes such as EB (for more see section 1.2.4.4) and is designated as the reference layer. The other one is made magnetically soft and decoupled from the other one in order to freely rotate with external magnetic field. With the linear combination of the two border cases, the behavior of the change of resistance with the orientation of the free-moving layer in respect to the reference layer can be obtained. GMRs can reach much higher relative resistance differences of 30-100%.

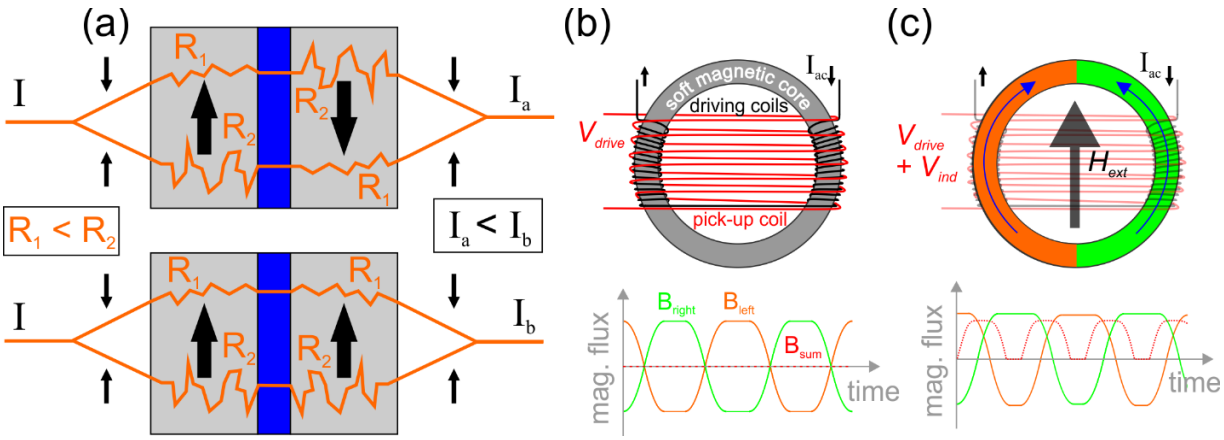

Figure 6: **(a)** A schematic representation of the GMR effect for the two border conditions: antiparallel (top) and parallel (bottom) magnetization alignment (large black arrows) of a double-layer GMR. The applied current I is schematically split into spin-up and spin-down current (spin orientation represented by small black arrows). The scattering in each layer for each current is denoted with a comparable resistance R_1 and R_2 (R_1 is larger than R_2). The final currents I_a and I_b give the corresponding relation to the change in resistance of the system with different magnetization configuration (lower current, higher total resistance). **(b)** A schematic of a one-axis ring fluxgate sensor with a pair of driving coils and a pick-up coil. **(c)** The schematic of **(b)** showing the influence of an external magnetic field on the induced magnetization (indicated by blue arrows) of the soft magnetic core. The two regions of the opposite geometry of the induced magnetization and the current direction are colored with orange and green color. Underneath **(b)** and **(c)** are graphs indicating the induced magnetic flux in the two halves of the sensor (left orange, right green) and the sum of these (red dash curve). The sum of the magnetic fluxes corresponds to the induced voltage that is used for the measurement scheme of the fluxgate sensors.

However, an even higher relative resistance difference of up to 600% is possible for the TMR sensors (TMRs). The working principle is very similar to the GMR, except that instead of a regular current a tunneling current is transmitted between the two FM layers. The base tunneling resistance is dependent on the insulating spacer layer and on the thickness of it as well as on the bias voltage that drives the tunneling probability to higher values. For both GMR and TMR there is a high dependency on the quality of the layers, interface and on the thickness of the whole stack through which the current passes through. The thickness can range from some 10 nm down to 0.1 nm. Due to both of these reasons, the performance is highly influenced by thermomechanical effects and defect density, which bound the sensor's LOD to 20 nT/Hz$^{1/2}$ [66] and 50 pT/Hz$^{1/2}$ [67] at 1 Hz at room temperature for GMR and TMR respectively (for comparison refer to Table 1). The sensors, however, can exhibit much better LODs in the several hundred fT/Hz$^{1/2}$ when cooling and long integration times are used [67] [68].

2.2.3 Fluxgate sensors

A more geometry determined magnetic field sensor is the fluxgate sensor. Such a sensor works on the principle of gathering the external magnetic field via a soft magnetic core shaped in a ring fashion. Around the core, driving coils are wound up opposite to each other (see Figure 6(b)), generating fields in opposite directions. The coils drive a magnetic field from positive to negative magnetic saturation of the core, for instance in a sinusoidal form. An additional pick-up coil is wound-up around the whole system, which then registers the change of the core due to the coil-driven magnetic fields. The changes of the core are seen as modifications of the material's permeability especially close to saturation where the non-linear change of the permeability occurs. Without an external magnetic field, the pick-up coil registers no induced voltage as the two driving coils (when the material has a symmetrical response) induce magnetization changes that cancel each other out (see Figure 6(b)). However, when an external magnetic field is applied then the responses shift and become inconsistent. This small difference causes an induced voltage to form in the pick-up coil, which allows the reading of the external magnetic field (see Figure 6(c)). The set of drive and pick-up coils can then be wound up into different axes allowing vector measurement of the magnetic field, which is one of the advantages of this sensor type. With a hybrid design of the fluxgate with an additional search coil that also acts as a flux condenser, the LOD as low as 8 pT/Hz$^{1/2}$ at 1 Hz [70]

was possible to achieve. The main disadvantage of fluxgates is the relatively large size and the limited spatial resolution with corresponding high sensitivity [71]. Additionally, there is the difficulty of creating sensor arrays due to cross talk and flux engulfment [72] that hinders further applicability of the sensor. Nevertheless, these sensors have been already used for conducting basic biomagnetic measurements [73].

2.2.4 Optically pumped sensors

A relatively newer developed concept is the optically pumped magnetometer (OPM), which utilizes the magnetic polarization change of a metal gas during light excitation. This excitation is done through optical pumping [74], which is achieved by applying a circularly polarized light with a frequency close to the Larmor frequency of the metallic atoms. This leads to transition from the ground state to an excited state of the atoms, which allows a net magnetic moment to occur and with it a bulk polarization of the metallic atoms. As such the previously uncoordinated atoms have a net polarization pointing in the direction of the propagating polarized light (see Figure 7(b)-(c)). In order to achieve high polarization close to unity, the prerequisite is to use a metal having an electron structure with a single valence electron (alkali metal atoms). The polarization of the atoms then changes with an applied external magnetic field leading to a change in the energy state due to Zeeman splitting effect forming a specific spectral line. Such change and spectral line formation results in a variation in the absorption of the light with the varying external magnetic field as the polarization of the atoms is non-colinear to the polarization of the light (see Figure 7(d)). The reduced intensity of the light, used for pumping, can then be read by optical readout devices and correlated with corresponding external magnetic field values. A sketch of a typical OPM module is given in Figure 6(c). The OPMs have become a very good alternative to SQUIDs, as they provide very good LODs at room temperatures, reaching as low as 100 fT/Hz$^{1/2}$ at 1 Hz [75]. The OPMs have also exhibited possibilities of usage in advanced biomagnetic sensing applications such as magnetoencephalography [74] [75]. The problem of these sensors is the necessity of magnetic shielding in order for them to operate as they saturate with fields higher than 2 nT. This limits their applicability to flexible ambient environment measurements.

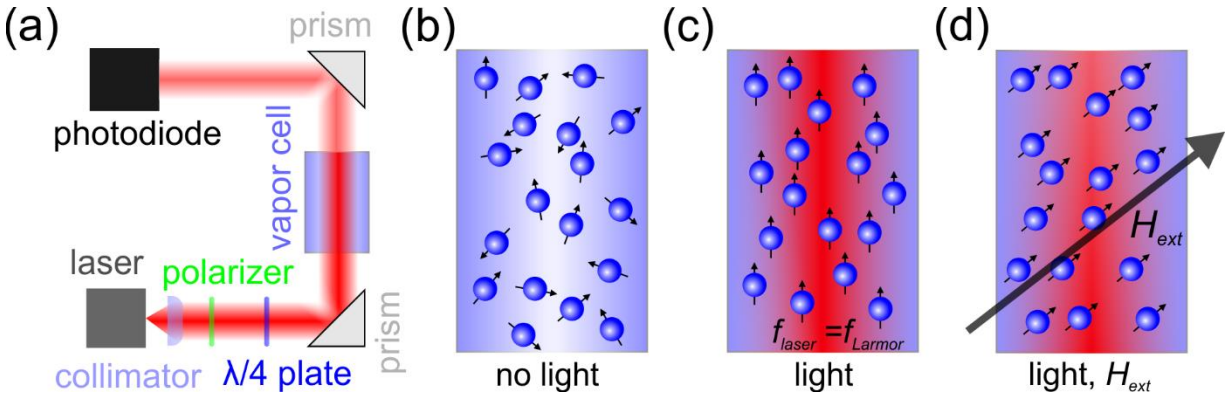

Figure 7: (a) A sketch of a typical optically pumped magnetometer (OPM) module with its individual components. The biasing coils, used for compensating external static magnetic fields and noise are not depicted. (b)-(d) The sketches show the change of polarization of the alkali metal atoms in the vapor cell with the application of polarized light and magnetic field. The polarization direction of the atoms is denoted by the piercing dark arrows.

2.2.5 Giant magnetoimpedance sensors

A completely different magnetic sensing approach is given by giant magnetoimpedance (GMI) sensors. These sensors are constructed out of a single wire of a magnetically soft, usually amorphous magnetic material. The GMIs use the principle of skin effect, where the conduction of a current occurs mainly in the outer shell of the wire. The skin depth is proportional to the magnetic permeability of the material. The connection originates from the induced internal field from the measuring current, which in turn generates an opposing current to the measuring current sent through the material. Now with a high frequency AC current, the permeability decreases with increasing frequency due to the generated eddy currents and phase lag in the formation of internal magnetic field. This results in a decrease of impedance. Additionally, the impedance will also change when the principle of permeability change with an external magnetic field is utilized (similar to flux gate sensors). This permeability change with external magnetic field applied along the axis of the measurement current is then the measure of impedance change used for sensing applications. GMIs have shown promising properties at which they have a significantly high bandwidth with a sensitivity reaching as low as 15 pT/Hz$^{1/2}$ at 1 Hz [77]. The main drawback of such sensors is the integration of wire-form sensors into an

integrated chip design, which has been compensated by the design of thin layered sensors, however these provide reduced sensitivity [78].

2.2.6 Summarized comparison

Table 1: Corresponding LODs and bandwidths at -3 dB for individual sensors (see text for corresponding abbreviations of sensor names). The values presented here were chosen from literature by considering the integration time of maximum 1 minute to provide comparative results also in terms of practicality for biomagnetic measurements.

Magnetometer	*Limit of detection at 1 Hz †*	*Bandwidth (-3 dB)*
Bulk ME [52]	5.1 pT/Hz$^{1/2}$	1 Hz
Wafer ME [21]–[23]	300 pT/Hz$^{1/2}$ (180 pT/Hz$^{1/2}$ at 10 Hz) *	2 Hz-100 Hz
SQUID [64]	3.8 fT/Hz$^{1/2}$ at 4.2 K	120 MHz
AMR [65]	40 pT/Hz$^{1/2}$	12 Hz
GMR [66] [79]	20 nT/Hz$^{1/2}$ 3 pT/Hz$^{1/2}$ at 4 K	100 kHz 300 Hz
TMR [67]	50 pT/Hz$^{1/2}$	1 Hz
Fluxgate search coil hybrid [70]	8 pT/Hz$^{1/2}$	600 Hz
OPM [75]	100 fT/Hz$^{1/2}$	80 Hz
GMI [77]	15 pT/Hz$^{1/2}$	50 kHz

†*measured at room temperature, if not stated otherwise*

**best values before the measurements conducted in relation to this work*

By comparing the individual figures of merit of the various magnetic field sensors in Table 1, it is clear that the composite wafer ME sensors are still behind in terms of sensitivity compared to most other sensors. However, as it will be stated later, the new research developed with low magnetic noise phase, provides LODs as low as 50 pT/Hz$^{1/2}$ at 10 Hz with MFC and LODs as low as 40 pT/Hz$^{1/2}$ at 2 Hz (30 pT/Hz$^{1/2}$ at 10 Hz) with electrical modulation. Such values are now already pushing the ME composite sensors beyond some of the competing sensor concepts, but not all. Nevertheless, with the research done in this work, new possibilities have opened to attain even better sensors with much better sensitives in future research and development.

Chapter 3

Experimental and modeling methods

3.1 Magnetization measurement techniques

To understand the fundamental process of the magnetization behavior in FM materials, one must understand the behavior of magnetic domains within them. Researchers have developed several techniques to understand the magnetic domain behavior from measuring the overall magnetic response down to measuring individual magnetic moments that construct a domain. The most historically important technique is the Bitter pattern technique, which allowed the first visualization of magnetic domains by using iron shavings in a colloidal suspension. With the suspension being applied on the surface of a FM material, the small particles would agglomerate and align with the domain pattern residing within the magnetic material. In principle, it shows us the H_{str} being exerted from the magnetic material. This means when the suspension is set around the magnetic material, it would disclose the magnetic flux lines that are emitted from the sample. Despite its powerful versatility and simplicity, the method provides little information about local magnetization configuration and provides low resolution. Additionally, the

technique is limited in usage for materials with low coercivity, complicated structures and small domain configurations. As such, it is also clear that investigation of thin film magnetic materials with in-plane magnetization is also limited by the Bitter technique as the generated H_{str} by the magnetization on the surface of the film are mainly insufficiently strong to cluster the iron shavings. With this in mind a more proper techniques had to be developed to gain the possibility to probe the magnetization on a local level and to investigate materials with weak H_{str} emission. By combining light and magnetization, in nature two seemingly unrelated phenomena, a new mighty group of techniques named magneto-optical (MO) imaging evolved. Although there are several methods and effects within this group, the focus in the next subchapters is limited to the technique used in this research, namely the magneto-optical Kerr effect.

3.1.1 Magneto-optical Kerr microscopy

3.1.1.1 Magneto-optical Kerr effect (MOKE)

In 1875 John Kerr discovered the so-called magneto-optical Kerr effect (MOKE). It describes that, when polarized light interacts with and reflects from a magnetic material, the polarization of the light rotates in the plane by a small angle in comparison to previous polarization plane [80]. The angle is dubbed the Kerr angle θ_k, which range is typically in the mrad scale (depending on the magnetic material and angle of incidence [81]). The actual phenomenon results from the exchange interaction and spin-orbit coupling interaction which influence the s- and p-polarized states of the incident light. The two different states inherit dissimilar absorption and reflection interactions with the material, which leads to the change in light intensity and the ratio of reflected s and p polarized state of light depending on the local magnetization state of the material [82]. All interaction variations can be described by the effective dielectric permittivity tensor $\hat{\varepsilon}$ [83] defined in equation (3.1):

$$\hat{\varepsilon} = \varepsilon \begin{pmatrix} 1 & -iQm_z & iQm_y \\ iQm_z & 1 & -iQm_x \\ -iQm_y & iQm_x & 1 \end{pmatrix} + \begin{pmatrix} B_1 m_x^2 & B_2 m_x m_y & B_2 m_x m_z \\ B_2 m_x m_y & B_1 m_y^2 & B_2 m_y m_z \\ B_2 m_x m_z & B_2 m_y m_z & B_1 m_z^2 \end{pmatrix} \quad (3.1)$$

Kerr **Voigt**

Where ε is the dielectric constant of the material, m_x, m_y and m_z are the directional cosines of the magnetization in the indexed Cartesian axis. Q and B_1 and B_2 are the linear (Voigt) and quadratic constants respectively. The left part of the tensor describes the linear (Kerr) contribution, whereas the right part represents the quadratic (Voigt) term of the MO interaction. For this work only the linear part is discussed further on.

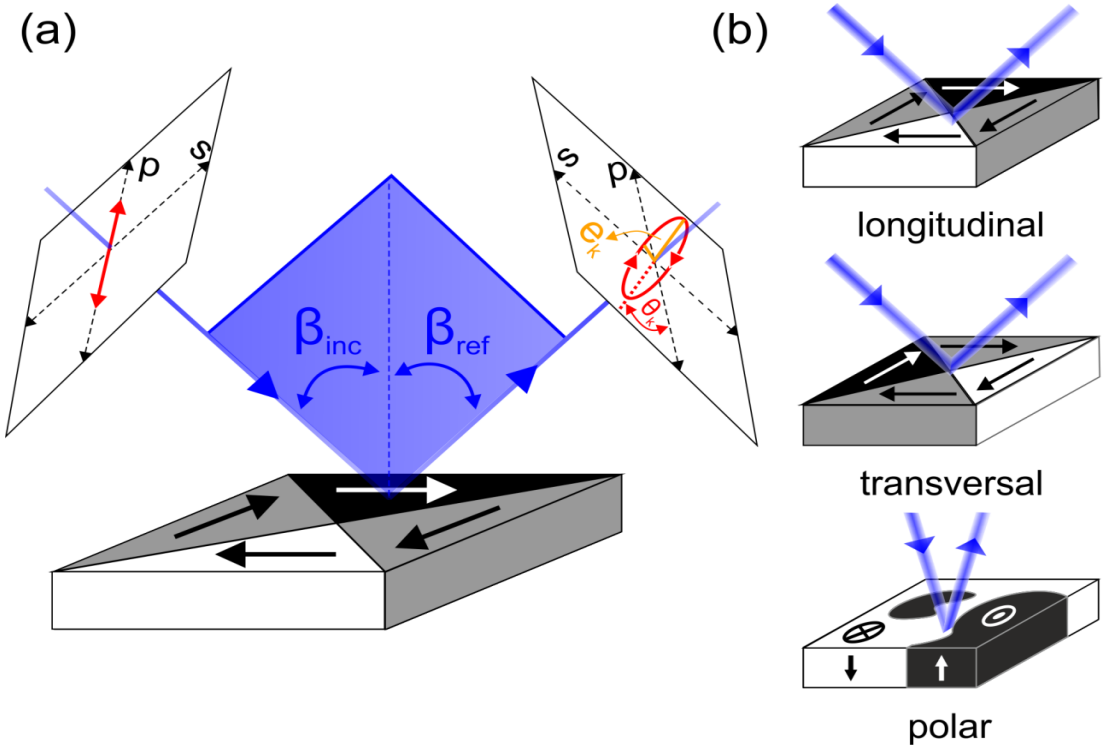

Figure 8: **(a)** An example of MOKE interaction of a linearly polarized (p-polarized) light with a magnetic material with in-plane lying magnetization (longitudinal MOKE). Basic terms such as p- and s- polarization axes and incidence β_{inc} and reflectance β_{ref} angles are marked. The polarization state before and after interaction are indicated with red arrowed curves. The resulting ellipticity e_k and Kerr angle θ_k are denoted. **(b)** Three possible MOKE configurations resulting from the geometry of the light path, polarization of the light and magnetization orientation (see text for more details). Images adapted based on [84].

The linear part can be separated firstly into two phenomena: magnetic circular birefringence and magnetic circular dichroism. The first one, describes the before mentioned rotation of polarization axis with the θ_k and occurs due to the different reflectivity of the two polarization states from a magnetic material. The second phenomenon describes the reshaping of a circularly polarized light, which after the interaction with magnetic material becomes elliptical. The effect is a result of the different absorption coefficients of left- and right-hand circular polarization states and the ratio of them is denoted as ellipticity e_k. The result of both phenomena is schematically sketched in Figure 8(a) for a linearly p-polarized light shining with an

oblique angle of incidence onto a magnetic material with in-plane lying magnetization. The sense or circular rotation of the linear polarized light is determined by the magnetization direction in the material with respect to the incident angle. The example shows a right-hand polarization rotation. In order to attain contrast from the resulting light a linear polarizing element is set close to 90° orientation to the polarization direction of the linear polarized light that was shinned on the material. By opening the polarizing element, also known mostly as an analyzer, towards the θ_k either left-hand or right-hand (shown in Figure 8(a)), maximal contrast can be achieved between the two antiparallel aligned magnetization directions (see magnetic structure in Figure 8(a)). This is a result of the two magnetization states rotating the light by the same θ_k, but opposite in sign, which the polarizer pertains as higher and lower light intensity due to the different maximum amount of coinciding projected part of the rotated polarization. The magnetizations pointing perpendicular to the incidence plane (blue plane in Figure 8(a) create no contrast change visible to the polarizer, resulting in a similar grayed contrast in intensity level between the bright and dark contrast regions.

However, the intensity reduction resulting from ellipticity persists and induces unbalanced contrast formation (bright and dark contrast are not equally spaced from gray region intensities). For this reason, an additional optical element is used named compensator, which is simply a λ/4 waveplate. This element creates a phase shift between the p- and s- polarized states leading to the formation of circular polarized light from a linearly polarized light. When the compensator is aligned under an angle from the axis of the linear polarized light, then the resulting light is of elliptical form. Now, when the compensator is aligned properly as to create opposite elliptical effect to what the magnetic material induces, the material induced ellipticity becomes compensated (the two elliptical forms have opposite lengths of long and short axis). The light reaching the analyzer is then circularly polarized leading to an evenly-set and strong contrast of the differently oriented magnetization directions. The simple illustration in Figure 8(a) shows the longitudinal MOKE effect, which is only possible for a specific geometry with an oblique incidence of angle of illumination. However, further geometric simplifications can be derived by examining equation (3.1), when the polarization axis of the incident light falls aligned with the orientation of various magnetization states. A schematic of the three possible simplified configurations of MOKE is presented in Figure 8(b) at which the first longitudinal effect has been explained beforehand.

The second possibility is the transversal Kerr effect, which is also common for oblique angle of incidence. In contrast to the longitudinal MOKE, the sensing of the transversal effect is set for magnetization aligned perpendicular to the plane of incidence (in Figure 8(a) this plane is depicted with blue color). In order to achieve such configuration, the most common way is to set the linear polarized light between the p- and s- polarized state at an angle of 45°. The analyzer is set 90° to the polarized state of the light. The result is the cancelation of the s-polarized state that results in a transition of its intensity caused by the Kerr rotation to the p-polarized state. From this, it is clear, that the result in contrast forms due to an amplitude change and due to the change of the angle of the polarization plane. However, such an effect normally results in a phase shift between the incoming and outgoing light forming a weak contrast. To correct the phase shift, the previously mentioned compensator is used to correct the phase shift, which is done by setting its fast axis close to 45° to the p-polarization and then turning by the angle of the θ_k independent of turning it right- or left-hand.

The third and final simplification describes the polar configuration, which describes the MO sensitivity towards magnetization lying out of the plane of the probed orifice. In this case, the light has to income onto the surface of the material at a perpendicular incidence. The polarization alignment and optical element positioning is analogous to the longitudinal configuration, only the incidence is perpendicular. A very important point is to mention, that the polar contrast is significantly larger (usually around an order of magnitude) compared to the transversal and longitudinal contrast. This occurs due to the different dependencies of the effects to the refractive index of the material (polar MOKE scales with the dependency of the longitudinal MOKE multiplied by the refractive index of the material [85]). Consequentially this outcome leads to the in-plane magnetic contrast longitudinal or transversal) to be obscured by the polar derived contrast, even for oblique angle of incidence. All discussed effects and their resulting contrast are highly determined by the incidence angle, which in microscopy is dictated by the numerical aperture (NA) of the selected objective. The NA is determined by the maximal incidence angle β_{inc}, formed by the optics constructing the objective, as well as by the index of refraction n_{med} of the medium through which the light transmits from the objective to the sample surface and back. The dependency is given in equation (3.2):

$$NA = n_{med} \sin \beta_{inc} \quad (3.2)$$

An exemplar dependency of the intensity to various NA and objective types is comprehensively and graphically presented by J. McCord [84]. In regards to MOKE signal intensity, this method is very surface sensitive. Since it is based on reflectivity effects, the penetration depth is limited to the range of about 50 nm (depending on light, material and surface quality). Nonetheless, this technique can indirectly probe information about the magnetic material lying much deeper. For instance in multilayer constructs, the magnetization structures can become coupled and an imprint of the features from lower layers can form in the top layer, which can then be detected using MOKE (see more in section 4.2). To practically use MOKE, two specialized microscope setups were used in this research, which are discussed in the next section.

3.1.1.2 MOKE microscopy

MOKE investigation can be conducted by the utilization of an optical microscope with specialized optics, magnetic field generating coils and a camera. As stated beforehand, two different microscope setups were used in this research, which are schematically shown in Figure 9. In Figure 9(b) the large view MOKE microscope is shown. This microscope setup is utilized to observe magnetic materials in an overview fashion, having a magnification of 0.35x and with it a field of view of around 3x3 cm. Such a setup allows seeing the magnetization configuration across whole sample surface simultaneously. However, it lacks in spatial resolution, which is limited to several µm. The microscope is constructed from a high-power LED source (520 nm wavelength) with a collimating, telecentric lens system, two linear polarizers (one for forming linear polarization of the light and the other one acting as an analyzer), compensator, a CCD camera and a telecentric condensing lens system set before the camera. The incidence angle of the setup is fixed with a 45° angle, as it allows the highest generated contrast to occur for longitudinal and transversal MOKE. Additionally, the setup has an integrated element called Scheimpflug mount attached before the camera that allows the focusing to occur across the whole image plane. Without the mount, the focus would be set to only a narrow line region perpendicular to the incidence path due to the incidence angle. Due to the correcting functionality of the mount, the acquired image is distorted by a linear compression along the axis along which the light path transits. The correction factor is

determined by the angle of reflection β_{ref} and the angle between the camera sensor plane and plane perpendicular to the incoming light β_{cam} [85]. For this specific setup, the correction factor of expansion is 1.33.

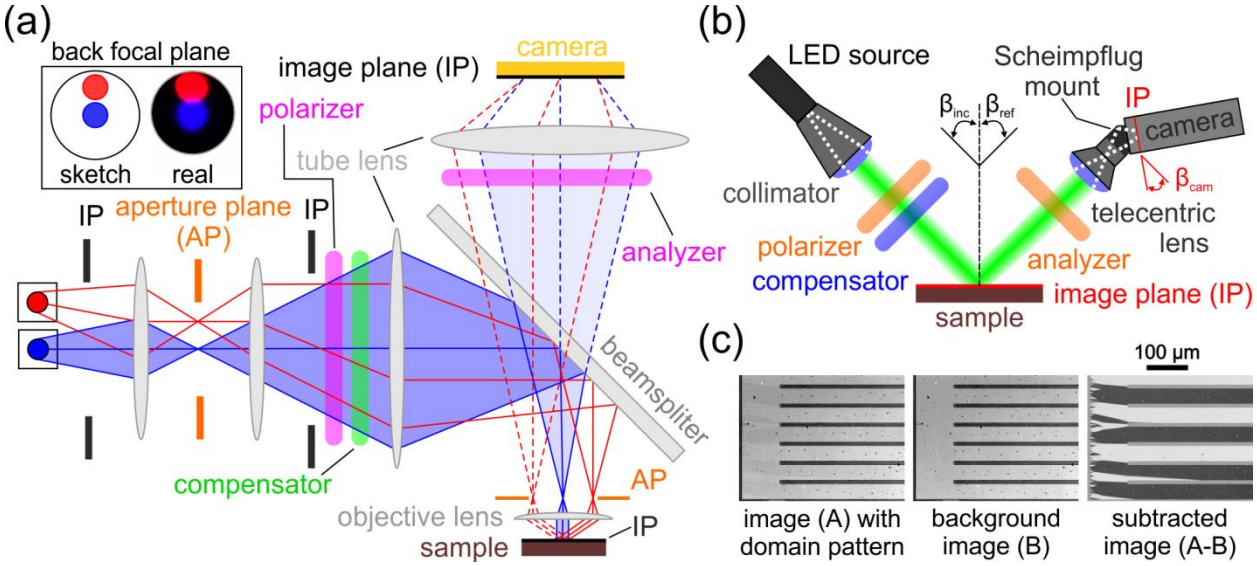

Figure 9: (a) Schematic of an upright microscope with Köhler illumination. Light trajectories of polar (blue) and longitudinal (red) MOKE configuration are drawn. The dashed lines represent the reflected trajectory of the light from the sample. For easier differentiation, the polar trajectory is spatially highlighted. The individual optical components as well as the various optical planes are marked. The polarizer, compensator and analyzer are 360° rotatable and are in reality slightly tilted in order to reduce back-reflection effects. The position of the light sources in the back focal plane are given and sketched in the box in the upper left corner. Image adapted from [84]. (b) Sketch of the large view microscope setup with the simplified light trajectory. The dashed white lines represent the light form in the optical components. (c) Example of acquiring an image with high magnetic contrast by image subtraction technique. The first two images (A and B) are acquired with same illumination settings and averaging (64x) and have same topological effects. Only image A holds information about the magnetic pattern, while image B displays a magnetic gray level. Image B is formed by exciting the magnetic material from positive to negative saturation with an external AC magnetic field with a frequency of 21 Hz. Due to averaging, the resulting magnetic contrast in the image is a uniform gray level set between the contrast maxima/minima of the two saturated states. By mathematical subtraction of the two images, the resulting image A+B is calculated. The image A+B is postprocessed with contrast shifting to gain highest visual contrast whilst withholding all the information in the image.

The second setup is presented in Figure 9(a). This setup is constructed from an upright polarizing optical microscope with a Köhler illumination system produced by Zeiss. The polarizers in this setup are wire grid type, which allow high transmission of light and high extinction ratio, allowing imaging of high contrast images. The light source used is a high-power LED system, which is coupled to the microscope via an optical fiber. For the

setting of different MOKE geometries (described in section 3.1.1.1) the optical fiber is coupled on a sliding system that allows repositioning of the light source with respect to the aperture plane. Effectively this results in the change of the incidence angle and the direction of incidence of the light onto the sample, thus allowing easy setting of longitudinal MOKE along various axes. In Figure 9(a) example of polar (blue) and longitudinal (red) setting of the light source and the resulting light path through the imaging system are portrayed. By inserting a Bertrand lens (not sketched in the figure) before the second tube lens, the positioning of the light sources can be visualized by the back-focal plane (image of it shown in top left corner accompanied by a sketch), which coincides with the aperture plane near the objective lens. The advantage of such setup compared to the previous one, is the possibility of exchanging objectives with various magnifications, leading to a variety of spatial resolution and field of view. In order to attain images with high contrast and free of topological artifacts with only magnetization information, a technique called image subtraction is utilized. An example of such a technique is given in Figure 9(c). The idea is to use a reference image that has no magnetic contrast variation and has the entire surface related artifacts and effect. Such an image can be formed by exciting the magnetic material from positive saturation to negative saturation with a high frequency and then the acquired image is formed by averaging. The resulting image forms with a magnetic gray level, but the non-magnetic components of the image are kept (Figure 9(c), image B). When this image is subtracted from an image with a certain magnetic pattern (Figure 9(c), image A), an image with pure magnetic information and contrast is produced (Figure 9(c), image A-B).

3.1.1.3 Time resolved magneto-optical Kerr effect microscopy

In order to observe the dynamic of magnetization during sensor operation at the mechanical resonance, the previously described setup in Figure 9(a) has to attain temporal resolution. This can be achieved in several ways. One way is to trigger the camera by an external signal, while the light source is driven continuously. The exposure time of the camera, time set for acquiring the light signal reaching the sensor, sets the temporal resolution of the viewed event as well as the frequency of the imaging. However, limitations are high, as cameras with sufficiently high spatial resolution have limited readout and image processing frequencies (up to about 100 Hz for sensing size of 2048x2048 pixels^2 [86]) leading to a temporal resolution of 10 ms, with full interval exposure. Nevertheless, the temporal resolution can be increased by limited readout

through synchronous readout scheme with an external trigger signal allowing temporal resolution of about 1 ms. In order to avoid such limitations high power light sources such as lasers can be implemented. The light sources can be then triggered with significantly higher frequencies reaching well into the GHz range. The camera and the laser can then be synchronized to either attain a single pulse per image (single shot imaging) or acquiring several pulses at the same phase segment of a reoccurring periodic event (stroboscopic imaging). With such systems picosecond temporal resolution has been reported [85] [86]. The systems, however, become limited in terms of spatial resolution for single shot imaging as with shorter pulse length the signal to noise ratio becomes lower, which decreases the quality of the resulting image. The fundamentals of this problem originate from the amount of photons reaching the camera detector to the amount of distortion from the sensors ending electrical output. The smaller the ratio between these quantitates, the smaller the quality of the image and thus smaller possibility to distinguish the real signal from pixel to pixel, resulting in reduced spatial resolution. For this reason, high power output of lasers is needed for such time resolved imaging. Yet, one additional limitation is possible in such systems, which is the restricted dynamic range of the frequency span of the laser. To attain high stability and coherence of the laser output, many lasers are constructed by having a specific base frequency (set by the cavity length of the laser) in a much lower frequency regime (for instance 50 MHz) that can be then multiplied to reach higher frequencies (GHz regime) [88]. This means, that probing of the sample is limited only to these multiples of the base frequency and this can be troublesome for imaging sensors during operation in mechanical resonance, as the frequencies can be hard to tune and can be far away from the technical reaches of the laser.

For this reason, the adaptation of a Kerr optimized microscope was done by implementing a pulsed diode laser setup CAVILUX Smart UHS from CAVITAR. The laser has the possibility to have a high tunable dynamic range from 30 Hz to 30 kHz with a minimum pulse width of 10 ns, whilst attaining the stable high power output of 400 W [89]. This offers time resolved in-operando probing of all the sensor concepts discussed in section 2.1. The new setup and the controlling scheme are schematically represented in Figure 10. The newly incorporated laser system is controlled by a TTL generated signal from a pulse delay generator. Analog signal output S_{PC} from the BNC box is applied to the bi-polar Kepco power supply for the driving of the magnetic coils or to the function

generator for electrical excitation of the sensor. The output measurement signal of the two components is then used as a trigger signal for the timing of the pulse generator and frequency regulation of the TTL signal P_{PD}. The TTL signal is then controlled via LabVIEW interface by selecting the individual pulse width t_{width} and delay from the trigger point t_{delay}. The pulsed signal is forwarded to the laser unit, which exerts a light signal L_{PD}, with the exact same pulse properties as of the TTL signal. The light is then transmitted through the microscope and optics towards the sample and reflected to the camera, where an image is then attained. The signal transmitted to the laser control unit is also transmitted to the camera, which allows synchronous readout of images with the same amount of laser pulses per frame. This allows shorter exposure times to be set allowing less noise to be gathered by the sensor during image acquisition. To acquire single shot images, the readout delay of the camera is compensated by administering a short delay to the laser unit and therefore guaranteeing the pulse is within the readout time range of the camera. In the sections of Chapter 6 the application of the new setup is further discussed segmentally for individual sensor observations.

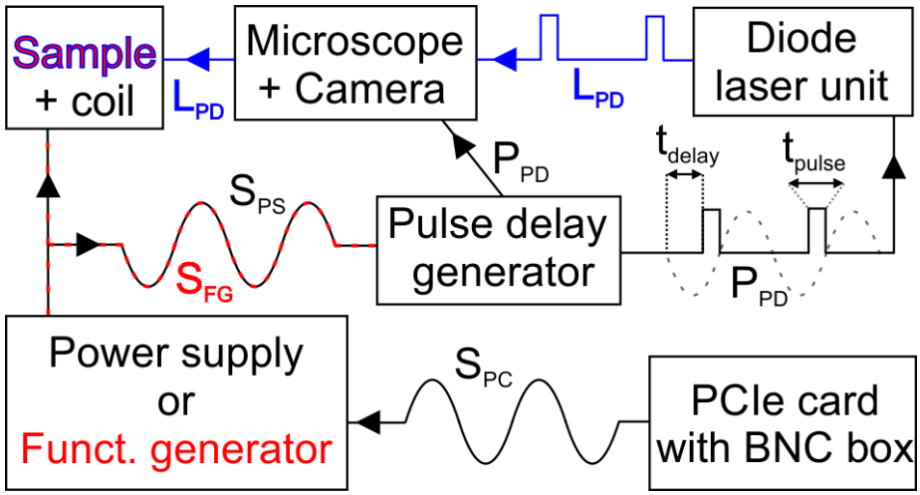

Figure 10: Schematic representation of the new setup with the working scheme. The various signal forms are drawn between individual components at which the starting and ending flat line represent the zero level of the signal. The arrowheads indicate the direction of the traveled signal. The dashed sine signal next to P_{PD} is given as a reference to indicate the relation between signals S_{FG} and S_{PS} to P_{PD}. The back-reference signals of individual components as well as the light signal reflected from the sample to the camera are not denoted.

3.1.2 Inductively measured magnetization response

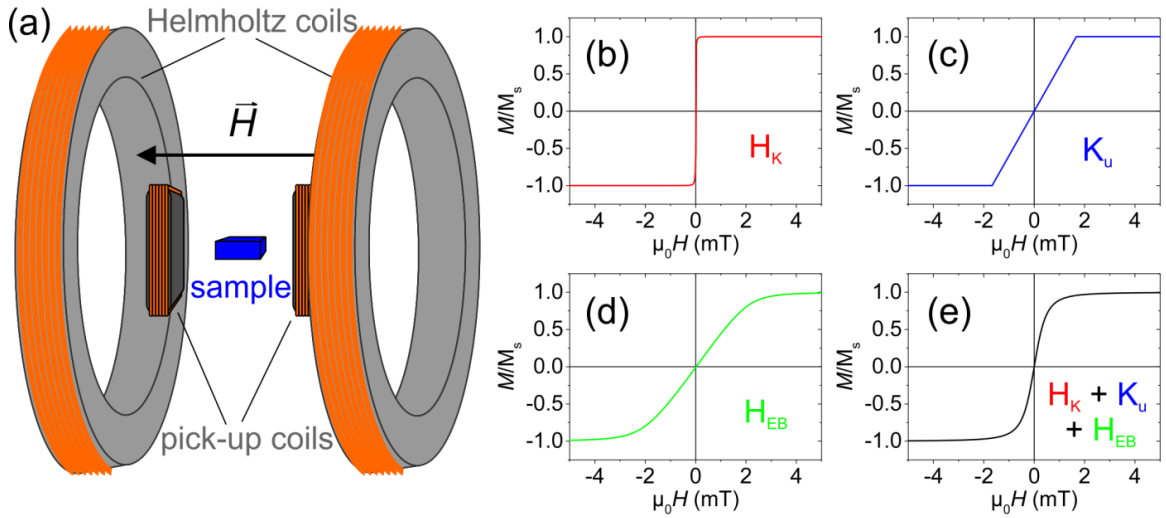

Figure 11: (a) A schematic representation of an induction measurement setup, dubbed as B-H looper. The large coils are in a Helmholtz configuration and provide the AC excitation field (frequency of the field can be set to 1 Hz, 5 Hz and 10 Hz). The smaller coils closer to the sample are the pick-up coils that register the magnetic flux of the material. Note, that the pick-up coils are beforehand calibrated to dismiss induction effects resulting from the interaction of the two pairs of coils. (b - e) Example of a modeled magnetization response curve for a FM layer with corresponding components induced by (b) shape, (c) uniaxial anisotropy and (d) exchange interaction (in this case with AFM). By merging all components, the total magnetization response (e) is modeled.

The described techniques in previous sections do not allow probing of the magnetization deeper than a few tens of nanometers. In some instances, the information about the overall magnetization response of a magnetic material is needed. This is especially important when the magnetic material is composed of several magnetic layers that can have different coupling mechanisms. One way to measure the overall response of the magnetization is by using a so-called B-H looper. It is a measurement scheme that firstly applies an external cyclic magnetic field onto the magnetic material by a pair of Helmholtz coils. Simultaneously another set of coils pick-up the exerted magnetic flux of the material in its current magnetic state by measuring the induced current in the coils due to the previously mentioned flux. In the Figure 11(a) is a sketch of such a measurement system. The result of such measurements is a magnetic flux response versus applied magnetic field. When the material is magnetically saturated with the appropriate maximum amplitude of the cyclic field, then the flux can be normalized. From such data, a normalized magnetization response or usually called magnetization loop is attained.

Convenient about this method is the possibility to measure the magnetization response very fast and under different angles based on the sample geometry. This allows easy and fast determination of anisotropy axis alignments and various coupling effects of a magnetic material. An example of such a loop and anisotropy determination is given in Figure 2(a).

3.2 Magnetization response modeling

In order to understand the overall magnetization behavior in terms of magnetic quantities explained in section 1.2 a macrospin magnetic model is used. This model is based on the well-known Stoner-Wolfarth model [90] which describes the behavior of the total magnetization with given parameters of an ellipsoidal system, when an external magnetic field is applied. In the simplest case, the model incorporates the basic magnetic energy terms described in sections 1.2.1 - 1.2.4. The model uses the derivate form of the total energy term and determines the minimal value by varying magnetization direction for a given field angle and sample geometry. The sequence is then conducted for a range of field values. The field dependent minimal energy states indicate the orientation of magnetization state for each field value and from these values the magnetization loop can be constructed. It should be clear that such basic calculation is limited to a homogeneously magnetized (single domain) state with a volumetrically and homogeneously defined anisotropy. In this work, a modified and more complex model is used in order to simulate the magnetic response of multilayered samples, which allows the incorporation of various coupling effects between up to 4 individual FM layers. For the purposes of this research, the basic model is expanded to accommodate the calculation of the demagnetization effects of a finite thin film. Additionally, the code gives the possibility to include directional anisotropy (EB), stray field coupling and other coupling mechanism between layers. The ending minimization total energy term used in this program is defined as:

$$E_{total,min} = \sum_{i=1}^{4}\sum_{j\neq i}^{4} -M_{s,i}\, H\, t_i \cos\theta_i + K_{u,i}\, t_i \sin(\theta_i + \omega_i)^2 + \frac{1}{4}K_{c,i}\, t_i \sin(2[\theta_i + \varphi_i])^2 + J_{AF,i}\cos(\theta_i + \omega_i + \varepsilon_i) + J_{F\,i,j}\cos(\theta_i + \theta_j) + S_{F\,i,j}cos(\theta_i + \theta_j) + \frac{1}{2\mu_0}N_x\, t_i\, M_{s,i}^2 \sin(\theta_i + \alpha_{rot})^2 + \frac{1}{2\mu_0}N_y\, t_i\, M_{s,i}^2 \cos(\theta_i + \alpha_{rot})^2 \quad (3.3)$$

Where the angles θ, ω, φ, ε and α_{rot} are the angles between the external applied magnetic field H and the magnetization (M), the axis of uniaxial anisotropy (K_u), the axis of magnetocrystalline cubic anisotropy (K_c), the direction of AFM exchange (J_{AF}) and orientation of the sample respectively. The M_s is the saturation magnetization and t is the thickness of a FM layer. The additional couplings between the layers are determined by the energy terms J_F (FM exchange coupling) and S_F (stray field coupling). μ_0 is the permeability of vacuum. The demagnetization effect calculation given in the last row of equation (3.3) is described by the demagnetization factors N_x and N_y (in-plane factors). The demagnetization factors are calculated based on the input dimensions of the sample and thicknesses of layers. The formulation used is the approach for a rectangular shaped FM prism described by Aharoni [29]. The minimization is conducted in a stepwise fashion determined by the step size of the external magnetic field. With this model, magnetizations loop and magnetization-derived magnetostrictive and ME responses are calculated (see section 1.2.6, Figure 4) which can be compared with experimentally attained data. From the comparison and adaptation of the model to the experimental data, the individual magnetic parameters of the material can be extracted. Thus, allowing further understanding of the magnetization behavior as well as the specific formation of magnetic domains. Furthermore, predictions of the magnetization response of various material and structure combinations with various parameters can be modeled, which is useful at establishing new-coupled systems. An example of a magnetization loop construct is given in Figure 11(e). The individual components that are modeled for the whole construct are given in Figure 11(b-d). See figure caption for more details. The code has been developed for a two ferromagnetic layer system (later known as 2 layer model) by Julia Dshemuchadse and Jeffrey McCord. The addition of modelling the ME response was done by Finn Klingbeil.

3.3 Electrical characterization of ME sensors

In order to determine the performance of sensors described in section 2.1, the sensors need to be characterized electrically, to attain the typical figures of merit. The measurements are conducted in an acoustically (acoustic foam), mechanically (decoupled and damped flooring), electrically (faraday shield) and magnetically (mu-metal encasing) shielded chamber in order to determine the performance in optimal and repeatable conditions. A battery driven charge amplifier is used to amplify the sensor signals in order to attain optimal signal-to-noise ratio with the subsequent readout devices. Although the various sensor concepts have some variations in terms of equipment and readout parameters, the general scheme of measurements are analogous to each other. To simplify the explanation only the measurement scheme for direct detection and MFC are discussed onwards, as it was also the most commonly used method in this work.

For both methods, two sets of calibrated coils are required. One is used to generate a DC bias field (H_{bias}) and an AC modulation (carrier) field (H_{mod}) for the direct detection and MFC respectively. The second coil is used for the application of the AC biomagnetic field signal (H_{sig}) for both methods. In the first step, the sensors are characterized for their mechanical resonance f_{res}. The resonance is estimated with a dynamic signal analyzer (Stanford research systems model SR785) when the sensor is excited with white noise. The approximate f_{res} is then used to measure the bias curve of the sensor (see Section 1.3), where the signal response of the sensor with different H_{bias} during excitation at f_{res} is measured. The common H_{sig} during both operations has amplitude of 100 nT. The measurement/signal field coil is driven by a Keithley 6221 current source, which allows precise current output for producing small (pT) magnetic fields. The bias coil is driven by a bipolar Kepco power supply. After the bias curve measurement, a new resonance frequency measurement is conducted with the previously determined optimal H_{bias}. The corresponding phase change is also measured. With this, a more exact resonance frequency is measured and inputted back into the bias curve measurement scheme. This is then repeated several times in order to attain the exact f_{res} and optimal H_{bias}. This is necessary due to the ΔE-effect, which shifts the resonance frequency [91].

With the optimal determined parameters, the linearity measurement is then performed, which allows the measurement of the LOD at resonance frequency. The process is done, by measuring the signal of the sensor (with the signal analyzer) with decreasing amplitude of the signal field until a certain value, where the noise floor can be characterized. The modulation field coil is in this case driven by Keysight power source (B2962A), which is a low-noise alternative to the Kepco power supply. The sensor signal over square root of Hertz in response to the applied field is linearly approximated. The linear approximation of the noise floor is also performed. The crossing of the two linear functions represents the signal to noise ratio (SNR) to be equal to unity. The signal field value corresponding to this point represents the LOD of the sensor at resonance frequency. This is presented in Figure 12(d) by the red curve. Until now, the measurements are related to the direct resonance enhancement scheme explained in section 2.1.1. For the evaluation of MFC performance, the sensor is exposed to a modulating field with a frequency equal to the resonance frequency minus the simulated biomagnetic signal frequency (usually 1-10 Hz). The resulting spectrum is then analyzed with and without the applied biomagnetic signal. With the biomagnetic signal, the sensor signal is then attained from the upper side band, whereas without the biomagnetic signal the sensor noise is determined from the highest level around the upper side band position. An example of such analysis is shown in Figure 12(a).

The process is then performed across a whole range of amplitude of the modulation signal. The results are signal, noise (Figure 12(b)) and SNR (Figure 12(c)) data versus modulation amplitude. With this data, the optimal modulation amplitude can be determined based on the maximum exerted SNR of the sensor (dashed line in Figure 12(c)). With the optimal modulation amplitude, the sensor is then measured with decreasing amplitude of the biomagnetic signal. Similarly, to the direct resonance enhancement method, the LOD is then measured with a linearity measurement. The processing of the data is done the same and the LOD of the sensor is the biomagnetic signal amplitude at SNR=1 (shown in Figure 12(d) red curve. The whole setup is automated and driven via a program written in Matlab. The setup and automatization were built and programmed mainly by Sebastian Toxværd and Phillip Durdaut.

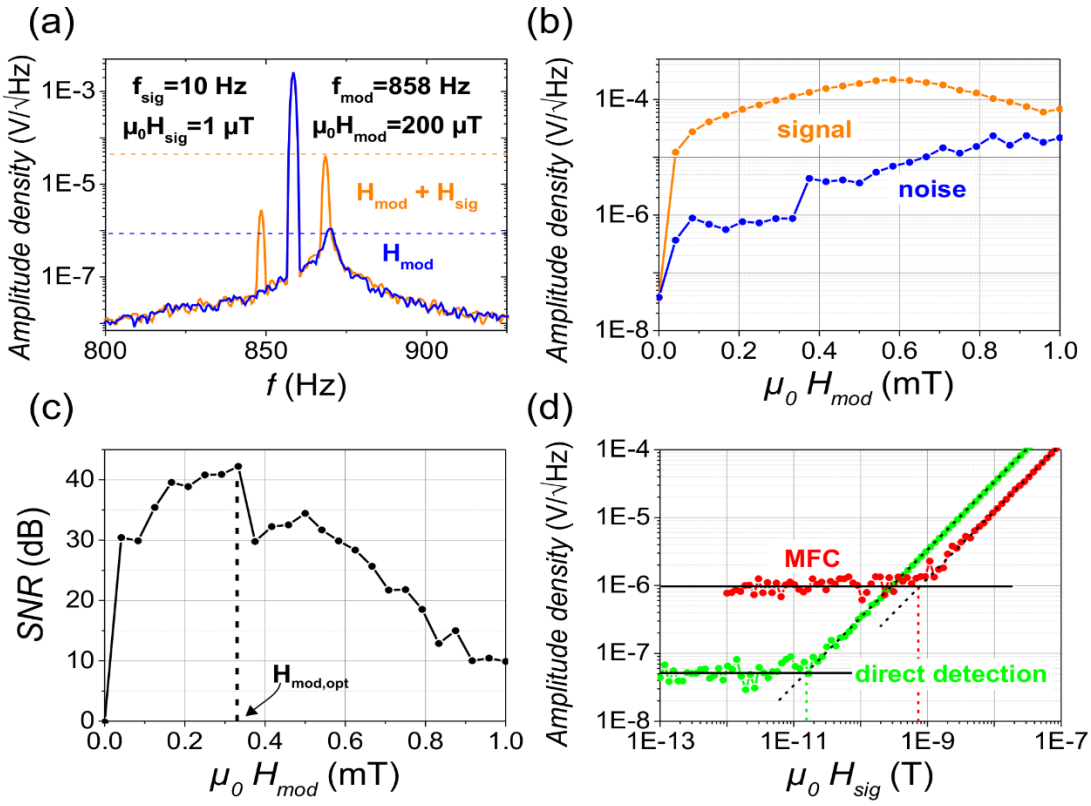

Figure 12: (a) Frequency spectrums of a sensor with (orange curve) and without (blue curve) the additional biomagnetic field. The specific values of the modulation and biomagnetic signal are given. (b) The extracted signal and noise response of a sensor with modulation field amplitude. (c) The resulting SNR in dependence of the modulation field amplitude. (d) Linearity plots of the sensor with direct detection and MFC technique. The colored dashed lines mark the resulting LODs. The data shown is attained from a sensor utilizing a 1 μm thick FeCoSiB single layer as the magnetostrictive phase.

Chapter 4

Magnetically induced noise

Basic understanding of domain induced noise ranges far back into the beginning of the 20th century. The classical example of magnetic noise is sudden depinning, or previously described as jumping of a domain wall pinned beforehand by a local energy minimum in the magnetic material. The affecting energy minima can be a result of structural inhomogeneity, imperfections, defects and even dislocations [92]. The sudden movement and jerking behavior of domain walls in a magnetic material creates sudden magnetization changes. When a pick-up coil is used to measure inductively the magnetization response, voltage spikes are generated due to the domain wall depinning. The accumulation of several jumps describes the noise effects of a magnetic material exposed to AC excitation. These spikes were discovered by Barkhausen, thus the name Barkhausen jumps [90] [91]. Later magnetic imaging techniques provided the information about the physical origin of the voltage spikes related to the domain wall depinning and it is still a very interesting topic until today´s time in various research topics [95]. An example of such a jump is shown in Figure 13 with sequential MOKE images attained at different external applied field showing movement, pinning, depinning and further movement of a domain wall through a defect. The whole process is also added as a movie (Video 1). Such phenomenon is used to explain many loss and noise effects exerted by magnetic materials [92]. Several publications give indication for electrical

steels and the electrical losses originating directly from the magnetic noise generated by domain wall movements [93] [94]. Despite vast investigation of Barkhausen jumps and their effects on magnetic material, the other noise sources in a magnetic material are more scarcely researched. The magnetic noise generated by the annihilation of domains and domain nucleation is more reserved for researches in the development of magnetic layers related to sensor, energy harvester, magnetic recording and shielding applications. In these applications, the reduction or complete omitting of magnetic noise is of great importance.

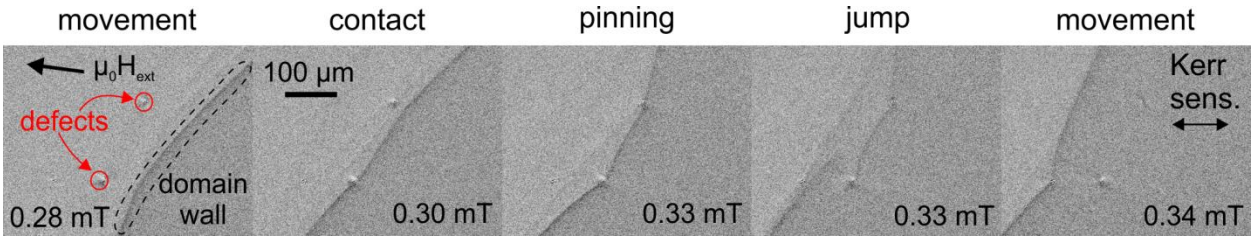

Figure 13: MOKE images indicating evolution of a Barkhausen jump with application of externally applied magnetic field with individual key points of the process in a multilayered sample (20 x 200 nm FeCoSiB). In the 4th image from the left, the exact moment of the jump is captured, where selective depinning of the lower part of the wall occurs independently of the still pinned upper part of domain wall. The residual contrast in front of the wall is the imprinted magnetic contrast of the domain walls from deeper layers. The imaging was performed with standard static MOKE setup without image averaging and image readout frequency of 12 Hz.

The most desired magnetic behavior of magnetic layers is to have coherent magnetization rotation with an external magnetic field. In AMR sensors, for instance, the magnetic layers are shaped in miniature strip-like layers that allow single domain formation and stability with externally applied magnetic fields [9] [11]. The same is achieved by creating very small lenticular magnetic elements [10], which induces a single domain behavior due to shape and edge effects. In recording media, this can also be achieved by creating nanograins or elongated nanograins shaped like columns [98]. Some applications in GMR as well as TMR are utilizing biasing techniques, which allow more freedom in terms of shape and production of the magnetic films. One commonly used biasing technique is EB. For the ME sensors, EB has been also integrated to achieve higher stability of the domain structure [13] [96]. To compare the magnetic behavior that relates to the noise properties of the sensors, various typical magnetic stacks in a model sensor form are presented and discussed in this chapter. It should be noted, that the

noise behavior and domain evolution with the magnetic field is preferentially discussed with field application along the long (sensitivity) axis of the sensor.

4.1 Single layer structures

To understand the more complex layer structures, it is important to understand the building block of them, the single layer structure. In this specific work the amorphous soft FM $(Fe_{90}Co_{10})_{78}B_{12}Si_{10}$ is used (later addressed only as FeCoSiB). The material is deposited by means of RF sputtering on a silicon substrate. The samples for testing are in the shape of standard sensor dimensions 2mm x 20 mm produced by means of UV-lithography and ion beam etching. This material is also magnetostrictive (λ_S= 3.4·10^{-5} [100]) and with its M_S (1.5 T [101]) and possibility to produce it with low K_u (range of 300-800 J/m^3 corresponding to H_k of 350-1000 A/m), is a very promising material for ME sensor applications. However, FeCoSiB can exhibit a branched domain structure that is a result of the soft magnetic behavior in combination with magnetostriction effects and demagnetization effects exerted from the physical edges of the material. Such structure results in a complex domain evolution with an applied field resulting in numerous domain wall jumping and domain rearrangement. An example of such a domain structure is given in Figure 14(a-d).

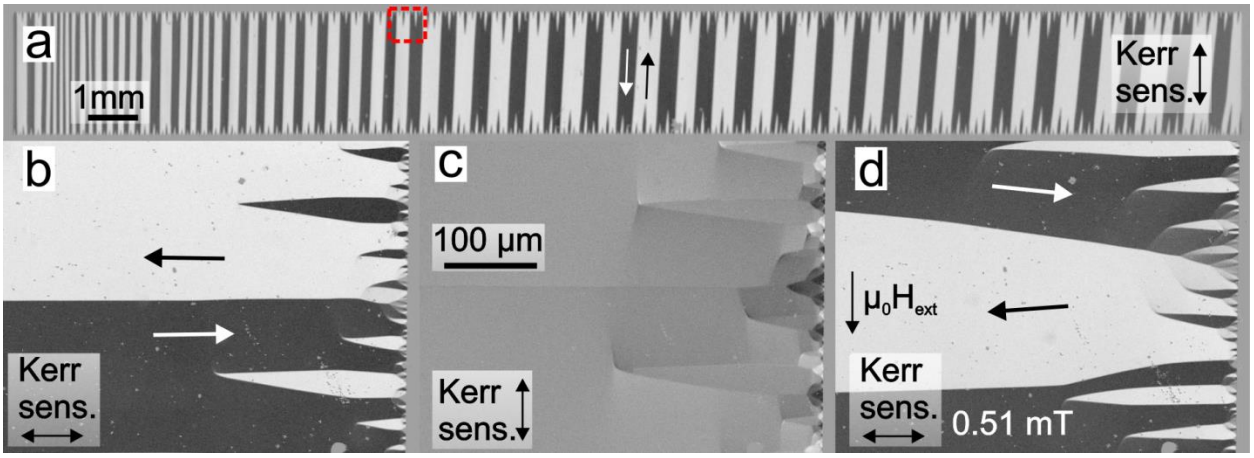

Figure 14: **(a)** Large view MOKE image of a demagnetized single layer 160 nm thick $Co_{40}Fe_{40}B_{20}$. The region marked with a red box is imaged with high-resolution MOKE **(b-d)**. The demagnetized state is visualized with the MO sensitivity aligned **(b)** horizontally and **(c)** vertically. **(d)** Selected domain image showing the growth of the spike domains and the

rearrangement of the 180° domains with an applied magnetic field along the long axis of the sample.

In Figure 14(a) classical magnetostriction related spike domains are visible in the sample exerted from the vicinity of the edge. Between the regular 180° domain and spike domains also closure domains form with their magnetization aligned parallel to the edge to compensate the H_{str} generation at the edge (Figure 14(b)). With an applied magnetic field, the whole domain pattern changes. The 180° domains reform in order to compensate the additional Zeeman energy. In response, the spike domains reform, grow and shrink to compensate the new domain state (Figure 14(d)). Additionally, generation of new spike domains from the edge can occur with increasing applied magnetic field. With further increment in applied field, spike domains with magnetization parallel to the field widen whereas others shrink. At a certain field value, the magnetization rotates sufficiently for the collapse of the domain state to occur, consequentially leading to a formation of a homogeneous single domain state. With the description above, it is clear that the sensor with such magnetostrictive phase yields large amount of magnetically induced noise. To omit such noise formations, a coupled multilayer structure can be utilized and even further, the multilayer structure can be additionally stabilized by integrating EB. Nevertheless, the behavior of such magnetic structures in the sensors is in reality very complex and hard to control (even with EB). The reason is the additional stress effects that occur due to the preparation and post production handling of the sensors which is discussed in the next section.

4.1.1 Stress effects and stress relaxation

Before the experimental results of further model structures are presented, it is needed to understand the effects of stress on the behavior of thin magnetic films. Stress generation in soft magnetic thin films can induce various changes in the magnetic structure. In the example given in Figure 15(a), the formation of various stress induced domains in a single layer 1 µm FeCoSiB film can be seen. The sample was sputtered without an external magnetic field. As shown in this figure, the local stresses across the sample and at the edges produced by sputtering dominate the domain formation. All edges show generation of spike domains giving the information of radially distributed stress axes with respect to the orientation of edges. The overall formation suggests a concave distribution of the local stresses with a slight eccentricity toward the bottom

edge. For formation of such a stress induced domain pattern, the magnetic material has to have very low overall anisotropy. In such cases the residing stresses in the MPa range can already have a significant impact on the domain structure [102], overpowering the rest of the anisotropy contributions [103].

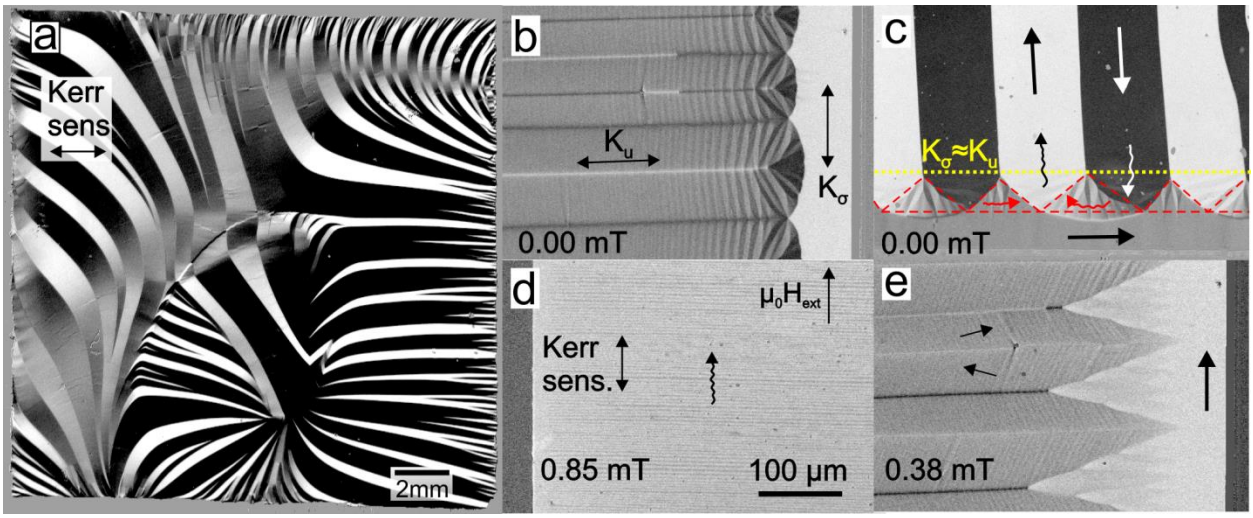

Figure 15: **(a)** Large view MOKE image of an as-deposited 1 µm FeCoSiB sample on a Si substrate showing domain configuration influenced by local variation of K_u. Sample also shows edge stress effects which is seen by the generation of spike domains from all edges. High-resolution MOKE images of 4 µm FeCoSiB **(b)** and **(c)** show the magnetization state at 0 applied field with different orientation of the sample with respect to the MO sensitivity. In image **(c)** the approximate closure domain structure is marked with the red dashed line and the magnetization within them by the red arrows. The yellow dashed line designates the region where the K_σ (from stress relaxation) is equal to the K_u, resulting in $K_{eff} = 0$. The corresponding anisotropy axes and magnetization directions are marked in the images. **(d)** and **(e)** images show the evolution of the domain pattern of the same sample with the magnetic history starting from saturation. The field is applied along the long axis. In (d) the blocked domain state is visible, whereas **(e)** depicts the 180° domain construct resulting from the collapse of the blocked state with reduced applied field.

Despite such formation of stress effects, the magnetic layers in sensors rarely show such behavior. This is because, the samples are usually sputtered with an applied external magnetic field, which allows the formation of a field-induced uniaxial anisotropy, which conceals the effects of local varying stresses [103]. The other option is to thermally handle the sensors with an applied magnetic field, forming a field induced K_u, which forms through diffusional process and local ordering [31]. Additionally, it has been shown, that the deposition with field does not produce sufficiently ordered anisotropy across a large area (see image Supp. 1 in Appendix). Such deviation can be corrected with field annealing. However, such thermal handling of the material can result in unwanted stress build-up, entitled stress relaxation. The relaxed stress originates from

the sputtering process of the magnetostrictive layers, during which the stress build-up occurs. The stress is a result of the different thermal expansion of the substrate and the sputtered material. The sputtering parameters and the selected substrate material can control the sign and strength of the inherited stress within the films. For the case of FeCoSiB layers sputtered on a silicon substrate for this project, it is strived to produce negative stress (compressive stress). It results in an overall compressive stress generated along the short axis of a cantilever shaped sensor, forming stress anisotropy K_σ also along the same axis. The additional anisotropy component does not create additional domain formation or domain refinement as it is aligned along the field induced anisotropy axis [103]. Nevertheless, the induced anisotropy is not always set exactly along the short axis, which is needed to achieve the highest sensitivity of sensors. An annealing procedure accompanied by an externally applied magnetic field along the short axis allows correction of the anisotropy misalignment. Sensors are typically annealed to a temperature from 200 to 250 °C for duration of 30 minutes. This allows the magnetic anisotropy to align along the short axis, but in doing so, the build-up stress within the film is relaxed at the edges. The relaxation is in the form of compressive stress buildup at the edges. As a result, stress induced anisotropy parallel to the long axis forms at the edges [102], leading to newly developed domains with magnetization aligned along the long axis [24]. These domains lead to new noise-generating sites that decrease the sensitivity of the sensors [24].

An example of such generated domains and the evolution in a 4 µm single layer FeCoSiB with an external magnetic field applied along the edge of the sample is shown in Figure 15(b-e). Due to the stress effects, the magnetization close to the edge forms a domain band with magnetization pointing with the edge. The width of the band is determined by the K_σ, scaling with the relaxed stress, which decreases in a steep parabolic fashion with the distance from the sample edge [102]. The K_σ at some point becomes low enough for the underlying K_u to effectively contribute to the domain formation. This results in the characteristic domain pattern with a fanned subdomain structure (Figure 15(b)). The fanning is a result of the self-magnetostrictive energy and it is formed in order to compensate the domain mismatch formed due to stress relaxation at the edge [24]. In the 180° domain the fanning also occurs and large fanning occurs up to the region until K_σ is equal to K_u, where the effective anisotropy K_{eff} is equal to zero. Further away from the edge, the K_u dominates the domain evolution and the fanning develops into slight

modulation of the magnetization of the 180° domains. The modulations surprisingly form even in the parts far away from the edge and can sometimes be seen to persist across the whole sample width. The reason for this could be the formation of a more relaxed state where no abrupt changes from modulated to non-modulated magnetization configuration occur. Such sharp changes would result in additional energy penalties from the flux closure being discontinuous and therefore making them unfavorable formations. By overseeing the substructures, exerted as spikes from the 180° domain construct, near the edge as a whole, the typical closure domain structure is visible (marked by red dashed line in Figure 15(c)). This shows the magnetization structure is in principle very similar to the state of the non-annealed single layer seen before, only that it is internally modulated and offset from the edge due to the present stress near the edge.

From the noise point of view, the occurring modulations may act as an additional noise source as these small structures cause numerous supplementary domain wall movements to occur with an applied field, adding to the already strong noise behavior of the 180° domains. With the application of a magnetic field along the edge the 180° domains reduce in width and the modulated closure domains enlarge. With further increase of the field, the structure is engulfed by the modulated closure domain structure and then sets to a saturated state. When the material is taken away from the saturated state, a different domain pattern occurs with much narrower domains. Example of such state is visible in Figure 15(d). With further reduction of the externally applied field, the blocked domains grow until a certain point, where a collapse occurs into wide 180° domain pattern (Figure 15(e)). This is a sharp transition in the domain structure that can be seen from the rapid change in magnetization orientation in the domains. The transition also creates a change in the domain wall structure from a low-angle asymmetric Néel wall type of the blocked structure [103] to an asymmetric Bloch wall [26] type of the 180° domain structure. This reforming occurs in order to accommodate the turned magnetization due to the decreased Zeeman energy and prevalence of the anisotropy energy. The most important part of the whole magnetization change is the strong hysteretic behavior that is a result of the transition between the blocked and 180° domain states. The transitioning has been already correlated in the past with sensor noise behavior in response to the domain structure present during sensor operation [24].

Even so, another crucial part for the noise response is in the instantaneous magnetization switching of the stress relaxation formed edge domains. The domains are reforming and switching close to the zero magnetic field point. This is predominately an important noise point, as the switching will occur already at the application of very small AC fields, leading to quick formation of magnetically induced noise. Additionally, the switching leads to further destabilization of the 180° domains, which also contribute to the noise behavior by domain wall movement. In order to diminish these severe noise sources, the stress relaxation needs to be compensated. For the correction of such effect, there are only limited possibilities. One of them is the edge patterning that allows local manipulation of the anisotropy near the edge through its shape, resulting in a reduction of the stress relaxation effect. This method is deeply researched and presented in Chapter 9. Another option is to use a hard biasing method by means of patterning additional permanent magnets close to the edge of the sample. This produces a gradient bias field affecting only the edge part of the sample, allowing the soft magnetic behavior of the middle part of the magnetic layer to persist.

4.2 Multilayer coupled structures

By combining several FeCoSiB layers separated by a non-magnetic spacer such as Ta, a stray field coupled system can be produced. The advantage of such a coupled system is the more stable domain configuration with the application of a magnetic field. The coupling reduces additionally also the effects of the demagnetization field H_{dem} that is important for larger thicknesses of the magnetic thin film. A typical coupling is the antiparallel coupling, where the magnetizations of neighboring layers are antiparallel to each other. This results in formation of domain patches (usually rounded form as the domain wall formation is energetically equally favorable in all directions leading to a radial growth of the domains) that are firmly coupled due to the closed flux system [104] [105]. The problem of such a system is that the antiparallel coupling can collapse quickly with an applied magnetic field, especially when the spacing between the layers is large leading to weak coupling. The collapse of the coupling at sufficient field is instantaneous and usually results in large regions of the domains changing in sign of the magnetization and inducing large movement of domain walls. An example of such coupled multilayer is presented in Figure 16(a), where the imprint of residual patches from lower layers is

visible. The imprinted walls (360° walls) show the transition from parallel to antiparallel coupled regions of the magnetizations from the neighboring layers [106]. The specialty about this structure is the strong strip like form of the antiparallel domains that occurs because of the influence of the K_U. Despite the drawbacks of the antiparallel coupling described above, it is still the most stable state a multilayer structure can attain. Nevertheless, the structure can couple also in a parallel fashion. In this case, the domain configuration is well dominated by the self-magnetostriction and stress relaxation at the edges. This leads to the branching, domain reforming and movement of domain walls similar to the structure seen in single layer systems (discussed already in 4.1). However, due to the internal coupling of the layers, the structure is more stable with the application of field.

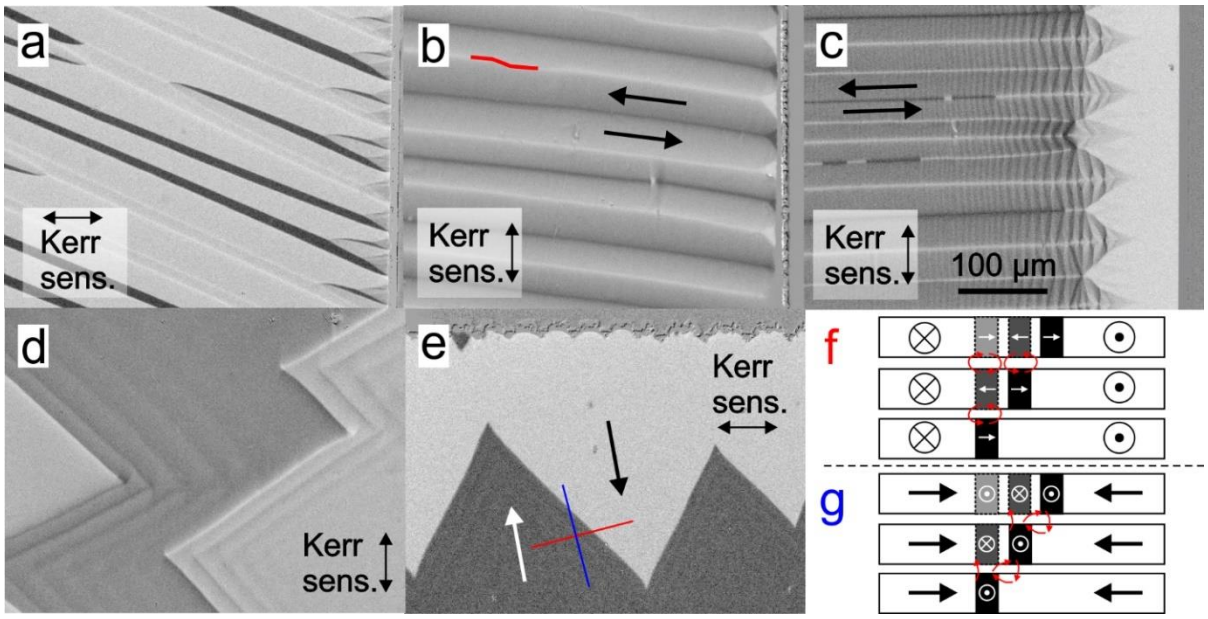

Figure 16: MOKE images of a multilayer structure (20 x 200 nm FeCoSiB, 5 nm Ta spacer) showing various coupling states at zero applied magnetic fields. (a) Antiparallel coupling with domain patches and imprinted domains/domain walls due to residing patches in lower layers. (b) Parallel coupling with low residual stress showing regular domain pattern with narrow domains and walls with shifted segments (marked with red curve). A 7° tilt of the anisotropy is present. (c) Parallel coupling with added stress relaxation from the edge. (d) and (e) Parallel coupling with a substantial amount of stress present in the system. In (d) the cascading domain walls are visible, showing up to 6 walls. In (e) with other MO sensitivity axis, the magnetization direction is marked. The colored lines indicate the sections of which the magnetization construct is sketched. (f) and (g) A side-view schematic showing the possible magnetic configuration of the multilayer structure in (d) and (e). The (f) shows the generation of the imprinted domain wall (grey) due to the stray field of the primary domain wall (black). The red arrows represent the stray field flux formation. In (g) the charging at the domain walls and the stray field coupling of the cascading walls is show (flux marked by red arrows). Note, that in (f) and (g), the flux is

represented in a two-dimensional form (projection onto the viewing plane) for simplicity. In reality, the flux would follow a 3D form turning simultaneously in-plane and out-of-plane. Samples **(a-c)** were fabricated by Rahel Kruppe and sample **(d-e)** by Erdem Yarar.

Despite the more stable domain structure, the multilayer system does include a higher number of domain walls per magnetic volume (however, in terms of volume ratio it is same as for a single layer with the same total FM thickness t_{FM} of the multilayer). The reason is the similar domain structure in individual layers, which couple through magnetostatic interaction. In the example of an as-deposited multilayer film in Figure 16(b) the domain structure shows very similar domain pattern as in the single layer system. The difference is the slight segmented step-like shifting of the domain walls that occurs due to the coupling of the walls from layer to layer [107]. Part of the shifting segmentation is marked with a red line for enhancement. With the addition of stress relaxation from the edge, the domain pattern still forms similarly to the single layer with the formation of additionally denser domain structure and wider domain walls (Figure 16(c)).

When the stress during deposition is larger, a special zig-zag domain structure can form. Such a structure can occur when the magnetizations from neighboring layers couple in a parallel manner. In this state the magnetization cannot sustain a single domain orientation due to H_{dem}, which leads to a multidomain state with head to head or tail to tail magnetization configuration. Since the energy state is unstable by straight domain walls, the energy is minimized by forming local flux closures by the zig-zag pattern of the domain walls. The pattern is constructed from compensated Néel walls [108] and it exhibits charging that occurs at the tips of the zig-zag spikes as there the flux cannot close properly. An example of such a structure is shown in Figure 16(d-e) at zero applied magnetic fields. The zig-zag spikes are correspondingly sheared in form with respect to the tilt of the K_u. The opening angle between the zig-zag elements of the walls in Figure 16(d-e) is on average 70°±2° which relates to the K_u direction and magnitude with respect to the demagnetization effects. Superfluous difference to the previous structures is also the cascading behavior of the walls with an applied magnetic field. The charging of the walls due to the head-to-head or tail-to-tail configuration induces stray field generation in the out-of-plane direction. The stray field couples the walls of neighboring layers resulting in a compensating structure with interlayer H_{str} exerted from layer to layer. A domain image of this effect is presented in Figure 16(d), where up to 6 cascading domain walls are visible. The lower domain walls are visible because of imprinting formed

through the generated H_{str} that copy the wall structure onto the magnetization of the top layer. Due to this feature, many mechanisms of the magnetic structure and coupling effects can be indirectly observed in multilayer systems. A schematic explanation of the formation of such coupling is presented in Figure 16(f-g). Due to the described possible behaviors that lead to a large amount of noise formation, the practical applicability of multilayer structures is very limited. However, the multilayer structures are important to research as they provide the possibility to understand the underlying coupling mechanisms that occur in the multilayer EB systems, which are utilized to stabilize the domain structure much more successfully.

4.3 EB multilayer structures

As stated already beforehand the EB system allows significant stabilization of the domain structure. The EB with proper preparation leads to a single domain structure as the EB field keeps the structure in a saturated state along its direction. When the EB is aligned along the short axis of the cantilever design, the sensor will exhibit only coherent magnetization rotation during operation, leading to a linear magnetization response and low noise formation. Although EB structures utilizing a single FM layer can be used, there is a thickness limitation of the FM layer as it reduces the H_{EB} with the increased t_{FM}. The thickness increase is needed, as the sensor signal is proportional to the t_{FM}. Nevertheless, such EB reduction can then lead to insufficient EB, which cannot then sustain the stable configuration anymore. For this reason, a multilayer system is used in order to retain the desired EB with larger total t_{FM} of the system. An example of such a system is in Figure 17(a). Such sensors have exhibited the best sensor performance at low frequencies, resulting in the best LOD of ME sensors utilizing MFC (180 pT/Hz$^{1/2}$ at 10 Hz) [21]. However, with the application of multilayer structures a new difficulty was observed. With increasing the overall t_{FM}, the demagnetization effects become stronger. At a certain thickness, the H_{dem} compensates the EB field, leading to a collapse of the single domain state into a multidomain state. Due to the gradual decrease of the demagnetization effect from the edge (see section 1.2.3) the compensation of EB field also occurs the same way. Together with the previously discussed stress relaxation effect the demagnetization effect leads to a gradual domain reforming, which leads to a complicated domain structure. The effect of the H_{dem} on EB multilayer is visible in Figure

17(b-d). The previously mentioned zig-zag domain pattern forms, since the compensated domains form oppositely to the EB (effective H_{dem} is opposite in sign to the EB field). This effect is very troublesome as it induces a thickness limitation. This was already reported with measurements of sensors where with increasing thickness the signal response is higher, but the noise formation of the magnetic phase also increases. After a certain thickness, the noise increases faster than the signal gain, leading to worsening of the LOD with further thickness increase. It is possible to make multilayers with a very thin individual t_{FM}, but then the material becomes much harder which results in a much lower signal response of the sensor. In this work, this restriction is battled with new coupling systems and structures that are discussed in Chapters 5 and 6.

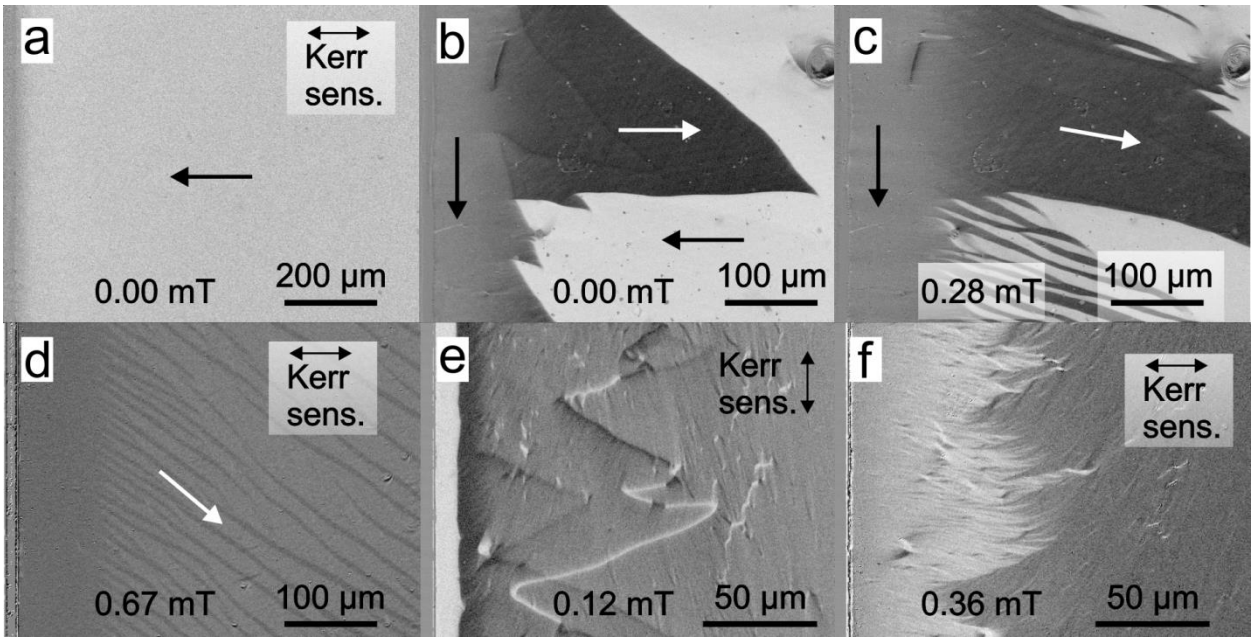

Figure 17: (a) Single domain state in a 10 x [100 nm FeCoSiB / 8 nm MnIr] sensor. (b-d) domain evolution with field for a sample, where the H_{dem} is compensating locally the EB (sample: 10x [200 nm FeCoSiB / 8 nm MnIr]). (e) Image indicating the ripple structure flowing perpendicular to the present magnetization. The sample is 10 x [90 nm FeCoSiB / 8 nm MnIr / 5nm Ta / 110 nm FeCoSiB / 8 nm MnIr] (f) sample showing irregularities in the domain structure caused by ripple formation and domain collapse (same sample structure as in (e)). For all images, the field is applied in the vertical direction (along the structure edge). The sensor was fabricated by Volker Röbisch.

Despite the expected single domain state, the EB system in reality is not completely homogeneous in terms of the magnetization in the single domain state. Due to the variation of the crystal structure of the AFM layer, the EB also locally varies leading to local magnetization variations. These modulations are named as ripples and are visible in Figure 17(e). The formations are always oriented/propagating perpendicular to the

magnetization direction. The ripples are especially important, when the FM layers are thin as the modulations become much more prominent and influential with lower t_{FM}, however with specific interlayer couplings the ripples can preserve the large sizes. In the preparation of multilayer EB sensors, the difficulty of aligning the EB was indicated as one of the main setbacks of achieving proper sensor behavior during MFC. The perfect alignment is needed, as the symmetrical signal response and low noise performance are directly influenced by it. With a slight misalignment, a component of the EB and/or K_u points towards the long axis of the sensor, which creates the asymmetric response. The tilted EB leads to the formation of narrow tilted domains (visible in Figure 17(d)) that are creating significant noise formation in the magnetic layer. This specific problem of proper alignment and the possibilities to attain it are discussed in the next chapter. Furthermore, improper preparation of the EB by either insufficient fields or temperature can lead to unordered EB with a variation in strength and alignment on a local scale. The variation leads to modulated domain formation that become especially prominent with the application of external field on the sample (Figure 17(f)). To gain a continuous and homogenous EB, the heat treatment needs to set correctly. This is also discussed further on in the next chapter.

Chapter 5

Parallel exchange bias

From the various model systems in Chapter 4, it was concluded that all of the various coupling schemes show limitations in withholding a stable domain configuration. The last scheme, EB coupled structures, showed the most promising results. Within this work, research was conducted in order to modify and possibly enhance the effect of the EB coupling. The exact name of this coupling is denoted as parallel EB coupling (PEB) as to discriminate from the antiparallel EB (APEB) coupling scheme discussed in Chapters 6 and 7.

5.1 Modified heat treatment

The previous subsection has indicated that the main problem is to attain proper alignment of the EB. Conventionally for the setting of EB, a heat treatment with an external magnetic field is conducted after the production of the magnetic layer system. The usual procedure is to heat the material to 250 °C and treat it for 30 minutes. During the whole procedure, the material is exposed to an external magnetic field that saturates the FM layers in the direction that is wanted for the EB to form. The process has worked well in the past, however, in certain cases the magnetic structure showed a certain misalignment (range of few degrees) of the EB away from the preferred direction. This

leads to a lack of symmetry of the EB in regards to the long axis that can lead to two undesired effects. Firstly, the EB can locally collapse into several domains leading to an instable domain configuration. The second effect is related to the MFC signal behavior, where it is crucial that the material behaves equally symmetrical during the translation from positive to negative field and back, otherwise the signal becomes reduced (see section 2.1.2 for more details). For this reason, it was investigated, if the alignment could be improved by modifying the heat treatment. The modification was researched by increasing the holding temperature. Experiments were conducted for temperatures of 250 °C, 275 °C, 300 °C, 325 °C and 350 °C with the same holding time of 30 minutes. From this chapter onwards, a standard sensor structure was used. The multilayer EB ME composites were fabricated on double side polished 350 µm thick thermally oxidized Si cantilever, where the functional piezoelectric and piezomagnetic layer stacks were deposited on the top and bottom silicon surface respectively. The Ta(24) / Pt(150) / AlN(2000) / Cr(5) / Au(100) (thicknesses in nm) piezoelectric phase was deposited by magnetron sputter deposition in pulsed DC mode in nitrogen atmosphere [53]. The piezomagnetic multilayer structure was grown by DC magnetron sputter deposition. Standard UV lithography processes and dicing of the substrates were used for the preparation of the ME cantilever sensors. The whole fabrication was performed either by Volker Röbisch or Lars Thormählen. The EB magnetostrictive layer stack consists of repetitions of [Ta(5) / Cu(3) / Mn_3Ir(8) / $(Fe_{90}Co_{10})_{78}Si_{12}B_{10}$(90) / Ta(5) / Cu(3) / Mn_3Ir(8) / $(Fe_{90}Co_{10})_{78}Si_{12}B_{10}$(110)] (thicknesses in nm). The Ta and Cu layers are seeding layers for better film adhesion and orienting the AFM (MnIr). More details about the preparation are given in [23]. The heating trials in this chapter were conducted on sensors with multilayer EB stack with total t_{FM} of 2 µm (10x repetition of upper structure).

The results of the experiments showed a slight gradual change of the hysteresis of the EB with increasing temperature up to 300 °C. Above 300 °C, the changes of the loops are then minuscule or show signs of crystallization. At 350 °C heating, the short axis loop shows a wide opening and the color of the sample surface develops a purple color from previously silver/light gray color (loop and images in Supp. 2). Both indicate a possible change of the material structure. The coloration change indicates oxidation effects, whereas the hysteresis opening could relate to crystallization effects. The later possibility correlates with the TEM findings for similar multilayer structures annealed at 350 °C [109]. For this reason only the loops of the sensors annealed with previously

standard 250 °C and new 300 °C are compared (Figure 18(a-b)) to show the most prominent changes in the magnetization response without the presence of possible structural changes.

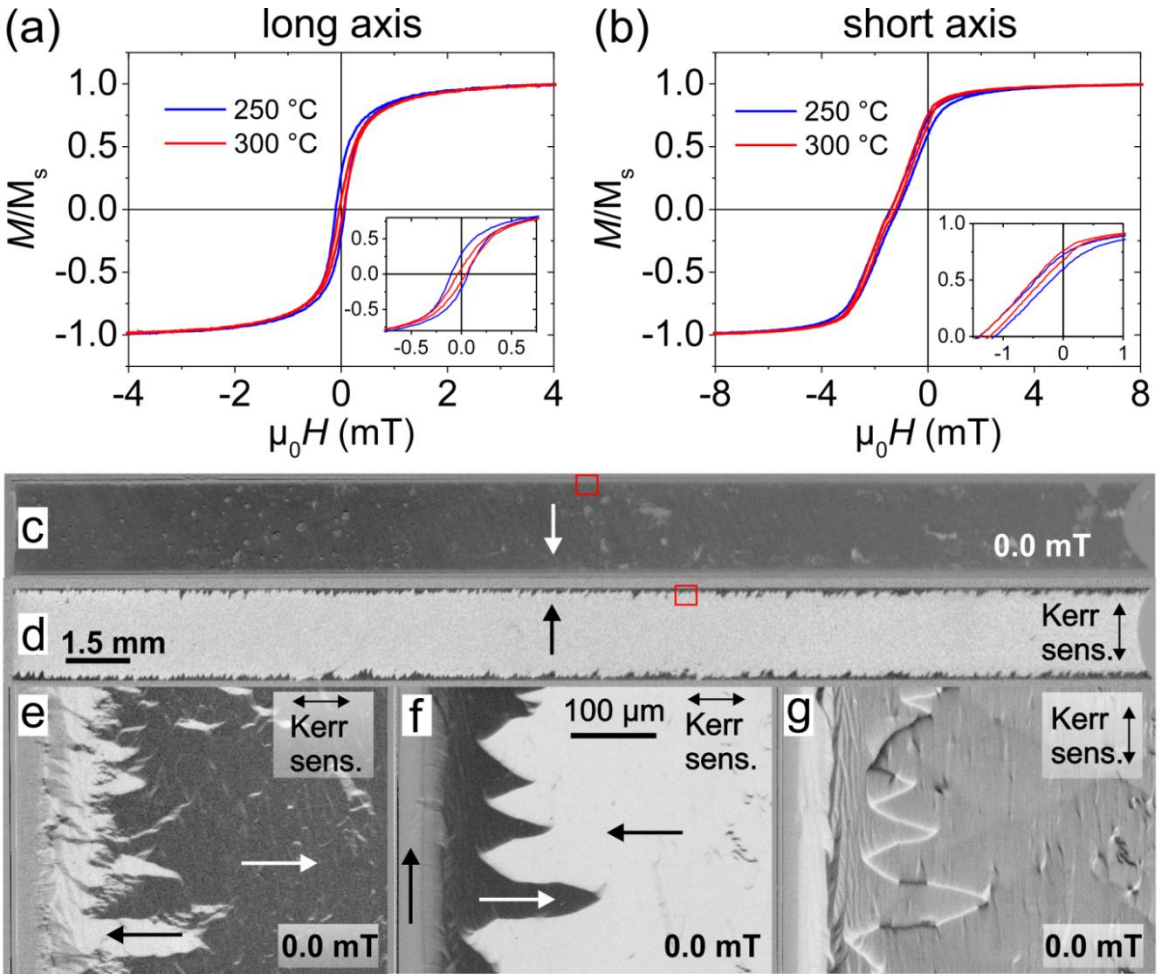

Figure 18: Inductively measured hysteresis loops for (a) long and (b) short axis of two PEB sensors annealed at 250 °C and 300 °C. Insets in the graphs are enlargement of the hysteresis for indicating the difference between the two sensors. Large view domain image of PEB sensor annealed at (c) 250 °C and (d) 300 °C. The marked red squares represent the approximate areas of domains observed with higher resolution. (e) High-resolution domain image of the 250 °C sensor showing unordered domain state with several local modulations and inhomogeneity. (f-g) Domain images with two different MO sensitivity axes of a PEB sensor annealed at 300 °C showing more determined domain structure with negligible inhomogeneity compared to (e). The structure of both sensors is 10 x [90 nm FeCoSiB / 8 nm MnIr / 5nm Ta / 110 nm FeCoSiB / 8 nm MnIr]. Sensors were fabricated (without the annealing procedure) by Volker Röbisch.

The long axis loops show a decreased opening with the new holding temperature. For the short axis loop, the change is very small, however the trend of slightly more closed loop and slightly softer character with higher temperature is visible. This gives a hint of a more

ordered and aligned EB. The slight step in the short axis loops at around 2 mT is the varying EB field exerted by the two different thicknesses of the FM layers. Such layer system was used due to conformity for later comparison, as they were also used for APEB investigation. Interestingly, there is also a decreased opening in the region of the remanent magnetization of the short axis for the 300 °C treated sensor. Such change can be related to a more stable domain configuration at H =0. This means that the demagnetization effects are decreased with higher holding temperature. In order to understand the origin of these changes, domain investigation has been conducted.

5.1.1 Domain structure modification

From the overall MOKE images in Figure 18(c-d), no significant modifications of the domain structure are visible. Both sensors show typical penetrating spike domains exerted by the edges as a result of H_{dem}. However, the 250 °C sensor shows a narrower region of the edge domain structures, which contradicts the changes seen from the induction measurements. With closer observation of the domain structure with high-resolution MOKE, the spike domain structures reveal a much more complex domain pattern. The 250 °C sensor shows high irregularities mixed into the base domain structure (Figure 18(e)). These strong modulations are most probably due to the insufficiently aligned EB leading to a local variation of the EB direction. With the application of an external magnetic field, the sensor shows high domain activity, at which several small domains randomly nucleate/grow leading to a conglomerated structure tilted at about 20° away from the short axis at zero field (Figure 19(a-c)). This structure occurs from the local variation of the EB and its relation to the K_u [110].

On the other hand, the 300 °C sensor shows much more homogeneous domain structure with only scarce modulations (Figure 18(f)), which can be attributed to local defects. From the other MO sensitivity direction (Figure 18(g)), the contrast reveals thick domain walls and imprinted domain walls from the lower layer(s), suggesting antiparallel alignment of the domains within a layer and between layers [106]. Such behavior could very well explain the narrowing of the loop near remanent state, as the antiparallel coupling compensates the local H_{str} leading to the reduced demagnetization effect and increased stability of the domains near remanence. The antiparallel coupling is also confirmed with the domain evolution with applied field along long axis (Figure 19(d-f)). The domain pattern near the edge does not change significantly and mostly coherent

rotation of the magnetization is visible. Nevertheless, the domains do slightly shift and show irreproducible changes of the domain edges, leading to minor reforming of the spike domains. The reforming occurs with gradual transformation of the magnetization in the antiparallel domains by nucleation and growth of thick ripples that overtime flip the magnetization in the whole domain. This leads to the collapse of the antiparallel alignment of the domains. From the alterations with each saturation cycle, instability of the structure and EB can be deduced. The instability is a direct result of the compensating H_{dem}, which generates the edge domain structure and due to the local variation of the EB the domain pattern slightly shifts.

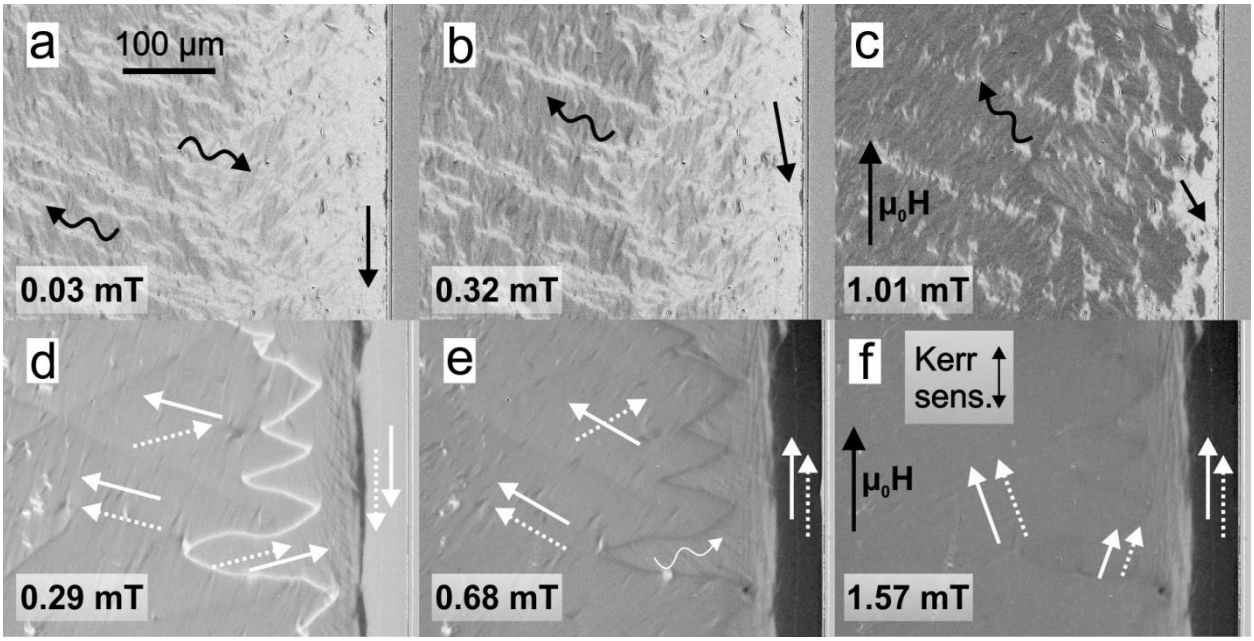

Figure 19: (a-c) Domain evolution with field application for the 250 °C sensor showing large amount of irreversible domain reforming and inhomogeneity of the domains. (d-f) Domain evolution with applied field for the 300 °C sensor showing much more stable domain state, showing mostly coherent magnetization rotation with only slight change of the domains. The domain state shows antiparallel segments (the relation between the magnetizations of the top and next lower layer is denoted with the dark and white arrows respectively). However, a collapse of the domain structure occurs at higher applied fields (e), leading to the formation of small elongated domains oriented perpendicular to the magnetization (marked with the curved arrow). With even more field, the antiparallel domain segments collapse, however the edge spike domains persist in an antiparallel configuration (f). The structure of both sensors is 10 x [90 nm FeCoSiB / 8 nm MnIr / 5nm Ta / 110 nm FeCoSiB / 8 nm MnIr]. Sensors were fabricated (without the annealing procedure) by Volker Röbisch.

In specific cases, the 300 °C heated sensors show a more complex domain structure. The general domain pattern explained beforehand has built-in periodic modulations that are very strong in contrast. With the application of the external magnetic field, it is visible that

the modulations behave adequately with the surrounding magnetization, turning coherently with the field. With sufficient field, the modulations collapse into fine ripple structure. Additionally, after releasing the structure from a saturating field, the modulations are set exactly back to the original position. This indicates that the structure is not caused directly by the demagnetization effects or hysteretic effects, but is indeed imprinted by the EB. This furthermore suggests that the structure is inherent throughout the other lower layers, otherwise residual imprinted contrast would be visible from the lower layers The understanding of the origin of these structures is not completely clear.

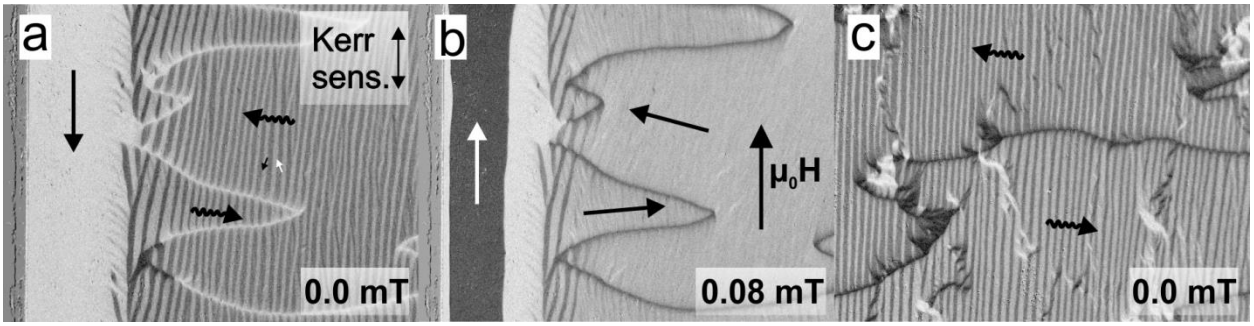

Figure 20: **(a-b)** High-resolution domain images at the edge of a PEB sensor showing the transition from the highly modulated domain structure **(a)** to more homogenous domain structure with ripples **(b)**. **(c)** Domain image of the middle of the same sensor showing the continuation of the modulations throughout the whole sensor. The structure of the sensor is 20 x [90 nm FeCoSiB / 8 nm MnIr / 5nm Ta / 110 nm FeCoSiB / 8 nm MnIr]. The sensor was fabricated (without the annealing procedure) by Lars Thormählen.

It is considered, that the structure originates from the magnetostrictive effects, as it resembles the modulations seen in single layer systems. The problem of this theory is that the EB is set with heating under the influence of a saturating magnetic field. By simultaneous domain observation during the heat treatment, it is confirmed that (at least) the upper layer is saturated throughout the process. A possibility as to why these modulations occur is that the EB changes with time due to H_{dem}, that is formed by the ferromagnet and is the only effective field once the sensor is released from the external field. The mechanism for this is the so-called training effect, which occurs due to local changes of the EB with an application of a continuous magnetic field. This has been observed in many EB systems including multilayer systems utilizing the same AFM as in this work, MnIr [111]. Various researchers indicated that such behavior occurs as a result of the time dependent switching of the AFM moments that are induced by thermal instability [112] and frustration effects [113]. With the application of saturating field the instability can be directed, leading to a gradual changing of the EB in its alignment and

also strength (EB field) [114]. In this case, the change of EB is prompted by the H_{dem} in combination with the stress relaxation edge that induce realignment of the EB over time.

Another possibility although less likely, is that the magnetization at the interface of the ferromagnet is not at all saturated due to interface roughness and interface coupled spins of the AFM and the ferromagnet. Instead, the interface is highly charged and tremendously branched due to self-magnetostriction that compensates the high mismatch of the saturated bulk part to the surface region. From such a state, varying compensated/uncompensated states at the interface between the AFM and ferromagnet form, leading to a periodic structure with a net directionality of the EB. This would then explain why such structure evolves even though the layers are perceived to be saturated and why the structure collapses into fine ripple structures at low applied fields. Additionally, this would also explain the tendency of such a pattern occurring more often for samples with larger overall thickness, as the surface roughness of the top most layers (and interfaces) increases with the overall stack thickness. However, the same tendency is also exhibited by H_{dem}, which increases in strength with higher thickness. A possible way to understand and confirm the origin of the structures would be to heat the sample in vacuum with high-resolution microscopy. This way the observation could determine any residual contrast in the top layer during the heating process or directly after it.

5.1.2 Comparison with electrical characterization

With the comparison of the domain structures, it is clear that there is a clear benefit of preparing the PEB sensors with 300 °C heating step compared to the previously standard 250 °C treatment. For this reason, a batch of sensors were produced and characterized with direct detection and MFC methods, to indicate the improvement also from the perspective of the sensor's sensitivity. In Figure 21, the electrical characterization data is shown. With the bias curve measurements, the significant increase of the 300 °C sensor's response is already visible, exerting 3.4x larger voltage output at optimal bias field. This is a clear sign of the increased alignment of the EB as the reduced variation allows a larger part of the magnetization to turn coherently with the applied field leading to a larger magnetostrictive response. With this, the LOD for direct detection also improved by around 2x. Similarly, for MFC the 300 °C sensor shows increased signal response, as the signal output is higher and the ME response has a more symmetrical

form. Interestingly, the noise response of both sensors is very similar. This indicates that the domain structures of the upper layer for both sensors are in fact related by having the same noise sources. This is also clear as the domain changes do occur for both sensors by the nucleation and growth of the small ripple structures that change the overall magnetization construct with increasing field. This means also that the PEB sensors are at a limit in terms of noise performance, as the heating and further alignment of the EB does not reduce the occurrence of the noise sources. For this reason, other coupling methods have to be researched in order to further reduce the noise behavior of the sensors. One such new coupling mechanism is introduced and explained in the next chapter.

Nevertheless, with the new heating temperature, the LOD is improved by a factor of 10, from about 1 nT/Hz$^{1/2}$ to around 100 pT/Hz$^{1/2}$ at 10 Hz. This is a substantial improvement and has already become the best sensor compared to the ones produced before this work. The LOD measurements presented in Figure 21(e) are determined differently to the other LOD measurements, as the analysis technique was done differently at that time, but the exactness of the technique is comparable to the one used later. Furthermore, the LOD of the 300 °C treated sensors improves with increased thickness (Figure 21(f)), which is now a different trend compared to what was observed in previous research on the standard treated sensors [23]. Interestingly, the noise level is very similar for the different thicknesses, indicating that the noise sources are similar and do not change significantly with increasing H_{dem}. The reason for such behavior is the harder EB stacks that were used in this research incorporating 90/100 nm FeCoSiB layers compared to the comparing research that utilized 200 nm FeCoSiB layers and same AFM layers. However, the previous research does give a hint, that the sensors cannot be improved very much more with increasing the t_{FM} as then the demagnetization effects compensate the EB, leading to higher noise response [23]. Nevertheless, the increased thickness behavior with the new heating temperature has to be researched to see the change of behavior of the system. With the current sensor stack utilizing PEB configuration with total t_{FM} of 4 µm, the best LOD of 85 pT/Hz$^{1/2}$ at 10 Hz was achieved.

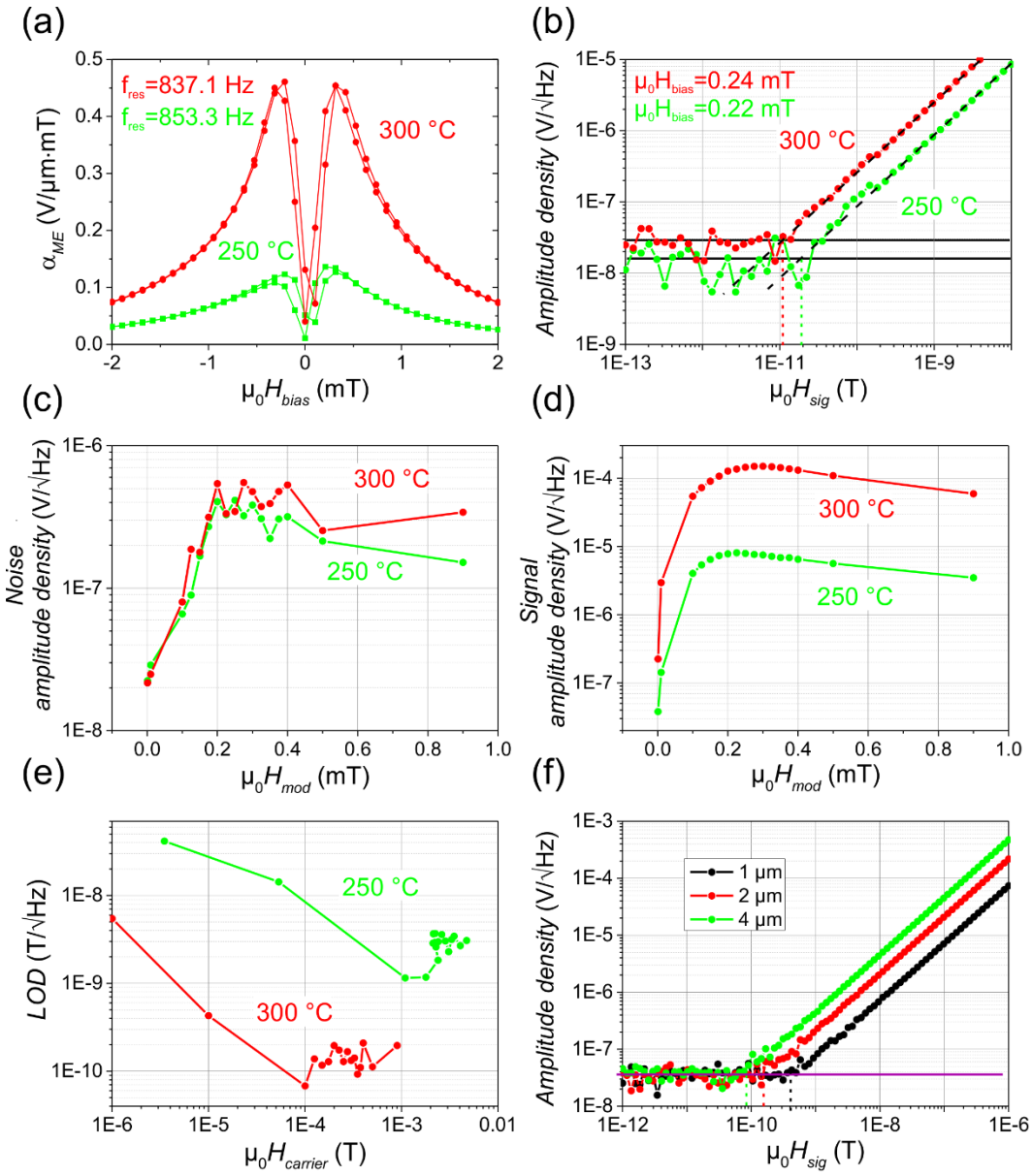

Figure 21: Electric characterization data for two 2 µm sensors heated at 250 °C and 300 °C. (a) Bias curve measurements, (b) LOD measurements with direct detection method, (c) noise response measurements, (d) signal response measurements and (e) LOD measurements with MFC showing the significantly better performance of the 300 °C sensor compared to the 250 °C sensor. The LOD measurements in (e) are presented differently due to an older method of characterizing the LOD of sensors with MFC technique. (f) LOD measurements with MFC for 300 °C handled sensors with different total t_{FM}. The sensor structures are 5x, 10x and 20x [90 nm FeCoSiB / 8 nm MnIr / 5nm Ta / 110 nm FeCoSiB / 8 nm MnIr] corresponding to 1 µm, 2 µm and 4 µm total t_{FM} respectively. Measurements were performed by Sebastian Toxværd.

Chapter 6

Antiparallel exchange bias (APEB)

The previously improved PEB has provided already an increase in signal response and with it a better LOD. Nevertheless, this method does invoke some shortcomings. Firstly, the EB does not resolve the problematic of the H_{dem} being exerted from the physical edges of the sensor that induces the formation of spike domains, which are one of the main source sites for noise generation. This is especially important when the t_{FM} is increased in order to attain higher ME response through reduced EB strength and higher magnetic volume. This effect has been reported in the past, which showed that increased t_{FM} induced increasingly larger penetrating spike domains with a much higher effective area. This in turn created higher magnetically induced noise, leading to an increased LOD [23] [96]. Such results indicate there is a limitation of the method to a certain t_{FM} until which the EB can still compensate the effective H_{dem}. The second weakness of the PEB is the instability of the system, exhibiting gradual change with an applied magnetic field. This feature is a result of the metastability of the magnetic moments formed during sensor fabrication and EB alignment. Due to the metastability, the magnetic moments within the AFM layers tend to align gradually with an externally applied magnetic field changing the overall EB field direction leading to a destabilized domain configuration [111]. For this reason, special consideration of such sensors is needed during measurements and storage, which makes the sensors harder to handle by needing more complex

measurement schemes. To counteract these two disadvantages of the PEB system, a new magnetostrictive multilayer stack is introduced, which incorporates interchangeably antiparallel aligned EB layers or in short antiparallel EB (APEB). This structure presented in the next subchapter, combines the effect of the flux closuring of antiparallel aligned magnetic multilayer system and the magnetic domain stability of EB coupled structures.

6.1 Model

In the sketch Figure 22(a), the new APEB configuration is presented. The structure is composed of a doublet of FM layers, which have domains with their magnetizations aligned antiparallel to the neighboring domains. Additionally, the domains between the layers are also aligned antiparallel. Each FM layer has an accompanying AFM layer that induces a unidirectional anisotropy (aligned along the short axis), which creates an H_{EB} exerted in the direction of the magnetization. With the additional EB, the construct of domains is withheld strongly in the presence of external field, increasing the stability of the whole domain structure. Due to the rigid antiparallel alignment of the new structure, a tight flux close system is formed through the interconnection of H_{str} between neighboring FM layers. This in turn allows a significant reduction of the effective H_{dem}, leading to a decreased noise formation compared to the previous PEB system. A simulated overall magnetic response of a bilayer APEB system (2x200 nm FeCoSiB) along the long axis and short axis of the sensor is portrayed in Figure 22(b-c). In the same figure, also the modeled PEB with the same physical structure is given for comparison. The modeled data shows, that the APEB delivers a slightly harder magnetic response. This is expected as it should reduce the effect of H_{dem} ,which effectively softened the PEB. Despite this, it is expected, that such construct would deliver superior reduction in noise due to the reduction of H_{dem}. In Figure 22(d) also the normalized ME response is given for understanding the possible sensor signal output. The graph shows the predicted 14% lower response of the APEB compared to the PEB, which results from the previously mentioned harder response of APEB. It should be stated that the model was done for single domain state of the magnetic layers and shows idealized behavior without considering stray field coupling effects. The model will be adapted later in the following subchapters, to consider additional contributions of the stray field coupling as well as

the effects of a multidomain state and demagnetization effects of larger total stack thicknesses.

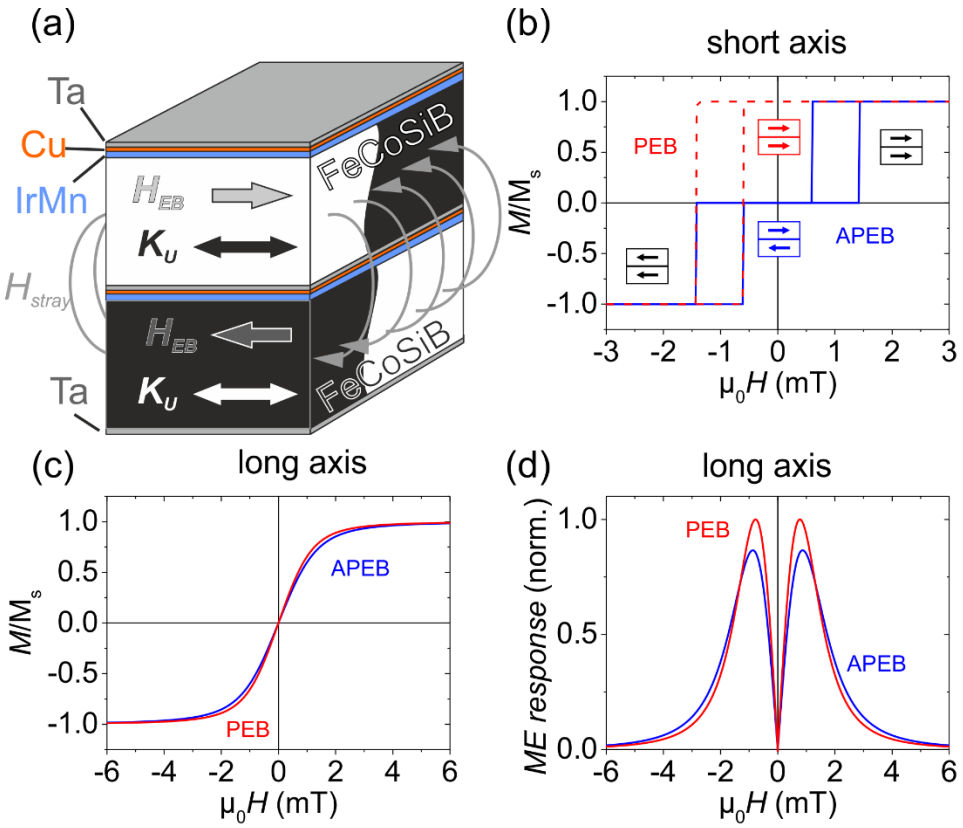

Figure 22: **(a)** Sketch of a model bilayer structure depicting the APEB structure. The K_u, H_{EB} direction and H_{str} are portrayed as well as the individual layers constructing the system. The black and white patches of the FeCoSiB are visualizing an exemplary domain structure. Modeled magnetization response along **(b)** long axis and **(c)** short axis of PEB and APEB model structures. The structures are composed of 2x200 nm FeCoSiB and have the standard cantilever size 20 mm x 2 mm. In **(d)** the ME response derived from the magnetization loop, showing the slight decrease of the signal of the APEB compared to PEB. The model considers a single domain structure of the individual layers, whereas the effect of stray field coupling is not considered.

6.2 Heat treatment

In order to attain the previously described system, there are in principle two possibilities. One is to sputter directly the magnetic stack in the antiparallel state by alternating the deposition field or rotating the whole wafer during the deposition. The other one is by means of heat treatment. Due to limitations of the sputtering systems available, the second option was chosen for attaining the APEB. This, however, is not straightforward

to achieve. The difficulty is to attain proper alignment of K_u and the EB. In the easiest sense this would be achieved by heating above the Néel temperature of the AFM (around 700 K [115]), allowing complete reinstatement of the EB in a new preferred direction. The problem is that this temperature is well above the crystallization temperature of the FeCoSiB [109], making this treatment unsuitable. Nevertheless, there is still the possibility to utilize the blocking temperature T_B of the AFM similarly to the procedure used for PEB. The difficulty of attaining appropriate alignment of individual layers is the correct coupling through H_{str} in an antiparallel manner at the required high temperatures. For this reason, a special heating procedure was developed, portrayed in Figure 23(a).

The beginning of the heat treatment is the same as for the PEB; the sensor is heated to 300 °C while continuously exposed to an external magnetic field (20 mT). During the process, the applied saturation magnetic field fixes the magnetization of the FeCoSiB layers along the short axis of the cantilever up to high temperatures. The procedure ensures proper alignment of K_u in the FeCoSiB layers. The sensor is then held at this temperature for a short time (2.5 min) and then the field is reversed in sign. This is done in order to relax the magnetic structure at the edges of the FM layer that is strained by the relaxed stress at the edges. This can be understood from the directionality of the still present impended EB structures at the edge (high demagnetization effects) that turn along the edge due to the preexisting anisotropy and K_σ. For this reason when one direction of the field is used, the anisotropy would have to turn into the edge to rotate the unidirectional anisotropy with the torque from the applied field. A sketch of this effect and an experimental counterpart are presented in Figure 23(c) and Figure 23(d) respectively. From the image, the clear bent spike domains are visible that form near the edge resulting in a formed tilted anisotropy within the layers at room temperature (RT). The effect of the tilted structure is also visible in the magnetization response along the short axis (Figure 23(b)), where a clear residual parallel character of the EB is present (offset of the magnetization at 0 field from $M = 0$). A sample with the switched magnetic field direction, showing non-tilted domain structure, is presented in Figure 23(e). The sloped character of the magnetization loop (different to the ideal modeled curve in Figure 22(b) is a direct result of the demagnetization effects.

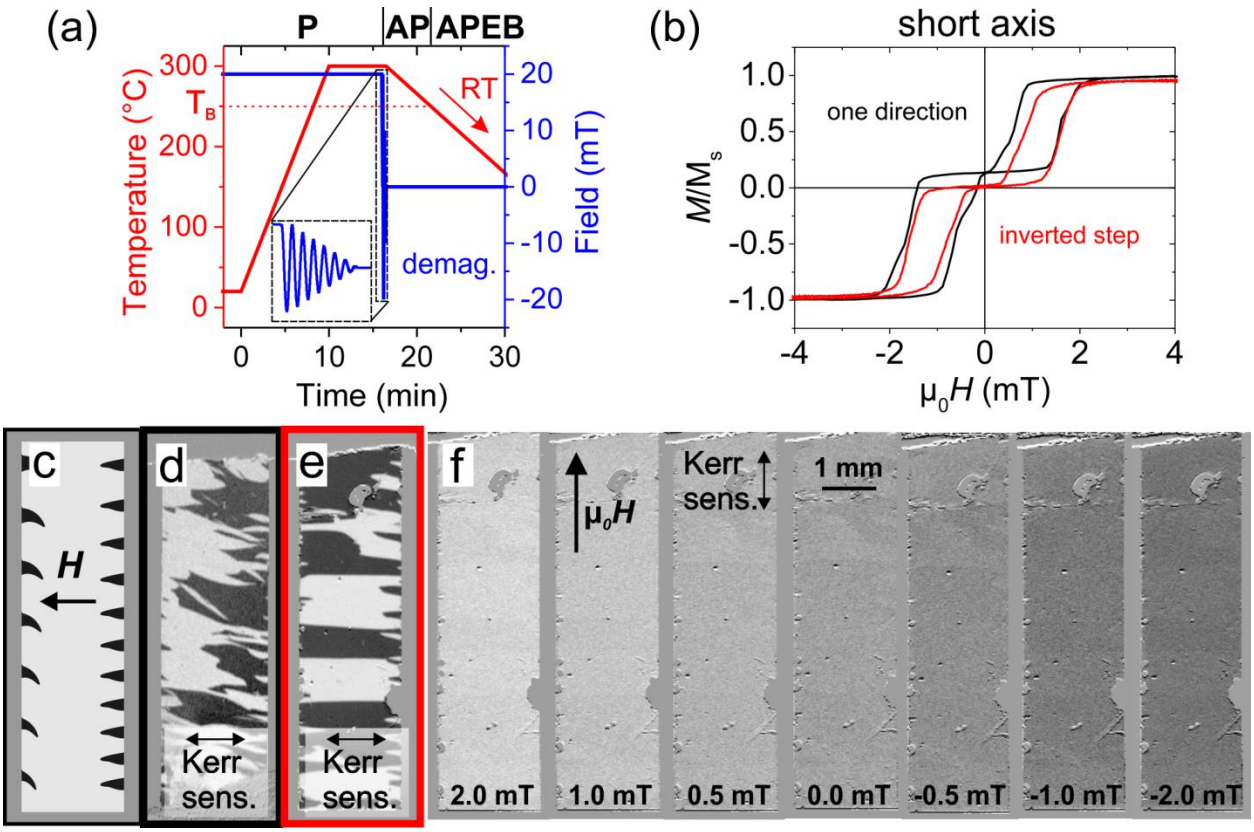

Figure 23: (a) Diagram indicating the temporal procedure of the heating scheme to attain APEB. The upper dark text indicates the state of the magnetic layers during the treatment. The inset shows the form of the decaying field for demagnetizing the magnetic layers. The inverted step of the field at 12.5 min is not included in the field procedure. The diagram is adapted from [58] (b) Inductively measured magnetization response along the short axis for samples (d) and (e) showing the difference in the alignment of the EB with the different field treatment method. In (c) a sketch of the domain configuration and bending of impeded spikes protruding out of the edge opposite to the externally applied field. (d) and (e) show domain structures of samples treated with field applied along one direction and along both of the short axis (with a switching step) respectively. Evolution of sample (e) with applied field along the long axis is depicted in (f), which shows only coherent rotation of magnetization to occur. The samples were fabricated (without the annealing procedure) by Volker Röbisch.

After the switching of the field, the sensor is left at this temperature for another 3.5 min. After that, the continuous field is switched off and an AC field is applied. This new field is then decayed, causing the sensor to become demagnetized by means of degaussing. Since the FM layers are nearly not affected by the EB, the FeCoSiB layers relax to a preferential antiparallel magnetization alignment due to the magnetostatic interaction. The sensor is afterwards cooled down without any applied field. At sufficiently low temperature, the EB is established in accordance with the set orientation of magnetization in the individual layers, fixing the magnetic structure in place. For the

development of the heat treatment procedure and domain control, simultaneous MOKE microscopy was employed. The first experiments were conducted in vacuum with a heating stage from Cryovac, allowing the simultaneous MOKE observations through a glass window. The samples used have a FM bilayer structure 2x200 nm FeCoSiB with the same accompanying layers described in Figure 22(a). Due to constrictions in size of the heating stage, the cantilever samples were broken into smaller pieces. The size of smaller pieces was approx. 2 mm x 4 mm. After several attempts by varying the treatment temperature, duration and properties of the demagnetizing field, a proper APEB configuration was attained (Figure 23(e)). The alignment of the EB was confirmed by inductive measurements (Figure 23(b)).

The structure shows very stable domain structure, which with the application of a field along the long axis exhibits only coherent magnetization rotation (Figure 23(f)). With the success of the annealing procedure on the smaller pieces, the heating scheme was applied then to a full-scale sensor. The heating was again conducted with in-situ MOKE (large view) observation, but in this case a heating plate in ambient conditions had to be used in order to heat the whole cantilever. However, the results of the whole heated sensor deviated from the previous experiments. The MOKE observations of the domain structure showed non-characteristic lenticular domains forming along the short axis and appearing somewhat periodically along the length of the sensor Figure 24(a). The different contrast of these structures gives indication, that the coupling of the magnetic layers is different in these regions compared to the rest of the sensor. Further observation with high-resolution MOKE confirms the site dependent varying coupling. The domain structure without application of external field (Figure 24 (b-c)) shows the antiparallel domain configuration of the underlayer, indicated by the imprinted domain walls (white above, dark below). From the ripple structures, the magnetization of the domains was determined. However, the layer couplings of the individual domains were determined from their evolution with the application of a magnetic field. With the field applied along the long axis (Figure 24 (d)), coherent magnetization rotation with minor growth of tilted spike domains at the edge is visible. The turning of magnetization is equal for all the domains, indicating, that the EB is aligned along the same axis for all of the domains.

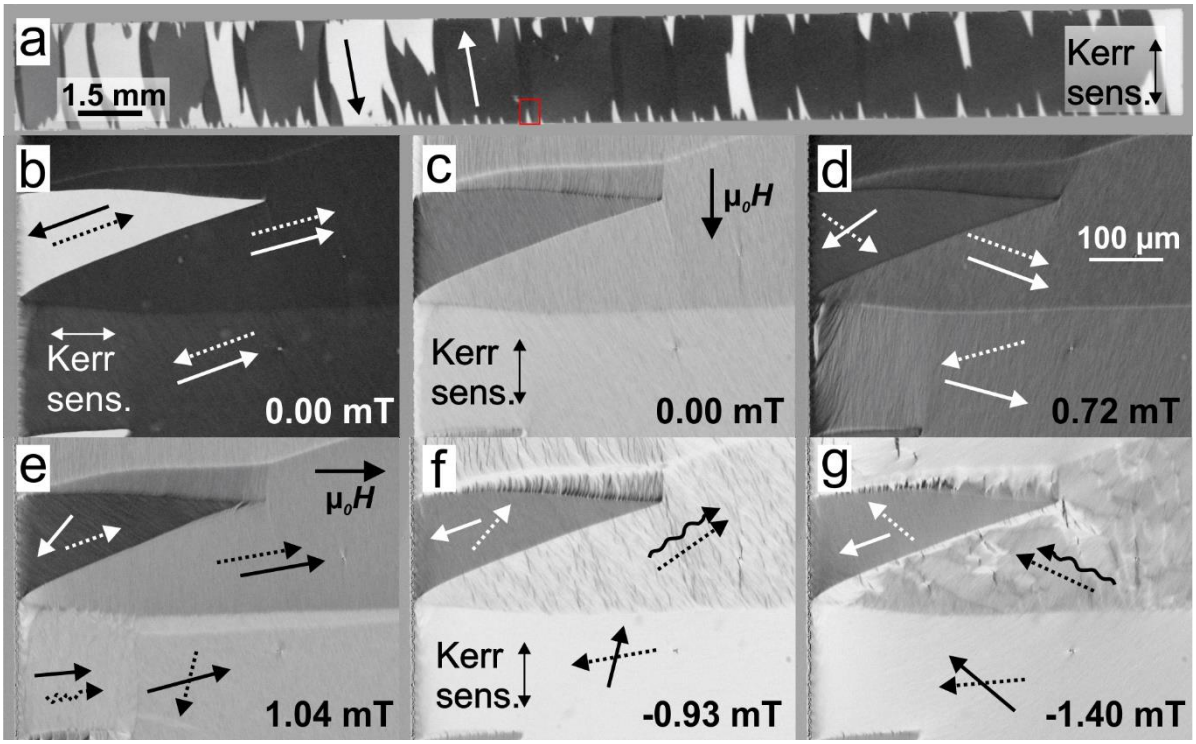

Figure 24: **(a)** Large view domain structure of a 2x200 nm sensor heated to attain APEB configuration. The domain structure shows different contrast regions, indicating the non-ideal setting of the APEB. The red box represents the area observed with high-resolution MOKE. **(b)** and **(c)** showing the domain structure of the previously mentioned region at zero field, with two different MO sensitivity axes. In **(d)** the change of the domain structure is shown with field application along the long axis. **(e-g)** present the domain evolution with the field applied along the short axis, compensating the EB field in the layers. The evolution indicates the coupling character between the domains of the two layers. The sensor was fabricated (without the annealing procedure) by Volker Röbisch.

With the field application along the short axis (Figure 24(e-g)) the various domains show different switching character. The middle band domain shows a parallel character (PEB), which is explicitly visible with the switching of the domain in Figure 24(f-g). With moderate fields, the domain structure shows thicker ripples indicating a state just before collapse of the structure. With higher fields, the switching into patched domain pattern becomes visible due to the local transiting from a parallel to antiparallel alignment of the domains. This has been already observed in other multilayer systems [106]. The patching occurs due to the variation of the EB and in the domain leading to individual collapse of the domain structure with the application of field along the easy axis of the system. The patches are visible because of the imprinted contrast of domain walls from the lower layer encircling the domains. Within the patches also very pronounced and dense ripple structure forms as a result of the compensated EB. The other domains show a persistent

antiparallel character (APEB), which can be seen by the continuous rotation of the magnetization of one of the layers with the applied field (determined from the ripple structures and assumed symmetric behavior with opposite applied field). In Figure 24(e), additionally two special features are visible in the lower band domain. The magnetization of the lower layer spontaneously switches in the direction of the field, parallel to the magnetization of the upper layer. It is assumed that this is a result of the influence of the nearby smaller spike domain that enforces parallelism of the local magnetization with the domain wall of the spike domain. The local changes of the magnetization are also visible around the larger spike inducing two distinct domain contrasts of the PEB domains. The second feature is visible near the lower imprinted domain wall, where a distinct brighter region is formed. This is an effect of the compensation of the region through local flux closure through the domain walls, allowing the conservation of the perfect antiparallel alignment of the domains in a narrow region. This flux closure is similar to the effect seen in multilayer samples (Figure 16(d and g)).

From the investigation from this sensor, it is clear that the setting of the APEB did not work perfectly. The reason as to why such varied EB coupling occurred, despite its applicability on smaller samples, could be a result of the local fluctuations of the thickness and roughness of the layers. This can then spawn the problem of the Zeeman energy to promote formation of both antiparallel and parallel coupling on a local scale. In order to reduce the occurrence of such formation, an asymmetric stack is introduced, at which the thickness of every odd FM layer is decreased by 10% of the nominal thickness and for every even FM layer the thickness is increased by 10% of the nominal thickness. This difference in the thicknesses of the layers is well above the possible thickness variations expected from the deposition of the magnetic stack.

6.3 Sensors 90/110

Based on the findings from the previous section, a system with an asymmetric stack (nominal thickness of 100 nm) consisting of a bilayer unit of 90 and 110 nm FeCoSiB is used (exact structure: 90 nm FeCoSiB / 8 nm MnIr / 5nm Ta / 110 nm FeCoSiB / 8 nm MnIr). The designation 90/110 will be from now on used to denote such system. The different thicknesses of the FeCoSiB layers result in a different Zeeman energy contribution, allowing a preference for an antiparallel coupling to occur. This physically means that

the thinner layer will switch with decreasing external field before the thicker one and then fixating the construct at zero external fields. This then eases the setting of the APEB with the heating procedure. The sensors were in this case constructed by repeating the bilayer structure 5x, 10x and 20x, resulting in a total t_{FM} of 1 µm, 2 µm and 4 µm (same as used in the PEB in Chapter 5). Batches of sensors were prepared with the previously explained heating scheme. Magnetization response measured inductively for these sensors shows a very distinct antiparallel ordering detected along the short axis of the sensor (Figure 25(a)). From this loop, the achieved splitting of the two groups of layers is detectable. Additionally, an asymmetry in the loop is visible as the portion of the magnetization represented by the lower and upper half of the loop is unequal, corresponding to the difference in the FeCoSiB thickness of the layers. The inclination of the loop (deviating from the ideal curve in Figure 22(b)) is a result of the gradual rotation/switching of the magnetization of the individual group of layers, which occurs due to the strong interlayer coupling of the multiple layers. However, for thicker sensors the asymmetry is reduced and ultimately removed (Figure 25(b)) as the stress relaxation of the layers allow intermediate coupling of the magnetization at the edge of the sensor leading to a more circular form of the stray field flux lines. Additionally, the H_{dem} is also larger, which also promotes the formation of such domain regions. These compensate the mismatch of the thicknesses and EB leading to a homogeneous splitting and transition of the two groups of layers.

The inductive response along the long axis in Figure 25(c) shows a distinct linear behavior of the sensors to about ±1 mT. This is a promising sign as the linearity appears to be symmetric, crossing the zero field point at 0 M/Ms, which is the ideal behavior needed for MFC driving of the sensors. Furthermore, since no opening is visible in this regime, very low noise response is expected from these sensors. Nevertheless, at higher absolute field values small openings of the loop occur. They seem to become larger with increased thickness of the sensors, providing a hint that it might be due to the demagnetization effect. In order to understand the behavior more in detail, MOKE observation of domains was performed. Examples of large view MOKE images of the resulting domain structures for each thickness group are presented in Figure 25(d). The domain structures confirm that all sensors have an antiparallel character, as the typical patch domain construct is formed. The patches are formed randomly with different shapes and sizes as the formation is a result of the local variation of magnetic properties

and hysteretic influence of the AFM during the setting of the demagnetized state at 300 °C.

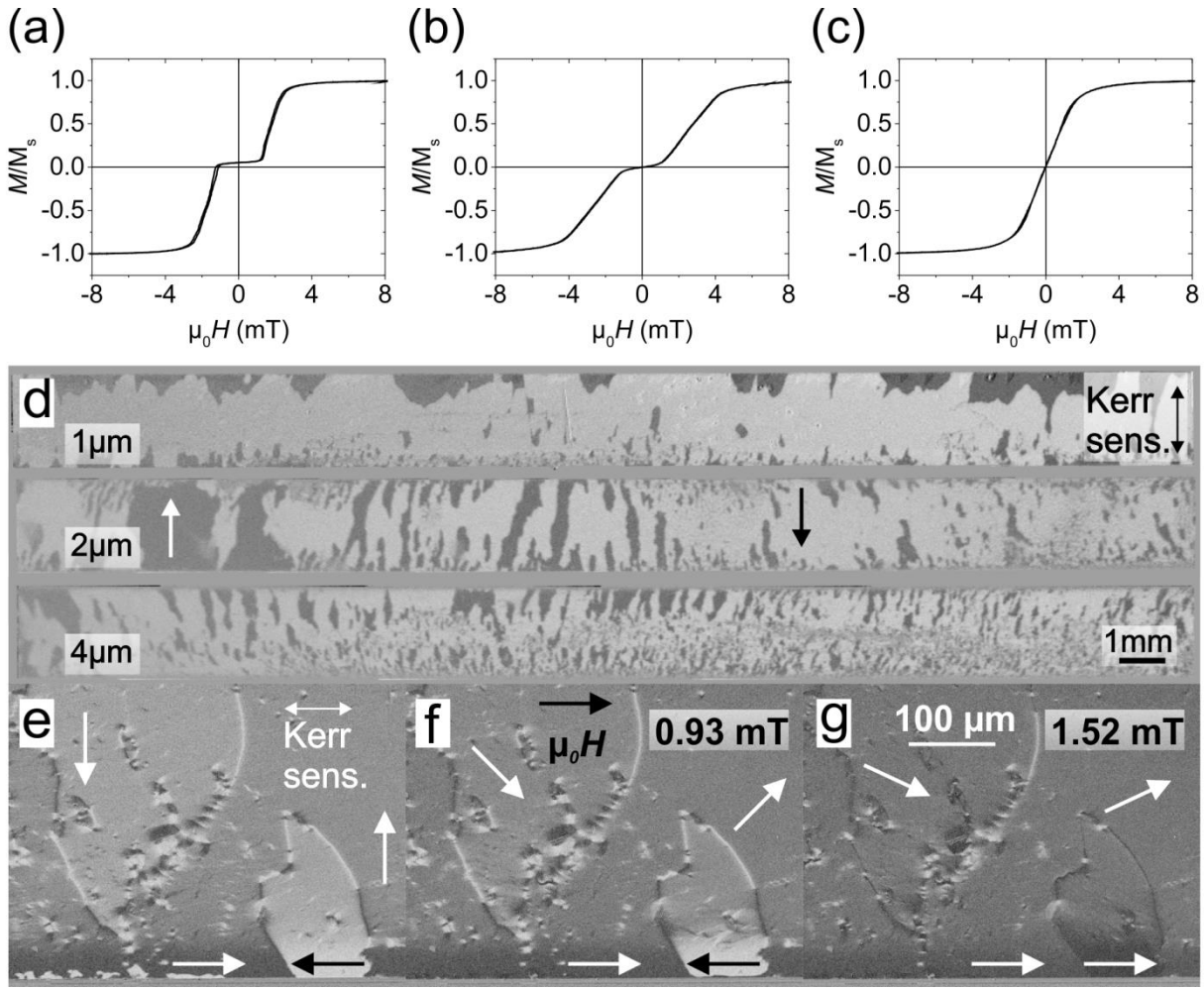

Figure 25: Short axis magnetizations loop of a 90/110 (a) 1 μm and (b) 4 μm sensor. (c) Long axis magnetization loop of the same 4 μm sensor. (d) Large view MOKE images of 1 μm, 2 μm and 4 μm 90/110 sensors at zero field. (e-f) Domain evolution with field applied along long axis of a 2 μm sensor indicating the prevailing occurrence of coherent magnetization rotation. The sensor was fabricated (without the annealing procedure) by Volker Röbisch.

With increasing thickness, it seems that the domain construct is more segmented. A possible reason could be the increased roughness with higher thickness, which correspondingly creates stronger magnetic properties variation in the magnetic films. Additionally, with the application of the field in any direction, the domain construct continuously returns to the original state. This shows the high stability of the structure and the reduced demagnetization effects expected for APEB. However, in order to confirm the APEB also on a local scale and to find the origin of the long axis hysteresis openings, high-resolution MOKE imaging was performed. With high-resolution

observations the very high stability and reproducibility of the domain structure with application of external magnetic field (in any direction) is confirmed, also with saturating fields. From the domain evolution with field applied along long axis (Figure 25(e-f)), the dominance of the coherent magnetization rotation is visible. In the bulk of the sensor, only switching of the domain walls and modulations around defects occur by changing their sense of rotation. However, the switching does not result in the movement of the domain walls, making it a very negligible noise source.

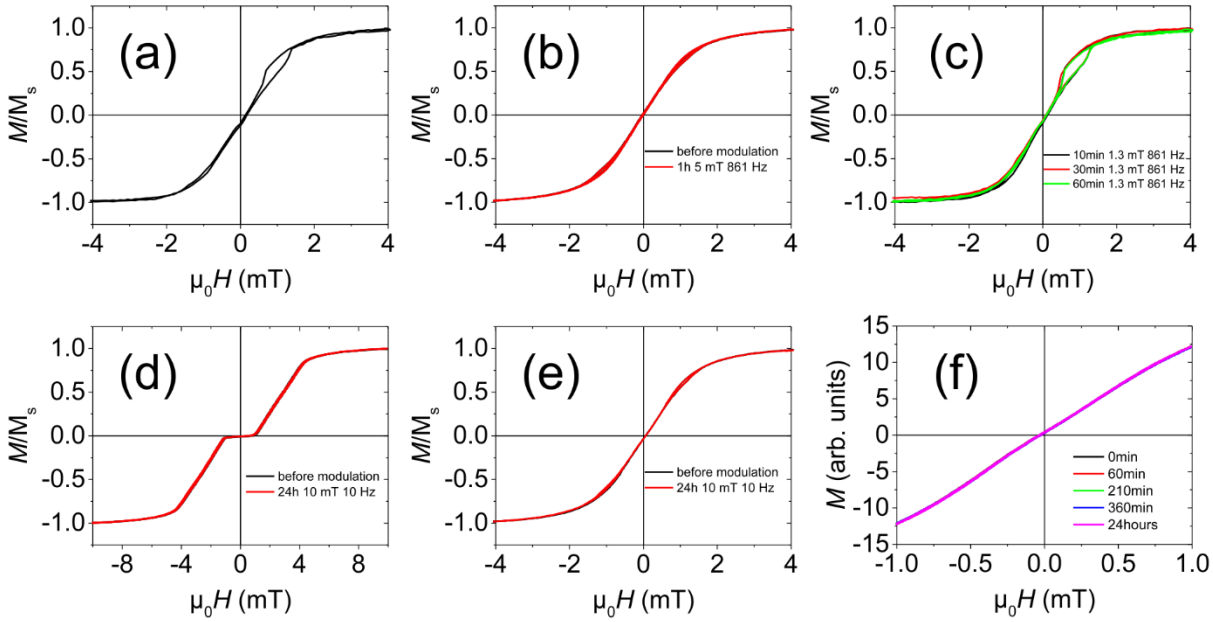

Figure 26: **(a)** Long axis local magnetization response loop measured with MOKE indicating the one-sided opening resulting of stress relaxation of the edge. **(b)** Inductively measured long axis loop of a sensor before and after 1 hour of exposure to a 5 mT AC field set at the resonance frequency of the sensor. **(c)** MOKE obtained long axis magnetization loops measured after 10 min, 30 min and 60 min of exposure to a 1.3 mT AC field at the resonance frequency of the sensor. **(d)** and **(e)** Inductively measured magnetization loops along both principle axes of a sensor exposed to a 10 mT AC field excited at 10 Hz for a duration of 24 hours. **(f)** Inductively measured long axis minor loops of the sensor exposed to the same field as in **(d)** and **(e)**. The 4 μm 90/110 stack sensors were used for conducting these measurements.

Nevertheless, the reduction of the defects is necessary in order to sustain low noise behavior, as they can lead to the formation of instable connective domains between them. The only real domain activity is visible near the edge of the sensor, where the stress relaxation effect arises. The domain arrangement aligned along the edge switch very easily with the application of the field as the EB is very weak due to the conjoined effect of the stress and demagnetization effect. This, as discussed beforehand, is a pronounced noise source and may endanger the low noise behavior of the sensors. With local long

axis hysteresis MOKE measurements of the region enclosing also the stress relaxed part of the sensor, the opening of the loop is visible, but only on one side (Figure 26(a)). This indicates that the openings of the loop seen beforehand are formed due to the stress relaxation and are not formed due to the multidomain state in the bulk of the sensors or demagnetization effects. This additionally addresses the point that the stress relaxation effects need to be compensated in order to achieve optimal magnetic noise reduction in the sensors. With the local measurements as well as with inductive measurements the stability of the system was evaluated. To assess the stability, the sensors were exposed to various AC fields applied along the long axis to indicate any changes of the magnetic response over time. (Figure 26(b-f)).

With various applied fields, the sensors show complete stability of the magnetization response, even with exposure to high fields (10 mT) for 24 hours (Figure 26(d-f)). Complementary domain investigation also showed no changes in the domain structure (not shown in image). The most important observation was to conduct continuous excitation of the sensor at working (resonance) frequency and with field amplitudes that suffice to reach maximum magnetostriction change (Figure 26(b-c)). This is needed, as the sensors are operated under these conditions and was needed to confirm that the sensor output does not deteriorate with long measurement time. This is also a superior improvement compared to the PEB sensors, which showed changes of the magnetic response during the measurements of the sensors as well as over time [60]. The time changes of the system were also tested, by evaluating the same sensor over an extended period of time (1 month). This was conducted by measuring the sensors ME response over bias field application. The resulting curves are given in Supp. 3(a). It is clear that the shape of the ME response is withheld over time, however, the amplitude of the response seemed to be inconsistent and showed a variation with time. This was further investigated and was determined to be related to the changing properties of the adhesive material used for the attachment of the sensor to the PCB chip. The problem with the adhesive is that it is a part of the cyanoacrylate family glues, which are known to deteriorate and lose their structural integrity with long exposure to water and humid environment [110] [111]. This was then also tested on a set of sensors to see the change of the ME response of the sensors with exposure to water (immersing for 15 min). An example of the ME measurements obtained from these tests are provided in Supp. 3(a). The measurements proved the reduced response of the sensors after exposure to water.

Additionally, after the submersion of the sensors in water and measurement, the sensors were vacuum dried at 50 °C for 30 min in order to allow the sensor and adhesive to dry up. After the drying the sensors exerted the same or even higher ME response to the response measured before the exposure to water. Based on literature [110] [112] it is determined that the cured bonds sever after being exposed to water and the adhesiveness as well as stiffness of the material is reduced. This also explains why the sensors lose their sensitivity, as the degraded properties of the adhesive allow higher damping and energy loss of the resonance mode of the sensor.

With the evaluation of several sensors from these batches, one additional feature became evident for the APEB configuration. The reproducibility of the magnetization response through the whole batch of sensors is extremely high. Both long axis and short axis measurements show very small deviations from sensor to sensor (example for one sensor batch is presented in Supp. 4). This is an encouraging quality as it allows producing a range of sensors with very similar magnetic properties and magnetic responses to an applied field. Despite the already very promising results of these sensors, the goal of the heat treatment was expanded to produce single domain state (in each layer) in order to dismiss any effects from the domain wall switching. This state is strived also for later adaptations of the APEB with higher individual t_{FM}, for which the influence of domain wall switching on the noise performance is expected to be higher. For this reason, the heating procedure is adapted in order to attain a single domain state APEB.

6.3.1 Single domain state sensors

The heating scheme was firstly improved by changing the basic parameters of the demagnetization cycle. More specifically, the frequency, time duration of the demagnetization cycle and number of demagnetization cycles before cooling. From parametric variation experiments it was concluded, that the most beneficial values are low frequencies and long duration of the demagnetization cycle. This was mostly visible near the edge where the stress relaxation domains form. With the optimal parameters, the number of domains near the edge could be reduced as well as the number of switching events per magnetization cycle.

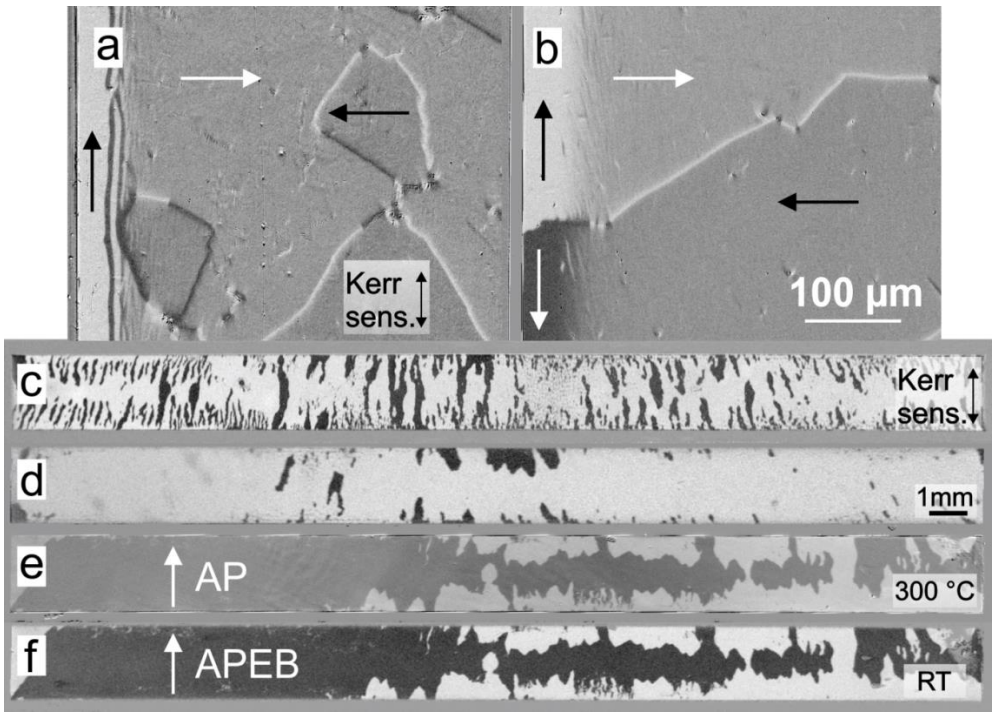

Figure 27: **(a-b)** MOKE micrographs of multidomain APEB sensors enclosing the region near the edge with stress relaxation effect. The state in **(a)** was obtained with a demagnetization cycle with parameters 21 Hz and 5 s duration. The state in **(b)** was obtained with a demagnetization cycle with parameters 13 Hz and 20s duration. Large view MOKE images of sensors prepared with a heating scheme using **(c)** 1 demagnetization cycle and **(d)** 5 demagnetization cycles. Large view domain images of a sensor obtained at **(e)** 300 °C just before cooling and at **(f)** RT after the heat procedure for attaining APEB. The images indicate the exact same domain configuration at which the contrast at 300 °C is lower due to lower M_s. All the images were attained from 2 µm 90/110 sensors. The sensors were fabricated (without the annealing procedure) by Volker Röbisch.

An example of two sensors indicating the effects of the previously discussed parameters is presented in Figure 27(a-b). However, the goal was to also reduce the number of the domains across the whole sensor volume. For this reason, the number of applied demagnetization cycles was varied. The previous examples were exposed only to one demagnetization cycle before cooling. It was postulated, that application of many demagnetization cycles would reduce the number of domains forming in the ending state before cooling. This is due to the altered history of the magnetic domains that occurs because of the spin recombination within the AFM with each additional demagnetization cycle. The changes are hysteretic and the new state partially reflects the characteristics of the previous state. After each cycle it is expected that the AFM relaxes in such a way that the domains in the ferromagnet enlarge, causing less number of domains to form. With several experiments, such behavior was confirmed. Exemplar domain states of

sensors treated with different number of demagnetization cycles are presented in Figure 27 (c-d). Additionally, in Figure 27(e-f) an example of a sensor at 300°C with the domain structure just before cooling and resulting frozen-in state at RT is displayed. The two images show that the set domain structure at 300 °C is upheld exactly at RT with the setting of APEB. From both groups of experiments, a set of parameters were determined: frequency 13 Hz, 20 s duration of a demagnetization cycle and 5x application of demagnetization cycle before cooling. These parameters were chosen in order to accommodate the largest effective relaxation of the magnetic state whilst keeping the demagnetization process as short as possible.

Despite the vast research of modifying the demagnetization cycle, a single domain state was never achieved. Nevertheless, an additional step in the heating scheme allows such formation. The idea goes back to the multilayer systems, where a single domain state is possible at the remanence, when a saturating field is applied and then slowly decreased to zero. The same procedure was incorporated into the heating scheme just before cooling after the last demagnetization cycle. The ending result is a single domain state, which with cooling is set into a single domain APEB configuration. Example of two images taken at 300 °C and RT of the same sensor (Figure 28(a-b)) showing, that the single domain state is sustained without the application of additional field during cooling. With the overview MOKE imaging only coherent magnetization rotation was indicated with applied field along the long axis. The behavior of a 2 µm sensor is recorded and presented in Video 2. With high-resolution MOKE observation, the single domain state is confirmed also at the edges (Figure 28(c-e)). It is clear that instead of multiple domains, which were observed in previous sensors, the single domain sensors show a transitioning magnetization rotation near the edge of the sensor. This is a preferred configuration, as domain wall switching is minimized extremely. Curiously, with the application of specific field, the magnetization near the edge shows rotation towards an antiparallel alignment to the field. Such behavior can be explained by the stray field coupling and EB that suffice to keep the antiparallel alignment of the magnetizations despite the applied field and resulting rotated magnetizations (to a certain field value).

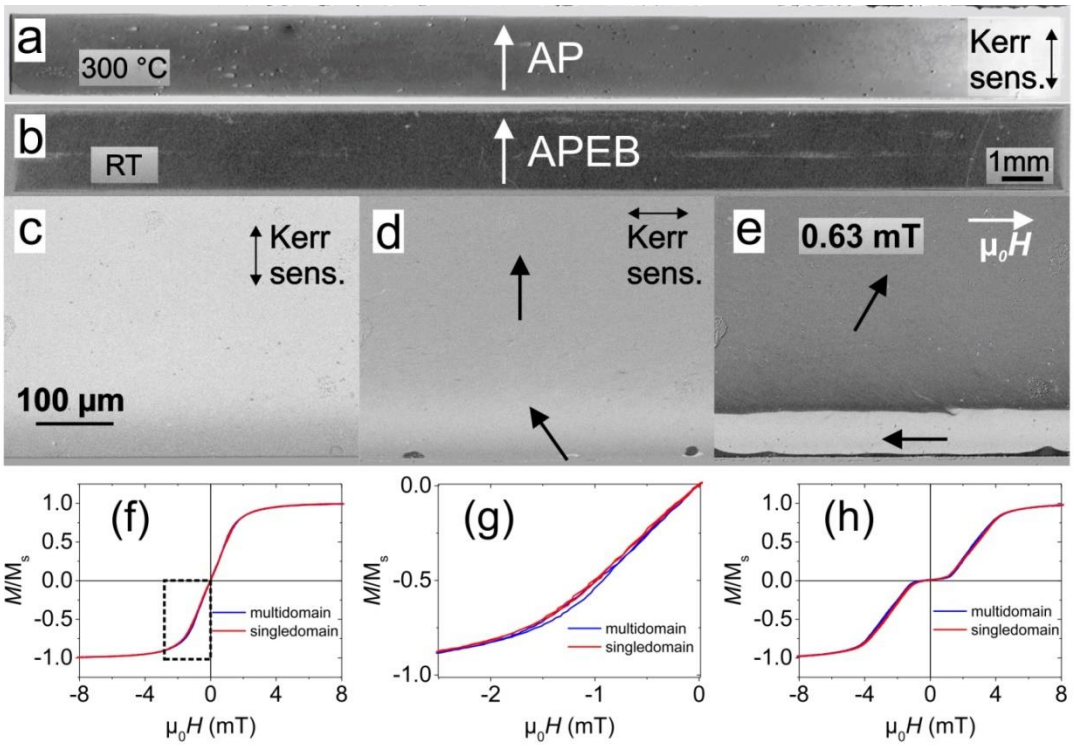

Figure 28: Large view MOKE images of a sensor at (a) 300 °C and (b) RT indicating the same single domain state structure. (c-e) High-resolution domain images of the single domain sensor showing the gradually rotated magnetization near the edge due to stress relaxation effects. With an applied field (e) the edge shows a switched local character showing the domain structure aligned antiparallel to the applied field. Comparison of magnetization response of single and multidomain sensors (f) along sensor's long axis and (h) short axis. (g) Enlarged part (dashed box) of (f), indicating the reduced opening of the magnetization response. Data was obtained from 4 µm 90/110 sensors. The sensor was fabricated (without the annealing procedure) by Lars Thormählen.

Additionally, the change of the edge relaxation region occurs now more in a transitioning manner with a bigger portion changing with coherent magnetization rotation. From this, it is expected that the opening of the long axis hysteresis should be reduced and indeed that is the case. The comparison of the inductively measured response in Figure 28(f) of a single domain versus multidomain APEB sensor shows, that the overall response is very similar, with the difference of the reduced openings of the single domain sensor. The enlarged portion of the loop in Figure 28(g) shows the difference of the opening more clearly. The comparability of the loop shapes is also a good indication that the single domain APEB sensor yields a good alignment of the EB along the short axis, similarly as in the multidomain APEB sensors. In Figure 28(h), the inductive measurement along the short axis of a single domain APEB sensor shows the bipolar EB character similar to the

multidomain APEB sensors. With the achieved optimal APEB sensor configuration and state, the new sensors were compared with the previously enhanced PEB sensors.

6.3.2 Comparison with PEB sensors

Before the sensors are compared in terms of their electric response and sensitivity, the comparison in terms of the domain behavior with the applied field along the long axis is examined. In Figure 29(a-d), two exemplary 4 µm thick PEB and APEB sensors are presented with their domain evolution with field applied along the long axis. Accompanying the images are also component selective inductively measured minor loops (Figure 29(e-f)). From the comparison of the two systems, it is immediately clear, that the APEB sensors surpass in the formation of a single domain state across the whole sensors surface (Figure 29(a)), which due to demagnetization effects is not achievable for the PEB sensors, developing additional domains near the edge (Figure 29(c)). Secondly, the evolution of domains shows a distinctly different behavior between the two sensor types. The application of a magnetic field along the sensor's long axis gives rise to pure magnetization rotation in the APEB sensor. At higher magnetic fields, the magnetization aligns parallel to the edge and subsequently switches at the edge region. This is a signature of a locally aligned EB parallel to edges due to stress relaxation, developed in the field free setting of EB. In contrast, the PEB sample displays immediate domain wall activity with the application of a magnetic field (Figure 29(d)). Note that with transverse MO sensitivity, the domain wall contrast, due to formed compensated Néel wall structures, indicates the domain construct in the buried layers in the MOKE images [119]. At higher fields, the magnetization in the domain collapses, leading to a slightly modulated magnetization configuration (resulting from a crossed magnetization arrangement between the layers) and numerous magnetic switching events (deeply discussed already in 5.1.1). Overall, the micrographs indicate a significant higher stability of the magnetization configuration with the applied field for the APEB sensors as compared to the PEB sensors. The signatures of reversal are confirmed by comparing the major and minor magnetization loops in the longitudinal and transverse directions with the field applied along the long axis of the sensors. For APEB sensors (Figure 29(e)), only minor hysteresis effects occur at high magnetic fields, which result from the before mentioned high field switching of magnetization at the edges.

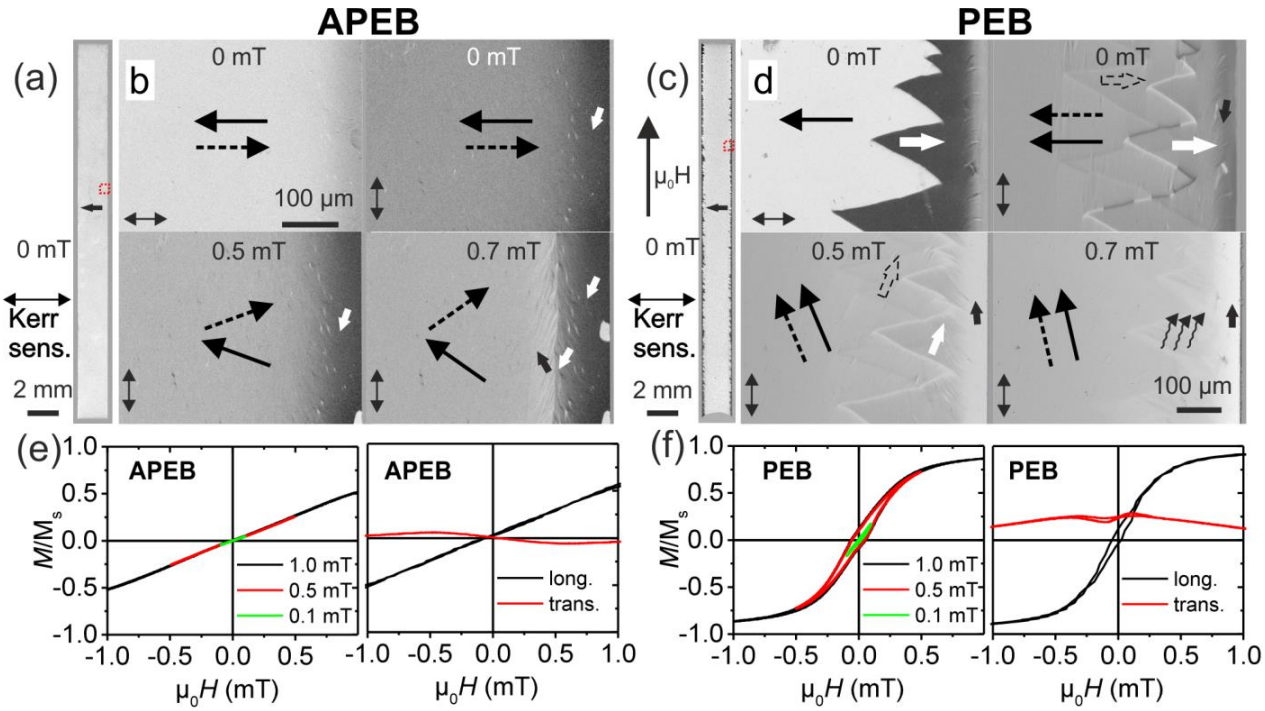

Figure 29: Zero field magnetic domain images of the remanent state of an antiparallel (APEB) (a) parallel (PEB) (c) EB sensor, showing the full sensor. Corresponding high-resolution domain images for APEB (b) and PEB (d) without and with magnetic field application. The regions of extraction (right edge of cantilevers) is indicated in (a) and (c). Inductively measured APEB (e) and PEB magnetization loops along the long axis (perpendicular to the directions of EB) for different magnetic field amplitudes. Transverse sensitivity loops are displayed for the high field loops. Magnetization directions are denoted with arrows, where dashed arrows represent the magnetization alignment in the not directly visible second FeCoSiB layer in (a)-(d). The double-headed arrows indicate the MO sensitivity. The whole figure is adapted from [58].

Only minor transversal magnetization signals M_T/M_S are recorded, indicating the pronounced antiparallel alignment of layer magnetization in the stack. In opposite, the PEB sensors display enhanced hysteresis related to the magnetic domain wall activity ((Figure 29(f)). Correspondingly, low field hysteretic effects become visible in the transverse loops. The mismatch in saturation field for the PEB structure relative to the APEB structure is due to the exhibited H_{dem} aligned opposite to the EB, occurring in the PEB structure. For the PEB sensor, the deviation of the transversal magnetization component at zero magnetic field from unity ($M_T(0)/M_S$ = 0.25) points toward a volume fraction of magnetic domains aligned opposite to the EB of $v_{dom\text{-}AP}$ = 0.33, which is more as expected from the top layer domain configuration (Figure 29(c)). This indicates a multidomain state in the lower layers indifferent to the top layer. The magnetic behavior superiority of the APEB structures also reflects in smaller magnetic field responses, as

seen by comparing APEB (Figure 29(e)) and PEB (Figure 29(f)) minor loop behavior. A significant magnetic hysteresis is only visible for the PEB structure.

6.3.2.1 PEB and APEB modeling comparison

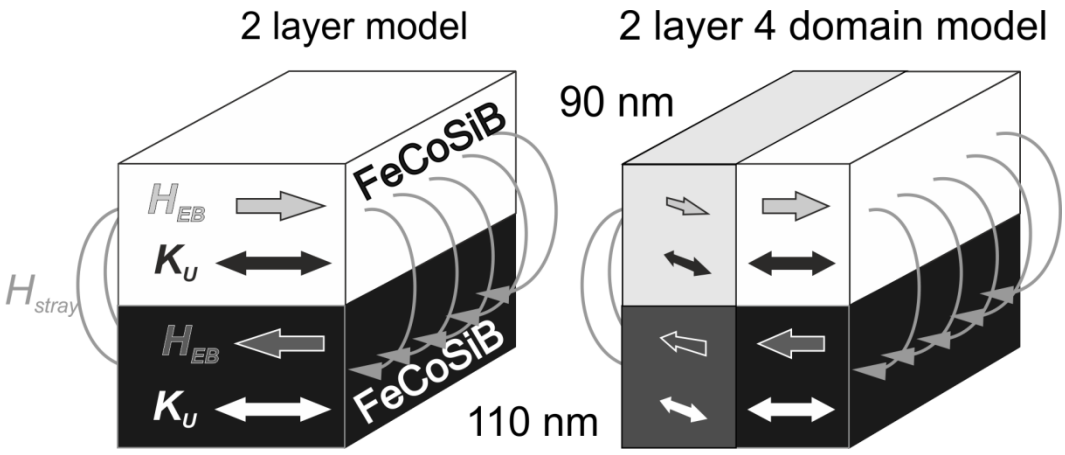

Figure 30: Illustration of the two models used within this work, the 2 layer model on the left and the 2 layer 4 domain model on the right. The individual components defined in the system are respectively marked. The major difference between the models is the addition of stress induced domain region in the 2 layer 4 domain model. This allows modeling the stress relaxation zone by introducing an average tilting angle to the anisotropies within the additional domain. Any additional coupling energy terms between the domains are disregarded.

In order to understand the difference macrospin modeling was conducted for both PEB and APEB sensors. The modeling was adapted by incorporating the two different t_{FM} of the two layers into two block layers. In order to incorporate the total thickness effect, a demagnetization correction factor was introduced. The correction factor is applied to the width, which creates a demagnetization effect equal to a shape with a very large length and small width. The EB strength was determined from the loop shift from the short axis as described in section 1.2.4.4. The M_S and K_u of the FeCoSiB layers were set to 1.5 T (courtesy of Cai Müller and Rasmus B. Höllander) and 400 J/m^3 (determined experimentally) respectively. The problem about this method is the limited modeling of the individual switching events that would lead to a tilted magnetic response. Additionally, the effects of tilted anisotropy and stress relaxation zone are not taken into account with this model. For this reason, an additional model was implemented that separates the two blocks into two equally sized domains. With this new model, simulation of a multidomain state formed by stress relaxation is possible for both PEB and APEB. For the stress relaxation domains, the average tilting angle was assumed to be 9° based

on the range of the stress relaxation zone. The angle is small as the two domains are of the same size (half size compared to the domain in the 2 layer model) and therefore decreases the average tilting angle. Both models are presented in the schematic in Figure 30.

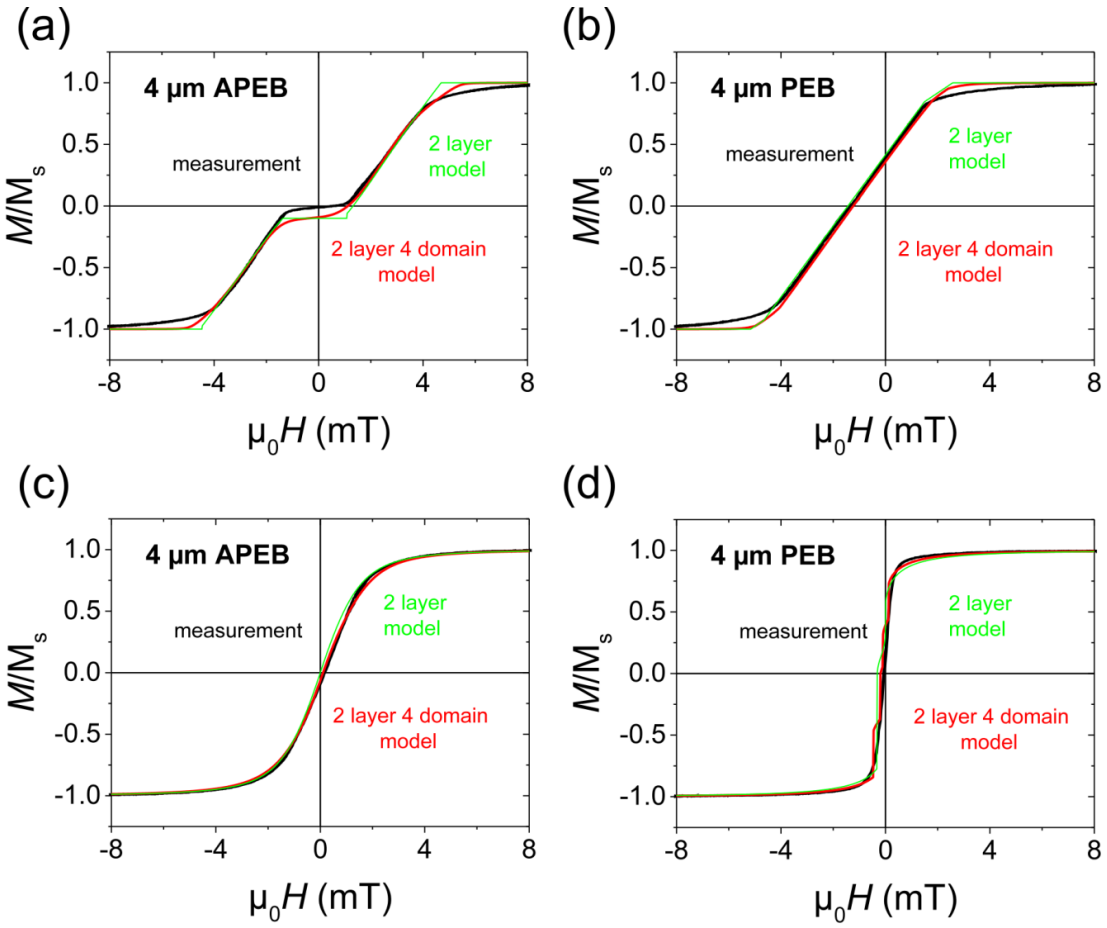

Parameters \ Sensors	Parallel EB			Antiparallel EB		
	1 µm	2 µm	4 µm	1 µm	2 µm	4 µm
Exchange bias 90 (10^{-4} J/m^2)	1.7	1.7	1.2	1.2	1.2	1.2
Exchange bias 110 (10^{-4} J/m^2)	1.7	1.7	1.7	1.7	1.7	1.7
Short axis stray field coupling (10^{-4} J/m^3)	0	0	0	-0.7	-1	-2
Short axis demag. factor (-)	0.032	0.022	0.0125	0.05	0.05	0.04
Long axis stray field coupling (10^{-4} J/m^3)	0	0	0	-0.7	-0.7	-0.7
Long axis demag. factor (-)	0.05	0.03	0.022	0.05	0.05	0.045

Figure 31: Measured and modeled magnetization response of 4 µm APEB and PEB sensors along the (a)-(b) short axis and (c)-(d) long axis. Below is the table with all the parameters used for the modeled data for each individual sensor type.

The results of the modeling of PEB and APEB 4 µm sensors are presented in Figure 31(a)-(d). For the other two thicknesses, the results of the modeling with the 2 layer 4 domain model are compared with the measured data in Supp. 5. The exact used parameters are given in the table in the bottom part of Figure 31. On comparing the experimental data with the modeled results of the magnetization response along the long axis, a clear correlation with the domain observations and magnetometry is visible. The PEB has a softer character (Figure 31(d)) due to the opposing domains exerted from the edge as a result of the demagnetization effects (Figure 31(b)). From the modeled data, it is also clear, that the PEB sensor exhibits a destabilized structure, indicated by the stepwise magnetization change. This also coincides well with MOKE observations, where a changing remanence state was visible for the 4 µm PEB sensor (Supp. 6). This indicates that the EB is compensated by the H_{dem}. This is also clear from the trend of the changing parameters, where the EB constants had to be changed to asymmetric values for the 4 µm thickness. The asymmetric values are incurred due to antiparallel coupling which is preferred by the demagnetization dominated regions (Figure 33(a)-(b)). In some cases the antiparallel coupling can be also seen by a small plateau at zero magnetization in the short axis magnetization loop (best seen in Supp. 5 for 2 µm sensor) It is theorized that the decreased EB of the thinner layer is effectively formed as a result of the combination of the aforementioned antiparallel coupling and H_{dem}, that compensate the EB more strongly in the thin layers to even-out the thickness mismatch. An indication of this can be seen from the evolution of the domain state during magnetization reversal with applied magnetic field in Figure 32. In this set of images, the clear difference in the magnetization reversal is visible when the external magnetic field transits from positive to negative field (in direction of EB) and vice versa. From the first three images the magnetization in the top layer switches in a swift domain wall motion from one side of the sensor to the other. This shows the switching of the layers to an antiparallel arrangement that occurs already at very small externally applied magnetic fields. This gives also the insight that the PEB sensors at this thickness are in fact far away from the idealized parallel aligned configuration that is expected based on the EB setting. From the next three images the other reversal is seen, which shows the collapse of the antiparallel arrangement and occurs from the middle and extends towards the edges. This transition is slow and requires large fields to completely switch the magnetization as the H_{dem} opposes the parallel arrangement of the magnetizations in the layers. Such change in the reversal suggests the strong influence of the intermediate antiparallel stray field coupling of the

layers on the evolution of the magnetization. It is postulated from the images that the two reversals are inherent to each thickness group of layers depending on the field history (from which saturation field direction the field reduces)

Further confirmation of this behavior was visualized with high-resolution MOKE by applying a magnetic field along the sensor's short axis (Figure 33). Due to the high enough contrast exerted from the imprinted domain walls, the domain construct of nearly all layers could be resolved (for an unknown reason the layer 9 could not be differentiated). From the micrographs the splitting of the layers is visible, at which the thinner layers (odd numbers marked in images) switch with the field firstly and the thicker ones (even numbers marked in images) follow at much higher applied field.

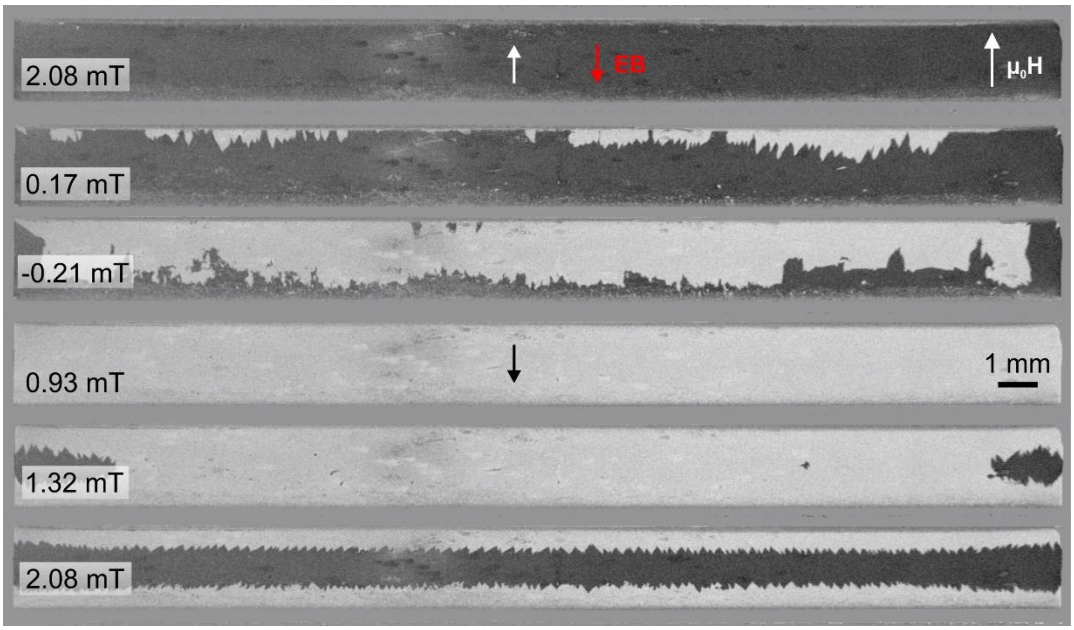

Figure 32: MOKE images depicting the magnetization reversal across a whole hysteresis measurement sequence along the short axis of a PEB 4 µm 90/110 sensor. The sensor was fabricated (without the annealing procedure) by Lars Thormählen.

The domain images show a gradual switching of individual layers (Figure 33(c)-(i)) in a step-by-step motion. Such behavior shows the changing effective H_{dem}, which then induces also the gradual movement of the domain walls without inducing any recombination of the domain walls. In addition, such behavior explains the narrow opening of the short axis loop and the nearly perfect linear slope of the short axis magnetization response. The directions of the wall motion and field ranges coincide well with the two magnetization reversal modes seen from the overview images. This also confirms the antiparallel configuration that was discussed beforehand.

Similar effect is also determined from all the APEB sensors, which was already determined by the asymmetric EB shift of the two groups of layers (Figure 31(a)). A further sign of the increasing compensating demagnetization effect is the decreasing correction factor with increasing the total thickness. The correction factor had to be set to different values for the short and long axis for the same PEB sensor type. This can be explained as the effect of the sensor geometry and the different coupling arrangements of the magnetization in the layers that influence the demagnetization effects.

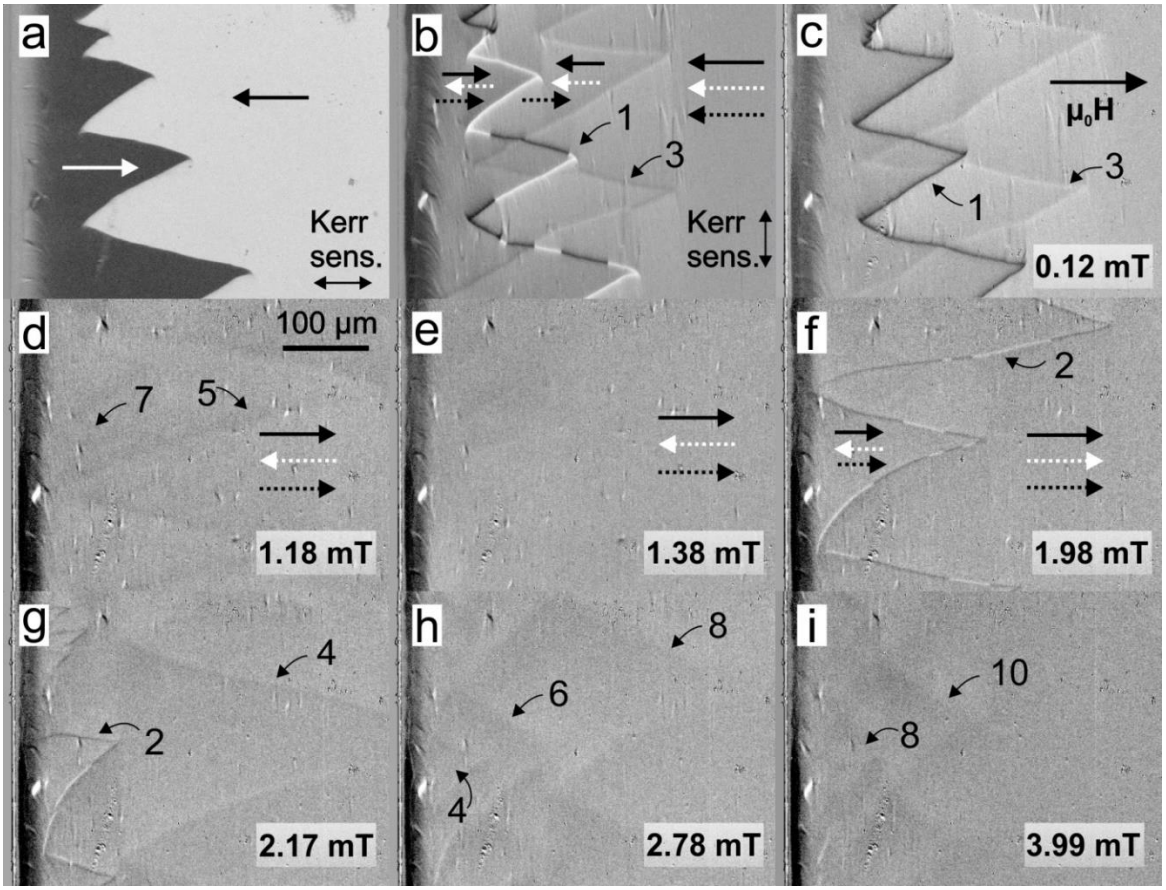

Figure 33: The domain structure attained with MOKE at zero applied field of a 1 μm 90/110 PEB sensor with MO sensitivity along (a) short axis and along (b) long axis. The images from (c) to (i) show the evolution of the domain contrast with an increasing magnetic field applied along the short axis of the sensor. The high imprinted contrast allows the visualization of the domain construct from all layers (except layer 9). In image (e) all the layers are set into an antiparallel state. The arrows indicate the magnetization orientation of the first 3 layers at which the full dark arrow represents the top (thinner) layer, the white dashed arrow the second (thicker) one and the dark dashed arrow indicates the third (thinner) layer. In image (a) the arrows correspond to the magnetization state of only the top layer. The contrast of individual images was set with different contrast windows in order to make the imprinted domain walls more visible. In addition, numerations and arrows are given to indicate the position and the layer relation of the individual imprinted walls. The sensor was fabricated (without the annealing procedure) by Lars Thormählen.

In contrast, for the APEB sensors the H_{dem} plays no significant role, which can be seen by the weaker change of the correction factor with thickness. The stability and fixation of the domain state from the antiparallel configuration is also confirmed by the similar correction factor for the long and short axis response. However, the values of the demagnetization factor are larger compared to those used in PEB. The reason lies in the missing element of the model to include the changing coupling of the magnetization in the layers during the reversal in a more complex manner. As a result, the lower demagnetization factor in the PEB sensors inherently holds information about the stray field coupling and antiparallel configuration of the magnetizations in the layers, which effectively reduces the value of the demagnetization factor. For the APEB, the short axis loop shows also a discrepancy with the model in the antiparallel region (within the margins of ±2 mT). The model shows a remanent magnetization, equal to the difference in the t_{FM} of the two layers, however the measured data shows nearly no remanent magnetization. The reason again is the compensation of the thickness mismatch in order to form symmetric stray field coupling.

From the model and MOKE observation, the compensation seems to be achieved by tilted and partial parallel domain states around the stress relaxation zone. This is also observed from the 2 layer 4 domain model where the added stress relaxed section gives rise to the shape of the antiparallel section of the short axis loop. The shift could not be modeled, as a domain system with parallel coupling between the layers would be required in the model. In terms of the validity of the modeling, the short axis modeling is with the used models limited. The main discrepancies are close to saturation, which is due to the changes of the multidomain state between layers and resulting different effective demagnetization effects. Additionally, the models are constructed based on the idealistic approach of a single domain state behavior, however along the short axis the magnetization changes by domain growth and not by coherent magnetization rotation. Therefore, the short axis modeling gives the indications of the coupling, but it gives little analytical information. To have a more correct model, the number of domains per layer would need to be increased in order to implement the varying magnetization switching with the applied magnetic field.

6.3.2.2 Characterization with magnetic frequency conversion

The previously indicated differences in the APEB and PEB magnetic structure have a direct influence on the sensitivity and magnetic noise characteristics of the two types of sensors. In accordance with the magnetization loop measurements shown before, the maximum ME sensitivity α_{ME} of APEB sensor is reduced relative to the PEB sensor (Figure 34(a)). Relating noise spectra of the two sensors (Figure 34(b)) with the same MFC modulation amplitude and signal amplitude show a significantly lower noise level of the APEB- as compared to the PEB-type sensor. Additionally, the shape of the surrounding noise is completely different. The background of the PEB increases already at a wider range of frequencies around the resonance, whereas for the APEB sensor the noise is limited to a very confined region close to the resonance frequency. The frequencies of the sensors are different due to the slight offset of the glued position of the cantilever, but this has no important impact on the performance of the sensors.

From the spectra, also the signal decrease of the APEB is visible. Further differences in the noise behavior of the two sensors become visible from measurements made across a range of modulation field amplitudes H_{mod}. The exhibited maximum noise level (Figure 34(c)) of the APEB sensor is improved by more than one order of magnitude relative to the PEB sensor. This same trend is also visible over a broad range of modulation field amplitudes. Two exemplary points related to a similar magnetic response $\triangle M$ are indicated in Figure 34(c). In contrast to the PEB sensor, where the noise level increases with increasing modulation amplitude, the noise level of the APEB is nearly constant with the amplitude of the MFC modulation field H_{mod}. To compare the overall performance of both sensors, the LOD was measured at the optimal modulation fields that yielded the highest signal to noise ratio (SNR) for each of the individual sensors (Figure 34(d)). In contrast to the PEB sensor (Figure 34(f)), for the APEB sensor no difference in the noise level was found, when comparing the direct and MFC technique (Figure 34(e)).

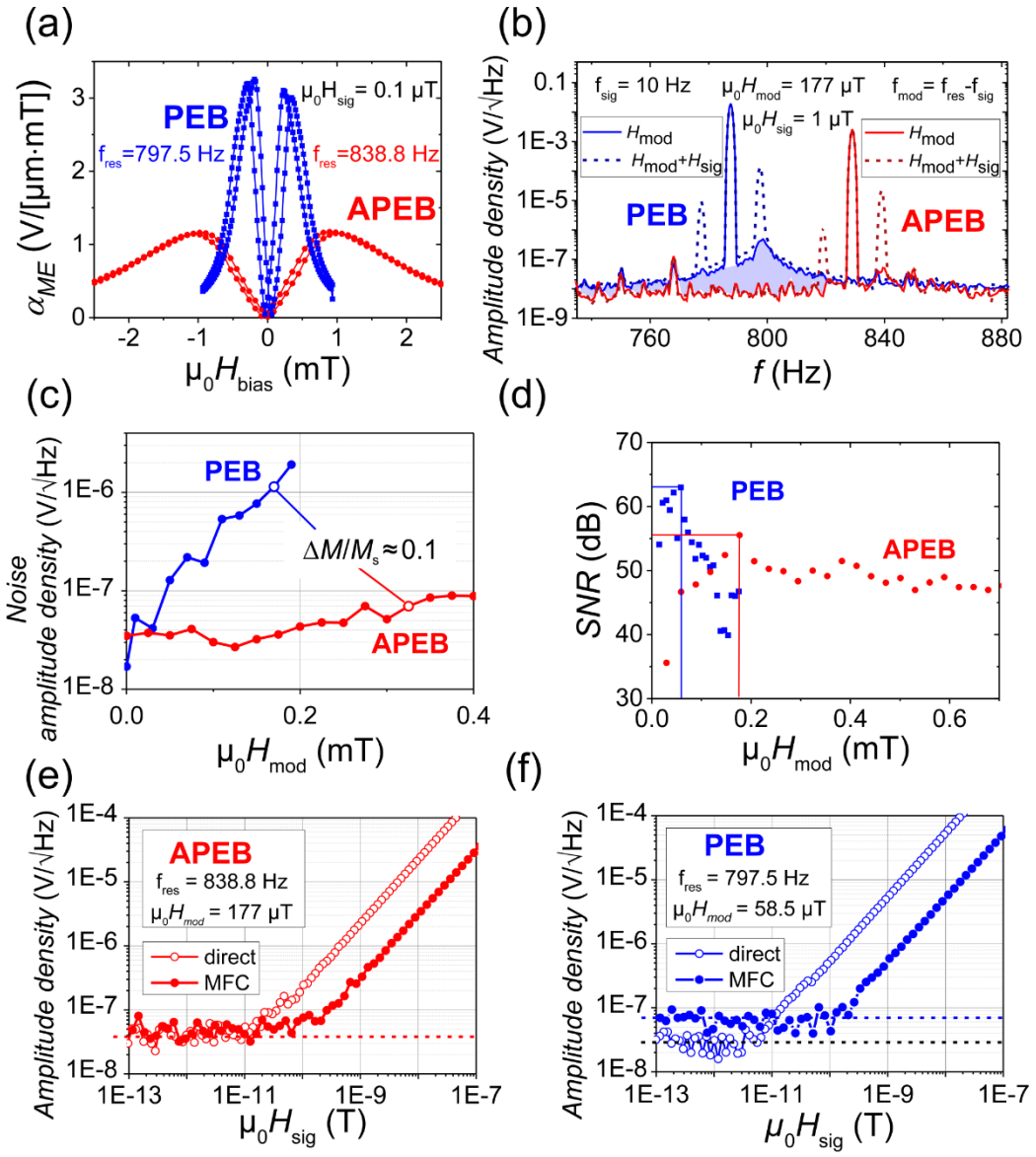

Figure 34: (a) ME response of PEB and APEB sensors with different bias fields. The resonance frequencies of the two sensors and the excitation signal amplitudes are given. (b) Comparison of the frequency spectra of PEB and APEB sensors at the same modulation amplitude of 177 µT. The spectra are obtained during MFC excitation of the sensors with the field signal set to 10 Hz and amplitude 1 µT. The blue colored area depicts the approximate difference in the noise response between the PEB and APEB. (c) Noise response of both sensors with changing modulation amplitude. The significantly lower noise behavior (more than an order of magnitude) of the APEB compared to PEB is indicated, where for both sensors the magnetization change from 0-field state is 10 %. (d) Signal to noise ratio (SNR) values with different applied modulation field amplitudes. The colored guidelines indicate the modulation field at which the highest SNR value is obtained for the individual sensor. Linearity measurements for (e) APEB and (f) PEB sensors with direct detection and MFC method. The parameters for the measurement are indicated in the diagrams. The sensors used are identical to the ones used in Figure 29. The whole figure, except for (d) is adapted from [58].

The data proves the dominance of the magnetically induced noise leading to an increase of the noise level with the MFC measurement for the PEB. In contrast, for the APEB sensor the noise level is merely determined by thermomechanical noise for direct and MFC measurements [25] [114] [115]. The magnetic noise floor is therefore not reached by applying MFC technique to the APEB sensor. For this reason and despite the higher α_{ME} of the PEB sensor, comparable low frequency detection limits of LOD = 120 pT/√Hz at 10 Hz for both PEB and APEB sensors are obtained. The significant reduction of magnetic noise was also confirmed by in-operando stroboscopic time resolved MOKE measurements. Two other sensors then before were driven at their resonance frequencies with the MFC technique (see image caption for more information). The domain structure was then observed for several modulation field values, at which the whole signal period was segmentally scanned through. The segmentation widths were 0.1 ms and the laser pulse width was 400 ns and 100 ns for PEB and APEB respectively. The different pulse widths were set in order to compensate the difference in the reflectivity of the samples with the same camera exposure time of 0.1 s. Complementary noise measurements were conducted for both sensors until the maximum sensor signal response was achieved in order to fully understand the noise behavior of the sensors. From the noise measurements, also selected modulation field values were chosen for the time resolved measurements. In Figure 35 the time resolved measurements and noise plots are displayed for APEB and PEB sensors. From the noise curves it is once more clearly visible that the noise response is extremely lower for the APEB sensor (mind the scaling of the x- and y-axis is different for the two sensors). For the PEB sensor the noise increases swiftly at already very low modulation field amplitudes. The domain images taken at the maximum amplitude of various modulation fields confirm similar behavior.

The domain wall movement occurs already at lower amplitudes (0.07 mT). When the first irreversible switching of the domains becomes visible (0.14 mT) the noise floor also increases much faster. Onwards the noise increases with a steady slope, which correlates well with the increasing amount of irreversible switching in the domain structure. At around 0.4 mT the domains already almost switch from saturation to saturation in one modulation cycle and with, the noise does not increase anymore. Instead the noise even decreases which originates from the fact, that form that point onward also the signal response is reduced. The signal reduces as the modulation

compensates over the maximum response point leading to an inversed slope therefore counteracting the response from before.

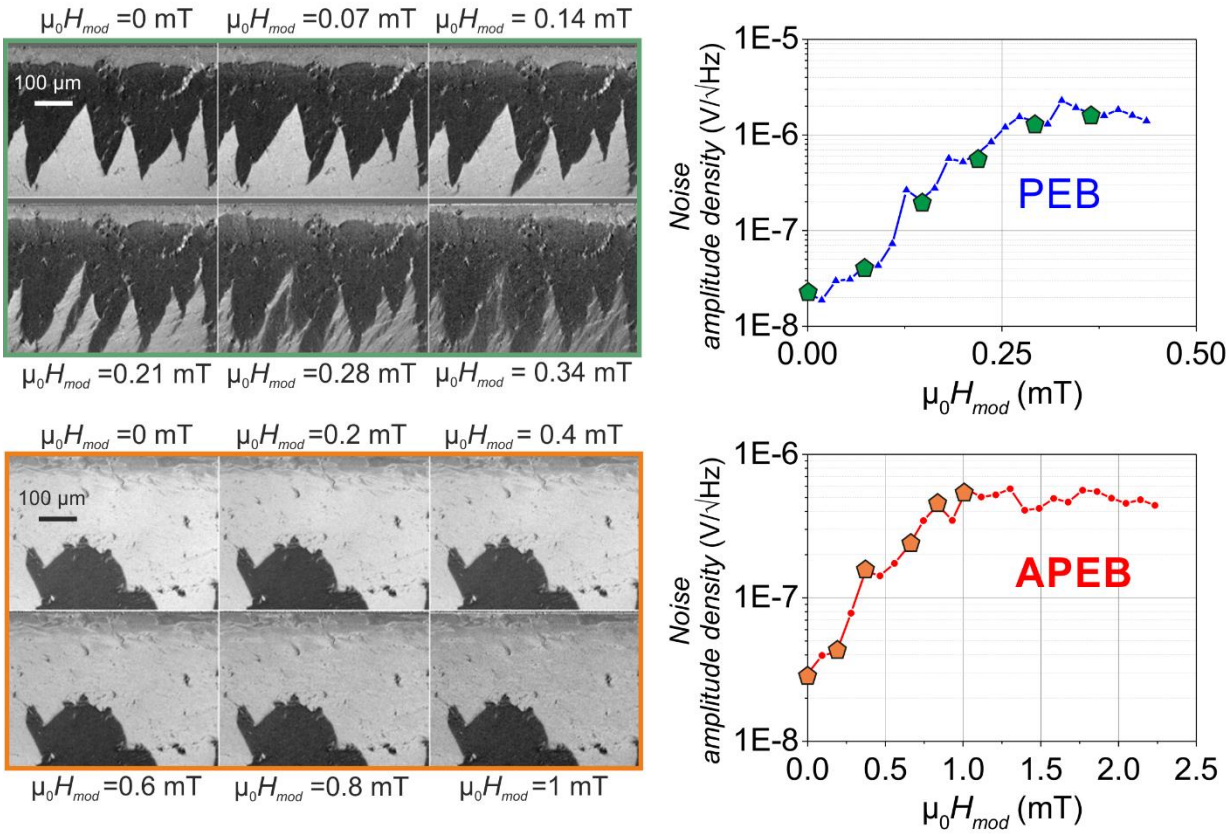

Figure 35: Time resolved stroboscopic images taken at the maximum amplitude for various modulation fields during MFC. Right to the MOKE measurements are complementary noise curves indicating the points corresponding to the expected noise values at the applied modulation fields used in MOKE observation. The resonance frequencies of PEB and APEB sensors are 843 Hz and 824 Hz respectively. The sensors were fabricated (without the annealing procedure) by Volker Röbisch.

Despite the much lower noise response at the same modulation amplitude as for the PEB, the APEB sensor does exhibit a gradual increase of the noise level up to about 1 mT. It was expected that the origin would be domain switching near the stress relaxation edge, but that was not the case. The MOKE images, taken at the highest amplitude of various modulation fields, show that the domain configuration is very stable. Even near the physical edge, only minute changes are visible and seem to not correlate with the change of the noise floor. This was puzzling, as no clear reason could be extracted from the domain behavior, as to why the electrically measured noise increases in such a manner. Furthermore, comparison of the noise floor behavior for all three sensor thicknesses of both PEB and APEB were conducted, which is presented in Figure 36(a). The comparison

shows that the noise level of PEB sensors scales with total t_{FM}. This has already been reported by Röbisch et al [23] through the worsening of LOD with thicker total t_{FM}. This shows the increasing effect of demagnetization effect compensating the EB, leading to the increased instability of the magnetic domains. The APEB sensors show a different trend. The 1 µm and 2 µm thick sensors show similar noise behavior, whereas the 4 µm sensors show a somewhat higher noise level. Between 0.2 mT and 0.4 mT modulation field the trend of noise increase is specifically faster, but later the noise increase is the same as that of the other two sensors. From the change of the noise level, no correlation with magnetic noise can be identified. If the noise would be formed due to magnetic effects (irreversible changes and domain wall motion) then the noise should increase with the same slope (or higher) onwards until the maximum ME response is reached (1 mT). Such trend has been observed for single layer sensors and for the PEB sensors. This observation and the additional magnetic domain characterization and hysteresis measurements indicate that the noise floor changes have to be related due to some other noise source originating not from the magnetic phase. With the help of Sebastian Toxværd and Philip Durdaut, the electrically determined noise behavior of the new APEB sensors was modeled and analyzed in detail. It was determined, that in fact the reason for the increased noise floor could be due to the noise originating from the excitation source (so called pump noise) [25] [60]. This noise is a function of the used modulation field and it increases proportionally with its magnitude. In order to confirm such behavior and minimize the contribution of this noise source, a high pass filter was built into the measurement scheme. This allows the reduction of the noise coming from the excitation, whilst withholding the main excitation signal at the same level. It needs to be clear, that the filters are custom made for individual sensors, as they need to be adapted to the resonance frequency of a sensor. The filtering showed positive results. The same sensors used as before were measured with the newly integrated filter and their noise response was evaluated.

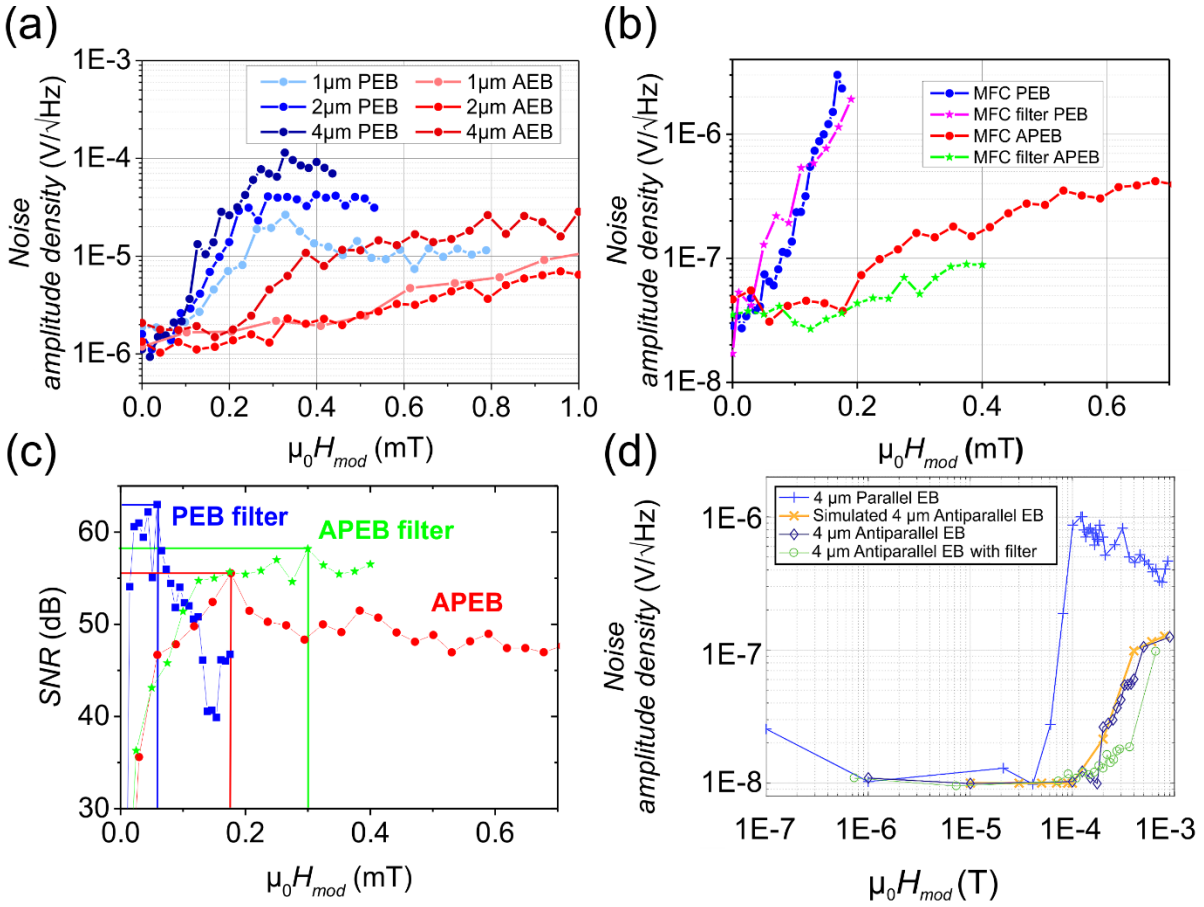

Figure 36: (a) Noise plots over a range of modualtion field amplitudes for PEB and APEB sensors with thicknesses of 1 µm, 2 µm and 4 µm total t_{FM}. (b) Noise plots over modualtion fields of the 4 µm sensors (PEB and APEB) with and without the additionally integrated filter. (c) SNR measurements against the modulation amplitude of the same sensors as in (b) with and without the application of the filter. Note, that the PEB sensor shows similar SNR behavior with and without filter, so only the data with the filter are shown. (d) Noise vs modulation field for 4 µm PEB and APEB sensors. The APEB sensor noise is measured with and without the additional filter. The non-filtered noise response is also modeled by using the expected noise of the excitation source. Measurements and simulation in (d) were performed by Sebastian Toxværd.

The results in Figure 36(b) show that the implementation of the sensor reduces the noise floor of the APEB sensor, whereas the PEB sensor shows no change in the noise behavior. This once more confirms the dominance of the magnetic noise contribution for the PEB as the filter cannot reduce the noise contribution of the magnetic phase. With the new noise floor, the SNR response with different modulation fields was determined (Figure 36(c)). It is now clear how much the additional contribution of the excitation noise changes the SNR behavior of the APEB sensor. The SNR trend now shows after about 0.2 mT modulation field a relatively constant value, which is expected for this new type of sensors, as the noise floor, should increase proportionally to the signal response change.

The reason is the increase of the thermomechanical noise that relates with the amplitude of the oscillation of the sensor. In terms of electrical characterization, it is the transposition (usually termed leakage) of the carrier signal energy density into the energy density of the sidebands. With this understanding and the new filter, the sensors LOD was remeasured with the new optimal modulation field and the LOD was improved to 80 pT/√Hz.

For another sensor from the same production batch and equivalent total t_{FM}, the signal response was measured to be higher as the heating procedure of the sensor was done more precisely. This was done by using an aluminum alignment holder allowing greater mechanical stability, better thermal contact and easier alignment of the sensor with respect to the applied field (perpendicular alignment). For this reason, the sensor was also electrically characterized with MFC using the additional filter. For this sensor also the exact modeling of the noise floor was performed. The noise behavior with and without filter accompanied by the model with the expected noise from the excitation source are presented in Figure 36(d). Since the data is plotted with a logarithmic scale, the noise behavior of a 4 µm PEB sensor is added for easier interpretation. With the new filter, a reasonably similar improvement of the noise response is attained. However, the improvement does yield a slightly lower noise performance for larger modulation field amplitudes compared to the model. This could be related to the higher quality of preparation as well as due to the possibility of better material properties resulting from the statistical variation of material properties from sensor to sensor. Irrespectively of the reason, the sensor with the higher signal response and low exerted noise provided a LOD of 50 pT/√Hz at 10 Hz, which is the best value achieved from all the sensors produced so far.

With the new filter it was seen that the SNR is stagnant across a whole range of large modulation field and this indicates another useful property of these newly developed sensors. Since the SNR is independent of the modulation field amplitude after a certain value, it gives an indication that the sensor should have independent performance to the presence of magnetic shielding. Measurements of the same sensor conducted with and without magnetic shielding (Figure 37(a)-(d)) prove such relation. The sensor in the direct detection (Figure 37(b)) shows a slight worsening of the LOD, which can be explained as the additional contribution of the surrounding on the damping of the sensor signal. With the MFC technique no changes are visible in terms of the noise, signal (Figure 37(c)) and

LOD evaluation (Figure 37(d)). This shows the high stability of the system and that it can be used in ambient environment where the mechanic distortion is minimized. This is also a great advantage to many other sensor concepts that deeply rely on magnetic shielding such as SQUID and OPM. In spite of all these advantages, the main limiting factor, sensitivity, is still insufficiently improved. For this reason, the APEB system was modified in the sense of increasing the thickness of individual FM layers.

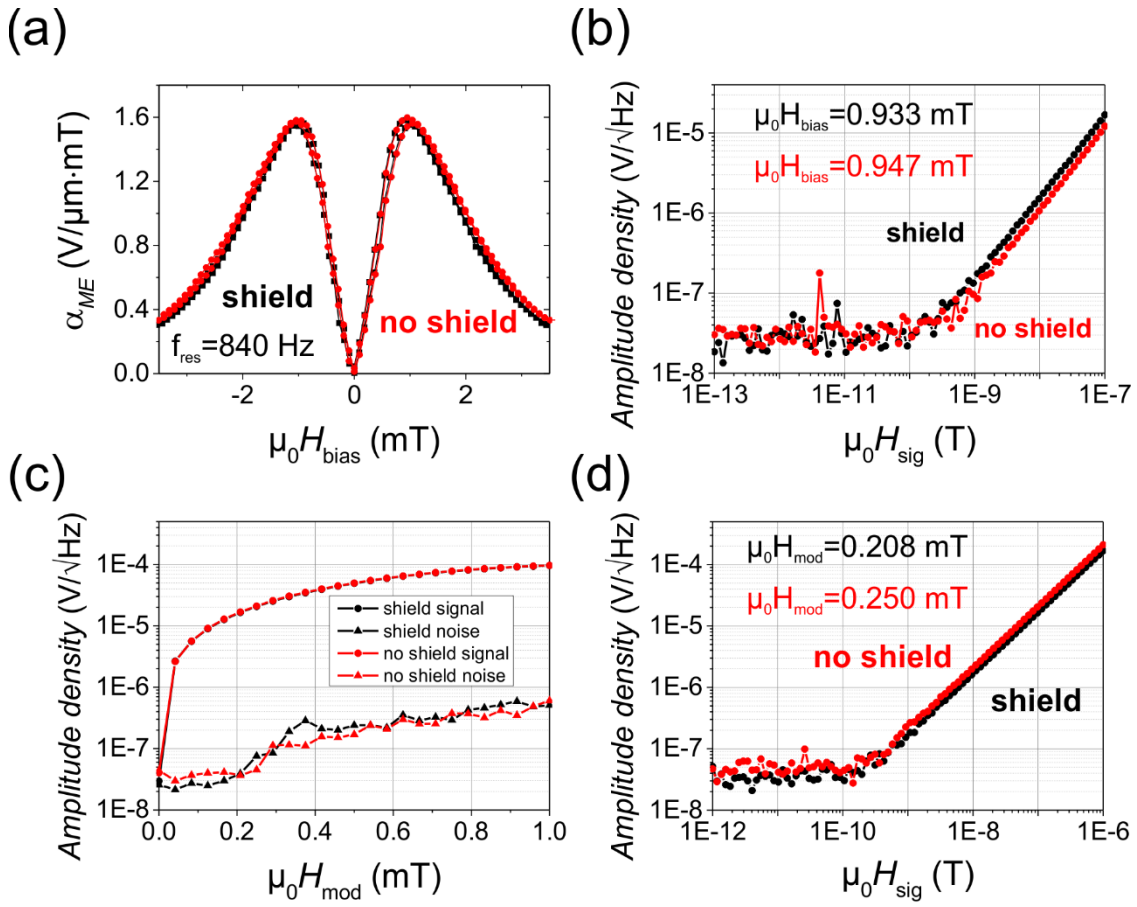

Figure 37: Electrical characterization plots for comparison of a 4 µm 90/110 sensor response with and without magnetic shielding. The **(a)** bias curve, **(b)** linearity plot of direct detection as well as **(c)** and **(d)** MFC data show the indifferent response of the sensor to shielded and unshielded magnetic environment. The signal response with and without shield overlap perfectly. The f_{res} given in **(a)** applies to both measurements.

Chapter 7

Modification of 90/110 APEB

7.1 Sensors 500

Despite the already respectable improvement of 6x lower LOD value at 10 Hz, the previous sensors are still insufficient for conducting biomagnetic measurements with meaningful averaging time [116] [117]. For this reason, the thickness of the individual FeCoSiB layers was increased from 90/110 nm to 500 nm and keeping the total t_{FM} of the sensors 1 µm (2 layers), 2 µm (4 layers) and 4 µm (8 layers). For these sensors a symmetric stack is used, as it was expected that due to the large t_{FM} of the individual layers, the antiparallel coupling would be preferred over the parallel arrangement of the EB. Before the actual sensors were produced, modeling was performed to extract possible information about the magnetic and ME response of the 500 nm system as well as other intermediate thicknesses. The modeling was conducted by assuming that the EB-field is reduced in strength proportional to the factor of increased t_{FM} of the individual layers. The modeled results for sensors with 1 µm total t_{FM} are displayed in Figure 38(a)-(b). The modelling was performed with a 2 layer model described in 6.3.2.1 at which the lowered EB-field was simulated by decreasing the EB exchange constant.

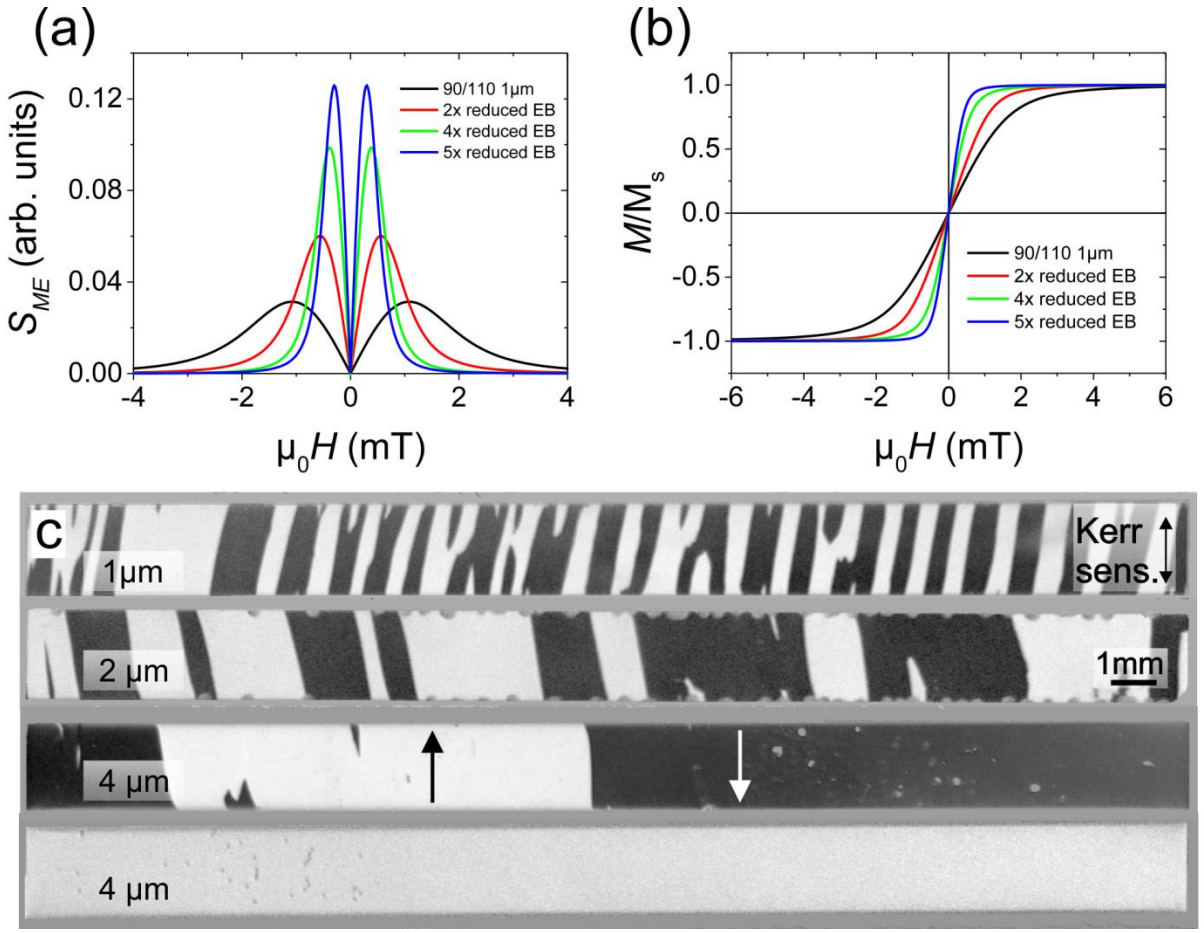

Figure 38: (a) Modeled ME response derived from the (b) modeled long axis hysteresis curves. The modeled data shows the effect of decreasing EB, which is proportional to the virtual increased t_{FM} of the individual FM layers for a 1 µm total thickness sensor. (c) Overview MOKE domain images of APEB 500 sensors with total t_{FM} of 1 µm, 2 µm and 4 µm. The final image below shows an example of a 4 µm sensor produced with a single domain state. All images were taken at zero applied magnetic fields. The sensors were fabricated (without the annealing procedure) by Volker Röbisch.

The Figure 38(a) indicates the softer magnetic response leading to a larger ME response of approximately 4x larger for the 500 nm FeCoSiB layer thickness variation. The modeled data showed similar trend to occur for the 2 µm and 4 µm sensors. The simulated long axis loops (Figure 38(a)) indicate that the system should still have sufficiently strong EB and coupling to withstand the demagnetization effects as no collapse of the system was visible from the modeled data.

7.1.1 Domain observations

The sensors were prepared with the standard heat treatment discussed in section 6.2. The first distinct difference in comparison to the 90/110 sensors was observed already with the in-situ MOKE investigation (Figure 38(c)), where very large domain patches form across the sensor. From the same figure, a tendency of larger patches forming with increasing total t_{FM} can be also seen. This larger domain structure and trend is understood as a result of the higher influence of the FM ordering reducing the effect of the local variation (structural, interface and EB alignment) exerted by the AFM.. With these sensors, the single domain state was also possible to achieve (example in Figure 38(c) below) by the same procedure as used for the 90/110 sensors. In addition, with these sensors the agglomeration of the domain patches with each demagnetization cycle could be well documented. An example of the agglomeration over several demagnetization cycles is given in Supp. 7.

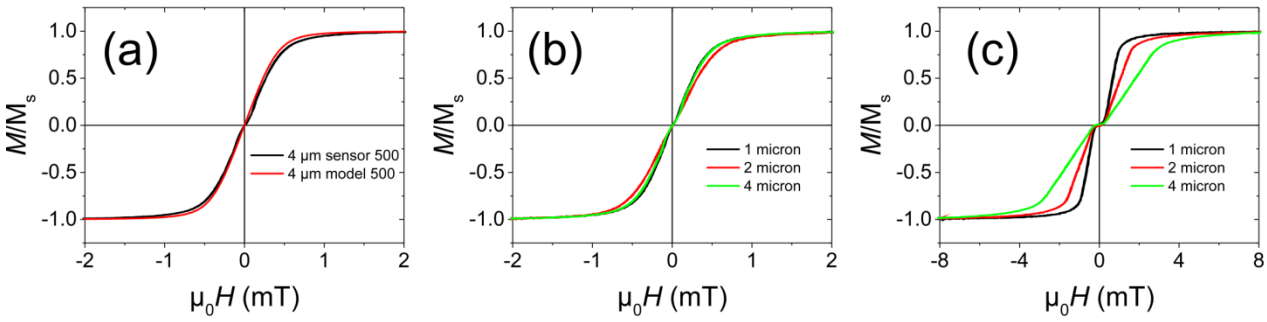

Figure 39: **(a)** Comparison of previously modeled magnetization response (5x reduced EB based on modeled 90/110 sensor loop) with the magnetization response inductively measured along the long axis of a 4 μm 500 sensor. Measured magnetization loops of the 500 sensors with different total t_{FM} along the **(b)** long and **(c)** short axis. The measured loops show the deviating response of the 2 μm sensors with the expected trend.

The inductive magnetization responses of the produced sensors coincide well with the expectations based on the modeled response (Figure 39(a)). However, the 2 μm sensors show a deviation from the expected trend as it exhibits a harder long axis loop compared to the other two thickness variations (Figure 39(b)). This is explained to be a product of bad processing of the sensors, which can be seen from the MOKE images in Figure 38(c). A possible reason, however very speculative without any direct proof, is an error of the ion beam etching procedure, which could have led to overetching of the edges and formation of additional build-up stress in the system leading to an additional anisotropy

in the system. From the short axis measurement, it was excluded that the deviation could originate from the EB or antiparallel coupling, as these matched with the response of the other two sensor groups.

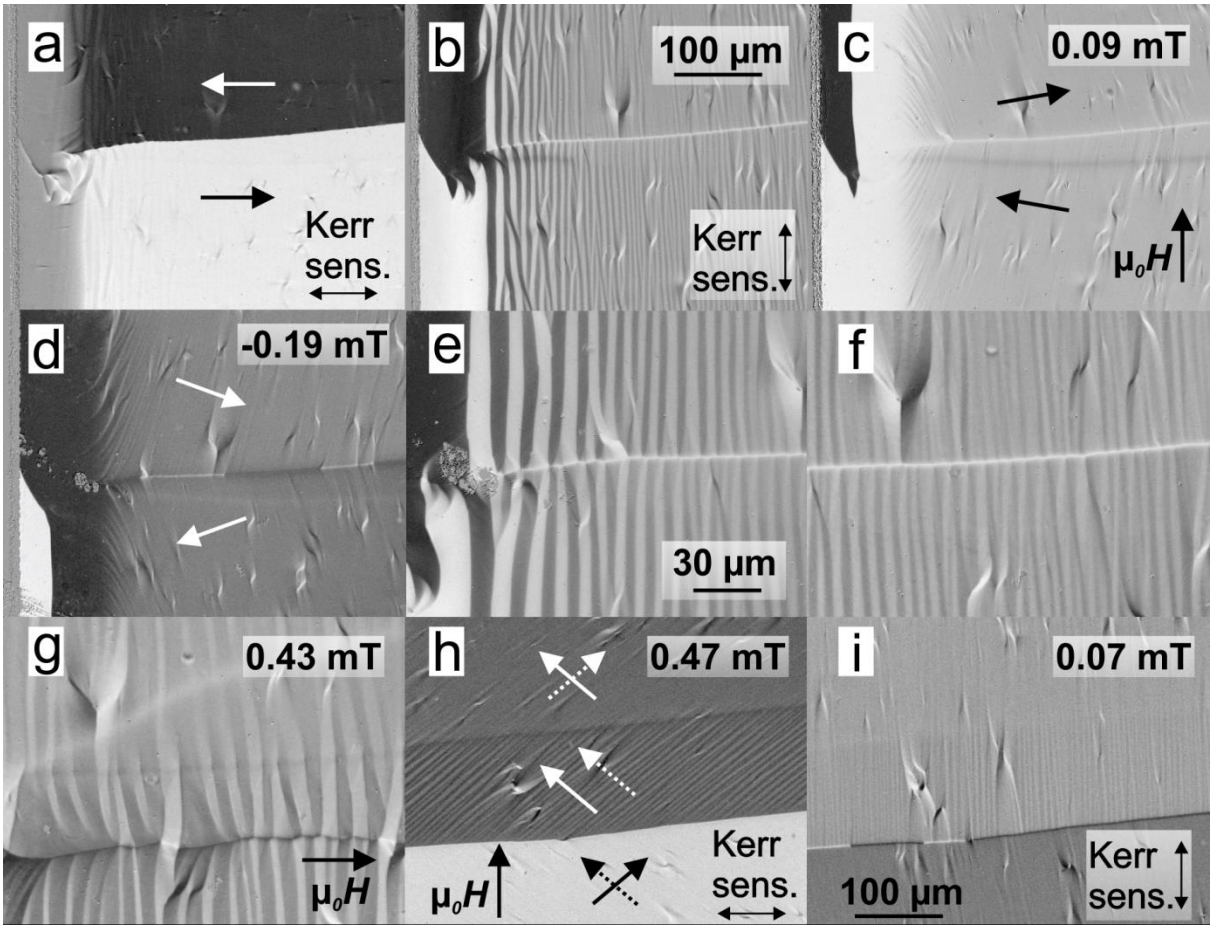

Figure 40: **(a)-(d)** High-resolution MOKE images of a 4 µm 500 nm sensor displaying the small perturbations and periodic stress pattern. **(e)-(f)** enlarged MOKE images of the domain wall displaying more features about the periodic structure as well as **(g)** the movement of domain walls of individual layers by the application of a field along the short axis of the sensor. **(h)** and **(i)** display a PEB patch formed in the domain structure and the induced stronger domain activity with field forming within the patch. The sensor was fabricated (without the annealing procedure) by Volker Röbisch.

The high-resolution MOKE investigation indicates additional attributes of the new sensors. Despite the formation of only a handful of domains, the magnetization is actually extremely perturbed across the whole sensor surface (Figure 40(a)-(d)). The reason for these artefacts could be low quality of the magnetic layers in terms of defects or maybe even the presence of formed nanocrystallites. However, the later could not be detected by any measurements conducted on the sensors: the magnetization response shows a

soft character, the XRD measurements show no signs of crystallization (not shown) and topographical features from MOKE observations also do not indicate any significant variation in the surface or presence of high amounts of defects. Additionally, the new system shows a presence of periodic modulations formed across the whole sensor (Figure 40(b)). The modulations decrease in width from the structural edge towards the bulk of the sensor until a specific width was reached. With higher magnification (Figure 40(e)-(g)) additional features of the wall structures and domains close to it are revealed. Triangular shaped closure domains form close to the domain wall. The formations are larger closer towards the edge, which suggests that they form as a result of the self-magnetostrictive energy induced by the relaxed stress near the physical edge and the magnetostatic energy to reduce the stray field generation and charging at the wall.

The images also illustrate the segmentation of the wall in a form of a flattened zig-zag pattern, which coincides with the modulations. The widening of the modulations with the application of field also induces a more pronounced zig-zag structure of the wall and with it segmented switching of the wall bounded to the width of the individual modulation (Figure 40(g)). Interestingly, the imprinted contrast from the domain walls and the switching of the domains from the lower layers seem to show no influence on the modulations. The pattern and behavior of it strongly resembles the pattern observed before in PEB sensors (section 5.1.1). However, it is clear that it cannot be due to the influence of the H_{dem} as the domains still show a clear antiparallel character present throughout the layers (imprinted domain walls). So, from this it was concluded, that the feature has to be induced by residual built-up stress across the whole volume of the magnetic films. It is possible, that sufficiently high residual stress Is present in the layers and since the EB-field has been reduced (and the Ku of the system is low), the modulation can then be formed by self-magnetostriction. This furthermore explains, why the modulations were not visible for the APEB 90/110 sensors, but for the PEB 90/110 they formed, because of the weakened EB-field due to H_{dem}. This possible explanation will be further discussed in the evaluation of the electrical modulation technique in Chapter 8, as there the effects of residual stress can be better interpreted. Despite the presence of these modulations, another more critical feature was found across many samples. Patches of parallel aligned EB domains (Figure 40(g)) were discovered ranging across the samples sometimes forming also in the middle of a single domain patch visible in the top layer. This is a very crucial sign that the system might exhibit higher noise levels, as

these patches are highly unstable and drive swift domain wall motion and irreversible domain growth. Additionally, these patches induced a denser formation of the modulations (even at zero applied field), which coincides with the previously proposed explanation for the modulation formation.

7.1.2 Electrical characterization

The electrical evaluation of the sensors partially agrees with the predicted sensor behavior described in the previous section. The magnetization derived ME response is comparatively similar to the modeled results (comparing Figure 41(a) and Figure 41(b)). However for the bias curve measurements, the 4 µm thick sensor (Figure 41(c), green curve) seems to show a much higher ME response than anticipated from the model and the inductive magnetization measurements. For this reason a second 4 µm sensor was also measured, which indicated a ME response expected for such a sensor (Figure 41(c), blue curve). The difference in the ME responses of these two sensors could be a result of the lower K_u of the first sensors, however, both sensors exhibit very similar magnetization responses and values of effective anisotropy (Supp. 8).

The sensors, due to lower EB-field, show a much higher signal response and with it an improved LOD (10 pT/√Hz) with the direct detection method (Figure 41(d)). At the same time the 4 µm sensors once more show the two different signal outputs, matching the different ME bias measurements. The noise increases proportionally with the increased signal, which corresponds to the increase of the thermomechanical noise with the increased sensor bending. Interestingly, the noise level is not a plateau, but instead shows an increasing curvature. This was later determined to be a measurement artefact and the actual noise level corresponds to the level at the beginning, before the curvature increase occurs.

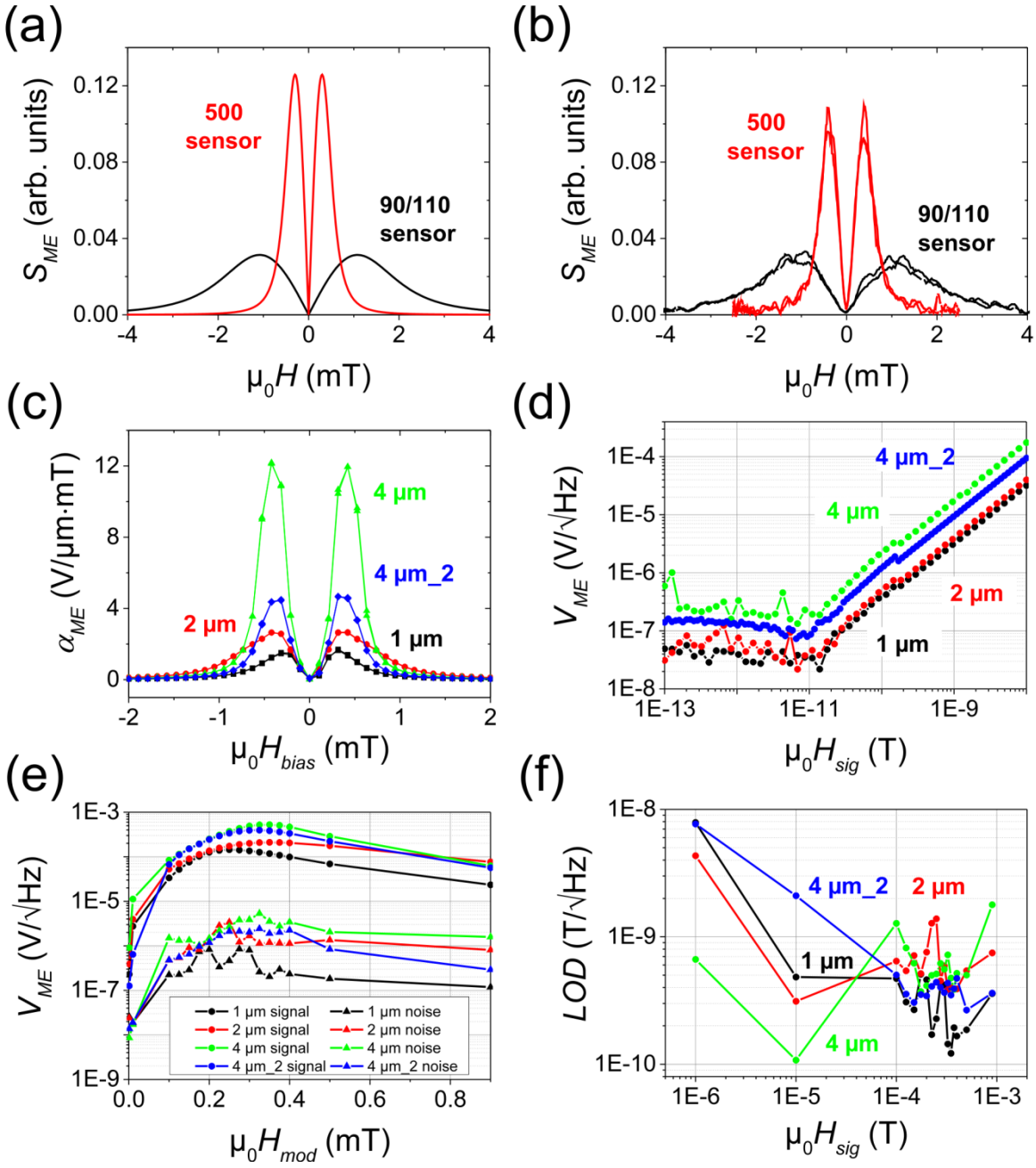

Figure 41: (a) Modeled ME response and (b) derived ME response from long axis magnetization loops of 4 µm sensors. Measured (c) ME response and (d) LOD with direct detection of 500 sensors with different total t_{FM}. A nonlinear jump occurs in the measurements at $2 \cdot 10^{-10}$ T due to an automatic change of the excitation source which is used at lower field values. Measured (e) signal response, noise response and (f) LOD with MFC technique. Measurements were performed by Sebastian Toxværd. The f_{res} for the 1 µm, 2 µm, 4 µm and 4 µm_2 500 sensors are 871 Hz, 848 Hz, 850 Hz and 846 Hz respectively. The $\mu_0 H_{bias}$ in (d) for the 1 µm, 2 µm, 4 µm and 4 µm_2 500 sensors are 0.32 mT, 0.36 mT, 0.38 mT and 0.36 mT respectively.

The MFC behavior presented in Figure 41(e) shows a much higher noise response of these sensors. The noise and signal behavior over a range of bias fields show a similar trend seen in the PEB 90/110 sensors. This indicates that the noise floor is now once more dominated by the magnetic noise and goes well in hand with the domain observations. For this reason, the LOD with these sensors could not be improved compared to the 90/110 sensors. The best LOD for the 500 sensors was determined to be 100 pT/√Hz at 10 Hz. Thus, with the new sensors the anticipated LOD enhancement was not achieved despite the improved sensitivity of the sensors. For these sensors it is crucial to understand, if the magnetic noise contribution is a result of the symmetric stack leading to PEB patches, insufficient quality of the magnetic films, stress or due to the H_{dem} compensating the weaker EB-field in the magnetic stack. This question will remain an open one as due to time constraints and delayed sensor production, the evaluation of this sensor type could not be conducted in full.

Concerning the different signal output of the two 4 µm thick sensors, a later repeated measurement of the first sensor showed that the sensor had changed with time. The antiparallel system seems to have collapsed and instead a much more complex arrangement was formed. The ME bias curve is provided in Supp. 8(d). Surprisingly, by comparing the long axis magnetization response measured directly after production and after the second ME measurement, no significant difference could be identified (comparison given in Supp. 8(c)). These results can be interpreted, that the 500 nm sensors are on the verge of being overwhelmed by the H_{dem}. From this, it can be postulated, that the sensor had already a partially destabilized domain structure resulting from the H_{dem}. The domain structure then rearranged in order to compensate H_{dem} by assembling into a structure with differently canted antiparallel domains, which overall cannot be detected by inductive measurements. Exemplar images of the different canted domains (seen by contrast difference) are presented in Supp. 9. This further suggests that the different behavior of the two sensors could be a result of the variation of magnetic properties of the FM and AFM layers from sensor to sensor.

7.2 Downscaled sensors for ΔE application

Despite the previous setback of the 500 APEB sensors not fulfilling the expected sensor improvement, it needs to be clear, that the MFC is only one of the many sensor

measurement schemes used to drive these sensors for biomagnetic applications. With this in mind, also the signal and noise performance of the same sensor type can differ by using different measurement schemes. For this reason, the APEB stack was applied to downscaled micro-machined sensors on thinner silicon substrates (50 µm) which are used for ΔE measurement scheme. This was firstly conducted on so called "dummy" sensors, which are full sensors without the deposited piezoelectric layer on the backside. This was done for two reasons; one is to make a testing sensor batch to research the applicability of the APEB on such smaller sensor design and possibly tailor the heating scheme to make the integration easier. The second reason is to have simultaneously a sensor batch as a reference to compare it with the full sensors and indicate the influence of possible stress formed during the deposition of the piezoelectric layer. This is an important factor to monitor, as the stress state of the whole sensor can lead to stress generated domain states and sequentially decreased performance of the sensor.

The sensors were prepared with the 90/110 stack sequence as well as with the 500 stack. The sensors were prepared with a total t_{FM} of 2 µm and two different geometries 1x3 mm^2 and 2x3 mm^2. In Figure 42 exemplary overview MOKE images are presented of the attained APEB domain construct for the two sensor geometries. A multidomain as well as a single domain state was possible to achieve for both geometries using the same heating procedures explained in previous chapter. With the high-resolution images the homogeneity of the magnetic domains is confirmed as well as the absence of any stress-induced domain structures.

With the domain observations it is already clear, that the application of APEB is successful, however, due to the sensor production procedure inductively measured magnetization responses cannot be measured. The residual redeposited magnetic material left on the chip holder, which adds additional magnetic signal and noise to the inductive response, makes the characterization of the sensors with this method impossible. An exemplary image of the magnetization response curve and the overview MOKE image indicating the redeposited material are in Supp. 10. For this reason, the magnetization response is only measured using MOKE derived loops, which limits the characterization to the upmost layer. Nevertheless, the loops show very promising results.

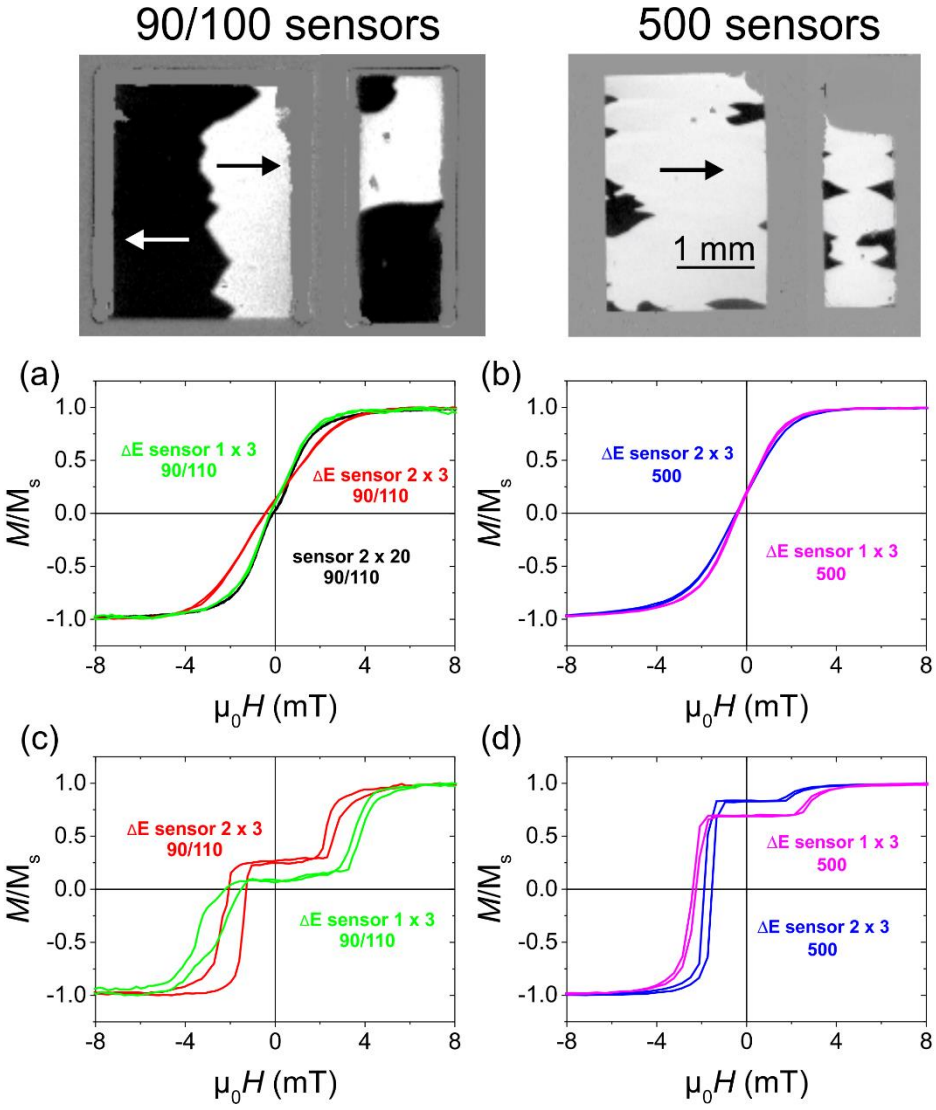

Figure 42: Top are exemplary overview images of the 90/110 and 500 sensors with the two different geometries. Below are the magnetization loops measured along the (a)-(b) long axis and (c)-(d) short axis of the corresponding different sensor types and geometries. The total t_{FM} for all the sensors is 2 µm. The sensors were fabricated (without the annealing procedure) by Lars Thormählen.

In Figure 42(a)-(b) the long axis loops of the two sensor geometries taken over the whole sensor areas are presented. The response of the 90/110 is additionally compared with the inductively measured magnetization response of a standard bulk sensor with the same stack sequence and total t_{FM}. The 500 sensors are not compared with the bulk sensor response due to the unreliable quality of the bulk sensors. From the comparison, the perfect fit of the 1x3 mm² sensor's response with the response of the standard sensor is apparent. On the other hand, the 2x3 mm² sensor shows a much harder magnetization

response compared to the standard one, which can be a result of the different shape effect. However, when comparing the responses with the responses of the 500 sensors, then it is clear that the demagnetization effects are not the reason. This is also visible from the shift of the long axis loops of the 90/110 2x3 mm^2 sensor and 500 sensors. This hints towards the presence of a higher amount of residual stress present in the sensor.

The possibly high stressed state is visible by the prebent position of the sensor. Despite the seemingly similar behavior to the standard sensors, the smaller sensors do have a different effective magnetic response. This can be clearly presented with local magnetization responses measured on different positions of the sensors. These responses presented in Figure 43(a) show the effect of stress relaxed edges and local demagnetization effects on the magnetization response and the substantial amount of the sensor influenced by this effect. For this reason, it is expected that such sensors will have low noise behavior but should have lower signal response due to the harder character of the sensor. The reason for why this was not visible from the overview magnetization response is that the opposite edges generate EB shifts in opposite directions and thus effectively cancel out in the overall response (in the top layer).

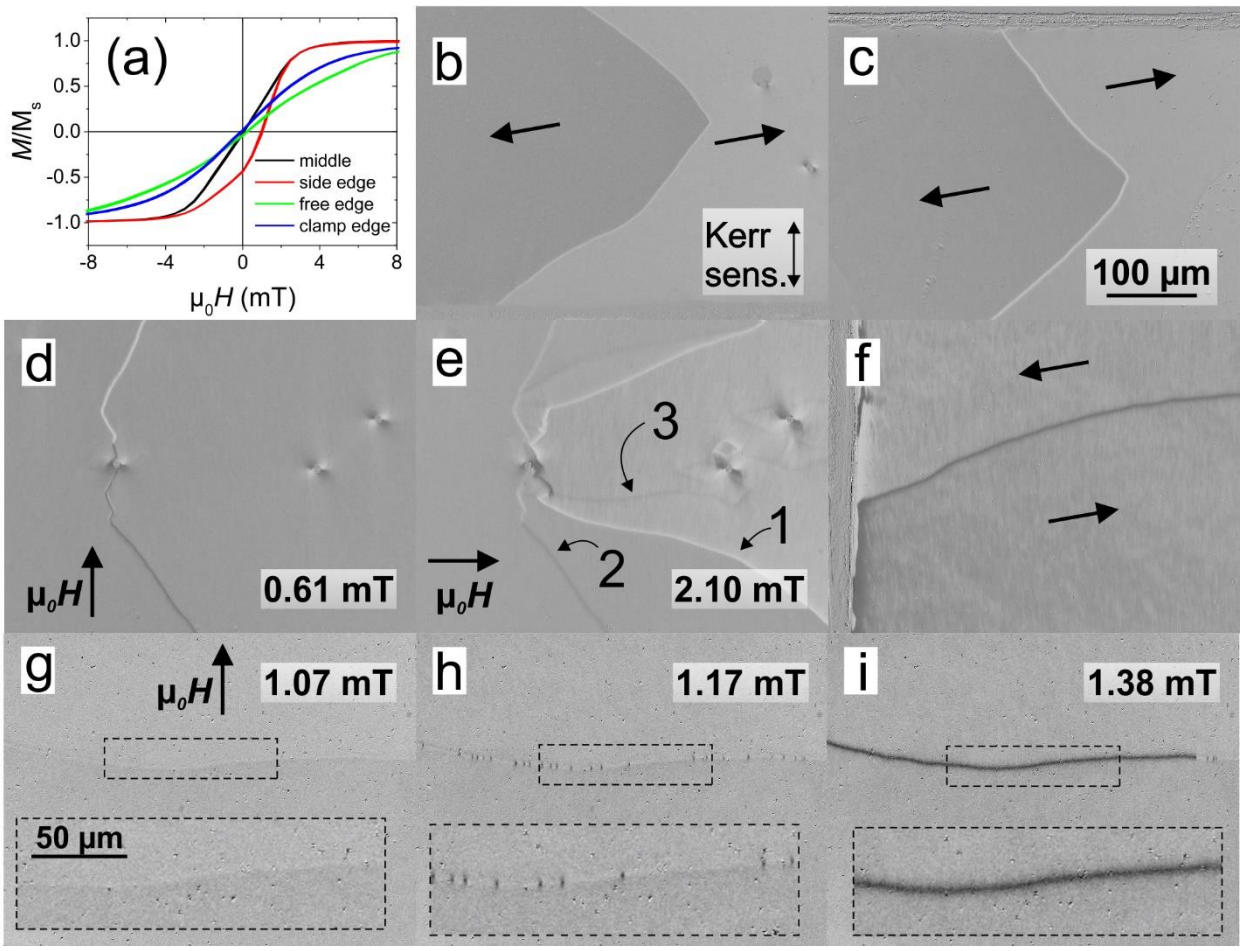

Figure 43: **(a)** Regionally measured magnetization response measurements with field applied along long axis of a 2x3 90/110 sensor. High-resolution MOKE images of the **(b)** clamped and **(c)** free edge of the sensor showing a clear antiparallel domain state with an Néel wall in between. In the middle of the sensors the domain behavior is evidenced with the application of the field along the **(d)** long and **(e)** short axis. In **(e)** the individual domains with their encompassing domain walls are marked by the index numbers. **(f)** The domain configuration near the side edge with small dense ripple formations is presented. **(g)-(i)** With the application of a field, the switching of the wall in the top layer is presented, at which the nucleation of small sections occurs before the switching. Within each image an enlargement of the middle section of the wall is inserted. The sensor was fabricated (without the annealing procedure) by Lars Thormählen.

From the high-resolution images a clear two domain state is visible (Figure 43(b)-(c)). Interestingly, the domains show no large influence of the stress on the domain construct. This indicates that the K_σ, EB and K_u lie in the same axis. By retreating into the middle of the sensor, the soft magnetic bulk behavior can be probed. The domain walls show an interesting decoupled behavior with the application of an external magnetic field. With long axis field application, the walls switch individually, which can be seen in Figure 43(d)

by the differing contrast of the lower (110 nm layer) and upper (90 nm layer) wall. With the application of short axis field (Figure 43(e)), the lower domain wall state (marked by 2) can be visualized without overlapping contrast of the upper wall (marked by 1). The domain wall from the second 90 nm layer (marked by 3) imprints a very weak contrast onto the top layer. Interestingly, the domain walls from the different layers exhibit similar width, which suggests a coupled behavior of the walls in form of compensated Néel wall formation.

From the investigation of the sensor edge, only a very small stress relaxation zone is revealed (Figure 43(f)). This is unexpected as for an unknown reason the stress relaxes differently compared to the bulk sensors. A possible explanation could be the thinner substrate that transmits more stress into bending therefore releasing the amount of relaxed stress at the edges. With the vertically oriented domain wall of the 1x3 90/110 sensor a special field evolution of the domain wall is exhibited. From Figure 43(g)-(i) the domain wall switching with an applied field along the long axis is analyzed. In Figure 43(h) the formation of small segmentations is visualized. These fascinating structures occur before the domain wall completely switches (Figure 43(i)) and they seem to form due to the local variation of EB. These images also show the formation of the compensated Néel wall in the top layer that is induced through the application of the external magnetic field.

Surprisingly, for the 500 sensors the stress formed modulations were never observed compared to the standard sensors. This could indicate that the standard 500 sensors were indeed produced with improper magnetic material as the stress influence and demagnetization effects should be higher for the smaller scaled sensors compared to the standard ones. However, the change of the residual stress with substrate thickness needs to be considered. It is possible, that the residual stress in the smaller sensors is just simply transformed into the strong bending, leading to low stress induced anisotropy. Such behavior would then provide a low influence of the stress, thus reducing the possibility for the modulations to form. Regardless of this, the 500 stack also shows a clear APEB formation and high stability of the domains for both sensor geometries. With both of these examples, it is clear that the application of the APEB on smaller scaled sensors is possible and with it also the domain stability and most probably ultra-low noise behavior. However, the last statement could not be proven using the ΔE effect readout method, as the production of sensors with a piezoelectric phase was not possible due to delays and setbacks in the sensor production. Thus, the advantage in terms of the ΔE

effect performance of the sensors with the APEB coupling as well as the effect of the piezoelectric on the stress state remains an open question.

7.3 Anisotropy manipulation

As it was presented in the previous chapter, the APEB yields the ability to tailor and modify the domain structure during the thermal annealing used for the setting of APEB. However, the system does allow not only the tailoring of the domain structure, but also the individual anisotropies incorporated within the system. This final ability of APEB is important in terms of flexibility of the system, as it allows creation of various highly stable domain configurations that could not be achieved by conventional magnetostatic coupling mechanisms. This gives rise to an entirely new group of APEB sensors that will be discussed in the next sections.

7.3.1 Tilted anisotropy magnetic analysis

The advantage of the low noise behaving APEB structure has given already significant improvement of the sensor performance. With also the previously described single domain structure, the APEB has even higher possibility to stay stable with higher thicknesses. Nevertheless, the APEB still shows a relatively low signal response. One possibility of increasing the signal response is to divert the K_u axis towards the long axis, whilst keeping the APEB along the short axis. This allows a softer magnetic behavior along the long (sensing) axis leading to an increased signal response. Such an increase is also confirmed by macrospin modeling at which the modeled long axis ME and magnetization response loop of a 2 µm 90/110 sensor are presented in Figure 44(a) and (b) respectively. In the model two different types of rotations of anisotropy were applied, the so-called coherent (rotation of anisotropy axes of all layers in the same direction) and anticoherent (rotation of anisotropy axes in opposite directions for the two different thick layer groups). For both types the same amount (18°) of rotation is applied. The most important difference between the two types is the loop shift that occurs for the anticoherent type, which is absent in the coherent type. The shift is also visible in the ME response curve, which effectively transfers the working point with higher amplitude to lower bias field values.

This shifting effect is desirable as with sufficiently high enough shift the maximum ME response can be shifted to 0 bias fields, resulting in a sensor not requiring bias coils for operation. The possible setback of this system is the symmetry breaking effect on the ME response, which could lead to a reduced response with the MFC technique. The coherent rotation instead conserves the symmetry of the ME response and only delivers the increase/decrease of one of the working points, however, with a smaller effect compared to the anticoherent rotation. Although in theory it seems a very straightforward system, attaining such a coupling in reality is far from simple. The problem is that the APEB coupling is set by utilizing the K_u aligned along the short axis of the sensor, which makes K_u predetermined by the heating scheme. This means that any modification of the anisotropy during the heating step would result in the change of orientation of the APEB and/or coupling of the individual layers. In order to not risk the destabilization of the APEB, a second heating step is introduced.

The anisotropy could be tilted by a high amount, up to about 36° without inducing domain state changes. The rotation was determined by modeling the inductive measurements presented in Figure 44(e) (modeled data not shown). The same data was also compared with the response of a sensor with much lower anisotropy rotation. It is clear that a higher rotation leads to a transition with the antiparallel splitting similar to the observed behavior of a short axis response of a standard APEB sensor. The middle splitting forms as the domains rotate at small fields coherently meaning the change of magnetization is small as the change of it only occurs due to the different torque of the two directional states. This creates a limit for sensible anisotropy rotation as the splitting decreases the middle part of the slope and increases at the sides, however, the sides are governed by the irreversible domain behavior leading to noise generation. For this reason, the optimal anisotropy rotation was determined with modeling for attaining the highest slope without formation of pronounced splitting. The optimal angle of the tilt was determined to be about 27°.

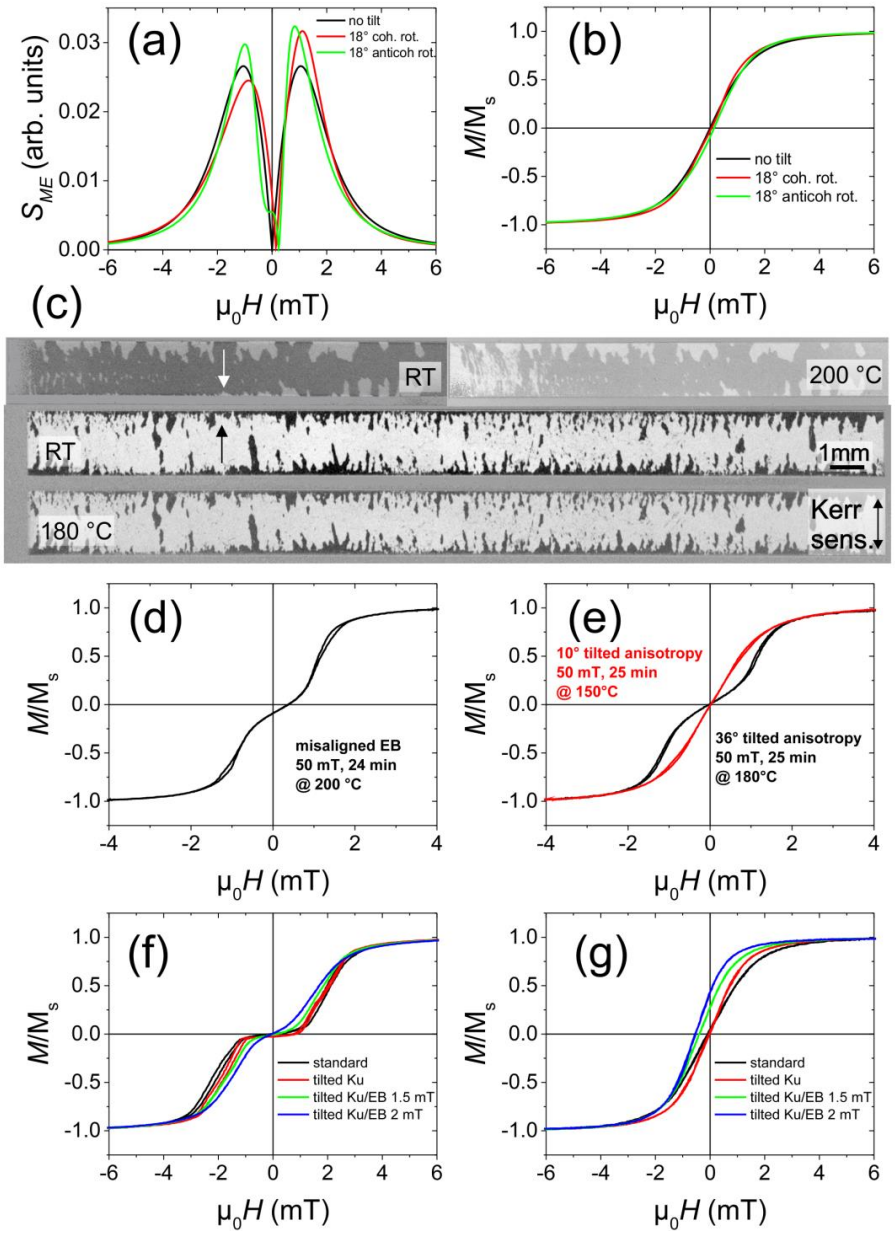

Figure 44: (a) ME response derived from the (b) modeled magnetization response of a 2 µm APEB sensor with coherent and anticoherent rotation of anisotropy. Both responses are compared with the response of a standard APEB sensor. (c) Domain images of two sensors treated for anisotropy tilting before the heat treatment (RT) and at the corresponding temperature after 30 min of heat treatment. The top sensor shows a change of the EB exhibited by the change of the domain structure indicated also by its long axis magnetization response in (d). The lower sensor shows no change of the domain structure despite the 36° anisotropy rotation. Its long axis magnetization response in (e) is compared with a sensor exhibiting smaller angle anisotropy rotation. Magnetization responses of sensors with different anisotropy rotation and type of rotation are compared with the response of a standard sensor along (f) short and (g) long axis. The sensors were fabricated (without the annealing procedure) by Volker Röbisch.

So far, all the data and sensors have been produced with the coherent rotation of the anisotropy. In order to induce an anticoherent rotation of the anisotropy, the same procedure, time and temperature for the second heating step is used with the exception of cooling down with the field still applied. With the confirmed new heating scheme, a new set of APEB sensors with a range of differently tilted K_u could be produced. An example of such a set is presented by induction measurements in Figure 44(f)-(g). In this case, the coherent and anticoherent rotation types are denoted as tilted K_u and tilted K_u/EB respectively and will be further on used to discriminate the two types. The rotation angle of the K_u/EB is highly determined by the amplitude of the applied field during cooling. In the example in Figure 44(f)-(g), the change from 1.5 mT to 2 mT applied cooling field results in a tremendous change of the rotation and with it the magnetization response. This gives the hint of the possibility to easily tune the shift just by the applied cooling field. Additionally, this also means that the preheating time could be significantly reduced, however due to time constraints, this was not proven. Upon closer inspection of Figure 44(f) a different effect on the short axis response is visible for the two different types of anisotropy rotation.

For the tilted K_u sensor, the thinner layer exhibits a decreased EB shift, whereas the other layer seems to show no change. This effect can be explained as the effect of compensating the stray field mismatch, which was already discussed in 6.3.2.1. In this case, this effect is amplified by the tilted anisotropy, which is compensated to a certain degree by the effective reduction of the EB field of the thinner layer. This effect can be seen more clearly in Supp. 11. For the tilted K_u/EB system, the compensation does not occur, but instead a gradual decrease of the slope and reduced splitting in the short axis occurs with the increasing angle of anisotropy tilt. Such change is attributed to the reduced stray field coupling, as the system is being pushed away from the antiparallel alignment towards the parallel state. This is also the reason for the symmetrical change of the short axis loop. The slope is then decreased due to the increasing effective demagnetization effect that was previously compensated by the stray field coupling. From this, also the limitation of the anisotropy rotation is revealed to be the stray field coupling reduction. As soon as the H_{str} is reduced to a degree, where the two split sections meet as one line, the APEB has no more effect on the long axis response. This leads to an effective collapse of the system, reforming itself to a parallel arranged state

along the long axis. The border value of the tilting angle before the collapse is determined at 32° based on modeling results.

From the previously discussed sensor types, individual sensors were then also observed with high-resolution MOKE in order to indicate the behavior of the individual domains within an individual layer. The purpose was also to indicate, if any counteracting turning of the magnetizations with an applied field occurs in order to see, if the total magnetostrictive response of these systems would be effectively reduced. In Figure 45(c)-(d) high-resolution MOKE images of a tilted K_u and tilted K_u/EB sensor are presented.

From the domain images a clear antiparallel construct is observable for both sensors. The difference is visible in the domains being shifted in two different manners as anticipated from the modeling and inductive measurements. With the application of a magnetic field along the long axis, both sensors show coherent magnetization rotation of the magnetic moments towards the field. This also means that there is no counteraction of the domains with respect to the long axis behavior (no cancelation of magnetostrictive effect). However, for the tilted K_u sensor a clear lag of magnetization rotation for one of the domains is visible with respect to the direction of the applied field along the long axis. This is expected as the tilted K_u creates a different torque to occur for the two differently oriented domains leading to the formation of the lower tilted middle section observed in Figure 44(e) for higher degrees of rotation. The lagging can be also clearly seen from the two different slopes of the magnetization responses for both domains in Figure 45(a). The high symmetry between the behaviors of the domains shows the equal rotation of the anisotropy for both domain orientations present in the system.

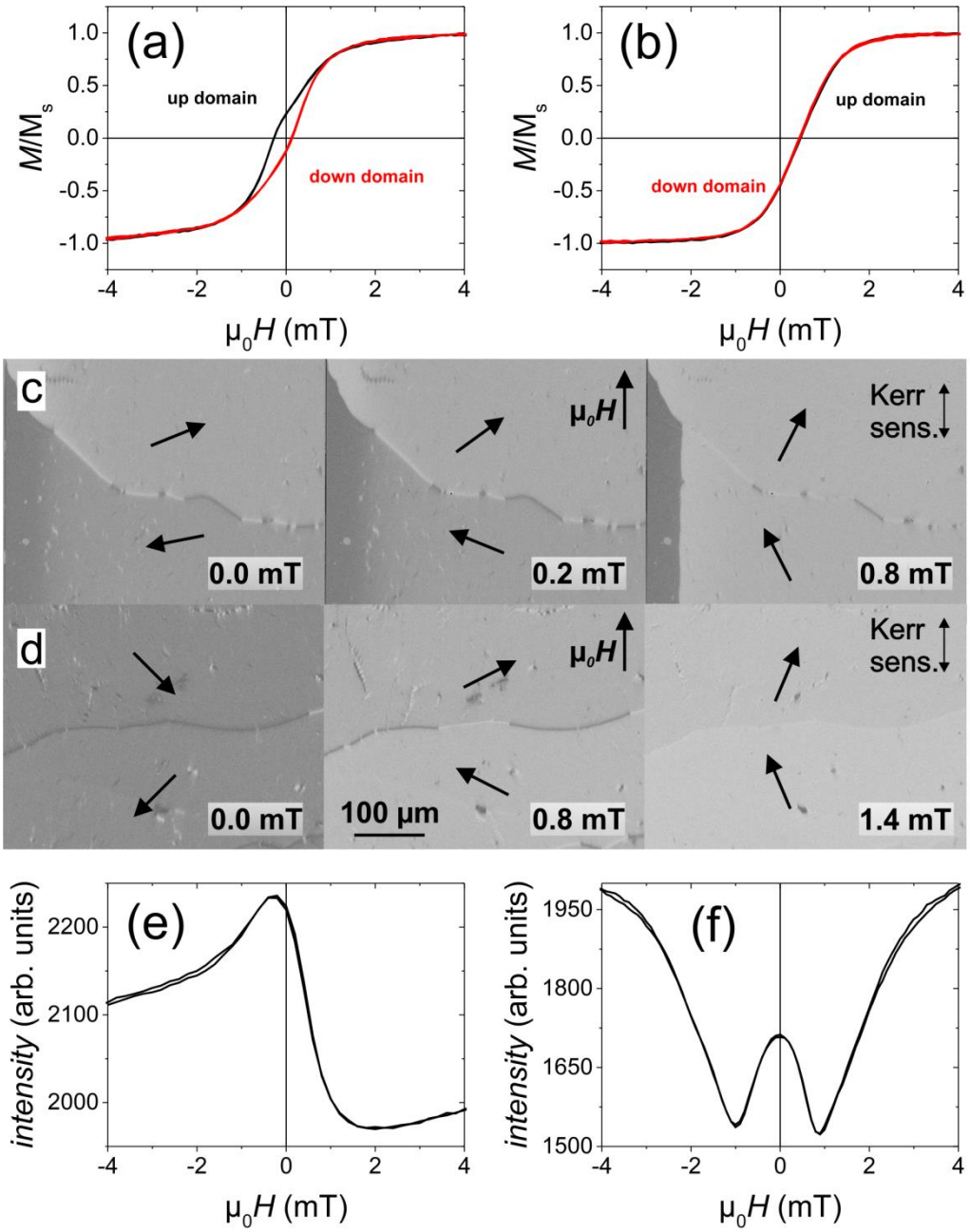

Figure 45: Magnetization loops measured with MOKE for (a) tilted K_u and (b) tilted K_u/EB 2 µm sensors. Each loop corresponds to one of the domains of the two-domain state of both sensor types. The loops are accompanied by (c)-(d) the domain evolution MOKE images with applied fields along the long axis indicating a coherent rotation with applied field for both domains. The transversal magnetization loops of the tilted Ku/EB sensor with fields applied along the (e) long and (f) short axis are also given. The sensors were fabricated (without the annealing procedure) by Lars Thormählen.

The equal rotation can be also seen for the tilted K_u/EB sensors in Figure 45(b), where both domains show an almost identical magnetization behavior. Due to the shifts of both loops, it cannot be directly indicated, whether the EB has also turned. For this reason,

transversal magnetization curves were measured with the field applied along the long axis (Figure 45(e)) and short axis (Figure 45(f)). With the first loop the coherent rotation of the two domains is confirmed, whereas the other loop indicates the symmetry of the EB effect confirming the absence of a tilt of the EB. This is indicated by the double peak with equal amplitudes and having a minimum at zero external fields. From the gathered data it can be concluded, that the manipulation of the anisotropy was successful and that with the heating schemes the anisotropy can be freely manipulated to meet the requirements of the ending application. Furthermore, the measurements indicate, that the domain patches as well as the layers do not counteract each other, which would lead to a lower ME response. This has been additionally confirmed with magnetostriction measurements presented in the Supp. 12. Moreover, the provided data in Supp. 12 also gives an example of a high tilted K_u sensor, which due to the formed flatter middle region exhibits correspondingly a minor magnetostriction response in the same field range. By avoiding these formations, tilted anisotropy sensors with higher ME response were developed. However, to indicate the impact of the magnetic qualities of the new tilted systems on the overall sensor response, they have to be tested in terms of performance with the direct and MFC technique.

7.3.2 Electric characterization

The new tilted anisotropy sensors (2 µm 90/110) were compared for their electrical responses with the response of a standard sensor. From the bias curve measurements in Figure 46(a) a clear increase of the ME voltage is visible for the tilted anisotropy sensors. The loops also show the shift related to the tilted anisotropy. The tilted K_u sensor also shows a slight shift, which could be due to a slight mismatch of the tilting angle due to the stress relaxation zone.

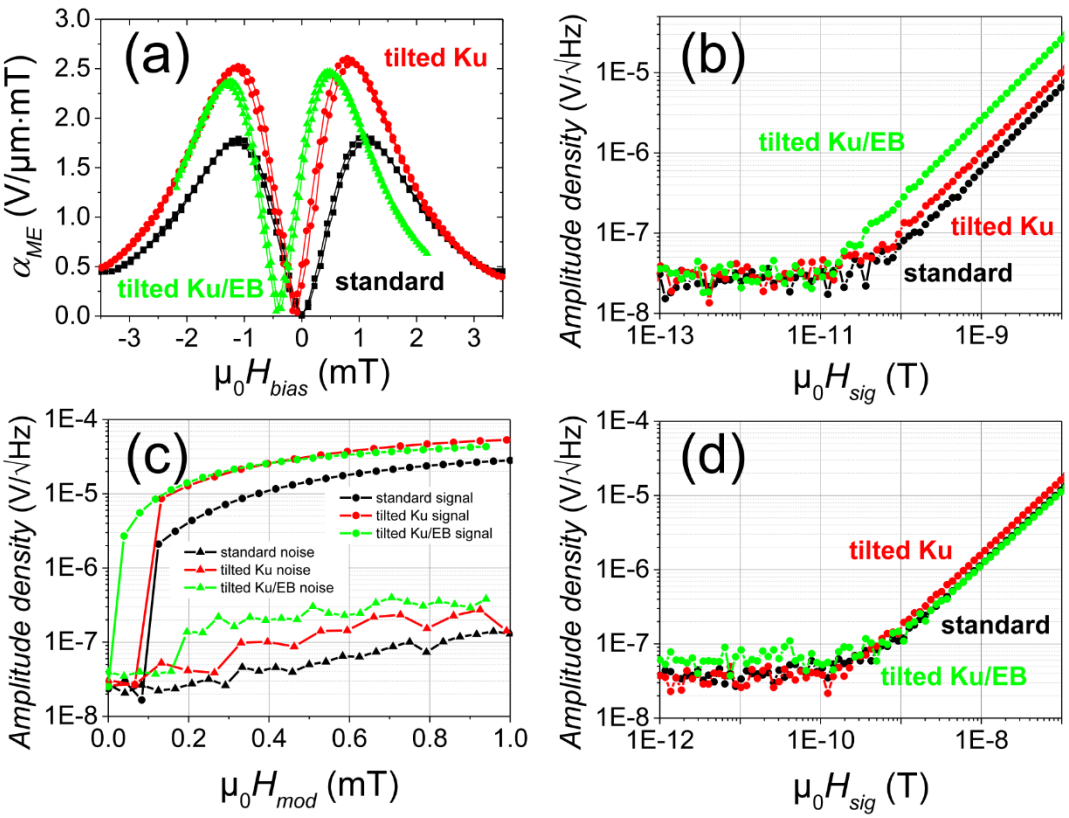

Figure 46: (a) ME response curves in dependency of bias field, (b) linearity plots with direct detection, (c) MFC signal and noise response curves and (d) linearity plots with MFC. The responses of both tilted K_u and tilted K_u/EB sensors are compared to the response of a standard sensor. The f_{res} for the standard, tilted Ku and tilted Ku/EB sensors are 827 Hz, 804 Hz and 818 Hz respectively. The $\mu_0 H_{bias}$ in (b) for the standard, tilted Ku and tilted Ku/EB sensors are 1.09 mT, 0.79 mT and 0.47 mT respectively. The $\mu_0 H_{mod}$ in (d) for the standard, tilted Ku and tilted Ku/EB sensors are 0.458 mT, 0.264 mT and 0.157 mT respectively.

The linearity plots with the direct method (Figure 46(b)) give interesting results. The tilted K_u sensor exhibits an improvement of the LOD (from 55 pT/√Hz to 30 pT/√Hz) due to about 1.5x larger signal output matching well with the bias plot. On the other hand, the tilted K_u/EB sensor displays an improvement of the LOD by 5-fold (from 55 pT/√Hz to 11 pT/√Hz) which does not match with the increased amplitude of the bias curve. The reason for the signal increase is the shift, which decreases the needed bias field leading to a softer magnetic response of the sensor and increased signal response in resonance.

With the MFC technique (Figure 46(c)) a signal increase is also registered for both sensors corresponding well with the bias measurements. However, with the increased signal also the noise increases for both sensors. The tilted K_u/EB sensor yields a higher

increase in noise compared to the tilted K_u sensor. A possible explanation is that the shift gives closer proximity of the linear regime towards the opening in the loop, leading to a faster increase of the noise with the increasing bias field. From the evaluated signal and noise response, the corresponding LODs are achieved (Figure 46(d)). The LOD is 300 pT/√Hz, 200 pT/√Hz and 520 pT/√Hz for the standard sensor, tilted K_u sensor and tilted K_u/EB sensors respectively. Based on this analysis, it can be determined, that only the tilted K_u sensors are appropriate for the MFC technique. However, it also should be stated that the MFC measurements for the Ku/EB sensors should be conducted by applying an additional external field during the measurement to compensate the H_{EB} along the long axis. The measurements in this case were done without the additional field as the necessary field could not be produced with the available power sources emitting low electronic noise. Regardless of this, both tilted anisotropy sensor types do show an increase of the signal response and could potentially allow an increased performance with other sensor methods. This, however, as well as the application on sensors with thicker FM layers needs to be further researched.

Chapter 8

Electric modulation scheme

Within the scope of this project, the analysis of the new promising sensor method, the electric modulation scheme, was also conducted. For this method, there is a significant difference in terms of the magnetic behavior compared to MFC. For the electric modulation, the excitation source modulates the stress state of the piezoelectric, which transits onto the magnetostrictive layer. The magnetostrictive layer then accordingly changes its magnetic state with the new stress state. In the next sections, the details of the magnetic changes are discussed with a variety of excitation amplitudes and sensors.

8.1 U1 and U2 modes

Before the analysis of the magnetic structure can be understood, the operating resonating modes of this sensor concept need to be explained. Based on the standard size of the bulk (2 x 20 mm^2) the modes lie in the high kHz regime, with U1 at around 515 kHz and U2 at 520 kHz [61]. These modes have a significantly higher generated output signal compared to the 1st bending mode, reaching 3 orders of magnitude larger amplitudes. Despite the high output, both modes exhibit a very complex flexure of the sensor leading to also a very complex stress state. A sketch of the bending motion for both modes is presented in Figure 47. The U1 exhibits a flapping-like motion that forms a

high stress state at the middle of the sensor and a large displacement at the side of the sensor across the length of the sensor [124]. The U2 resembles more the classical bending motion, but has an additional nodal point forming at about 1/3 away from the free end of the sensor [61]. This mode also exhibits an anti-phase behavior of the two regions separated by the nodal point. With these modes a different domain behavior is expected compared to the behavior observed with MFC, as the excitation source only influences through magnetostriction, whereas for the MFC there is a cross effect of Zeeman energy and self-magnetostriction energy. Additionally, for these modes the effect of the excitation is also not constantly axial compared to MFC. Instead, here the stress state transits from compression to tension leading to a corresponding change of the K_σ along the two principle axes of the sensor.

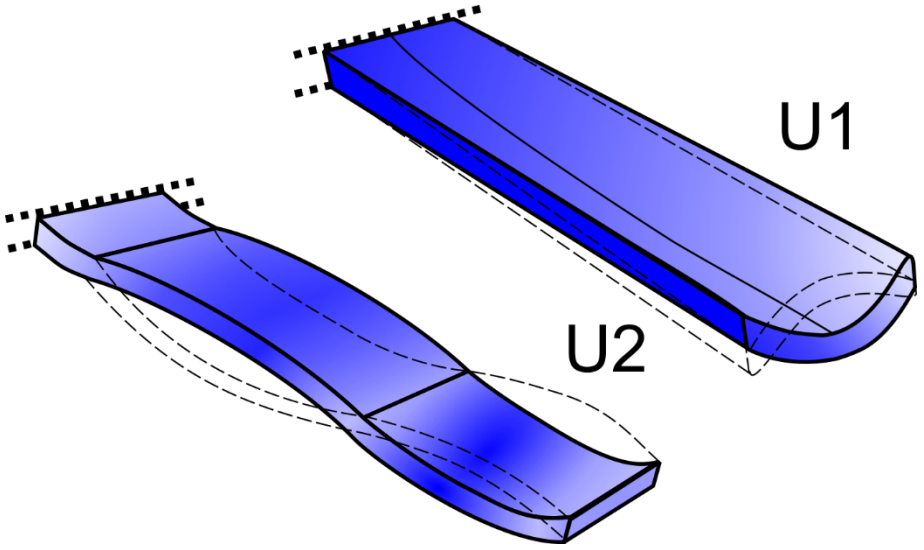

Figure 47: Sketches of the two high frequency modes indicating the mechanical motion of the cantilever. The antiphase of the motion of the cantilevers is outlined with the thin dashed lines. The thicker dashed lines indicate the transition to the clamped region of the sensor.

8.2 Single layer

Before the discussion of the single layer behavior, it needs to be stated that the sensors used in this section were developed/produced by Viktor Schell under the mentorship of Patrick Hayes.

To understand the overall effect of the two modes on the magnetic phase, a sensor with a 2 µm thick single layer FeCoSiB was observed with overview MOKE during the

excitation of the sensor. Such observation allows the indication of the stress effect on the domain structure as well as the indication of the general trend with various excitation amplitudes. In Figure 48, the averaged domain evolution with changing excitation amplitude over several thousand excitation cycles is displayed.

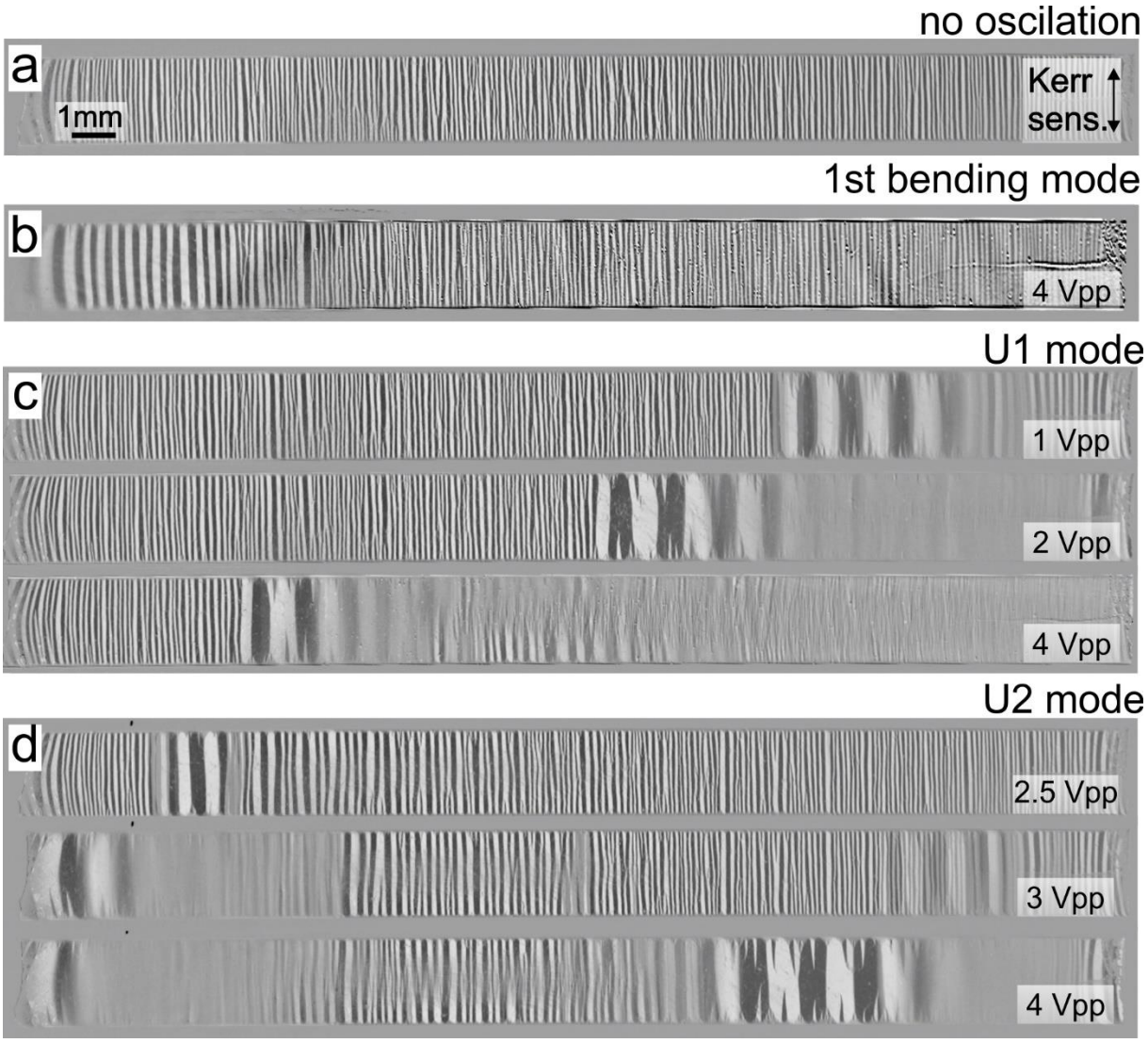

Figure 48: (a) Domain image of a sensor with a 2 µm thick FeCoSiB layer without exciting the sensor. The sensor is in a hysteretic state from the application of the field along the long axis. (b) Image indicating the domain state formed by the 1st bending mode exhibiting high displacement visible by the defocused image. In (c) and (d) the domain evolution with different excitation amplitudes is presented for U1 and U2 mode respectively. For all the images the clamped edge is on the left. The sensor was fabricated by Viktor Schell.

From both sets of images the trend of changing domains follow well with the measured displacement from vibration measurements [61] [118]. For the U1 mode, the stress is

highest at the free end of the cantilever and it decreases across the length. This is confirmed with the domain states changing also in the same manner with increasing amplitude. The region showing a wide domain state should correlate to the position of where the induce stress is in the range of the induced anisotropy. This can be explained as then the two anisotropies at the upward motion cancel each other and effectively creating a reduced anisotropy system, enabling the formation of a wide domain state. The region then correspondingly shifts with the excitation amplitude as the magnitude of local stress changes in a similar fashion. The domains also give indication of the flapping motion with the separated domains (looks like a phase shift) across the middle of the sensor, which is most visible at 4 Vpp amplitude. The domains also show a slight tilted nature, forming due to the cross effect of the flapping and slight bowing of the sensor across the whole length. The most cryptic nature occurs beyond the wide domain states on the right. There the domain states cannot be resolved and instead a greyed out average image is revealed.

The possible explanation is the formation of horizontal domain states in the downwards flap motion and the stabilization of the narrow domain state with the other motion. The states then switch within the resonance swiftly through the wide domain state and therefore provide only a short duration for such a state to endure. From the time dominance of the other two states, the cross formation gives rise to the blurred-out gray contrast. This hypothesis will be verified with time resolved MOKE. With the U2 mode, the behavior also corresponds well with the expectations from the vibration measurements. This mode has a bending motion near the clamping region similar to the 1st bending mode (Figure 48(b)), where the stress generates a wider domain construct. The U2 mode has an additional bending node that is also a stress region and allows the formation of wide domain states. In the region between these two nodes, a slightly stronger domain contrast is visible near the edges. This can be interpreted to be related to the supplementary motion of the edges in a wave like flapping, which was also visible from the vibration measurements [61]. From these overview images, a general idea of the relation of the domain formation with present stress states could be concluded, but the exact domain evolution cannot be resolved. For this reason, time resolved investigations were conducted on the sensors excited with both high frequency excitation modes.

8.2.1 Time resolved high-resolution MOKE

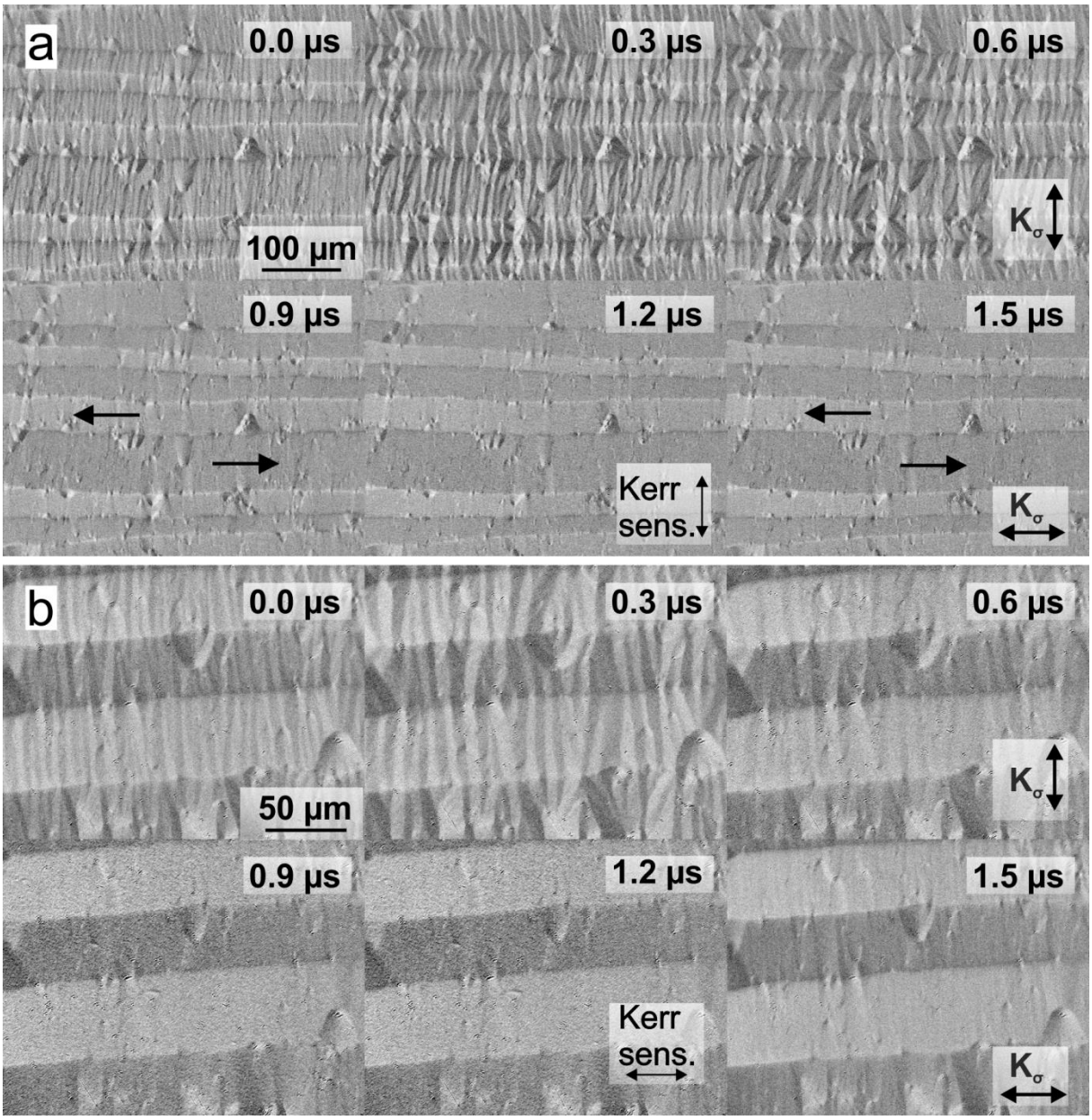

Figure 49: (a) Domain evolution through one cycle of excitation with 3 Vpp amplitude. The position is set in the middle and close to the tip of the sensor. The long edge of the sensor is positioned vertically. (b) Same domain evolution as in (a) with higher resolution and MO sensitivity along the short axis. The expected K_σ axes are denoted. The total duration of one excitation cycle is 1.935 µs. The sensor was fabricated by Viktor Schell.

In order to resolve the domain evolution for both excitation modes, the laser setup described in section 3.1.1.3 was used. Due to the limitation of the laser to lower frequencies, the laser was driven at 100x lower frequency then the excitation frequency.

For this reason, the stroboscopic imaging method was used. The pulse duration was set between 10-20 ns based on the amount of light needed for the observation of different regions of the sensor.

The images discussed in this section are selected at specific time steps of the cyclic excitation. The images show the evolution from positive (0 µs to 0.9 µs) to negative phase (0.9 µs to 1.5 µs) of the oscillations. The phase of the excitation does not necessarily match with the phase change of the stress (phase shift). For the U1 mode, the first region investigated is close to the tip of the sensors, where the highest stress state is expected. The domain evolution presented in Figure 49(a) indicates the two characteristic states present in this region. With the first part of the cycle (0.0 µs to 0.6 µs) the stress counteracts the K_u, resulting in a perplexing domain structure induced by the increased stress anisotropy combined with the magnetostrictive-self energy. At 0.6 µs the interaction leads to the magnetization turning, which is visible from the orientation of the low angle domain walls. With the recessing stress state of the sensor, the sensor regains its previous narrow domain structure with magnetization lying along the sensor's short axis. With the opposite phase of the oscillation (0.9 µs to 1.5 µs), the domain state does not change as the two anisotropies are collinear. In Figure 49(b), an enlarged portion of the previous field of view is shown in order to resolve the small stress structures more easily and to determine the presence of them in the other time steps. The result is same as extracted beforehand, except for the clear initialization of the stress induced formations before the complete ending of the opposite phase oscillation (1.5 µs). Such behavior indicates the prestressed state of the sensor, which was also visible from the static domain images (not shown).

The domain states, at the position of 1/3 length of the sensor from the tip, show a different behavior. At the edge (Figure 50(a)) the domains are comparatively large and sustain their size throughout the modulation. The stress is insufficient to cause significant shape change of domains, but does induce a fair amount of magnetization turning. Highest change of magnetization is visible at 0.9 µs excitation time. Despite the relatively stable size of the domains, their position occasionally changes through the modulation, which seems to be of statistical nature. The reason for the ambiguous state is most probably the variation in the domain states residing in the middle of the sensor, which form due to the large saturating K_σ. The stress changing domains are clearly represented in Figure 50(b).

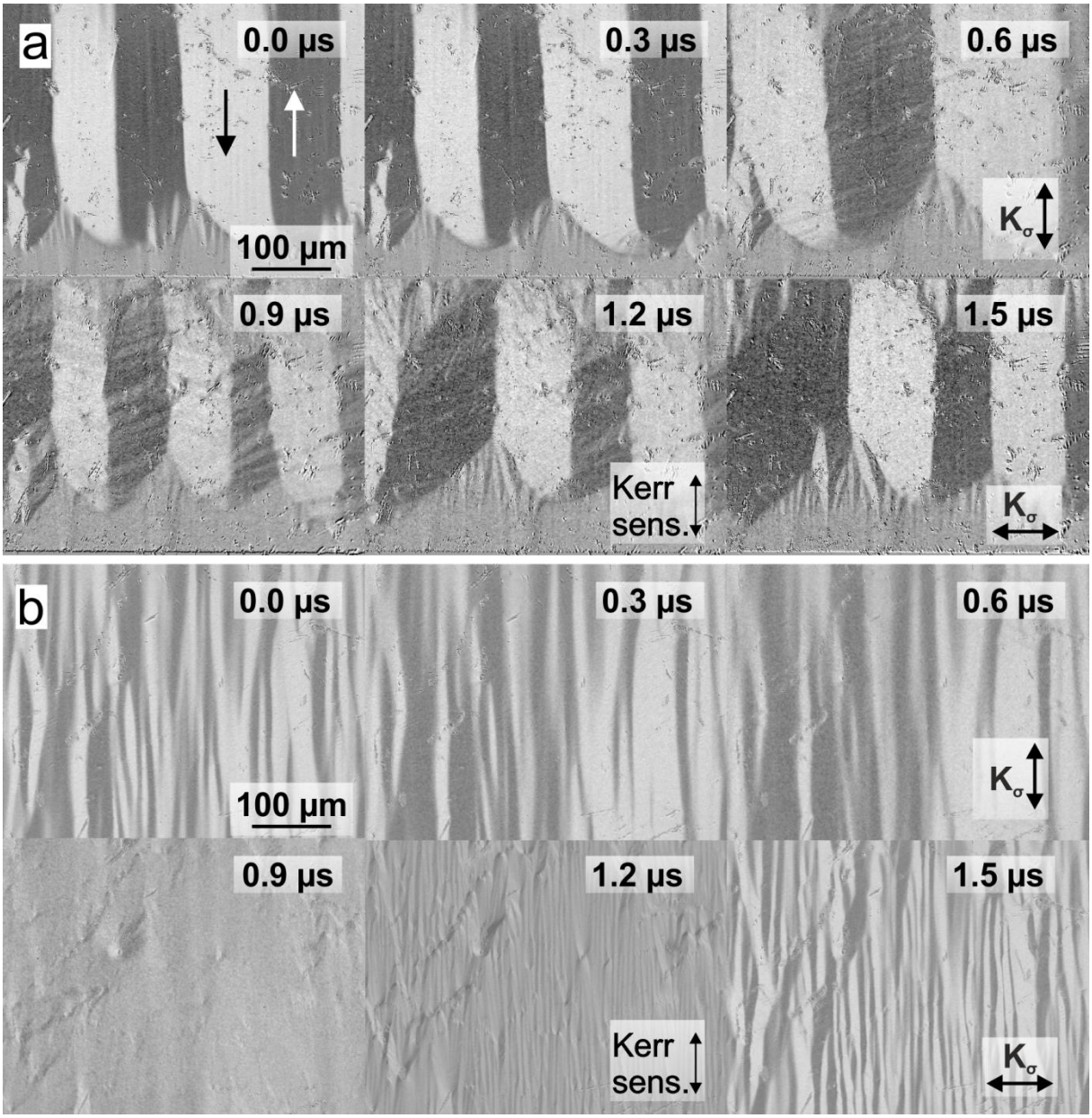

Figure 50: (a) Domain evolution through one cycle of excitation with 3 Vpp amplitude. The position is set at the long edge of the sensor in the region of 1/3 of sensor length away from the tip. The long edge of the sensor is positioned horizontally. (b) Domain images taken at the same conditions and distance away from the tip as in (a), but in the middle with respect to the sensor's width. The expected K_σ axes are denoted. The total duration of one excitation cycle is 1.935 µs. The sensor was fabricated by Viktor Schell.

The domains from 0.0 µs to 0.6 µs show a blurred state, which corresponds to the changing positions of the domain walls from cycle to cycle at the same phase resulting from the transition from wide to narrow domain states. With the transition to the opposite phase of the excitation, the domains start forming into narrow domains aligned along the short axis (1.2 µs), which grow up until 1.5 µs. Surprisingly, in Figure 50 (b) no

modulations or domains arranged along the long axis were not observed throughout the whole modulation cycle (with this exemplar excitation). This can be explained by the fact, that the narrow domains lock the domain formation due to local H_{str} interaction of these domains. From this state, the modulations of these domains occur in a short time period and with it a delayed swift magnetization change occurs (from 0.6 µs to 0.9 µs and from 0.9 µs to 1.2 µs). Due to this, the contrast is blurred out as the switching region can form domains at a random position and size. These results confirm the overall domain behavior of the edge from the figures before, as the time sections of the two regions strongly correlate. Furthermore, these time sections also show the connection to the agglomerated states observed in the overview measurements.

The domain images discussed so far are only representative for the 3 Vpp excitation amplitude. The sensors were investigated with a variety of excitation amplitudes and selected results are given in Supp. 13. From this data, a clear evolution of the states at a certain position can be resolved for various excitation amplitudes with emphasis on the phase forming perpendicular induced stress to K_u. With small amplitudes (0.5 Vpp to 1.5 Vpp) the domain state hardly changes indicating only minute changes in the magnetization and few stress induced domain formations. From the 2 Vpp excitation onwards, the domain state then significantly changes. At 2 Vpp, the wide domain states form which persist throughout the excitation. It needs to be indicated, that the domain state before the excitation activation is formed in the same manner and newly reinitialized for each excitation amplitude as to allow similar beginning conditions for the evolution of the domain states. This allows minimal discrepancies for the analysis, as the beginning state is the same for all measurements. At 2.5 Vpp excitation, the wide domain state seems to be not visible anymore and the images indicate only greyed and blurred-out domain states. This indicates that there is high instability of the domain construct which forms from cycle to cycle into a different state (similar to swift moving domains) causing the resulting stroboscopic images to form. The second state into which the wide domains switch can be seen in the evolution with 3 Vpp and 3.5 Vpp excitation amplitude. The state is comprised of a curved narrow-banded domain structure, which still holds the magnetization aligned along the short axis, the same as seen in Figure 50(b). By comparing the state at 1 µs for the two large amplitudes, it shows that the reproducibility of the same domain construct is higher with increasing excitation amplitude. The more clearly visible state shows the separation of the domains that forms at the middle. The

sudden ending of the domains in the middle and curved form is related to the gradient stress with the maximum in the middle.

The analysis of the domain changes with the operation of the sensor in U2 mode gives an indication of a similar response with stress compared to the observations in U1. The domain evolution from Figure 51(a)-(b) indicates the transition from the domains oriented along the short axis towards a highly modulated domain state with the magnetization lying along the long axis. For the U2 mode it seems the stress-induced modulations are stronger compared to the U1 mode. The states at 0.3 µs explicitly show the modulation effect on the previously inhabited domain structure. The modulations expand from the walls and form a fir tree pattern. Similar domain structures with externally applied stress on soft magnetic thin films have been reported by McCord et al. [103]. With larger stresses (0.6 µs) the magnetization is strongly turned close to 90° from the beginning magnetization direction. Due to the sufficiently large anisotropy, the modulations enlarge into banded domains and nearly omit the previous domain construct (still slightly visible with MO sensitivity along short axis). Further on through the excitation, the K_σ is formed with K_u, which once more leads to the beginning domain state. The modulated structure at first seems to be counteracting the behavior of the domains seen for the U1 mode. In reality, the same state occurs at 2.5 Vpp excitation amplitude, where the grayed-out contrast is visible (Supp. 13). However, due to the larger stress gradient for the U1 mode, the transition from the regular short axis domain orientation to the perpendicular one occurs at a very narrow time range. For this reason, in the previous images such structures could not be visualized. This then also proves that despite the different excitation modes, the behavior of the domains is similar. The magnetization change occurs by the anisotropy modulation with the applied stress, which also induces a different noise behavior.

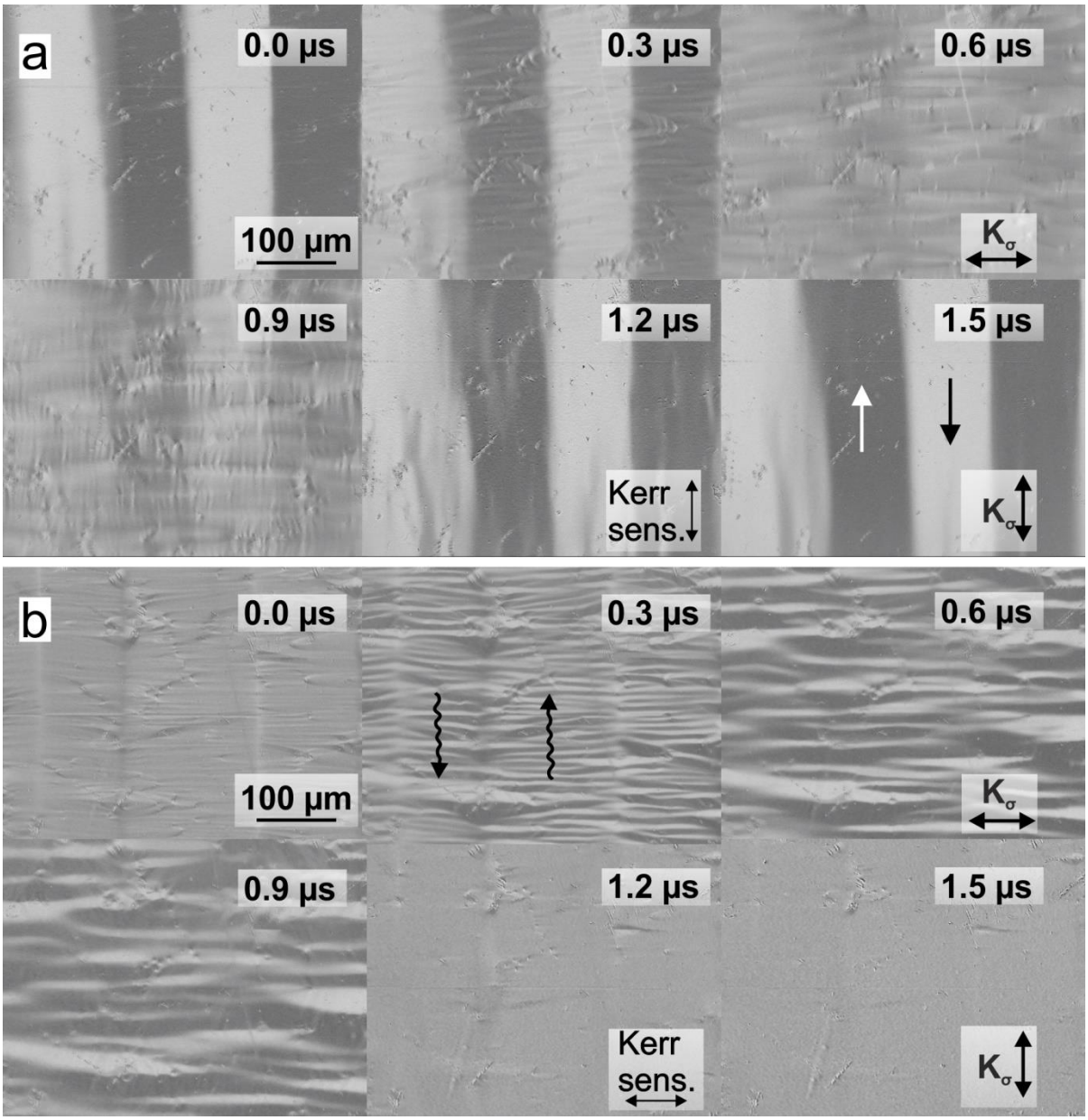

Figure 51: (a) Domain evolution through one cycle of excitation with 3 Vpp amplitude. The position is set in the region of 1/2 of sensor length, in the middle of the sensor. The long edge of the sensor is positioned vertically. (b) Domain images of the same region at the same time steps as in (a), but with 90° rotated MO sensitivity. The expected K_σ axes are denoted. The total duration of one excitation cycle is 1.920 µs. The sensor was fabricated by Viktor Schell.

In contrast to MFC, the domains barely show any noise inducing formations at the edge of the sensor, but instead the middle part exerts the largest domain wall movement and domain changes. Consequently, the different noise formation also leads to the independency to the stress relaxation effects, as the domain state at the edge has little influence on the sensor's response. In addition, the noise formation is dominated by the

development of the local modulations, which produce noise through the incoherent and dissimilar magnetization change near the modulation structures. The relation of the modulations with the noise rise in these sensors has been seen by preliminary measurements, where the driving amplitude at which the electrically measured noise response started to rise matched with the magnetic states at which the modulations started to form. However, more thorough measurements need to be performed to conclude this with certainty. With that in mind, the sensors should in principle produce less noise with the electrical modulation, compared to the MFC method.

The main reason for such expectation is that the noise formation occurs by the gradual formation of the modulations. Whereas with MFC the main noise mechanism is the movement of domain walls and collapse of domain structures, which is expected to cause larger abrupt changes in the magnetization. Furthermore, it is also expected that the EB sensors will be very advantageous for this method, since the EB can easily withhold the domain changes in the middle of the sensor. This would then allow the magnetization to turn with the induced stress without the formation of strong modulation in the domain construct.

8.3 Exchange biased sensors

With the evaluation of both modes with the single layer sensor, it was clear that the modulation formations needed to be rendered to gain the best noise performance with these excitation modes (from the magnetic point of view). For this reason, the developed sensors presented and discussed in Chapters 5-7, were measured by the electrical modulation scheme. The sensors were evaluated only with the U1 mode as this mode has shown a larger single response [61] and similar domain (noise) behavior as the U2 mode. The evolution of the magnetics of a 4 µm 90/110 PEB sensor and a 4 µm 500 APEB sensor is presented in Figure 52(a) and (b) correspondingly. Intentionally a PEB sensor with preexisting modulation in the magnetic construct was chosen, in order to see the effect of the stress on these complementary structures. From the evolution of the PEB sensor, a clear correlation with the single layer behavior can be seen. The change of the magnetic state occurs by rotating the local magnetization structures along the axis of the generated stress. The preferred orientation of the magnetization of the modulations along the long axis as well as the misaligned orientation of the EB is also confirmed from

the evolution. This can be seen by the density reduction of the modulation when the stress is formed along the long axis (0.3 µs and 0.6 µs). The less dense modulations also preferentially grow with the domain character aligned closer to the direction of the misaligned EB. Furthermore, the growth of the modulations leads to the extension of the domains near the domain walls as a result of the K_σ overcoming the local EB. The domains preferentially grow with the orientation of the domain wall, which occurs due to the reduction of the magnetostrictive-self energy and leads to stronger demagnetization effect. The directionality of the growth is induced once more because of the misaligned EB towards one direction of the long axis. With the opposite phase of the excitation cycle the modulations alter and nucleate back to the original form. With further stress along the short axis, the modulations become increasingly denser and their magnetization tends to turn towards the stress axis. In the larger white domain region, the modulations also become undetectable giving a hint of the dominance by the sum of stress energy and anisotropy energy over the self-magnetostrictive energy.

With the analysis of the APEB sensors, the obtained results are positive in terms of the noise performance. With the APEB 90/110 sensors, there was no domain wall motion, even at the stress relaxation zone. The downside of these sensors was the determined lower response as the anisotropy change with stress is significantly reduced compared to the single layer sensor. For this reason, the APEB 500 sensors were evaluated using the electrical modulation technique. From the domain evolution in Figure 52(b), the clear formation of modulations with higher stress along the long axis is visible. Additionally, the magnetization orientation can be determined by the orientation of the modulations, which allow interpreting the amount of rotation of the magnetization.

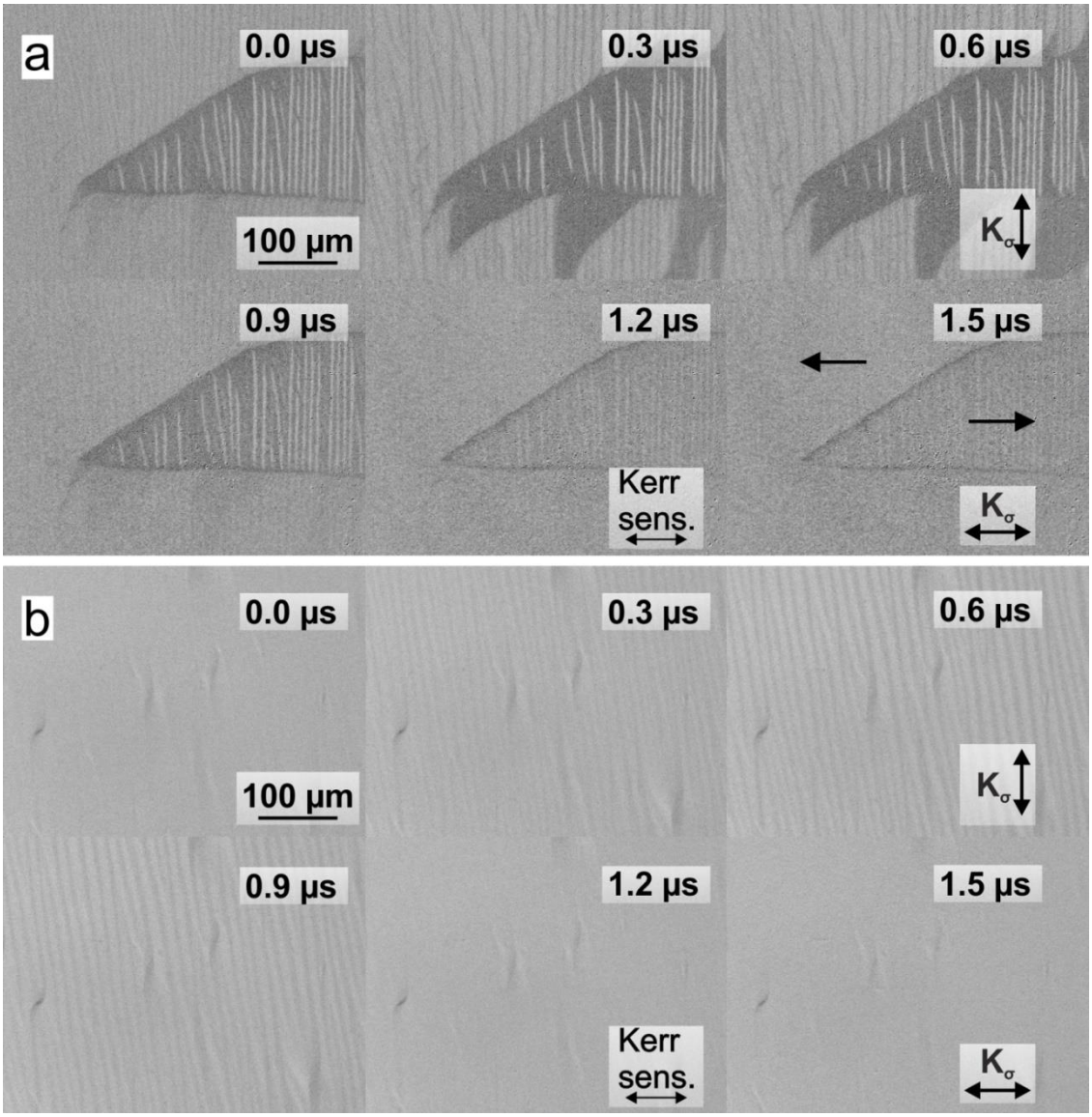

Figure 52: (a) Domain evolution of a 4 µm 90/110 PEB sensor through one cycle of excitation with 7 Vpp amplitude. The position is set in the region of 1/2 of sensor length, close to the long edge of the sensor. The long edge of the sensor is positioned vertically. The total duration of one excitation cycle is 1.949 µs. (b) Domain evolution of a 4 µm 500 APEB sensor through one cycle of excitation with 4 Vpp amplitude. The position is set in the region of 1/2 of sensor length, close to the long edge of the sensor. The long edge of the sensor is positioned vertically. The total duration of one excitation cycle is 1.946 µs. The sensor was fabricated by Viktor Schell.

Besides the occurrence of the modulations, the sensor exhibits no additional noise sources or instantaneous incoherent domain changes, despite the high excitation amplitude of 7 Vpp. Such minute changes prove the hypothesis that the APEB sensors should exert an even better signal to noise ratio compared to the MFC technique. The main advantage of this technique is the small influence on the edge, which is strongly

influenced by the excitation with MFC. For this reason, the APEB 500 sensors are very usable with this technique and still show the possibility to use systems with even weaker EB-field (further increase of FM layer or manipulating the thickness of the AFM to reduce the EB-field). From this then the question arises on the sensor's response evaluated with electrical characterization. This analysis has been partially done on the EB sensors and still needs further proper measurements to have a decisive conclusion on this matter. Nevertheless, a clear improvement of the noise floor and behavior of it is visible by comparing the frequency spectrums of an APEB sensor and single layer sensor at a comparable excitation voltage (Figure 53). With first trial APEB 500 sensor with a total t_{FM} of 4 µm an already record breaking LOD of 30 pT/Hz$^{1/2}$ at 10 Hz and 40 pT/Hz$^{1/2}$ at 2 Hz was achieved. Such values show the tremendous potential, not only of the APEB sensors, but also of the electrical modulation scheme.

The further in-depth analysis of this method for all the discussed sensors will be presented by Patrick Hayes, who has developed the method to this point. Patrick has conducted all the electrical measurements with the electrically modulated technique presented in Figure 53.

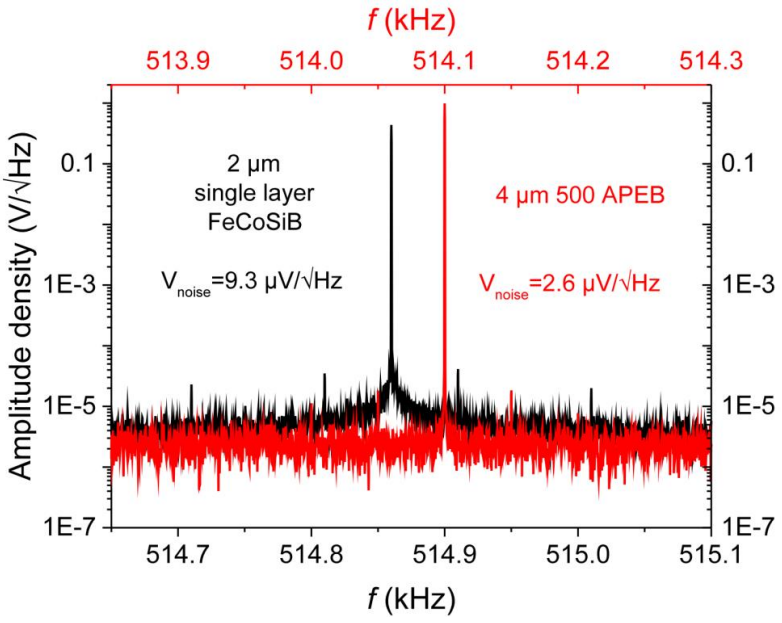

Figure 53: Frequency spectrums of a 2 µm single layer sensor and 4 µm 500 APEB sensor. The sensors were excited with comparable excitation voltages. The noise values are determined by the average signal exerted in a region near the carrier signal with a width of 30-50 Hz. The measurements were performed by Patrick Hayes.

8.4 Magnetization modulation interpretation

Based on the observations in the previous section, the domain evolutions give the means to understand the modulated structure of the PEB for individual thick PEB sensors in section 5.1.1. The periodic modulations are confirmed to be a result of the self-magnetostriction effect. The self-magnetostriction forms these bands near the edge in order to compensate the mismatch in the domains caused by superimposed anisotropies of the system formed by the stress relaxation and K_u. The modulations, which penetrate across the whole sensor with the conserved width and angle of modulated magnetization, are related to the EB. To understand this effect, the interpretation of the single layer system is firstly provided.

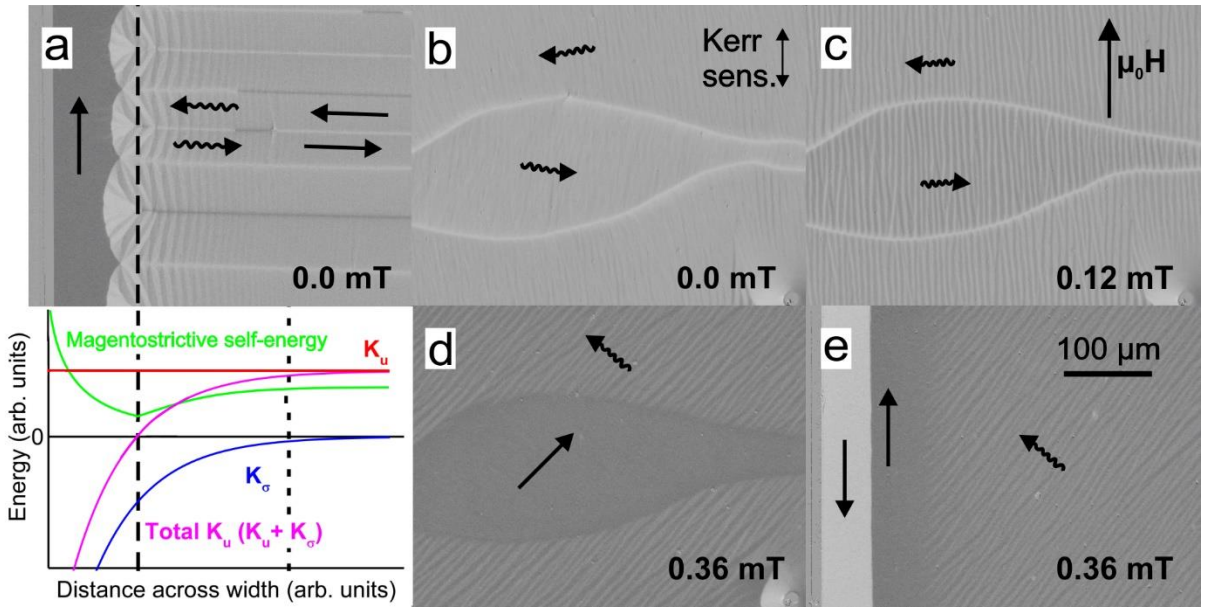

Figure 54: **(a)** Domain image of a single layer sensor at zero applied magnetic field accompanied by a diagram depicting the change of individual energy density terms across the width of the sensor (limited to the size of image). The total anisotropy energy density is also given for easier interpretation of the effects. The dark line in the middle represents the zero energy level. The critical transition borders are marked with dashed lines. With longer dashes, the equivalence of the K_σ and K_u energies is marked. The short-dashed line indicates the threshold level from which the magnetostriction self-energy is insufficient to modulate the magnetization. The graph indicates the absolute value relations of the energy densities. The diagram is only a depiction of the approximate evolution and does not represent actual values. **(b)** Domain image of a 4 μm 90/110 PEB sensor displaying a tilt in the EB and a tilted modulated domain structure. **(c)** With the application of a correction field along the long axis, the domains orient along the short axis and the modulation form in the size as seen with well-oriented PEB sensors. **(d)** and **(e)** depict the formation of

secondary modulations at higher fields which form across the whole sample ((**d**) middle of sensor, (**e**) edge of sensor). The sensors were fabricated by Lars Thormählen.

The modulation formation effect is exerted by the transfer of the stress caused by the mismatch between neighboring domains formed by magnetostriction at the regions where K_σ and K_u are similar in magnitude. For this thinking experiment, it is assumed that the domains are formed uniformly near the stress relaxation zone and that the stress transfer is linearly decreasing with increasing distance from the edge. Considering the single layer is released from any field, the typical domain structure will form (Figure 54(a)). Now, if a single domain modulation is assumed to form near the compensation position (where K_σ is same as K_u energy), the transfer of the stress will be related to the magnetostriction energy and the angle of the turned magnetization from the bulk domain magnetization orientation. The next formed domain due to the imposed stress of the first domain relates a similar form, however due to the increased dominance of K_u (K_σ is reduced), the domain exerts a smaller width. With the smaller width, the self-magnetostriction energy increases. The sum of the energies results in a decreased magnetization turning in the modulation. Furthermore, the modulations will become thinner and respectively exert a smaller magnetization change further away from the physical edge. For a clearer understanding of the energy effects on the sensors, a sketch of a diagram with the approximate evolution of the energy densities across the width of a sensor is depicted underneath the micrograph in Figure 54(a).

With keeping all these interactions in mind, the PEB modulations can be interpreted. The main difference between the single layer and the EB sensor is the multilayer structure and the presence of the EB system (AFM). It is assumed, that with the heating procedure, to set the EB, a stress state is imposed into the magnetic system. With the saturation of the FM layers, the H_{dem} is formed internally that continuously counteract the saturated state. In addition, the stress relaxation state forms, which causes stress build-up at the edges. With both of these effects, the magnetostriction self-energy continuously tries to compensate the formed mismatch by imposing internal stress to the structure. The stress is homogeneous as it relates to the effective field and the K_u, which are constant in the center of the sensor. It is clear, that this newly generated stress transfers itself to the AFM structure effectively changing the AFM magnetic ordering [125]. As a result, the EB inherits it by locally changing its structure into a modulated state. With the newly formed internal structure in the EB, the domain state is imprinted onto the low-anisotropy FM layer.

This behavior explains the reason for the consistent width of the modulations across the bulk of the sensor. The modulations only increase in width close to the structural edge as the relaxed stress starts to overcome the sum of K_u and EB. This effect can be also seen, when a larger misorientation of the EB from the short axis is attained near the edge, at which the modulations in the middle are significantly thinner, similar size as ripple constructs (Figure 54(b)). However, with the application of a field along the long axis, a domain construct in a form of thin lancets is exerted from the edge and protrude through the whole sensor (Figure 54(d)-(e)). The structure forms only at a small field range and direction, which seems to be related to the EB tilt. These growths form, because the H_{dem} effectively follows the magnetization direction and compensates the EB by turning the magnetization by the EB mismatch angle. In addition, with very small fields applied along the long axis (only one direction) the modulations become thicker, similar to the size as observed for the sensor with a well-oriented EB (Figure 54(c)). The reason is that the external field compensates the field component of EB that is aligned along the long axis. This then effectively generates a state similar to the one of the well-aligned EB sensor. From this it can be concluded, that a very well defined EB orientation is needed in order to elude such secondary formation of the modulations and domain structures. In the end it is also clear, that in order to prevent the formation of modulations either a stronger EB is needed (only applicable for the PEB case) or a material with larger K_u in order to compensate the self-magnetostriction energy effects.

As it was seen, the effects of the stress relaxation as well as the H_{dem} develop significant hindrance for the sensors to reach low noise behavior. For this reason, in this project a series of edge structured samples were developed in order to dismay such effects. The various structures and the effect of these on the domain construct are described in the next chapter.

Chapter 9

Edge and shape patterning

As has been discussed thoroughly in the previous chapters, stress relaxation can have a significant negative impact on the magnetic configuration and domain behavior of the magnetic layers. For this reason, this work also focused on counteracting this problem by edge manipulation through patterning. Different shapes of edges can allow manipulation of local shape anisotropy and H_{dem} as well as the flow of the relaxed stress. In the following parts of this chapter, selected structures are presented that showed the most promising results with different magnetic stacks. The assessment of the effect of the structures was conducted by patterning a 4 µm thick FeCoSiB single layer, which provided the basic understanding of the edge effects and the domain structure change without any special interlayer coupling present. Finally, the same EB stack as before (90/110 system) with a total t_{FM} of 4 µm in a PEB form was employed for the patterning and was investigated using MOKE. At this time, the reader is advised to review sections 4.1-4.3, which explain the stress effects of a non-structured edge, as the phenomena discussed there are used for the explanation of the structured edges and the effects that come with them.

9.1 Structures overview

Before the domain analysis of the various structures is presented, the design and the physical structures are firstly revised. In Figure 55(a), the blueprint of the structures used for the production of the lithographic mask is depicted. The whole design is sectioned into 9 chips which hold different structures for analysis of various shape effects as well as structures for the analysis of the magnetic material with different methods. Chip 1 holds rectangular elements with various lancet edge structures (example in Figure 55(b)) as well as sample structures that are devised for heating experiments in a vacuum tube system. Furthermore, the chip has structures that are used to analyze shape effect of tips and oval structure shapes (Figure 55(e)). Chip 2 holds a large circle with a diameter of 15 mm in order to analyze the deposited material with induction magnetometry. Chip 3 holds rectangular elements with various edge structures of saw shape and oval-tooth shape. Examples of both types are presented in Figure 55(c). In addition, the chip also holds rectangular elements with various insets near the edge (example in Figure 55(d)). Chip 4 holds the standard rectangular structure (15 mm x 1.25 mm) with various tilts with respect to the vertical axis (±5°, ±10° and ±15°). The chip 5 holds various rectangular structures in order to investigate the size and aspect ratio effects. Chip 6 holds additional rectangular elements with inset structures near edge as well as rectangular elements with the same standard length, but with the varying width in order to vary the demagnetization effect. Chip 7 holds rectangular elements tilted at a 45° angle and varying length in order to indicate demagnetization effects with anisotropies aligned under a large angle to the long axis of the element. Chip 8 has triangular shaped elements of the standard length and bottom width equal to the standard width. The triangles are positioned in both vertical directions under the angles 0°, ±5°, ±10° and ±15°. The final 9th chip holds ring structures that allow the indication of demagnetization effects mimicking infinitely long structures with the effect of stress relaxation through the different widths. The chip also holds circular structures of various diameters allowing the analysis of the overall anisotropy without demagnetization effects. In addition, the chip also inhibits a circular structure of 5 mm diameter for VSM measurements.

For the purpose of this research, the chips 1, 3 and 6 were used as these hold all the elements with the various structured edges. It is important to mention that each element

holds two sets of edge structures, which are positioned in the vertical halves of the individual element. In the nomenclature of the structures, they will be noted as up and down of the numerated element. The numeration of the elements is done by indicating the chip number and the position of the element on the chip from left to right. In total, there are 16 elements with 32 different edge and inset structures. All the structures with their dimensions are given in the Appendix as Supp. 14 and Supp. 15.

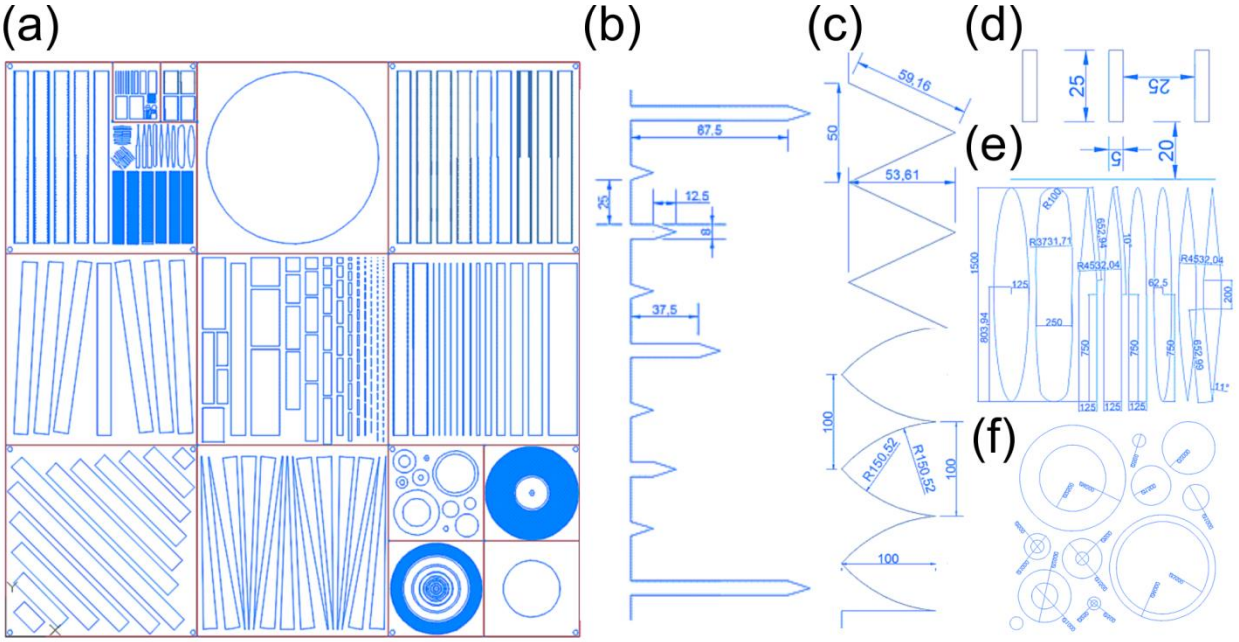

Figure 55: **(a)** Blueprint of all the structures design. Individual chips are sections by the red line and marked with a number. **(b)** Example of a lancet edge structure. **(c)** Example of triangle and rounded edge structure. **(d)** Example of an insert structure. The line below depicts the structure edge. **(e)** Structures for evaluating tip shape effect. **(f)** Ring and circle structures for anisotropy and stress relaxation evaluation. The dimensions are given in µm.

The structures were patterned with the same process as described already in section 5.1. In order to fully comprehend the extent of influence of the edge on the magnetic structure, the structures were investigated by scanning electron microscopy (SEM). This way the patterned structures can be compared to the design and indicate specific changes of the structures that occur due to limitations from the lithographic and etching process. Additionally, a sample was broken after the finished MOKE analysis, in order to determine the thickness profile and side edge structure. The SEM images of the patterned structures of a 4 µm thick FeCoSiB are displayed in Figure 56. The thickness profiles of both concave and convex edges are displayed in Figure 56(a) and Figure 56(c) respectively.

Both profiles indicate a smooth inclined (about 22°) edge profile and a good adhesion of the thin layer to the substrate. The convex edge indicates a slightly more bulged profile at which it also shows band-like formations across the curvature of the structure, of which the origin is unknown. In addition, the edges indicate a step-like formation at the top of the layer, which is developed due to under etching (Figure 56(d)). The effect of the etching process on the shape and dimensions of the structured edges is displayed in Figure 56(e)-(f). For the curved edge shape in Figure 56(e) the dimensions and shape are within the range of the schematic (Figure 55(c) down). The displacement of the peaks is exactly 100 µm as in the schematic, however, the height of the structures is lower compared to the schematic. This is attributed to the rounding of the tips and edges, which lead to a too low etching of the concave corners and too high etching of the convex corners. In addition, the etching of the concave corners does not form a sharp corner as wanted. This could potentially lead to an anisotropy rotation along the long axis near the corner, which was thought to be avoided with the sharp corner structure.

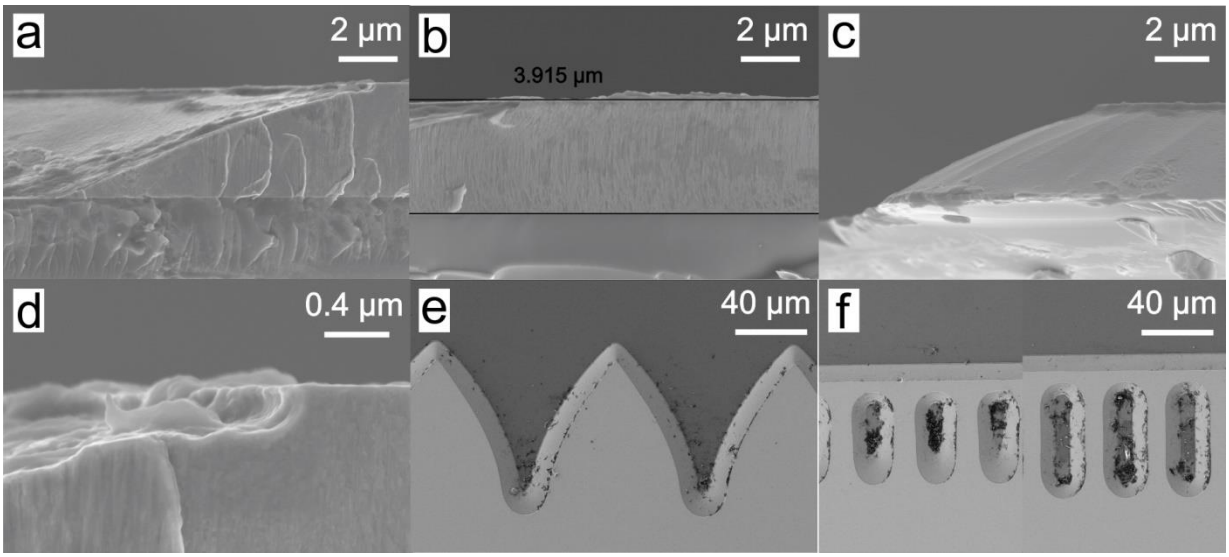

Figure 56: **(a)** Cross section of a concave edge indicating the gradual slope formed from the etching process and the good adhesion of the thin film onto the substrate. **(b)** The side-view of the edge indicating the thickness profile of the thin film and the measured thickness of it. **(c)** Edge profile of a convex edge displaying a clean edge with a step-like feature formed on the top of the layer as a result of under etching. **(d)** Enlargement of the step-like formation on the top of the layer as a result of under etching. **(e)** Top view of a rounded edge structure showing the effect of the etching process. **(f)** Two images of a triangle and rectangle insert structures showing the effect of etching. The SEM investigation was conducted together with Lars Thormählen, who operated the SEM.

For the insert structures, (Figure 56 (f)) the patterned structures deviate much more strongly to the schematic. The 50 µm long and 10 µm wide triangle structures (left part of

the image) and the 50 µm long and 10 µm wide rectangle structures (right part of the image) have a strong rounded shape of the tips and corners. Additionally, the desired structure is the hollow part inside and matches well in terms of the planned dimensions for the rectangular shapes. Nevertheless, because of the edge profile, the structures are in principle larger as the edge expands the effect of the structures. Moreover, for the triangle structures the tips are severely cut off. This leads to a distorted shape, effectively creating much shorter elements than intended. From these measurements, deviations from the etching process are also identifiable, at which the highest impact is seen for the insert structures. Despite this, the general form is withheld and it is expected that the shape effects will manipulate the domain structure in an anticipate fashion.

In the next sections, example structures will be presented and discussed which represent the general behavior of a group of structures with similar features. The evaluation will be done simultaneously on single layer and multilayer stack with EB.

9.2 Rounded edge structures

The first structures discussed are the rounded edge structures. They are designed in order to curve the stress relaxation near the edge allowing a smooth transition of the anisotropy from one axis to another. Within this group, the most promising structures are the half-circular structure and the bullet-shaped structure. The latter is presented in Supp. 16 and Supp. 17, as both structures provide similar influence on the domain construct. The half-circle structures were designed based on the average width and shape of the closure domains that form in a non-patterned sample thus mimicking their flux closure effect. The patterned single layer system shows a clear coupling of the regular domains to the edge structure. With the transition from the saturated state, the typical blocked domain state forms (Figure 57(a)). However, the domains are bulged toward the corner of the structures, which is a result of the effectively rotating anisotropy near the structure corner. From the structure, also an array of fixated domain walls forms and progresses deeply into the layer, which forms due to the bipolar character of the half-circle structure. With further decrease of field, the blocked state collapses into a wider 180° domain state, which shows the preferential growth and orientation with the patterned structure (Figure 57(b)).

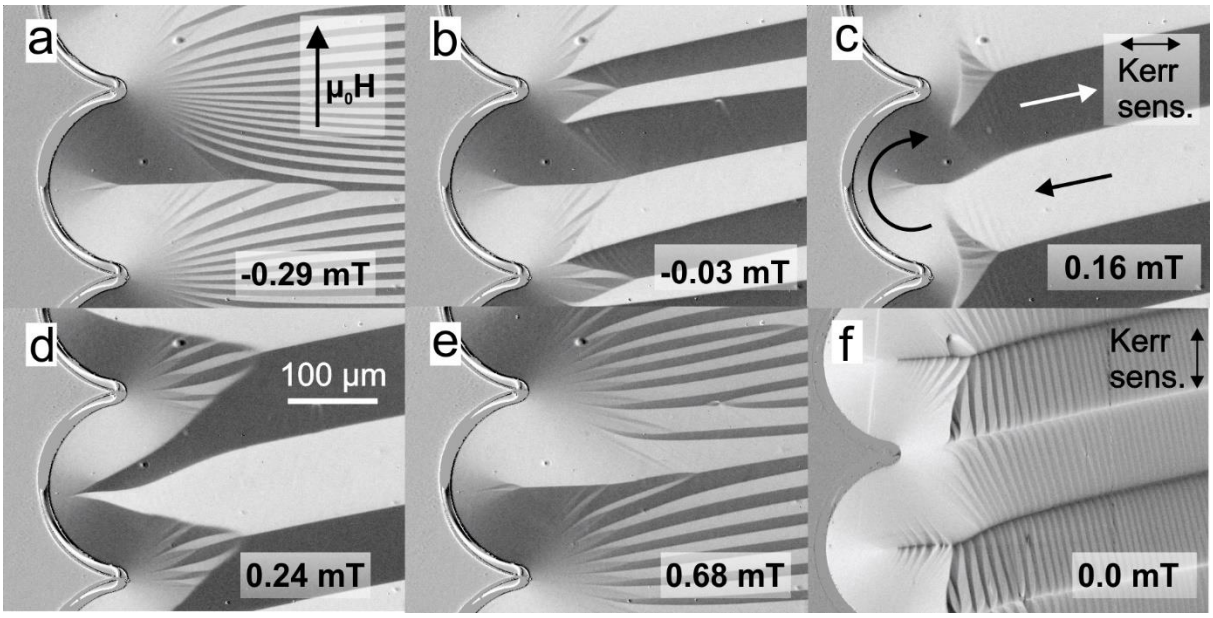

Figure 57: **(a)-(e)** Evolution of domain states with applied magnetic field along the long axis for the half-circular edge pattern of a single layer system. **(f)** Image with MO sensitivity along the long axis, indicating the directional character of the edge and modulated structure inside the 180° domains. The sample was fabricated by Rahel Kruppe.

After the zero crossing of the field, the domain construct rearranges in order to develop a periodic domain structure following the periodicity of the edge (Figure 57(c)). This is formed due to the large curvature of the edge element, which allows the magnetization of a domain to rotate gradually near the structure and couple directly to the adjacent antiparallel domain. This in turn creates a tight flux closure that reduces the overall energy state of the domain state. Such construct is exactly what is aimed for, as it counteracts the excessive formation of closure and supplementary domains. In addition, it also reduces the effective area of the turned anisotropy along the long axis formed due to stress relaxation. Nevertheless, the domain state is not considerably stable, as with further field application, the edge magnetization switches leading to an abrupt domain restructuring (Figure 57(d)). The domains, however, still follow the edge shape and with further field application, the domains recess towards the bulk with narrower domain width (Figure 57(e)). Surprisingly, the domain states have an inherent strong modulation of the magnetization inside the 180° domains, which is explicitly visible in Figure 57(f). The modulations are a result of the magnetostriction self-energy formed due to the low K_u of the ferromagnetic layer. Interestingly a bright contrast is visible near the edge, indicating a continuous magnetization flow along one direction in the vertical axis. From this behavior, a clear tendency of domain tailoring is visible and it indicates the possibility

for forming a domain structure with a significantly reduced formation of closure domains for the PEB layer.

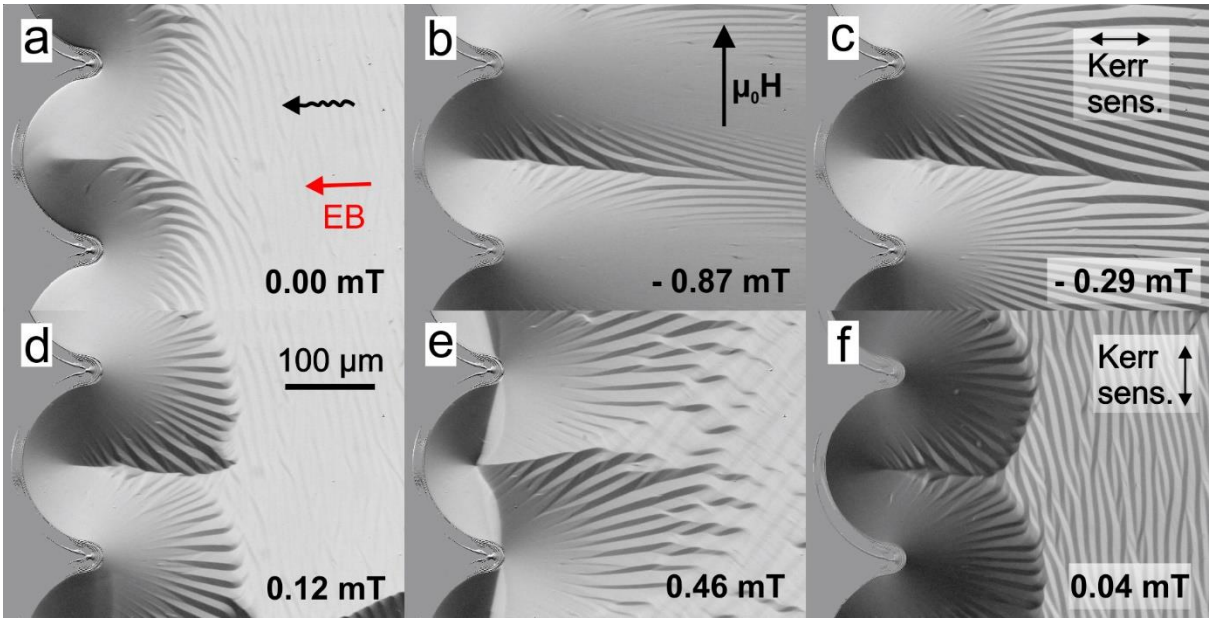

Figure 58: **(a)** Demagnetized domain state of a half-circular edge structure of a PEB layer system. The magnetization direction is portrayed by the black curved arrow. The direction of EB-field is marked by the red arrow (the EB alignment is about 2° off from the sample's short axis) **(b)-(e)** Evolution of domain states with applied magnetic field along the long axis. **(f)** Image with MO sensitivity along the long axis, indicating the directional character of the edge and modulated structure. The sample was fabricated by Rahel Kruppe.

The structured PEB multilayer system shows a completely different domain structure. As for the single layer system, the edge magnetization still shows a continuous flow along one direction of the edge (Figure 58(f)). This indicates that the stress relaxation is still more preferentially formed along the long axis. Regardless, at zero magnetic fields, a preferential alignment of the magnetization along the short axis is visible (Figure 58(a)). However, with the application of an external magnetic field, the domain state resembles the structure formation as seen for the single layer system (Figure 58(c)). This is surprising, as such structures have not been observed beforehand in PEB sensors (see Chapter 5). This suggests that the EB is insufficient to form and withhold a single domain state, which is a result of the strong H_{dem}. A fascinating feature of the edge structure is the preferential nucleation of domains around the extending domain wall, which can be seen in Figure 58(b). Such behavior might pose a problem also when the EB is strong enough for counteracting the H_{dem}, as it could lead to the formation of small domain clusters making the domain construct overall unstable. When the field is reduced

towards zero, the blocked domain state transforms into a single-like domain state Figure 58(d). The state is described as such, as it is highly modulated by the magnetostriction self-energy (Figure 58(f)). The transformation is progressed with a clear wall transition from the middle towards the edge of the sensor. Such switching is considered as an effect of the coupling of the individual layers from a misaligned state to a parallel state. With further application, the domain states near the edge gradually switch onwards by the progressing switching. Nevertheless, the previously single-like domain state collapses with further increase of field into a complex domain network showing two distinct orientations (Figure 58(e)). The underlying spike structure aligned along the short axis is induced by the stress relaxation zone, whereas the second structure is related to the modulations formed by magnetostriction self-energy. The tilt of the modulations is a result of the turned magnetization.

The analysis of the effect of the half-circle edge structure on the domain structure showed a decrease of formation of complementary closure domains. Furthermore, for the single layer system a complementary closure domain structure forms, which is the sought effect to be achieved with such edges. Unfortunately, the stress relaxation zone still forms for the PEB layer. Additionally, the PEB layer shows insufficient EB strength causing a multitude of domains and modulations to form. From this it can be concluded, that such structure is applicable for single layer systems and not for the EB multilayer systems.

9.3 Triangle edge structures

For the triangle structures the effect on the domain pattern is much weaker compared to the previous structure. The structures induce an extended wall formation exerted from the midpoint of individual triangle element, which can be observed in all images in Figure 59. In the demagnetized state (Figure 59(a)), the 180° domain construct resembles that of a non-patterned edge, indicating the weak influence of the patterned edge. The evolution of domains (Figure 59(b)-(e)) with applied field along the long axis also shows very similar behavior to that of a non-patterned edge. The exception is the highly ordered and periodic blocked domain structures that hold up close to zero magnetic fields ((Figure 59(b)), when the material is brought from saturation. In comparison to the half-circle structure, the modulations in the 180° domains is much lower and is more

analogous to the non-patterned edge behavior. The reduced effect of the patterned structure is considered as a result of the higher periodicity of the elements compared to the periodicity of the 180° domains.

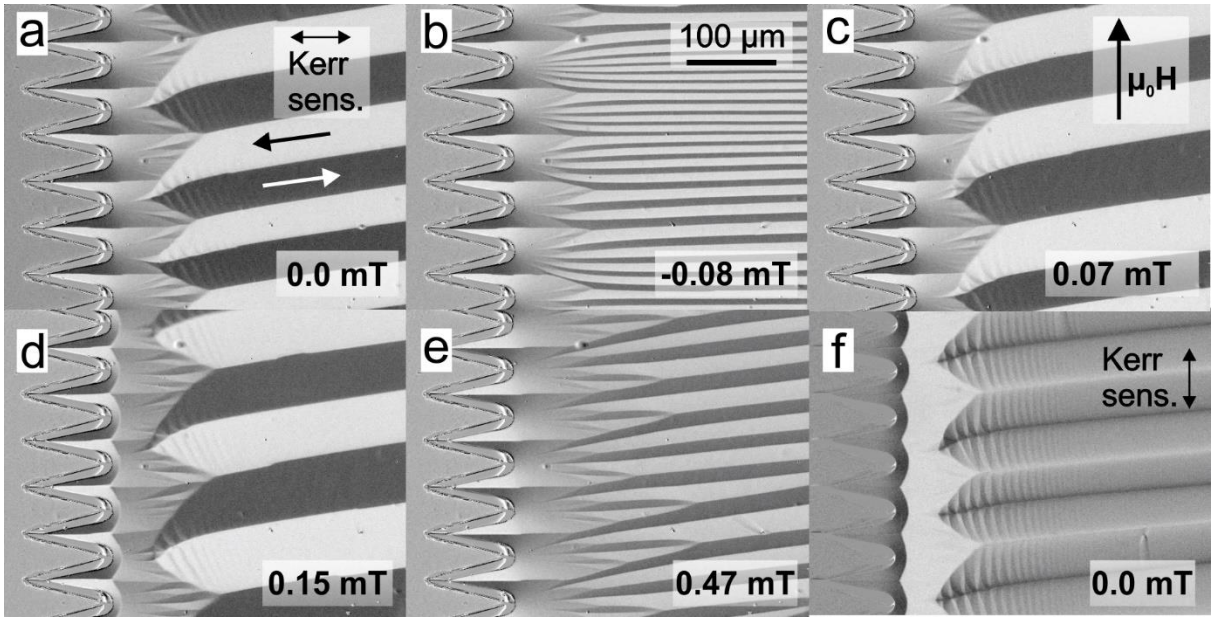

Figure 59: **(a)** Demagnetized domain state of a triangle edge structure of a single layer system. **(b)-(e)** Evolution of domain states with applied magnetic field along the long axis. **(f)** Image with MO sensitivity along the long axis, indicating the directional character of the edge and modulated structure inside the 180° domains. The sample was fabricated by Rahel Kruppe.

For the PEB system, the effects are similar as has been seen for the half-circle structure (see Supp. 18). The greatest difference is visible in the character of the collapse of the blocked domain state into the broad domain formation. A domain wall motion along the long axis drives the collapse. Such change of the transition could be related to the pinning of the domain walls as a result of the higher density of the elements creating a network of domain walls forming across the short axis. As a result, also the local collapse of the blocked domains is more complex, leading to a network of domains formed due to the shape and misaligned anisotropy/EB (Supp. 18(c)).

From the observation, it is concluded that the triangle elements are not suitable for manipulation of the edge. However, the structures could have a potential to be applicable, if the element size in width would be increased. This would allow coupling of the structure to the 180° domains as has been observed for the half-circle structures.

9.4 Lancets edge structures

The lancet edge structures were designed in order to pull the magnetization along the short axis by the elongated protruding lancets. The periodicity of the elements was set in order to mimic the periodicity of the 180° domains observed in non-patterned samples. This would allow the coupling of the domains to the structure and potentially stabilize the domain construct. In addition, shorter lancets surround the longer ones in order to reduce the stress relaxation along the long axis between the long lancets.

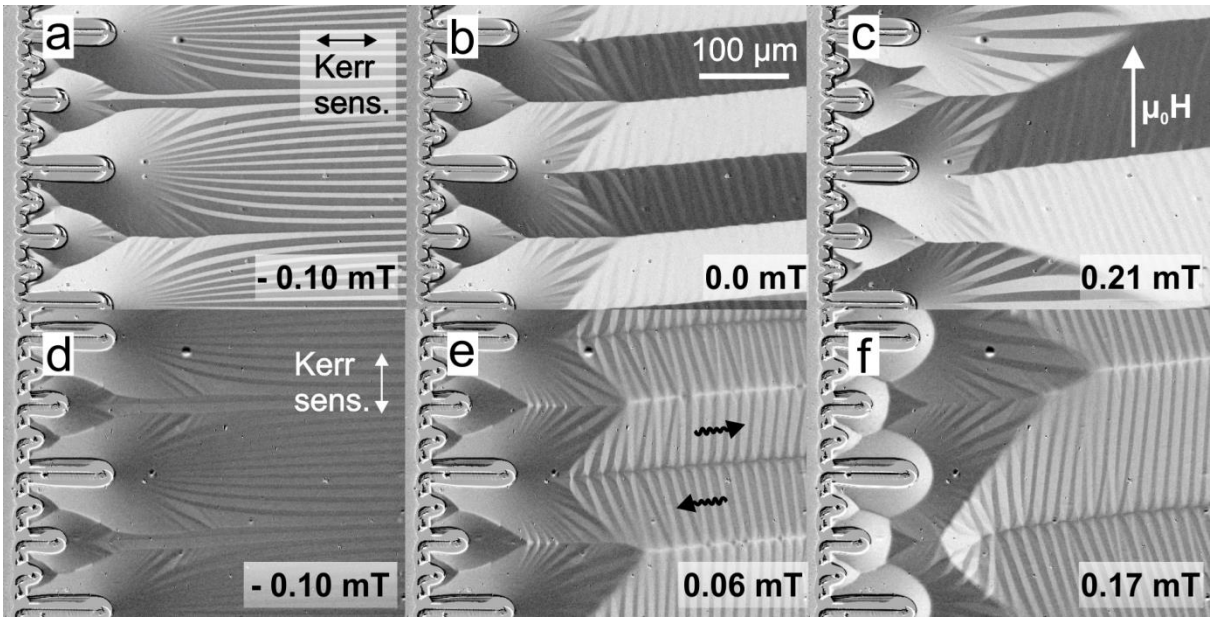

Figure 60: Evolution of domain states with applied magnetic field along the long axis for the lancet edge structure of a single layer system with the MO sensitivity along **(a)-(c)** short axis and **(d)-(f)** the long axis. The sample was fabricated by Rahel Kruppe.

The single layer shows a strong coupling of the domains to the structure. With the reduction of the applied field from saturation, the already known finely ordered blocked domains form (Figure 60(a) and (d)). The interesting effect of these structures is the formation of the extending domain wall that forms in-between the longer lancets. The wall forms because of a triangle shaped structure induced by the complementary shorter lancets due to stress relaxation. With the reduction of field to zero, the wide 180° domains form with a width corresponding to the periodicity of the edge pattern (Figure 60(b)). The transition from the blocked to the wide domains is less abrupt compared to the previous two structures, which suggest the strong influence of the edge on the domain behavior.

In addition, the 180° domains have a much stronger modulation formation (Figure 60(e)). This can be explained by the forced domain formation, which in turn forms a higher magnetization mismatch with the relaxed stress, leading to an increased magnetostriction self-energy. With the application of further field, the domain state switches near the edge and the 180° domains switch into an even wider state (Figure 60(c)). The origin of such an effect is not completely understood, but it is supposedly related to the partial switching of the stress-relaxed zone, which can be seen in Figure 60(f). The partial switching forms a halo-like domain structure that causes destabilization of the previously well-organized complex domain construct at the edge.

As it was stated before, the analysis of the domain behavior is representative for similar structures of the same character group. However, for the lancet structures a significant difference was visible from structure to structure. The clearest difference can be seen by observing the demagnetized states, which are presented for all the lancet structures in Supp. 19. The difference can be seen in the orientation of the 180° domains, which was more offset from the short axis for the structures with shorter lancets. This indicates that longer lancets are preferred as the distribution of the relaxed stress is set more along the long axis, leading to a better-aligned domain state.

For the PEB system, the lancet structure also shows a strong influence on the domain behavior. Starting from saturation the blocked domain states form, however, they do not show a uniform ordered character as for the single layer system (Figure 61(b)). Instead, a complex crossed structure forms. At higher fields (Figure 60(a)), two distinct patterns of the blocked domain states are visible. One pattern shows a much weaker contrast and it seems to originate from the domain state from the lower layer, being imprinted onto the upper layer. The interaction of both patterns results in the domain state observed at lower applied fields (Figure 60(b)-(c)). Observing the state with the other MO sensitivity (Figure 60(f)) reveals the state to have complex magnetization orientation. The contrast reveals bands of tilted magnetization, which seem to be antiparallel to each other. This shows the tendency of the domain structure to form the 180° domain construct as seen in the single layer system. With further increasing applied field, the complex structure is transformed by a wall transiting along the width of the layer (Figure 60(d)). The new state resembles the blocked state that has been observed in the single layer system. However, the overlapping secondary tilted domain structure is still present (Figure 60(d)), but with higher fields these domains disappear and the blocked domains slowly quench.

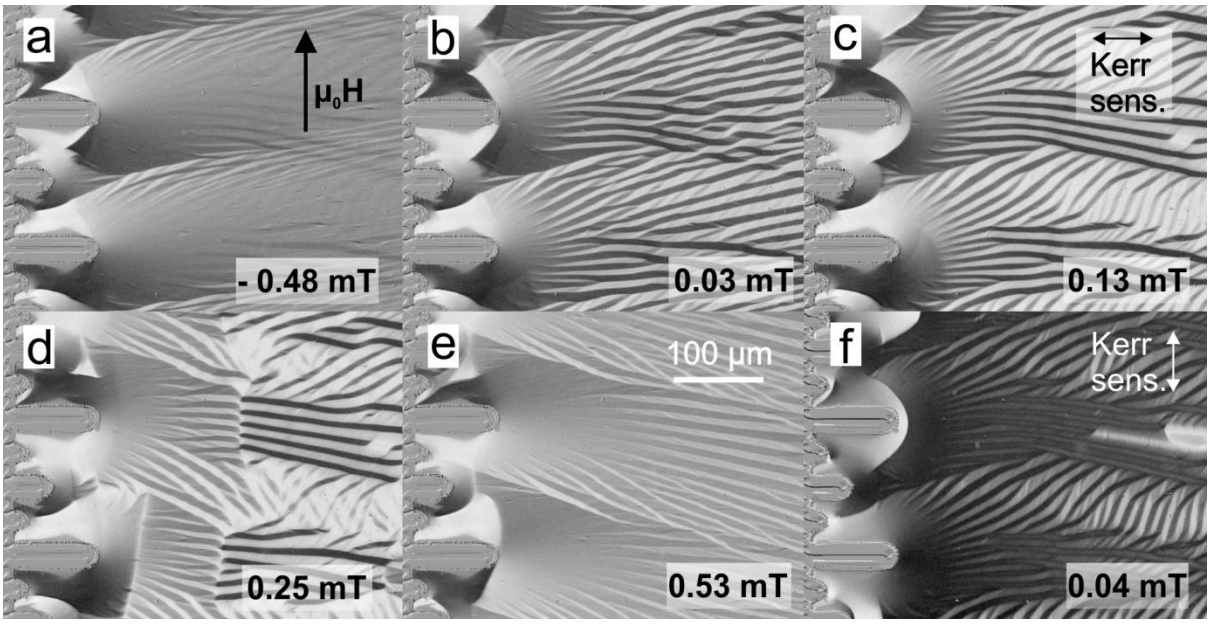

Figure 61: (a)-(e) Evolution of domain states with applied magnetic field along the long axis for the lancet edge structure of a PEB system. (f) Image with MO sensitivity along the long axis, indicating the directional character of the edge and modulated structure. The sample was fabricated by Rahel Kruppe.

From the observations it is clear, that the lancet edge structures work relatively well in terms of manipulating the domain behavior for the single layer system. For the PEB system, the structures also manipulate the domain construct and form a narrower stress relaxation zone. However, due to the insufficient EB, the domain states are plagued with modulations that seem to even couple between layers through magnetostatic coupling. For this reason, the applicability of the edge structure to the EB is not clear and would require to be tested on another sample set to indicate the potential of usage. Despite the setback, the observations did give the preference to choose lancet structures with longer lancets and with longer secondary lancets. It is also predicted that the ternary set of lancets can be omitted from future structures as they posed an inferior effect on the domain structure.

9.5 Insert structures

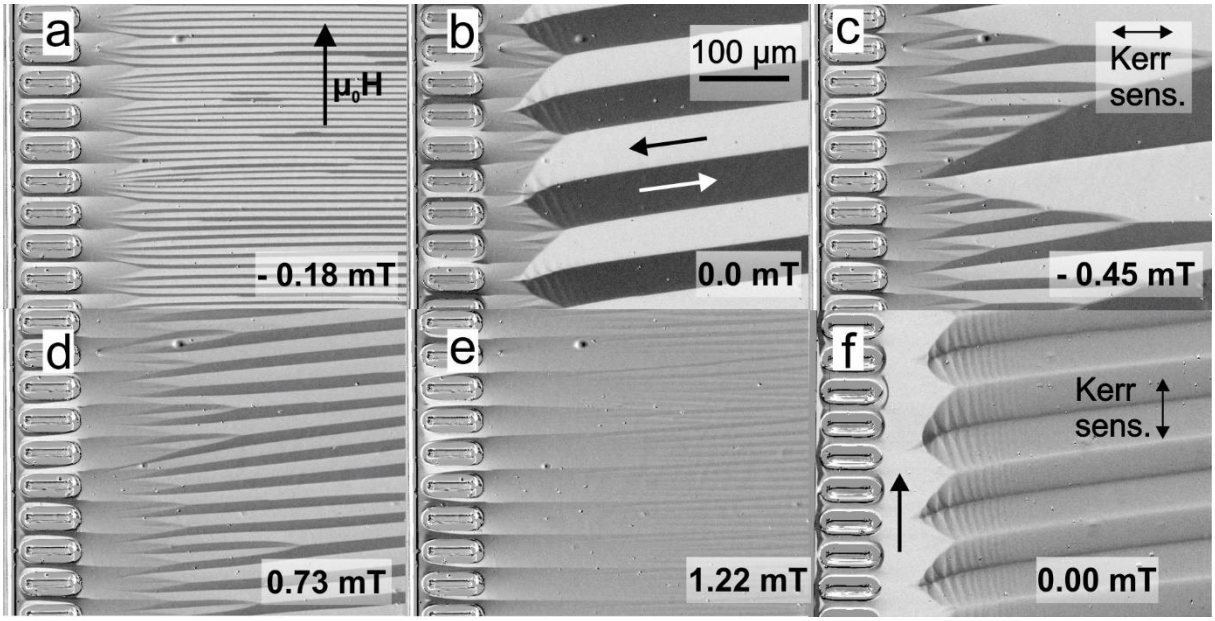

Figure 62: (a)-(e) Evolution of domain states with applied magnetic field along the long axis for the square insert structure of a single layer system. (f) Image with MO sensitivity along the long axis, indicating the directional character of the edge and modulated structure inside the 180° domains. The sample was fabricated by Rahel Kruppe.

The intention with the insert structures is to allow the stress relaxation to form along the long axis and then induce a preferential alignment of the domains with the demagnetization effects of the inserts. As can be seen from the example in Figure 62, the structure has nearly no influence on the domain behavior. The domains behave as regular non-patterned single layer sample. The only difference is the induced extended domain walls protruding in-between the structures (Figure 62(e)). The reason for the ineffectiveness of the structures is the insufficient length of the individual element as well as the too high periodicity of the elements. Based on the observations, the periodicity should be reduced by 2x to 3x and the length of the elements increased by at least 2x. The various other insert structures showed similar effects as the example here (one more example is given in Supp. 20). For the PEB system, the effect is also minimal and is very similar to the triangle-shaped edge structure. Therefore, in order to reduce redundancy, the discussion of the PEB inset structures is left out. The MOKE micrographs of the domain behavior of the PEB system are given in Supp. 21.

The inset structures have shown insignificant effect on the domain behavior, thus making them unsuitable in their current state. With the possibility of element elongation and reduced element density, the inset structures might become useful. Nevertheless, to confirm this, a new set of inset structures with the recommended alterations would need to be investigated.

9.6 Summary

From the various edge structures, it was observed, that the manipulation of the domain construct is indeed possible. With the rounded and lancet edges showing the largest influence, the sought domain coupling with the edge could be achieved. The other structures provided inferior effect on the domain behavior. However, with the proposed modifications of the structures, a stronger effect is expected to be achieved. Furthermore, through the evaluation of the structures a proposal for new structures incorporating different elements could be formulated. The two main forms for new edge structures are given in Figure 63. The new structures could possibly combine the effect of the individual edges thus providing the optimal modification of the edge and domain behavior. However, to extract the whole potential of the structures, great care has to be taken towards the lithographic and etching processes. It is essential, that the sharp corners are transferred onto the structure in order to avoid anisotropy curling from the stress relaxation around the element corner. Finally, it is crucial to test the structures on PEB samples that are not overcome directly by the H_{dem} in order to assess the real effect of the structures on the EB multilayer construct.

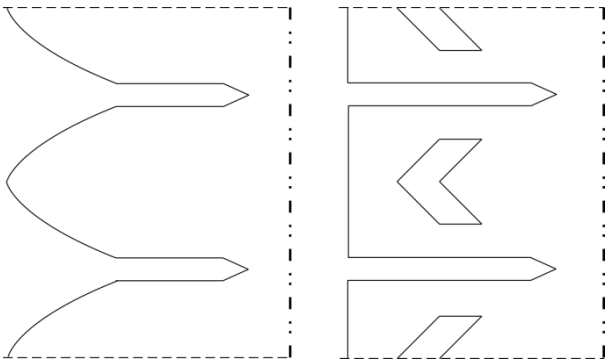

Figure 63: Two newly proposed edge structures for the manipulation of the domain behavior and stress relaxation zone.

Chapter 10

Conclusion and future work

Within this work the sensitivity of magnetoelectric (ME) composite sensors was sought to be improved. This was mainly done by improving the magnetically induced noise response of the magnetic layer. At the beginning, the standard multilayer exchange bias (EB) system was investigated and improved by an adapted heating scheme, which increases the signal yield, but did not reduce the noise response of the sensor. For this reason, a new magnetic stack system, antiparallel EB (APEB), was introduced and developed. With a convenient heating procedure, that can be performed even in ambient room conditions, a multilayered EB system can be converted into an antiparallel arranged system. The antiparallel state allows flux closure making a highly stable domain structure to form even with very high total ferromagnetic thicknesses t_{FM}. With this procedure, also a stable single domain structure is easily possible, which opens many possibilities of APEB utilization in various applications that are in dire need of a single magnetic domain state. The applications can range from energy harvester, to magnetic shielding as well as other sensor designs that utilize magnetic thin layers. The APEB would allow relatively soft magnetic properties, repeatability of the ground state, low noise due to its single domain state and most importantly low external flux emission in its ground state due to the antiparallel configuration.

With the integration of APEB into ME composite sensors, the limit of detection (LOD) could be enhanced by approximately 3-fold, leading to the best value of 50 pT/√Hz at 10 Hz with magnetic frequency conversion (MFC). The LOD improvement is a direct result of the severely reduced noise output of the sensor compared to the previous generation sensors (Figure 64(a). In addition, the new sensors have a stable signal to noise ratio over a large modulation field span (Figure 64(b) making them insensitive to external magnetic noise, thus allowing measurements without magnetic shielding. The sensors were then further optimized by tilting K_u away from the short axis through a second heating step. The tilted anisotropy allowed the increase of sensors' output whilst withholding the low noise response. In turn it was proven, that the sensitivity and LOD can be potentially increased by a factor of 2.

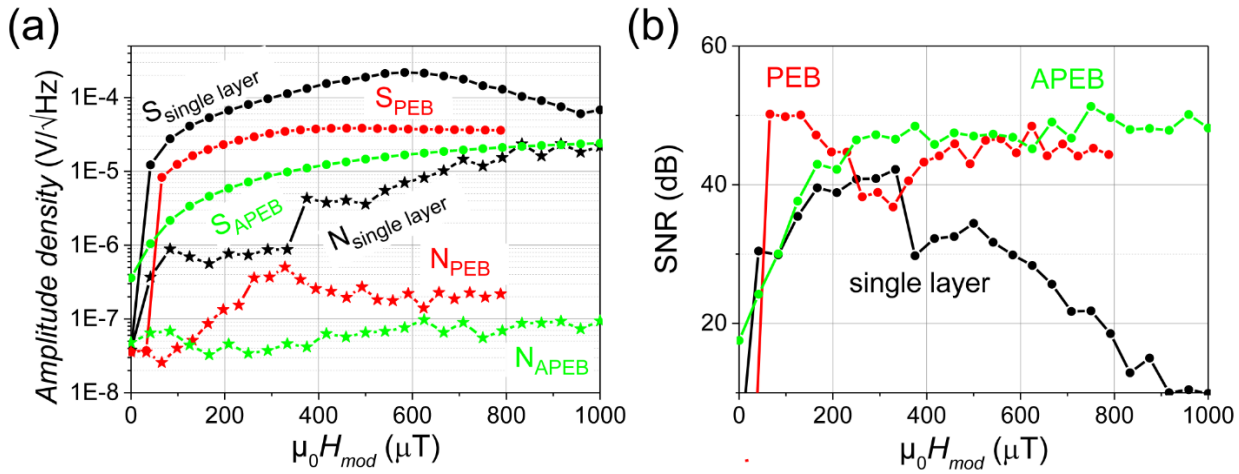

Figure 64: (a) Plot comparing the signal (S) and noise (N) output of a single layer, parallel EB (PEB) and APEB sensors with modulation field. (b) Comparison of the signal to noise ratio (SNR) of the three sensors in dependency of the modulation field. The t_{FM} thickness of all the sensors is 1 µm. The PEB and APEB sensors are of type 90/110.

Within this work, the electric modulation scheme was thoroughly evaluated using time-resolved MOKE. The observations allowed the interpretation of the domain behavior that influences the signal and noise response of a sensor. It was determined that the signal is generated by the anisotropy rotation through stressing of the sensor. Whereas the onset of magnetic noise is induced by the formation of stress-induced modulations formed during half a period of the excitation. The evaluation was conducted on a single layer system as well as on EB sensors. The analysis provides first hand evidence that the APEB sensors will incur significantly better noise response compared to the other sensors. With preliminary measurements of specialized APEB sensors already a record-breaking LOD of 30 pT/Hz$^{1/2}$ at 10 Hz was achieved.

In the last part of this dissertation, the edge modification of both single layer and multilayer PEB sensors was investigated. The edge modification was introduced in order to manipulate the stress relaxation zone in order to minimize the effective are of tilted anisotropy along the long axis. The analysis of altogether 32 different edge structures allowed the first evaluation of the applicability of such a method. From the study, the most promising structures were selected and possible modifications of the other structures were determined. In addition, a couple of new proposed structures could be determined for the future research on this matter.

For the future work, several parts of this project need further investigation. For the APEB sensors, the effect of t_{FM} variation still requires further research. A possibility would be to increase the t_{FM} to an asymmetric stack 225-275 (thickness of the FeCoSiB in the bilayer unit of the stack). This would allow going halfway towards the 500 system and evaluating, if the EB is sufficient to retain the noise properties observed for the 90/110 sensors. The second possibility is the variation of the antiferromagnet in thickness or forming asymmetric EB through asymmetric antiferromagnet thicknesses instead of varying the ferromagnetic layers. Further on, the tilted anisotropy scheme needs to be applied and researched on thicker APEB sensors to indicate, if the LOD with MFC can be further reduced. In future, the applicability of these new magnetic layers needs to be tested on real ΔE sensors as well as on sensors for electrical modulation scheme. For both methods, an increase of the sensitivity is expected compared to the standard single layer sensors and that these methods will provide even better LOD in comparison to the MFC technique. Lastly, the investigation of the edge manipulation needs to be carried further on and new structures need to be developed and researched. The structures should be then applied on the ME sensors and measured for the possible improvement of the sensors noise and signal response.

To finalize, this work provides a new method of producing ultra-low noise ME sensors, which are required for the sensing of bio-magnetic signals in the low frequency range. The work also provides helpful insight into the noise mechanics as well as the base of eliminating these effects with future research. In the end, the work provides a stepping-stone towards the ending goal of producing ME sensors with biomagnetic signal sensing capabilities in the sub-pT range.

B-side of research

During research many things can take on a different course than expected. From that, many times unpredicted results and phenomena are observed and recorded. In this post-chapter a selection of interesting data is provided, that do not follow the research interests within this work. However, the data is intriguing and it should be definitely sought to research them further. A short description and information about the experiment is given for each data set. To note, the data is of preliminary nature and does not in any way correspond to a full analysis of the discussed phenomena.

Escalator domain motion

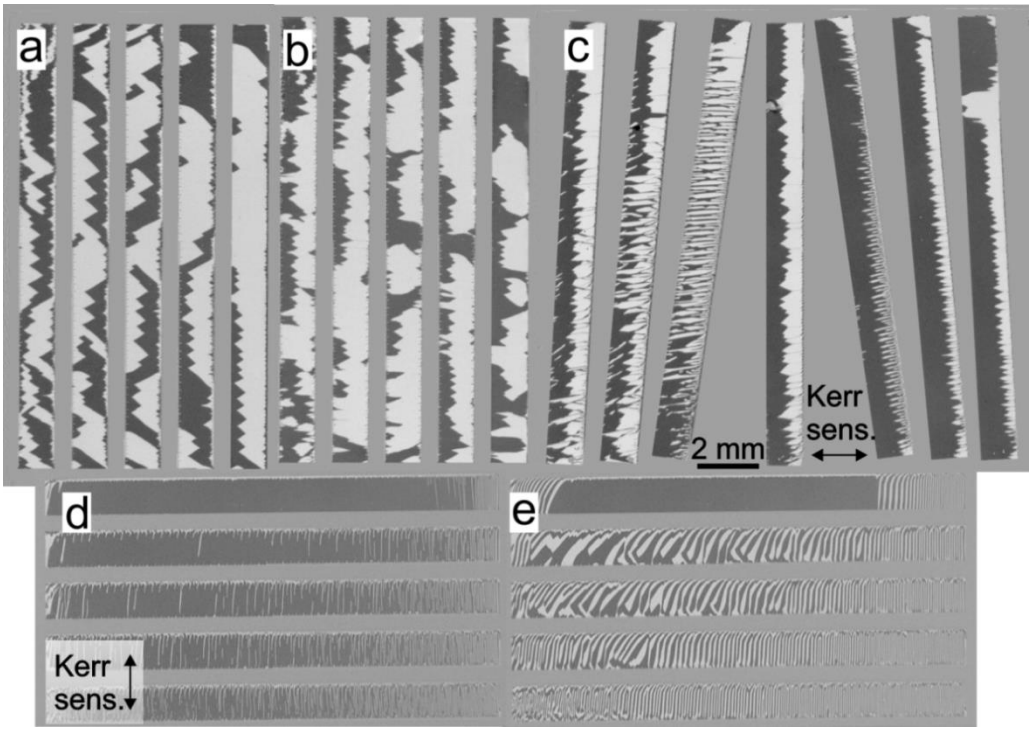

Figure 65: Overview MOKE domain images of patterned structures of a multilayer system in a **(a)** demagnetized **(b)** and remanence state with field applied along the short axis. **(c)** The same multilayer system with different patterned structures showing different domain states based on the position of the individual structured elements. The sample is demagnetized along the short axis. The same structures from **(a)** and **(b)** with **(d)** remanence and **(e)** demagnetized state with field applied along the long axis. The samples were fabricated by Erdem Yarar.

With the application of the edge manipulated structures, described in Chapter 9, on a 20x200 nm FeCoSiB multilayer system a fascinating domain structure forms. At first the demagnetized (Figure 65(a)) and remanence (Figure 65(b)) structures with the field

history along the short axis show a domain configuration expected from a multilayer system. However, with the application along the long axis of the structures, the remanence state shows narrow worm-like domains (Figure 65(d)). Furthermore, when the structures are demagnetized along the long axis, a completely new domain construct forms that resembles the regular 180° domain construct in a complex twisted form (Figure 65(e)). The same domain construct was also observed for other patterned structures (Figure 65(c)). It is hypothesized that such a domain configuration forms due to a local gradient of the K_u and with it the impact of the stress effect is stepwise increased. In addition, the anisotropy is assumed to be tilted by approximately 15° away from the short axis. From such a state, a very interesting behavior could be observed with an application of an AC magnetic field. The behavior was documented and is presented as two movies (Video 3 and Video 4) for both set of structures presented in Figure 65. From the videos, a preferential movement of the domains with the oscillating field is visible. The movement is in a form of domain wall jittering of the domains at which a step-like overall motion is visualized. Fascinatingly, the domain construct shows nucleation and annihilation regions, which allow the cyclic movement of the domains. Due to the stepwise motion and cyclic vanishing and formation of domains, the behavior is described as escalator domain motion.

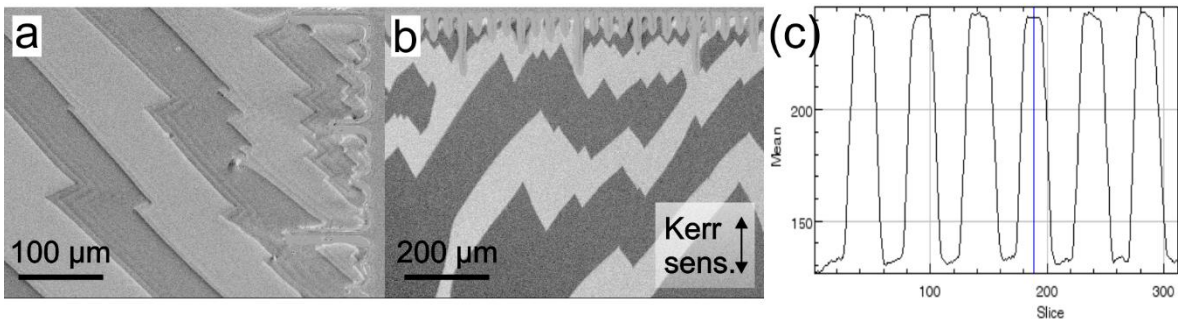

Figure 66: High resolution MOKE images of the multilayer structured edge presenting the domain structure during the AC field excitation with the MO sensitivity along the (a) long and (b) short axis. (c) The contrast data at a certain position taken during the excitation of the magnetic structure with an AC field. The data shows the periodic contrast change resulting from the gradual movement of the domain pattern. The data is complementary to the data presented in Video 7 and the x-axis corresponds to the consecutive number of the frame from the video. The sample was fabricated by Erdem Yarar.

By observing the domain motion with high-resolution MOKE, the mechanism of the motion is clearly visible (Figure 66(a)-(b)). The domains with each cycle shrink and expand at which the step segments move from the top edge to the downward edge. During longer observation, it is visible, that the domain walls do not return to the same position after a

field cycle, but instead slightly drift in the same direction. This leads to an overall motion of the domain in the same direction. During the research on the rest of the structures, also regular domain structures with a slight anisotropy tilt were found. These structures were also exposed to the cyclic field excitation and the gradual motion of the domains in a certain direction was also observed. The motion is presented with a set of movies. One video shows the motion with 1 Hz AC field (Video 5), the other one with 21 Hz AC field (Video 6) and the third one also with 21 Hz, but with 8x averaged images subtracted from the beginning domain state (Video 7). All the videos show the progressive domain motion and that the motion is cyclic, however with a much smaller frequency compared to the excitation field frequency. A randomly selected position was measured for intensity and then plotted over the frame number. From the graph, the clear cyclic motion could be determined (Figure 66(c)). The plot is extracted from Video 7. It is understood, that a gradient in the anisotropy strength has to be present for such movement to occur. With such a state, the domain walls would move preferentially along the decreasing anisotropy energy with each field cycle. This is a very interesting feature, as if such behavior can be controlled, then this would allow a novel way of creating movable self-forming domain tracks with relatively small energy input.

Lithography resist imprinted anisotropy

With the production of the edge patterned structures an interesting feature of the anisotropy was discovered. The centerpiece (chip 5) was investigated for several 4 µm thick single layer systems. In Figure 67 three different 4 µm single layer systems are presented at which all show an underlying anisotropy distribution. Two of the samples were also field annealed and still show the secondary anisotropy distribution (Figure 67(d)-(f)). Based on the shape and position of the anisotropy distribution it is postulated, that this feature is related to the lithography process. More specifically it is thought, that it is related to the deposition of the resist on the surface of the wafer and leaves a spread-out form of a thicker resist. This formation leads to a different stress state of the magnetic film that then is transferred during the lithography and etching process. This is only a theory and should be more exactly and thoroughly investigated.

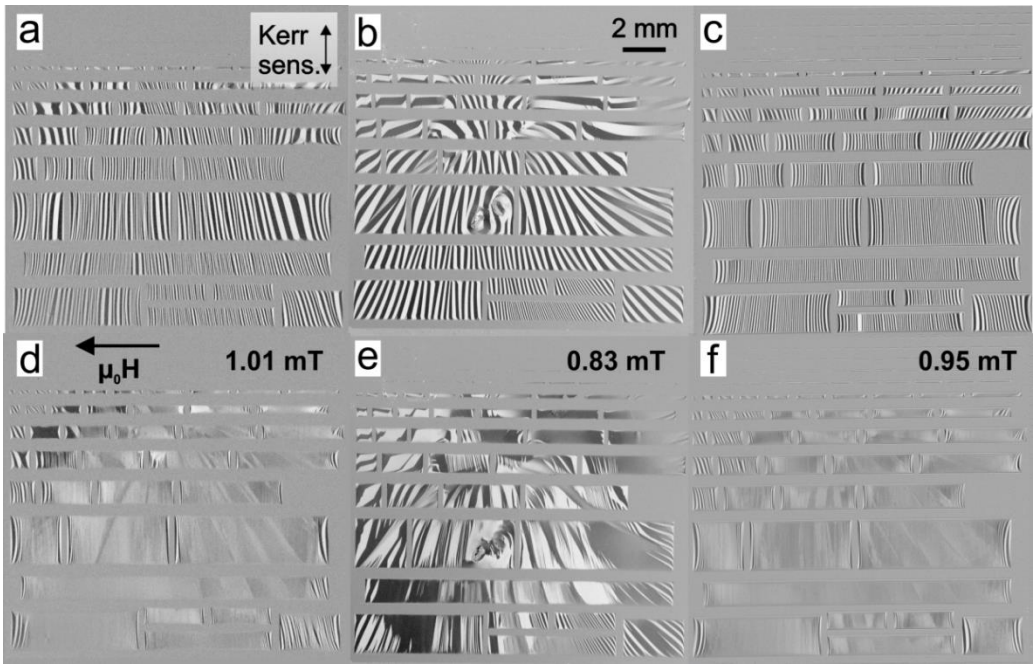

Figure 67: Domain images of three different 4 µm single layer systems showing the (a)-(c) demagnetized domain state and (d)-(e) a corresponding state at an applied field. All samples were deposited without field, but samples (a) and (c) were afterwards annealed at 250 °C for 30 minutes in order to align K_u. The samples were fabricated by Rahel Kruppe.

Special anisotropy effects in µm thick thin films

During deposition of magnetic materials with an additional applied magnetic field, several cases of single layer FeCoSiB showed unfamiliar domain structures. In this section a handful of examples of such structures are presented.

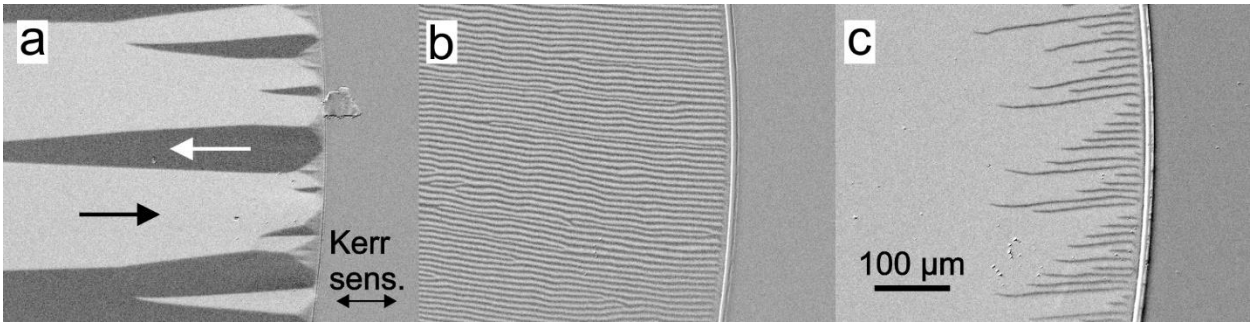

Figure 68: (a) Domain state of a regular 2 µm thick single layer FeCoSiB sample. Another sample with the same layer structure shows a different domain construct with field history along the (b) horizontal and (c) vertical axis. Both samples were deposited with field assisted sputtering. The sample was fabricated by Erdem Yarar.

The first example is of a 2 µm thick FeCoSiB layer structure deposited in a form of disks. Compared to the regular domain structure (Figure 68(a)), this specific example exerts a domain construct with very fine stripe-like domains. They extend across the whole length

of the structure with the field history along a specific axis (Figure 68(b)). With the application of the field 90° to this axis, the domains shorten and form a construct seen in Figure 68(c). The domain structure is assumed to be a result of a very low K_u, which is dominated by the K_σ, leading to the formation of this fine domain pattern.

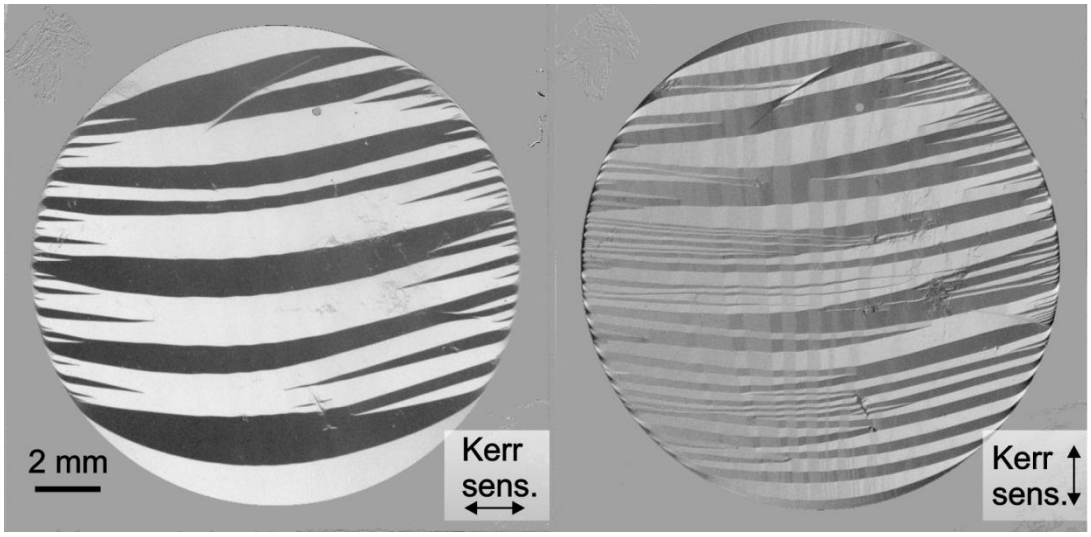

Figure 69: Domain images of a circularly shaped element of a 4 µm thick FeCoSiB layer with MO sensitivities aligned along both principal axes. The sample was fabricated by Erdem Yarar.

Another example is given in Figure 69, for which a clear overlapping of two anisotropies is presented. The main, stronger contrast shows the standard domain structure expected from the direction of the field, applied during the sputtering. However, the weaker contrast indicates a domain structure perpendicular to the other one. The reason for the formation of such a structure is not clear. A possible explanation could be a mismatch of both orifices of the thin film, which leads to a different domain state above and below the thin film. Due to this, the anisotropy locally turns from one state to another, forming such a domain state as seen in Figure 69.

The third example shows a similar effect of having two overlapping anisotropies as seen before, but in this case, the anisotropies seem to be collinear in orientation (Figure 70). In addition, the anisotropies lead to a very complex domain structure visible with high-resolution MOKE (Figure 70(b)-(e)). Fascinatingly, the weaker anisotropy forms a granular domain pattern that resembles formations formed by crystalline materials. The origin of such structures is also postulated to be related to the lower anisotropy energy. However, for this structure the K_σ overcame K_u leading to different axis of domain

formation. This is based on the fact, that the deposition field was supposedly aligned perpendicular to the evolved domain state. In addition, the overall domain configuration in remanence is highly variable, which is represented by the images in Figure 70(b)-(e) with the field history along the horizontal axis.

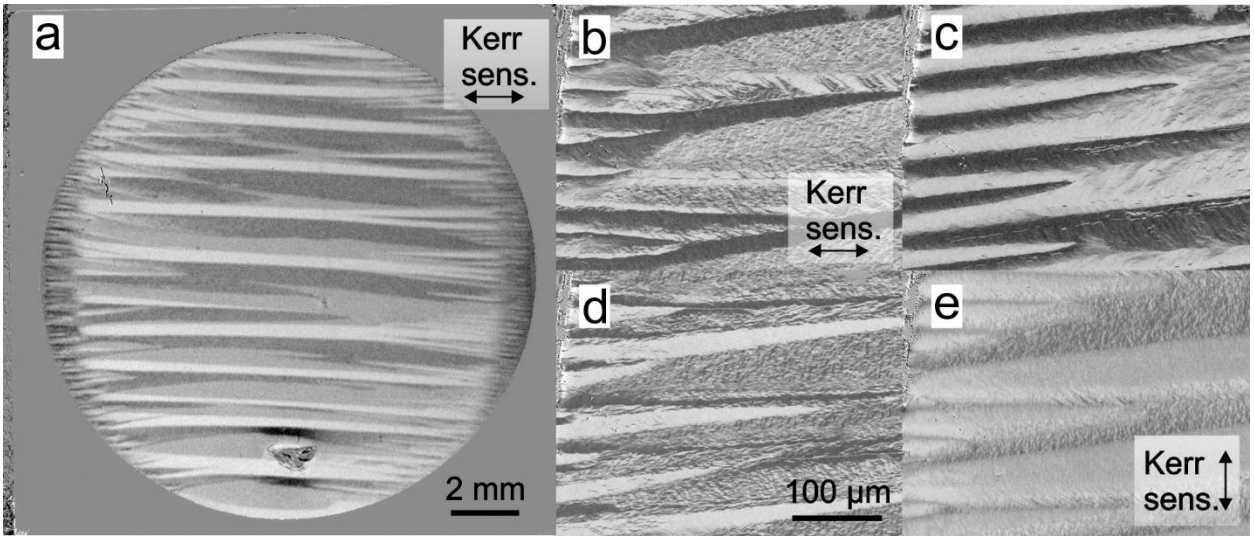

Figure 70: **(a)** Domain state of a 4 µm single layer patterned as a disk-shaped structure at low magnification indicating a complex domain structure. **(b)-(e)** The high resolution images of the domain state near the edge of the sample from **(a)**. The images in all cases show a remanence state with field applied horizontally. The sample was fabricated by Rahel Kruppe.

With another example of a 4 µm single layer FeCoSiB sample deposited with field another completely different domain structure was observed. For this example, a gradient of the anisotropy is visible, similar to the state seen before for the escalator domain motion. However, in this case the stack is of a single layer type, which gives a direct interpretation of the anisotropies, as no interlayer coupling is present. From Figure 71(a)-(c) the change of the domain construct of the sample under different conditions is visible. The state on the right-hand side shows the stress dominated region, where strongly modulated and reorganized domains form. The exact domain structure was determined with high-resolution MOKE. The images in Figure 71(d)-(f) show the transition from slightly modulated domain construct towards a completely modified structure due to the prevailing K_σ. The similar regions are also presented with the MO sensitivity in Figure 71(g)-(i). The domain structures indicate the folded domain structures forming near the edge as well as the very fine modulation that are formed perpendicular to the magnetization orientation. With the overwhelming stress, the domain construct is very

complex, showing perplexing modulation orientation and propagation. In addition, the images show, that despite the large influence of the K_σ, the overall magnetization direction is still dictated by K_u (aligned along the short axis).

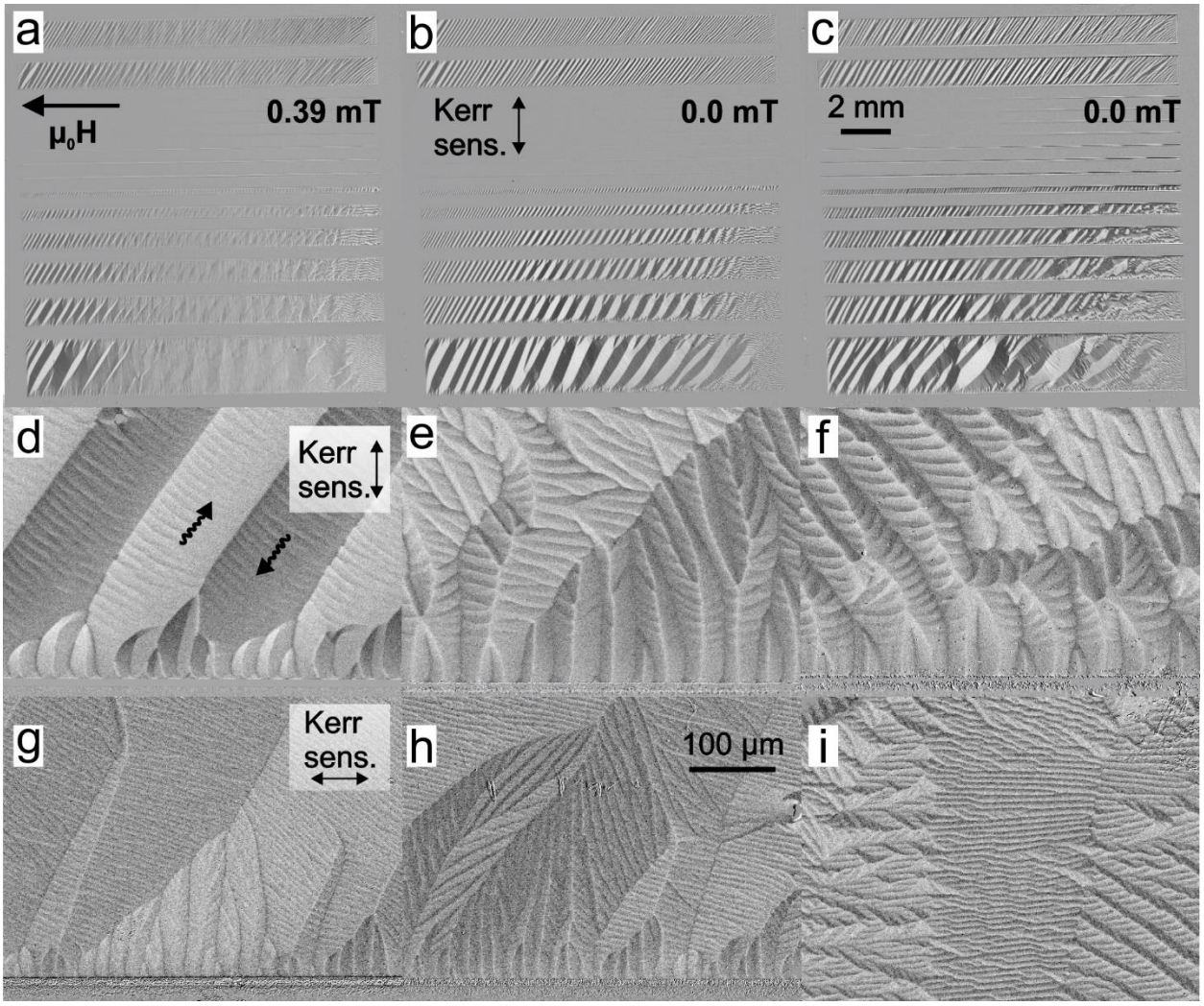

Figure 71: (a)-(c) Overview MOKE images of a 4 μm single layer deposited with field. Image (a) is with an applied field along the long axis, (b) is the demagnetized state and (c) the remanence state with the application of the field along the long axis.(d)-(f) and (g)-(i) are high-resolution MOKE images indicating the domain structure with increasing stress effect on it with MO sensitivity set along the short and long axis respectively. The sample was fabricated by Erdem Yarar.

The final example of this subsection is shown in Figure 72. This example is also related to anisotropy variation, but most probably related to a variation of the K_σ. This is assumed due to the complex and fine domain structure present across the whole sample (Figure 72(a)). The local variation of the anisotropy is seen by the varying directionality of the

domains as well as by the uneven switching of the domains with applied field (Figure 72(b)).

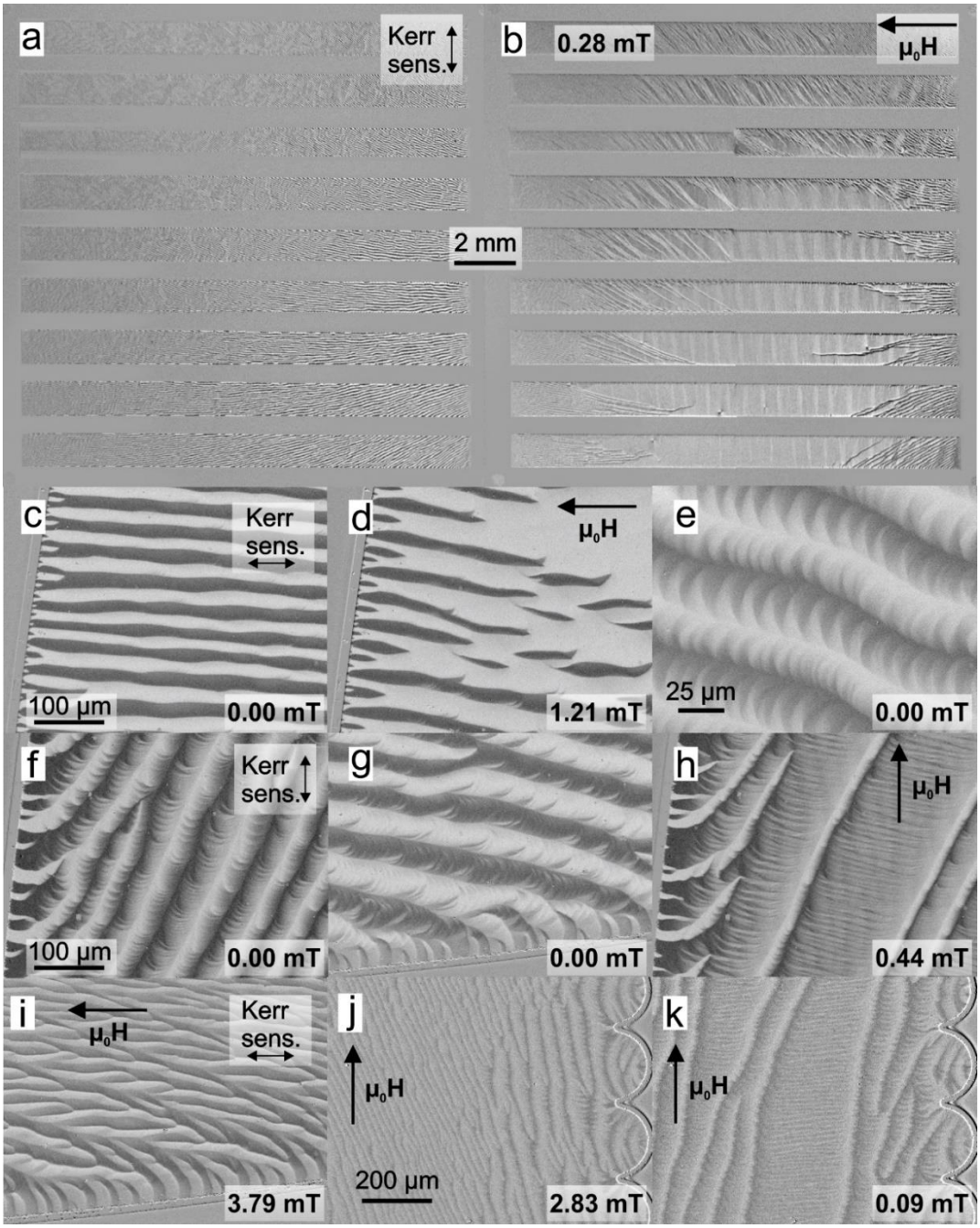

Figure 72: (a) Overview MOKE images of a field deposited 4 μm single layer FeCoSiB patterned sample. (b) With the application of field, the underlying additional ansiotropy is revealed. (c)-(k) The domain states with various field applications, field hystories and MO sensitivity. (c) and (d) indicate the domain state with the field application along the short axis, whereas images (f)-(k) show the domain states resulting from the field application along the long axis of the structures. The samples were fabricated by Erdem Yarar.

In addition, the domain configuration shows a wave-like movement with an applied AC field, which is presented in Video 8. It is understood, that the behavior is related to the crossed anisotropy, which then moves the domains in each section with the direction of the local total anisotropy. With the application of an external field, a secondary domain construct is revealed (Figure 72(b)). The surprising part about this secondary construct is the good alignment with the short axis (axis along which the field during deposition is applied). This suggests that the underlying pattern is formed by the K_u. This then also confirms the suspicion, that the primary domain structure is formed due to K_σ. With high-resolution MOKE imaging the primary domain construct is resolved. With field application along the short axis of the structures, the structures show a remanent state with narrow 180° domains with a modulation of the form, which resembles a wave pattern (Figure 72(c)). With a sufficiently high field, the domains collapse and segments of certain domains remain (Figure 72(d)). Such behavior also confirms the crossed orientations of K_u and K_σ.

By applying the magnetic field along the long axis of the structures, the typical fir-tree domains form (Figure 72(e)) [26]. With variation of the applied field and MO sensitivity direction the behavior of such domains was recorded (Figure 72(f)-(k)). With further application of the magnetic field, the fir-tree pattern is omitted and larger domain patches form with fine modulations residing within them (Figure 72(h)). With very high fields, the modulations bend and reform into twisted domain pattern (Figure 72(i)), providing further evidence of the mismatched K_σ and K_u. With intermediate fields, the underlying domain patches are visualized, which are in fact constructed from the regions of differently oriented modulations (Figure 72(j)). With lower fields, the patches collapse into a single domain state with the overlaying fir-tree domains. Despite the observations, it remains puzzling, as to why the various domain patterns and gradients of anisotropy are formed and why such a high variance of the effects is present from sample to sample. Based on this data it is advised to research further on this matter and indicate the sources of such high variation of the magnetic films.

High temperature domain effects in FeCoSiB

During temperature setting of the anisotropy of single layer FeCoSiB samples, a remarkable domain behavior with temperature was determined during in-situ MOKE observations. The domain state of a slanted 4 μm thick FeCoSiB layer was considered to

be manipulated with field annealing. After a predecessor showed no anisotropy change with the field annealing, this sample was simultaneously observed with large view MOKE. This allowed domain state determination and the observation of any changes of the anisotropy during the annealing procedure. During the observation at 300 °C and after 30 min of heating, a well-oriented alignment of the anisotropy along the short axis of the elements was determined. In addition, the slight curvature of the magnetic field due to the inhomogeneity of the field is visible (Figure 73 (300 °C)). With cooling the sample after the heating procedure, changes of the domain orientations are visible. With decreasing temperature, the domains once more become less oriented along the short axis (comparing state 300 °C to state 50 °C). Additionally, at around 200 °C to 150 °C sudden changes of the magnetic state are visible (comparing 200 °C, 190 °C and 130 °C states). During these changes, sudden reforming of individual domains is visible. Furthermore, the before seen spike domains at the edges suddenly vanish within this temperature range. The change can be seen in a more stepwise manner from the movie (Video 9), indicating the domain state changes from 300 °C to 50 °C by steps of 10 °C. It is considered, that the reason for such behavior is the increasing effect of the stress formation at the edges with decreasing temperature.

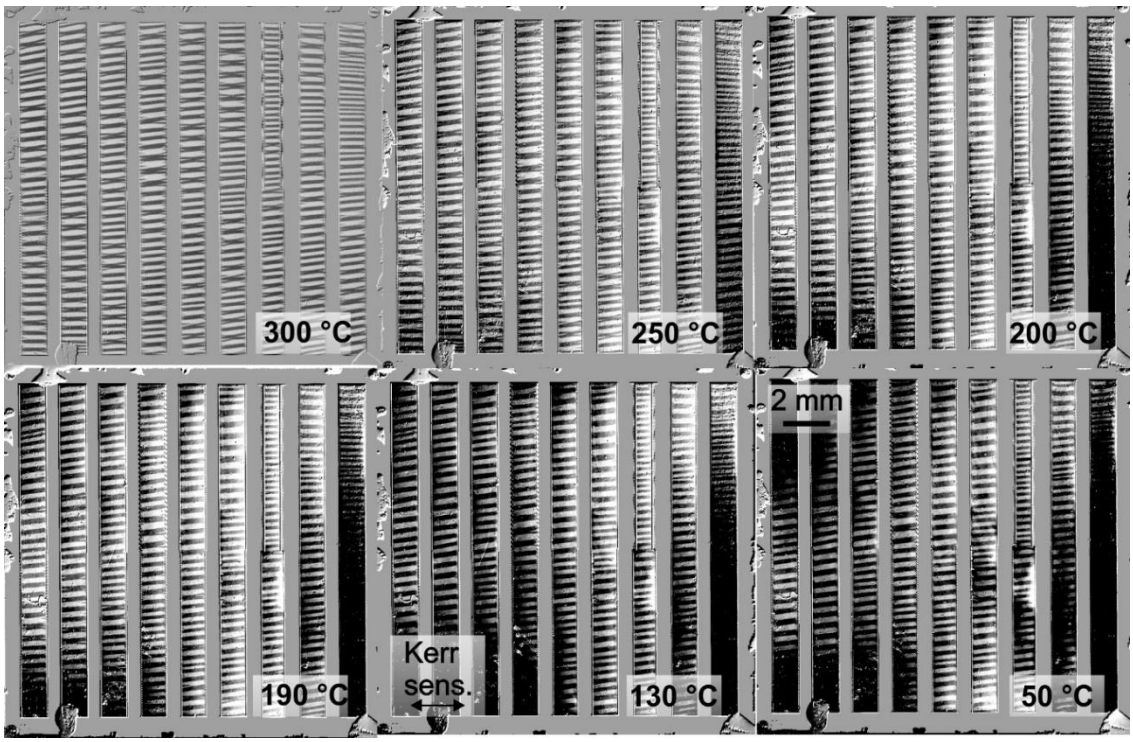

Figure 73: In-situ overview MOKE images obtained during heat treatment of the structured 4 µm thick single FeCoSiB layer. The images are taken duirng the cooling procedure. The sample was fabricated by Rahel Kruppe.

To indicate the reasons and to prove the reproducibility for such changes additional samples were investigated. For a disc-shaped 4 µm FeCoSiB thin film sudden changes of the domain state was also visible during the heating of the sample to 300 °C (Figure 74, comparing states 50 °C, 100 °C and 150 °C). For this sample, also a special behavior was witnessed during the sample observation at 300 °C. The domain structure shows twitching motion formed by the pulsed heat addition to the system in order to hold the temperature at 300 °C. This effect can be seen in Video 10.

The same sample was also investigated at higher temperatures up to 375 °C. The sample showed a very interesting domain structure change during the heating. At around 325 °C the domain structure started to show a single domain state gradually forming from one side of the sample to the other (Figure 75(a)). The change is very spontaneous and engulfs the whole sample within a small temperature range of about 10-15 °C. Exemplar images portraying the change from the regular 180° domain state to the single domain state are presented in Figure 75(a). The same behavior was also observed with other samples of different patterned geometries.

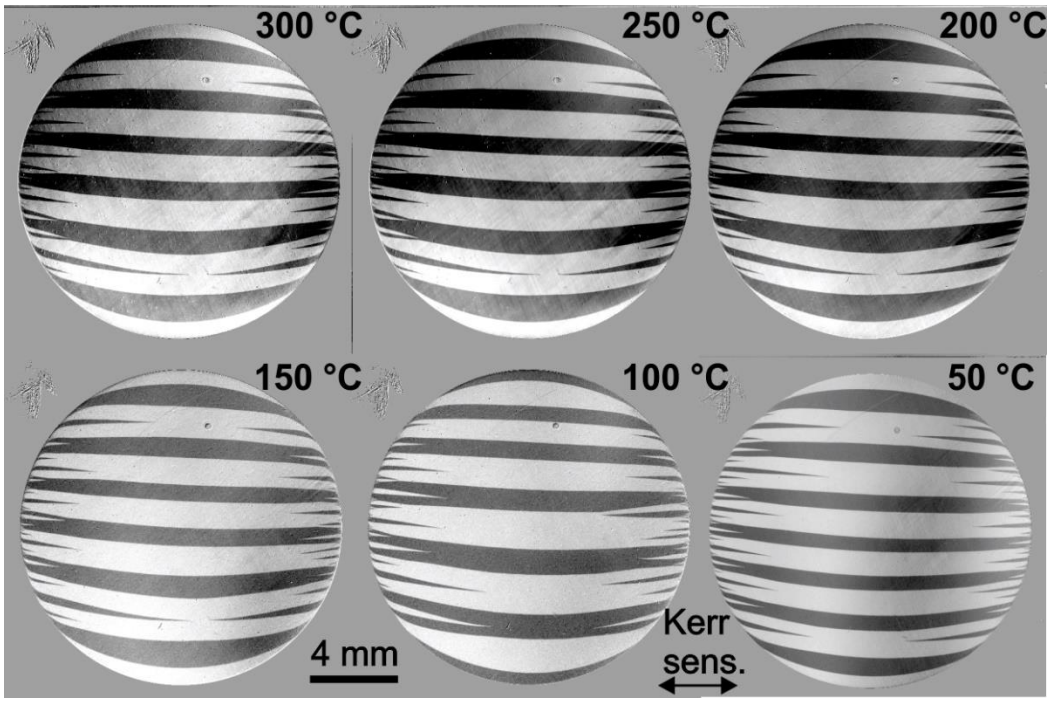

Figure 74: Overview MOKE images of a field deposited 4 µm single layer sample at selected temperatures during heating of the sample. The sample was fabricated by Rahel Kruppe.

With the discovery of such a drastic change, another measurement was conducted, at which the magnetization response with field was measured from the domain contrast at

specific temperatures. By comparing the change of the contrast, a temperature dependency of M_S could be extracted. In addition, the measurement showed that the high temperature formed single domain state still shows hysteretic behavior and a clear remanence state formation. This proves that the sample exerts domain changes that are not related to the paramagnetic transition at the Curie temperature. This also means that the origin of such a structure could be related to changes of the anisotropy of the system. A possible explanation of the change could be the reduction of K_u to critical value where the stress state dominates and forms very narrow domains (similar as seen in Figure 68(b)). Such domains are visualized as a large single domain state as due to their size the two domain contrasts are homogenized into one contrast state. In order to investigate the behavior of such samples with temperature in more detail, vibrating sample magnetometry (VSM) measurements were conducted. The measurements were conducted on different samples as presented before. The resulting normalized M_S with temperature behavior is plotted in Figure 75(b) for two VSM measurements accompanied by the results of the MOKE analysis. A correlation between the MOKE and VSM measurements is visible, however, the MOKE data shows additional features, which are most probably related to the temperature induced drift of the sample during measurements.

The VSM measurements show various interesting sections of the M_S behavior. The first section occurs at around 150° (marked with arrow), where a plateau forms. This region is in the similar range as the range where the sudden change of the magnetic state was observed (Figure 73). The next regions are at much higher temperatures, where three characteristic peaks are visible. It is assumed, that the first peak (marked with blue) is associated with the primary crystallization of the α-Fe crystallites. The second peak (marked with yellow) is presumed to be formed by the crystallization of borides. Both of these peaks have been observed in similar amorphous alloys with differential scanning calorimetry (DSC) [120] [121]. By comparing the published data with the VSM data, the peaks match to a very high extent, not just in temperature range, but also in the shape of the peaks. The final peak (marked with green) has not been reported by the references. However, it is postulated that the peak is created probably by reconfiguration of borides that could occur with the intergranular mitigation of boron at this temperature. Nevertheless, this needs to be proven with further measurements.

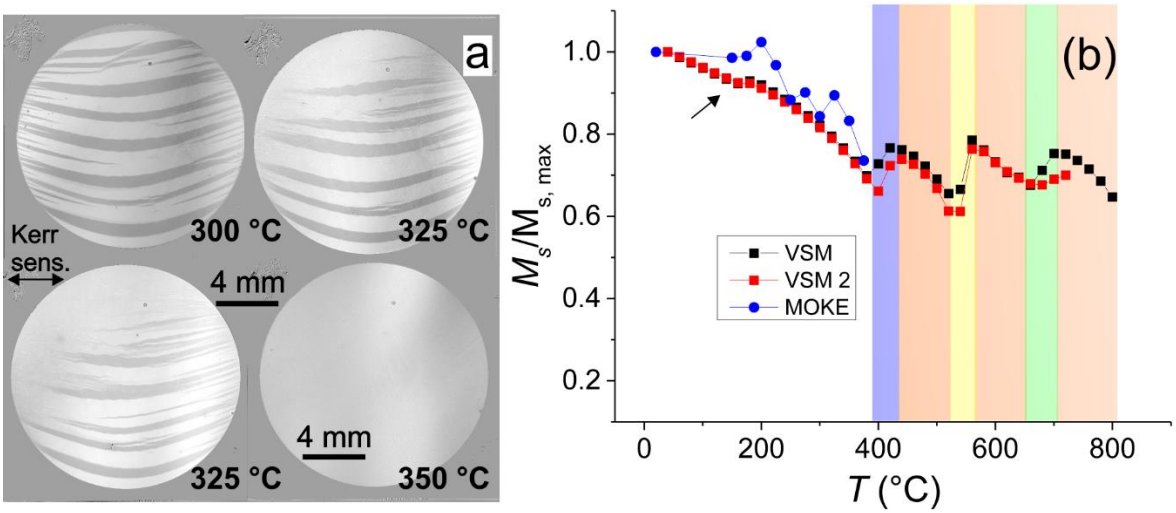

Figure 75: (a) Overview MOKE images at high temepratures indicating the transition from a 180° domain state to a single domain state with the intermediate state observed at 325 °C. (b) Plot of VSM and MOKE derived normalized M_S temperature dependency. The colored regions indicate the various peaks associated with crystalization and diffusion effects. The orange colored regions represent the temperature ranges of dominating growth processes of the crystalittes. The sample was fabricated by Rahel Kruppe. The VSM measurements were conducted by Lars Thormählen.

Appendix

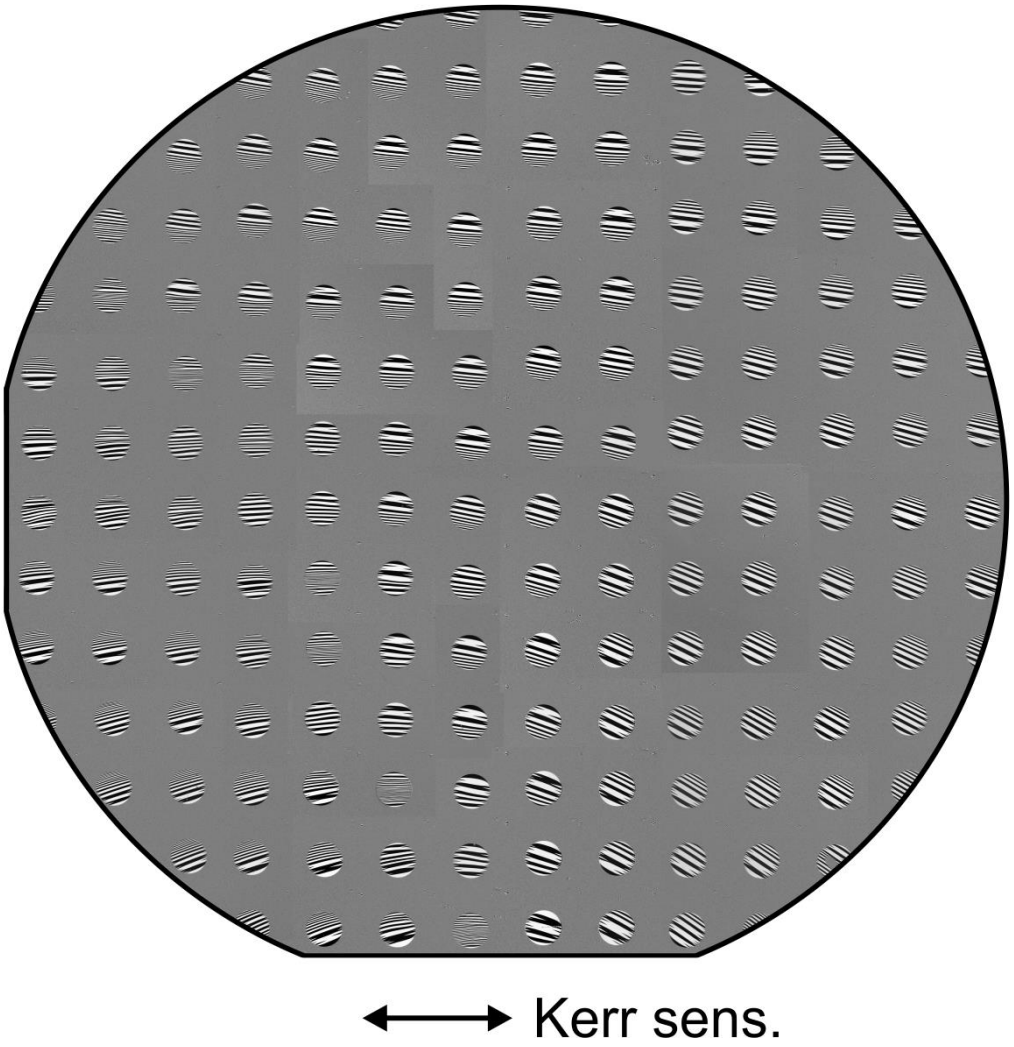

Supp. 1: Large view stitched image of a whole 4-inch wafer of 200 nm FeCoSiB single layer, structured with periodic circles for anisotropy determination. The image shows the distribution and local variation of the anisotropy direction. The sample was fabricated by Lars Thormählen.

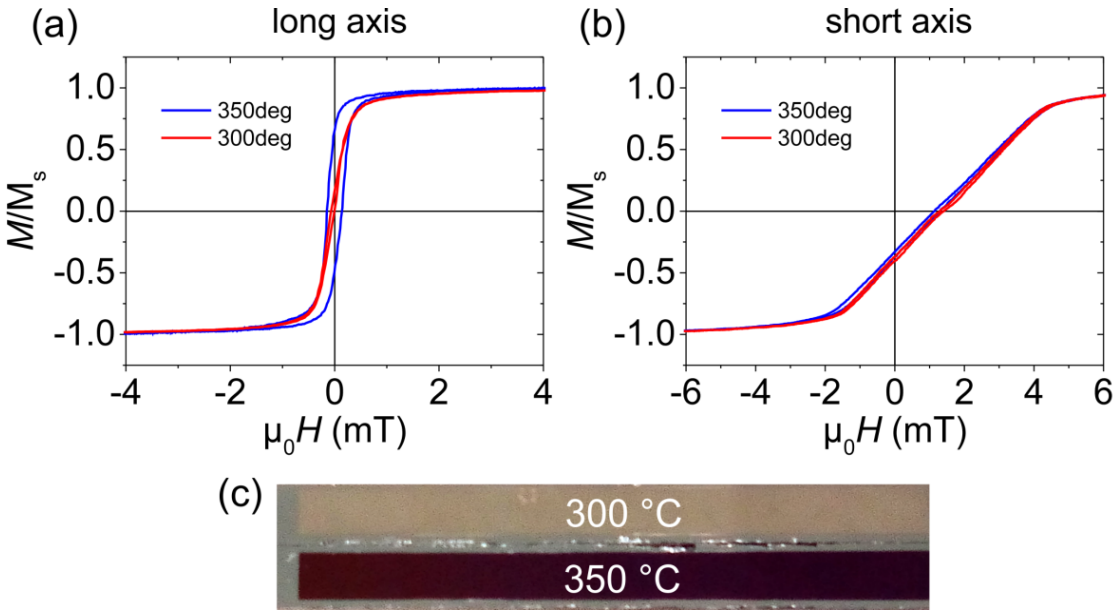

Supp. 2: Inductive measurements of 300 °C and 350 °C heat treated 2 µm 90/11 PEB sensors along their (a) long axes and (b) short axes. (c) Images showing the effect of heat treatment on the sensor's surface coloration.

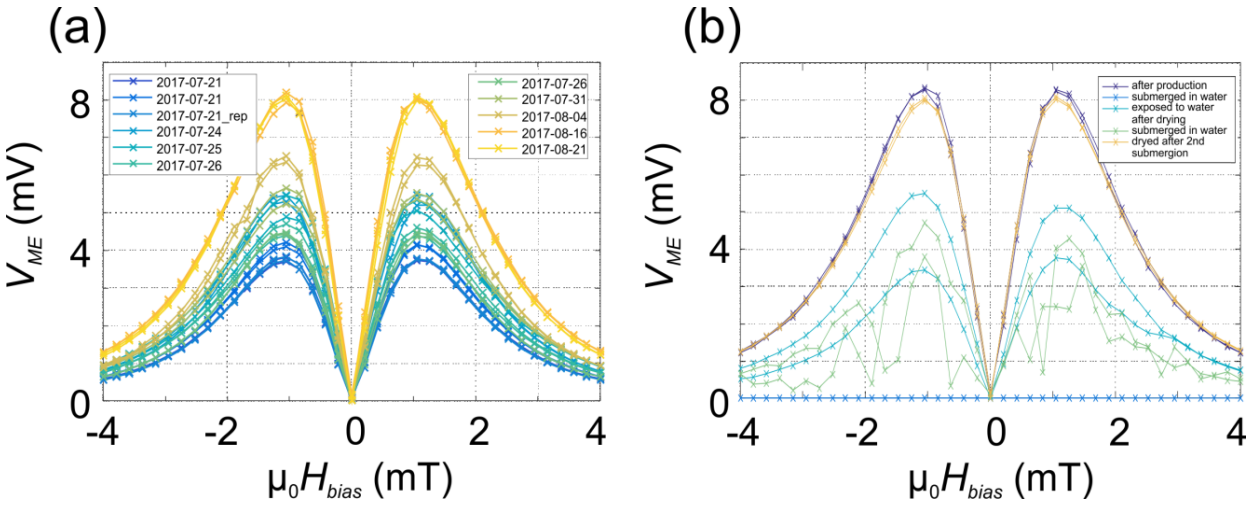

Supp. 3: (a) Bias curve measurements of a 4 µm 90/110 APEB sensor over a period of 1 month. The measurement on the first day was repeated and then done once with reinstalling the sensor (notated as rep) in the measurement holder (showing variation due to repositioning in the holder). (b) Bias curve measurements of another APEB sensor (equivalent to the previous one) displaying the change of the ME response with exposure to water and indicating the effects of drying the sensor after exposure to water. The measurement series were conducted by Sebastian Toxværd.

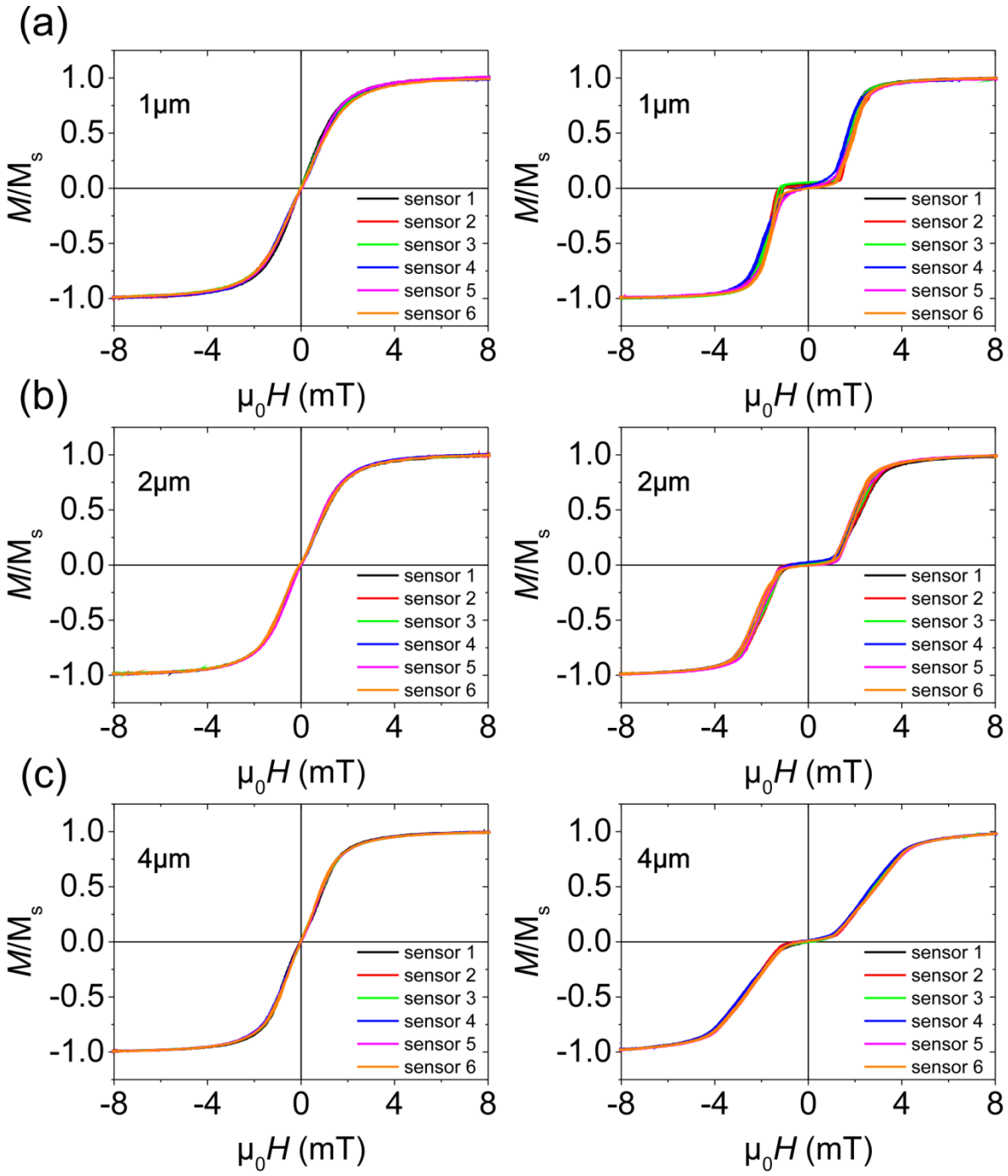

Supp. 4: Long axis (left) and short axis (right) inductively measured magnetization responses for sensors with (a) 1 µm, (b) 2 µm and (c) 4 µm total t_{FM}. For each thickness group 6 sensors were measured to give the overall variation of the magnetization responses from sensor to sensor. The sensors utilize the 90/110 stack structure.

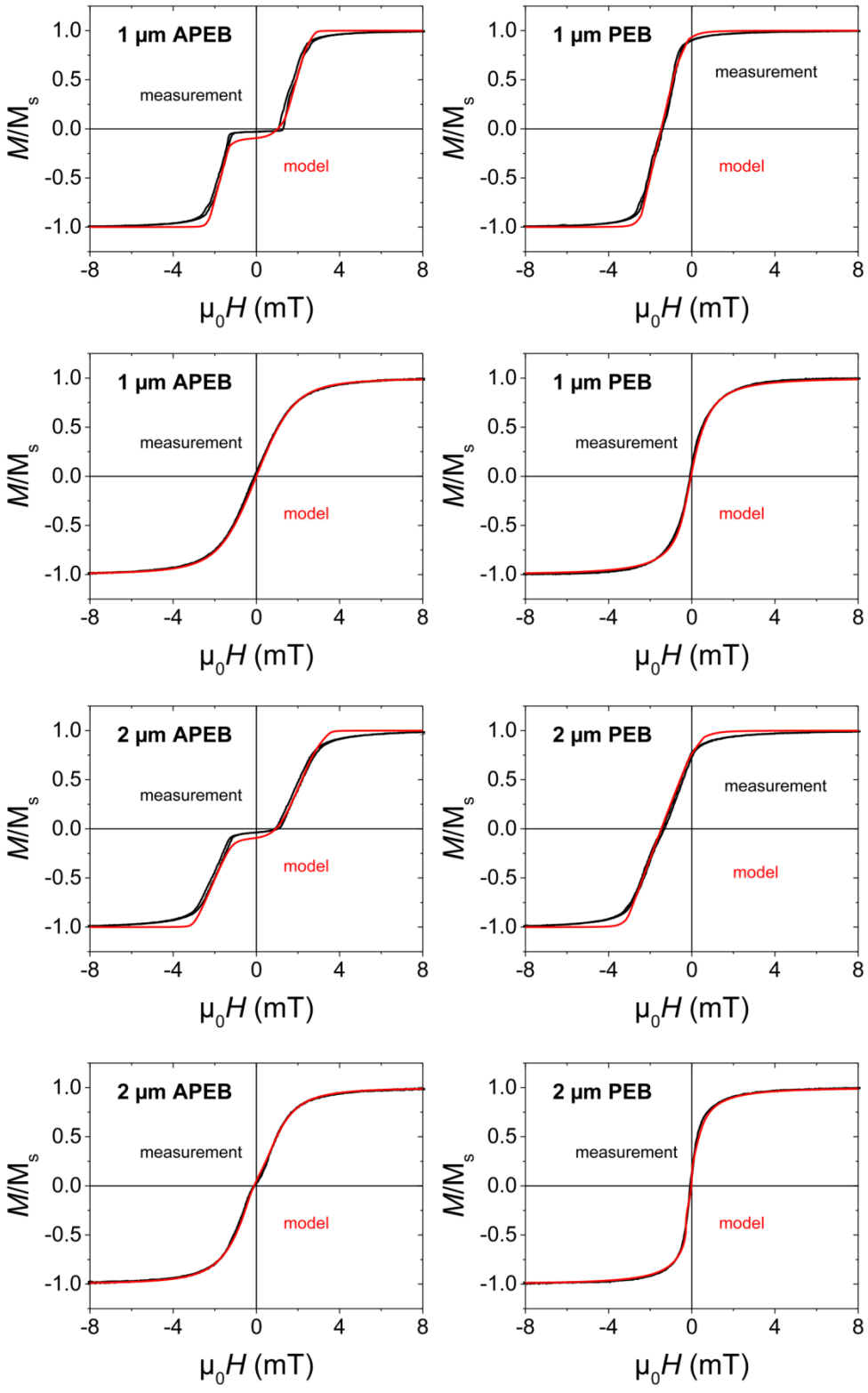

Supp. 5: Comparison of modeled magnetization response with the measured data. The modeled loops were performed with the 2 layer 4 domain model.

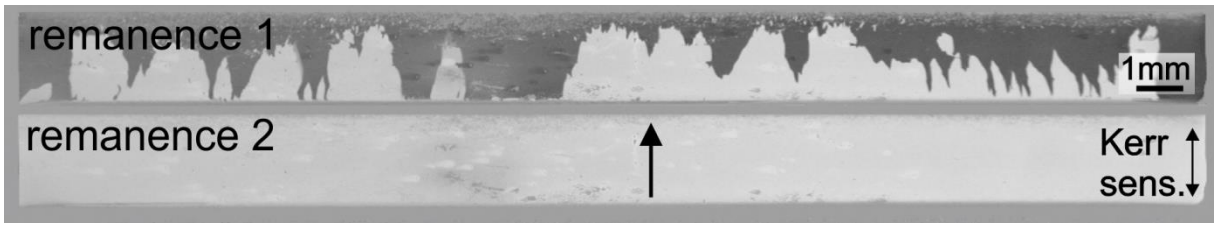

Supp. 6: MOKE images of a 4 µm 90/110 PEB sensor showing two reoccurring remanence states formed with field history along the long axis. The sensor was fabricated by Volker Röbisch.

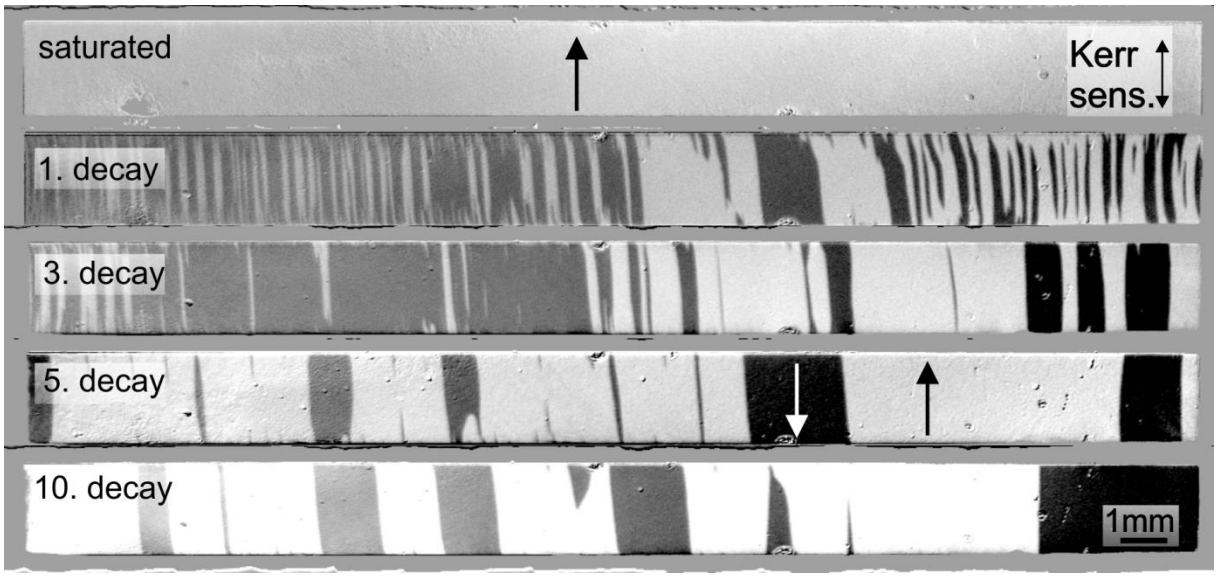

Supp. 7: In-situ domain images of a 4 µm thick 500 sensor showing the evolution of domains at 300 °C with starting saturated state. The number of domains decreases with each demagnetization cycle. The last state below is the state chosen to be cooled down to RT. The sensor was fabricated by Lars Thormählen.

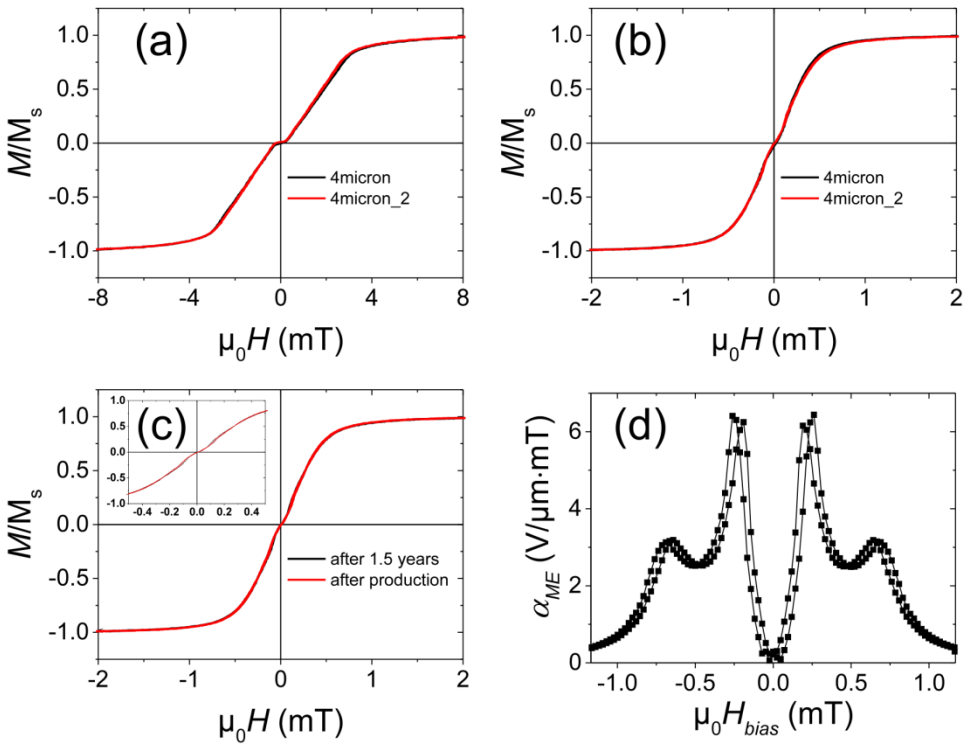

Supp. 8: Induction measurements of the two 4 µm thick 500 sensors along the (a) short axis and (b) long axis. Both graphs indicate the strong likeliness of the two sensors. (c) Repeated measurement of the magnetization response along the long axis of the first 4 µm 500 sensor displaying the same magnetic response as measured after production of the sensor (note the 1.5 year time difference within which the sensor was exposed to countless measurements). (d) The corresponding repeated ME bias curve measured for the same sensor indicates a different magnetic state.

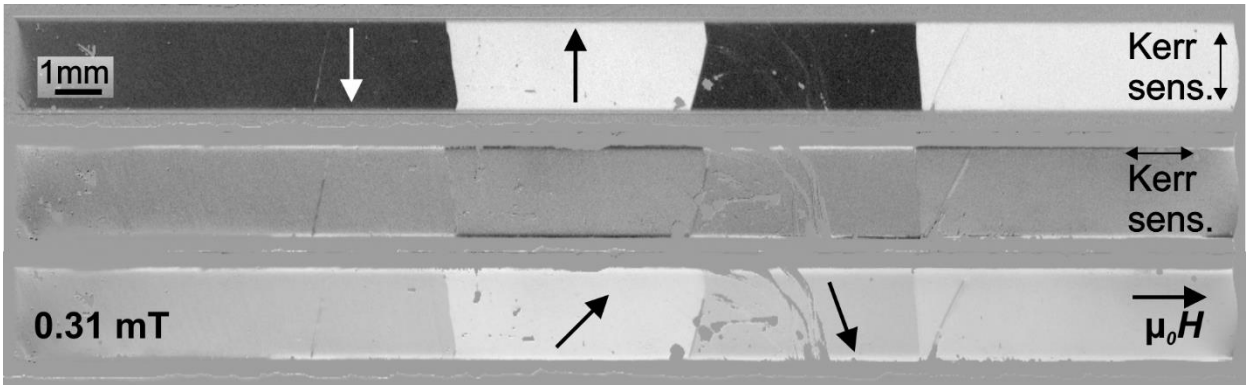

Supp. 9: Overview MOKE images of a 4 µm thick 500 sensor with a 4 domain construct. The first two images indicate the magnetic state with both MO sensitivities. The last image indicates the change of magnetization orientation with an application of an external magnetic field. It shows that one domain (second from left) rotates its magnetization faster than the others, which explains the double-peak bias curve in Supp. 8(d). The sensor was fabricated by Lars Thormählen.

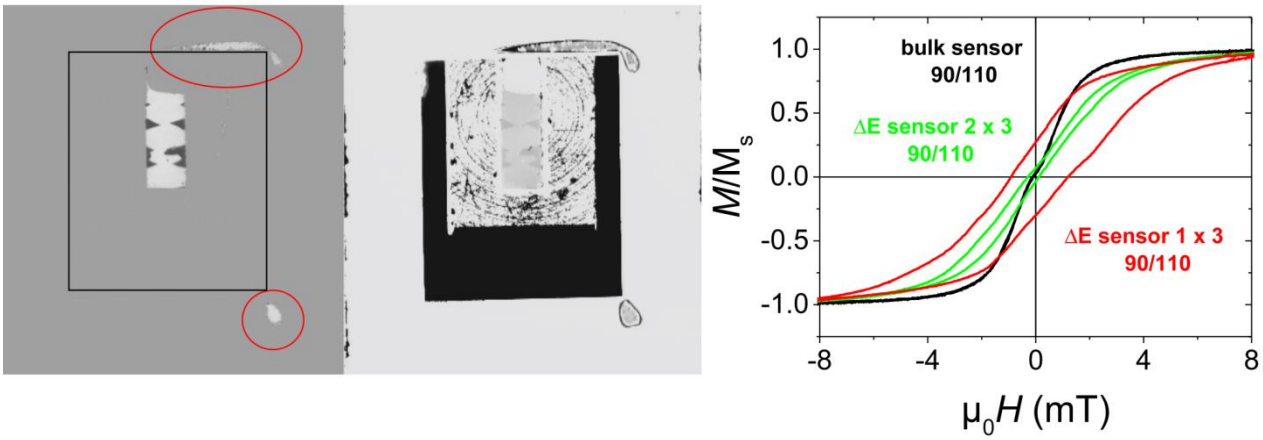

Supp. 10: Large view MOKE images of a ΔE sensor with the redeposited material at the edge of the sensor frame marked by large circles. The complementary image shows the geometry of the chip. The sensor was fabricated by Lars Thormählen. On the right the exemplary inductively measured long axis hysteresis are presented and compared with the response of a bulk sensor. All sensors are of type 2 µm 90/110.

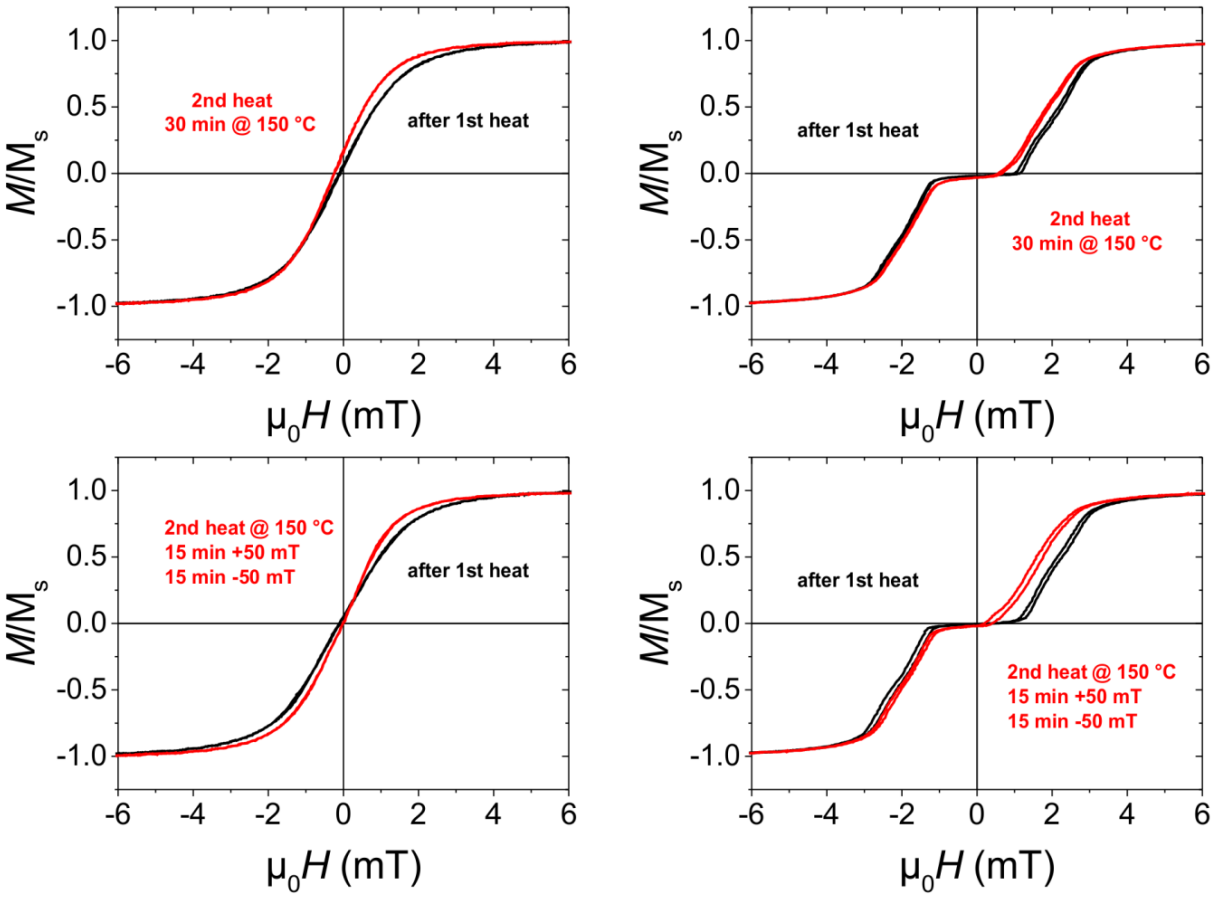

Supp. 11: Inductively measured magnetization responses along the long (left) and short (right) axes for two different sensors with tilted anisotropy. The measurements indicate the effect of different temperature handling on the change of anisotropy.

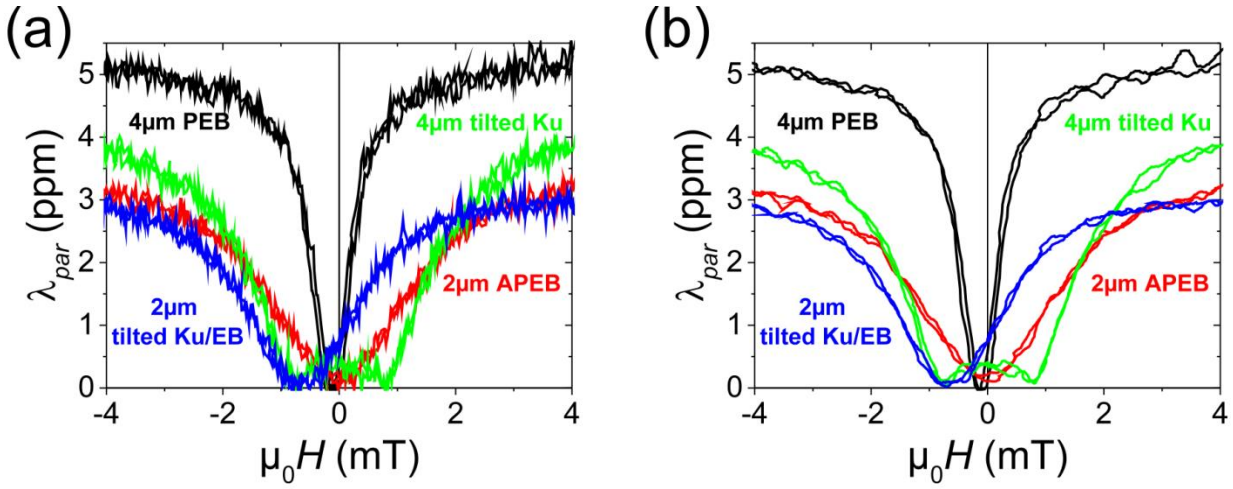

Supp. 12: (a) Magnetostriction measurements along the long axis with the field application along the same axis (measurements conducted by Lars Thormählen). (b) Smoothened magnetostriction responses of the data presented in (a). The smoothening was done with Savitzky-Golay method, 4th polynomial order and with a 30 points smoothening window. The data is obtained for all the different sensor types discussed so far. The 4 µm tilted Ku sensor holds a large degree of anisotropy rotation forming the middle flat region in the magnetization response. From the magnetostriction the counteracting rotation in this region is confirmed by the minute magnetostriction response in the corresponding field range.

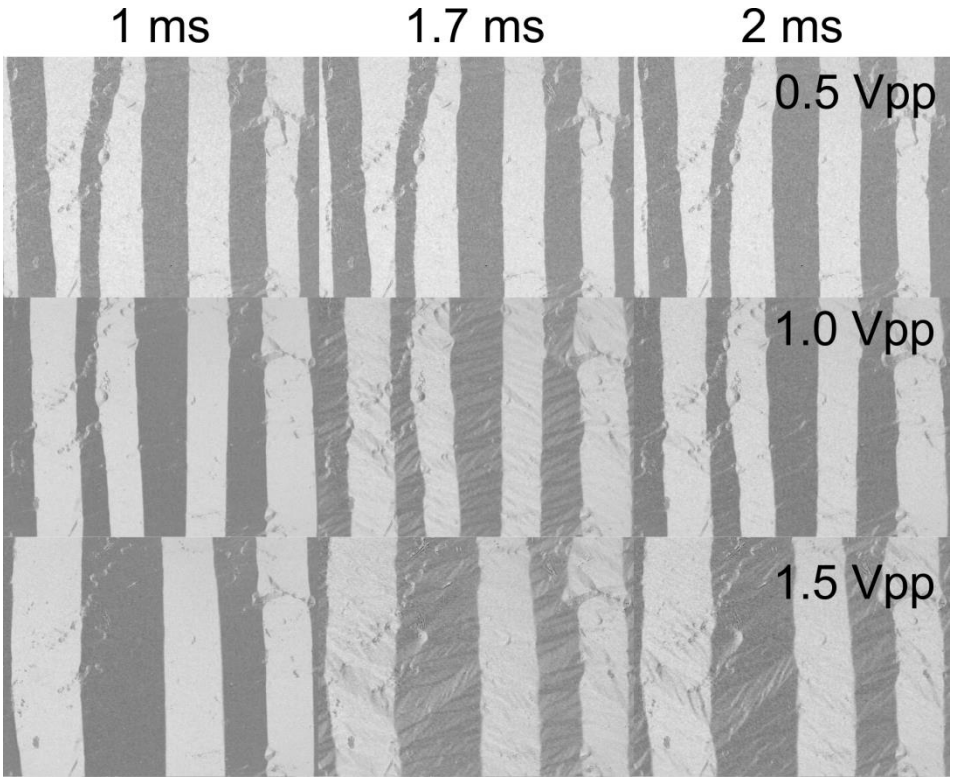

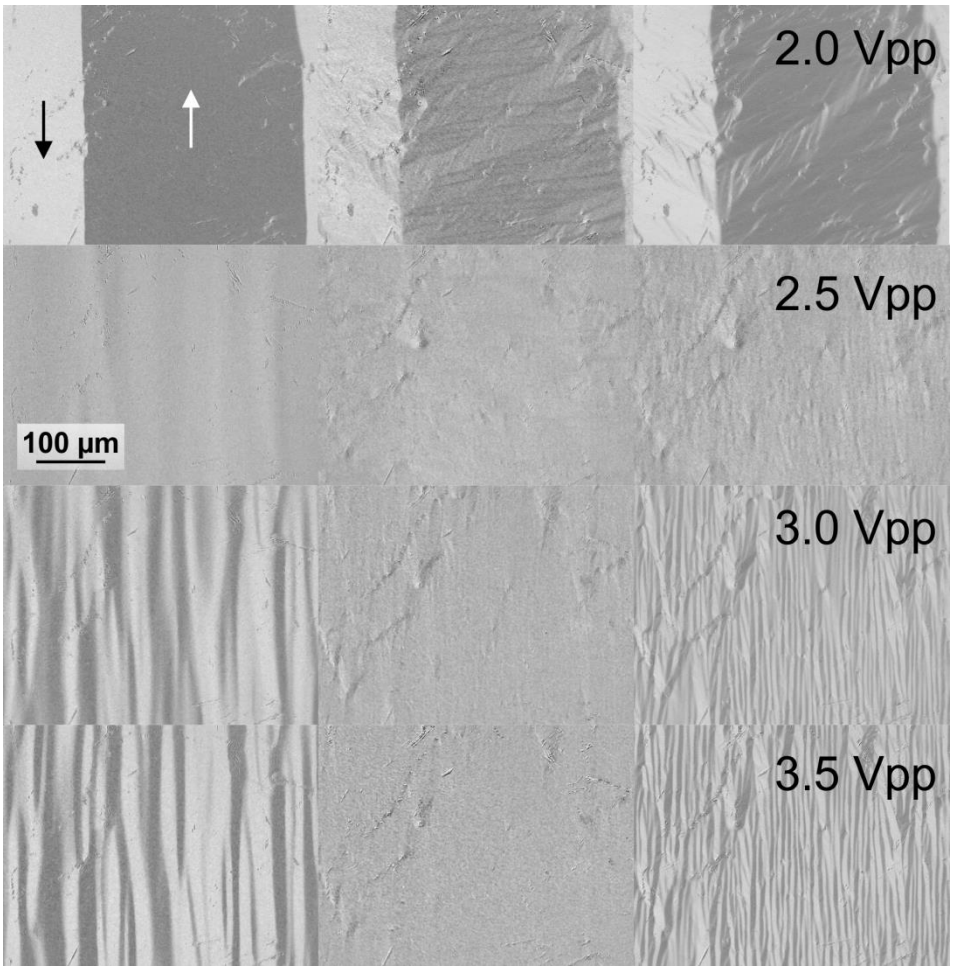

Supp. 13: Domain states at 3 specific time points of excitation corresponding to the upward flapping motion of the sensor through a range of excitation amplitudes. The position is at 1/3 of the length of sensor from the sensor tip. The total time of one oscillation period is 1.935 µs. The MO contrast is set along the short axis at which the long edge of the sensor is aligned horizontally. Note, the image is separated into two parts on two separate pages due to the size of the whole image. The sensor was fabricated by Viktor Schell.

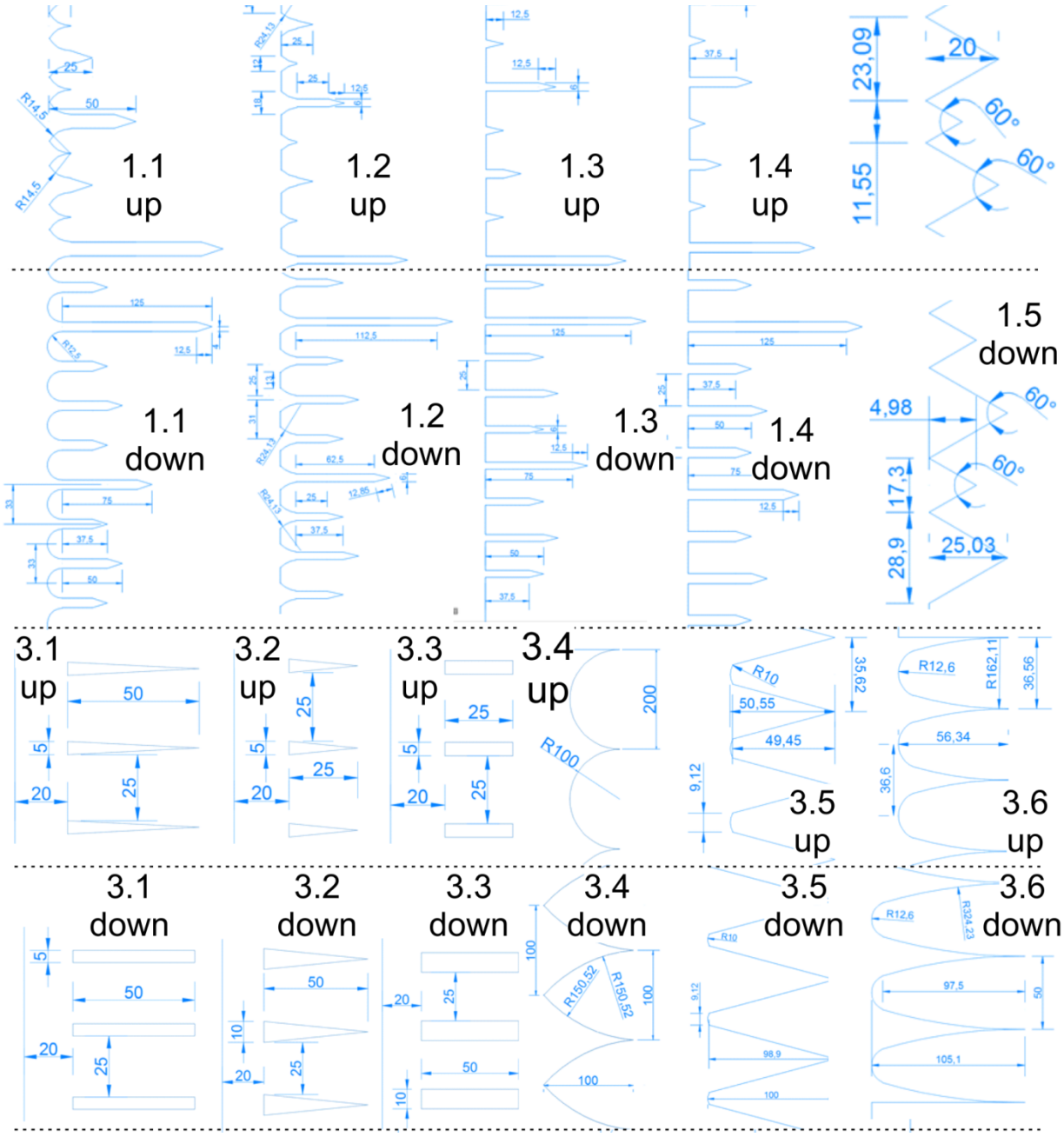

Supp. 14: Schematic of the various edge and insert structures to manipulate the magnetic structure. The marked dimensions are in µm.

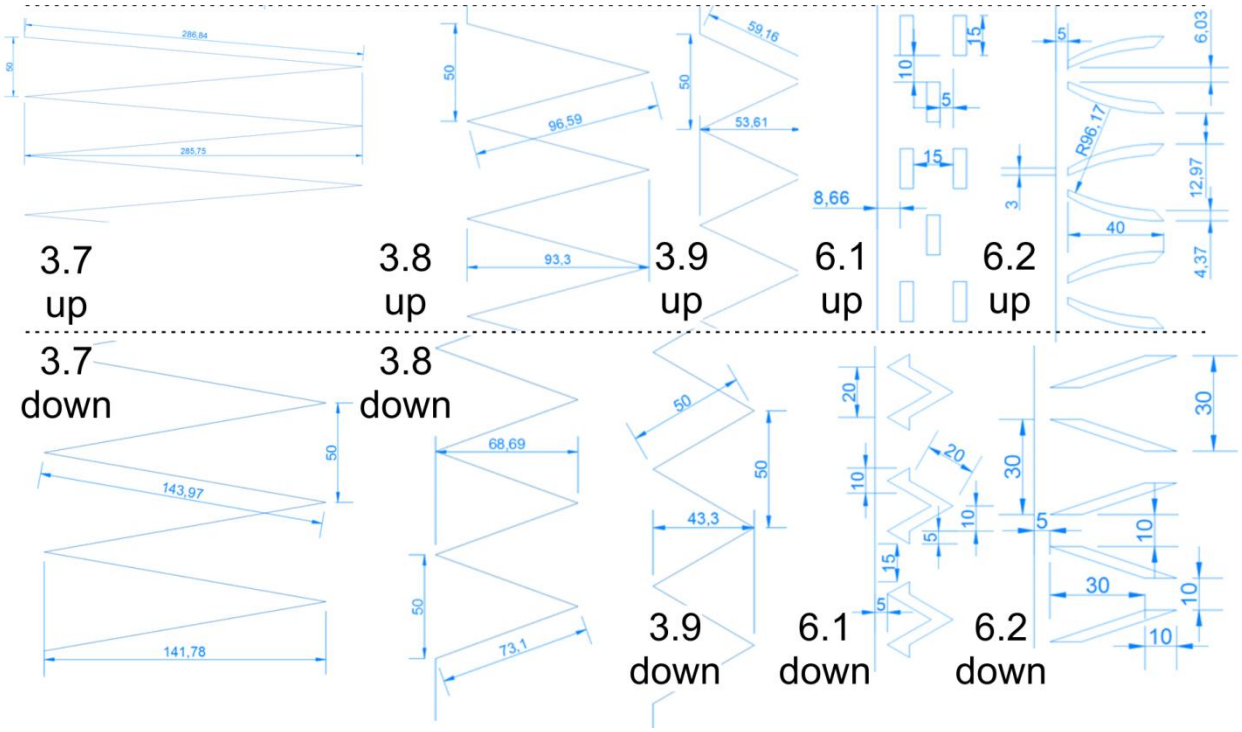

Supp. 15: Schematic of the various edge and insert structures to manipulate the magnetic structure. The marked dimensions are in µm.

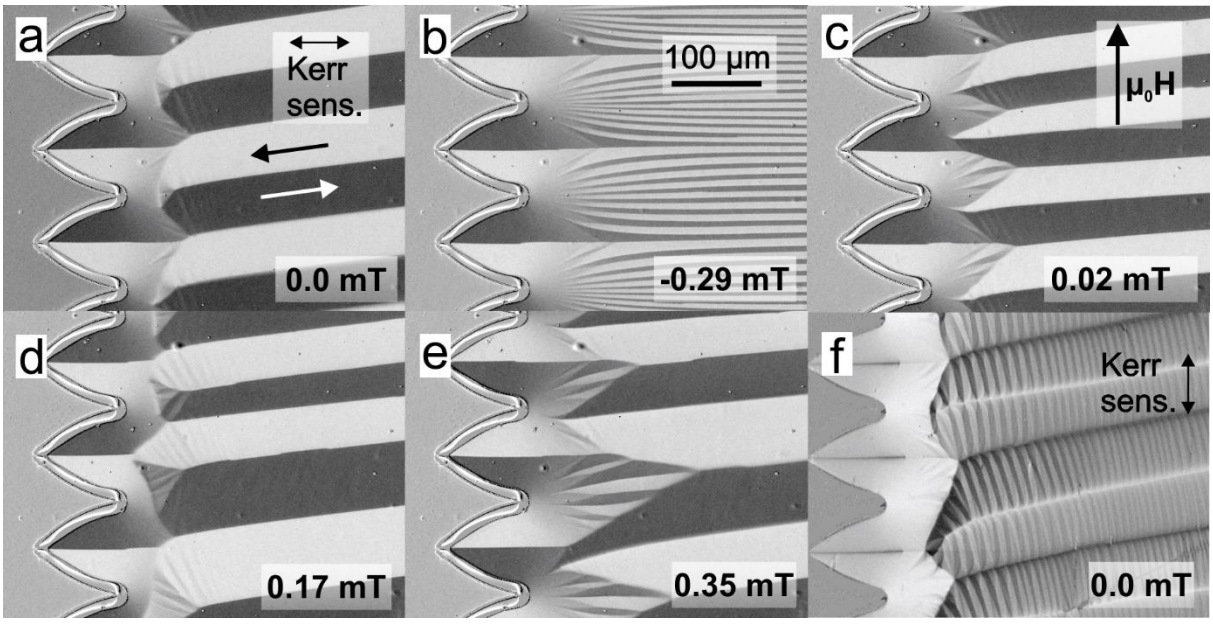

Supp. 16: (a) Demagnetized domain state of a bullet-shaped edge structure of a single layer system. (b)-(e) Evolution of domain states with applied magnetic field along the long axis. (f) Image with MO sensitivity along the long axis, indicating the directional character of the edge and modulated structure inside the 180° domains. The sample was fabricated by Rahel Kruppe.

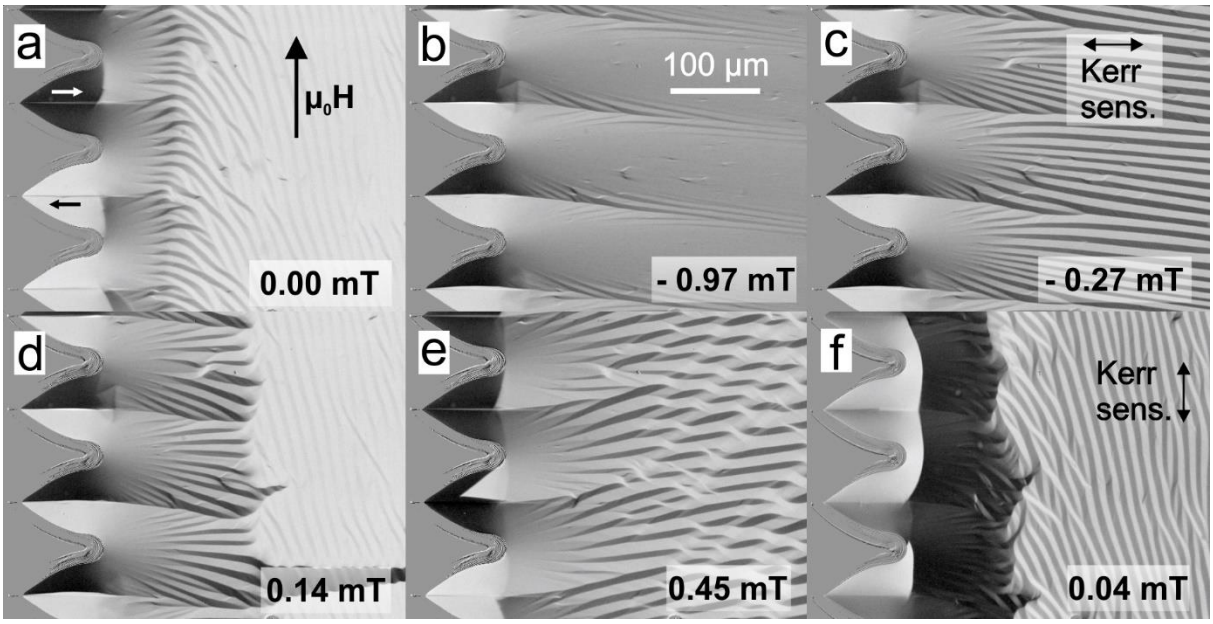

Supp. 17: (a) Demagnetized domain state of a bullet-shaped edge structure of a PEB layer system. (b)-(e) Evolution of domain states with applied magnetic field along the long axis. (f) Image with sensitivity along the long axis, indicating the directional character of the edge and modulated structure. The sample was fabricated by Rahel Kruppe.

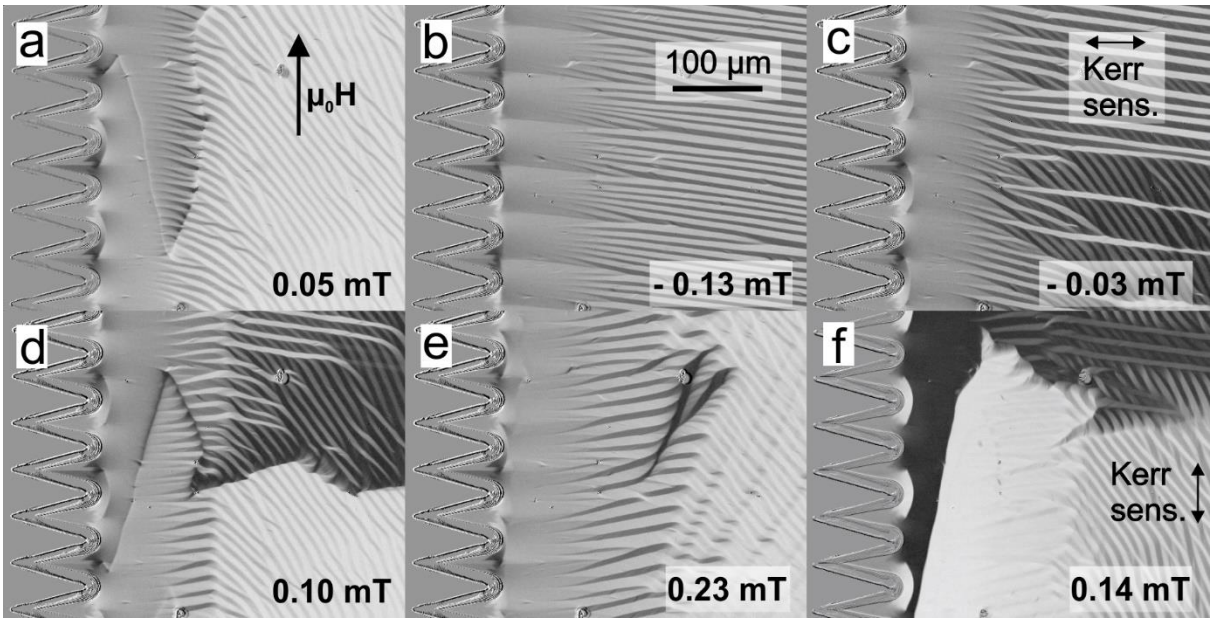

Supp. 18: (a) Near zero field domain state of a triangle-shaped edge structure of a PEB layer system. (b)-(e) Evolution of domain states with applied magnetic field along the long axis. (f) Image with MO sensitivity along the long axis, indicating the directional character of the edge and modulated structure. The sample was fabricated by Rahel Kruppe.

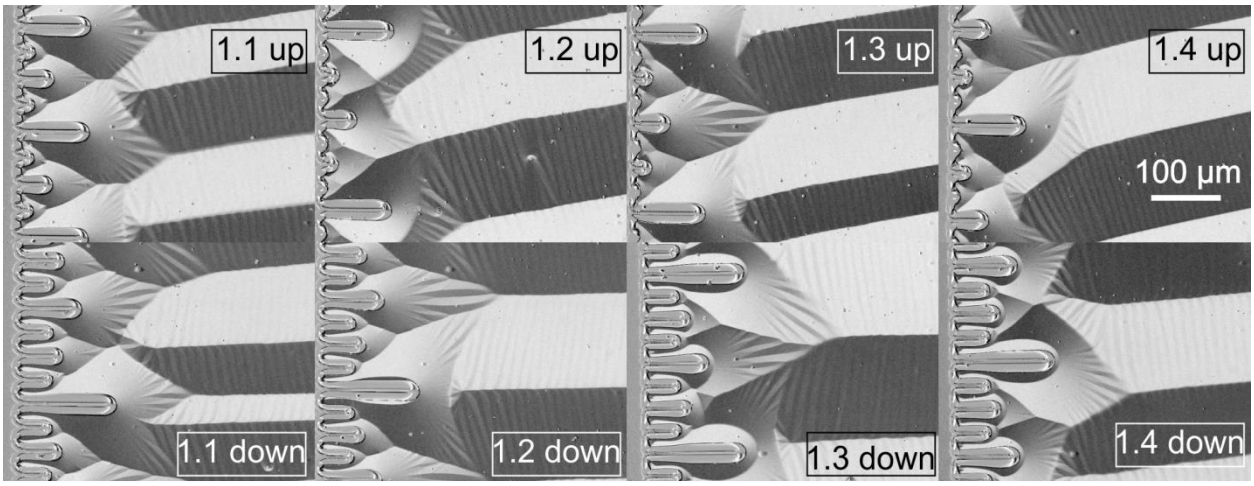

Supp. 19: Comparison of demagnetized states of the different lancet structures of a single layer system. The comparison shows the preferential alignment of the domains along the short axis for the longer lancet structures. The MO contrast is set horizontally. The sample was fabricated by Rahel Kruppe.

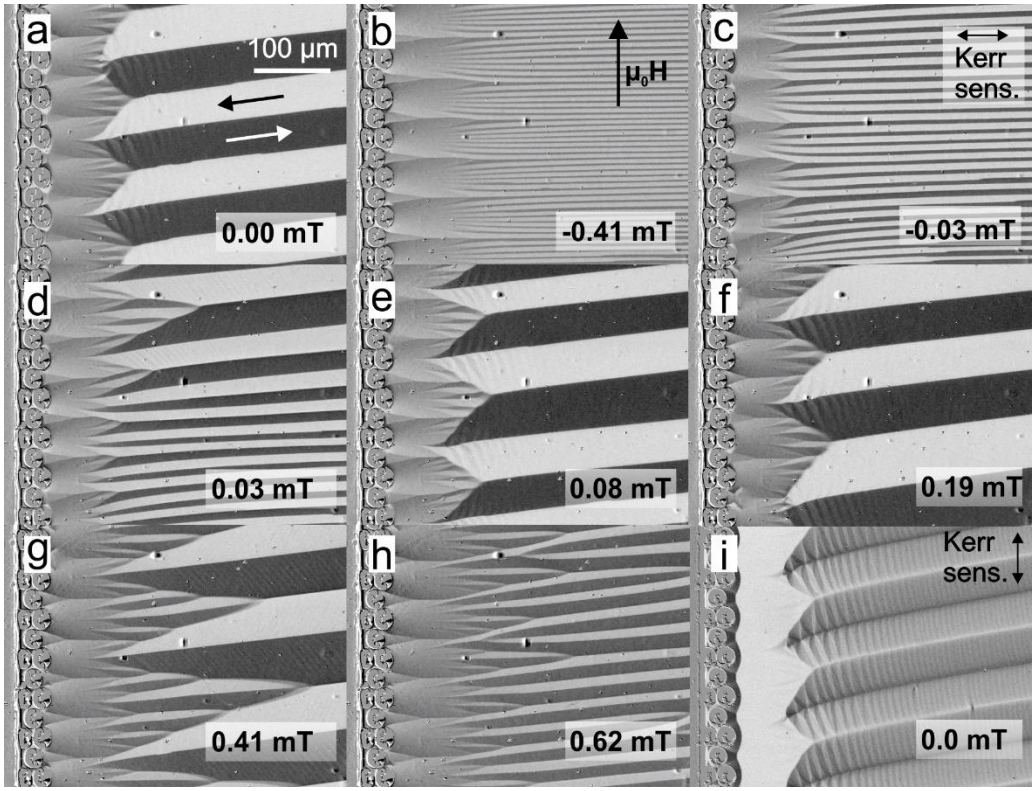

Supp. 20: (a) Demagnetized domain state of a 3 square insert structure of a single layer system. (b)-(h) Evolution of domain states with applied magnetic field along the long axis. (f) Image with MO sensitivity along the long axis, indicating the directional character of the

edge and modulated structure inside the 180° domains. The sample was fabricated by Rahel Kruppe.

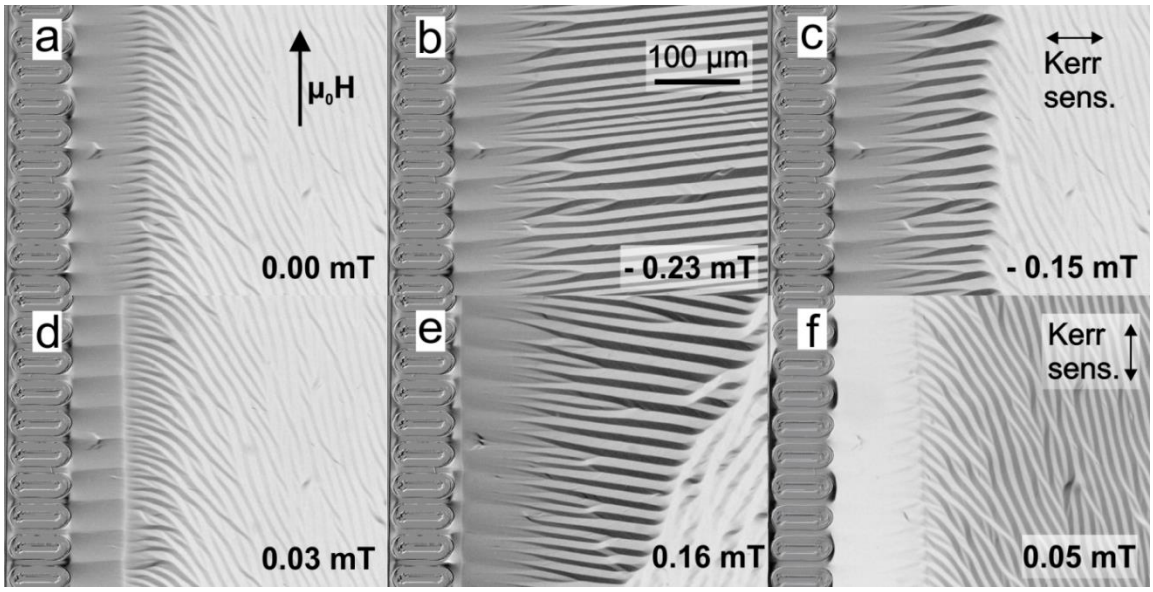

Supp. 21: (a) Demagnetized domain state of a square insert structure of a PEB layer system. (b)-(e) Evolution of domain states with applied magnetic field along the long axis. (f) Image with MO sensitivity along the long axis, indicating the directional character of the edge and modulated structure. The sample was fabricated by Rahel Kruppe.

List of appended multimedia

The list holds the referenced video files. The files are in AVI form and should be playable on standard coded video players. Note of caution, the files have uncompressed full data and can lag during visualization, due to insufficient processing power of the computer. In case of difficulties, the reader is advised to use ImageJ, a freeware program used for image processing and visualization.

Video 1: Barkhausen jump, wall impedes on two defects. The wall moves due to a horizontally applied field directed towards the left-hand side. The field values are given in the bottom section of the video. The MO sensitivity is set along the vertical direction.

Video 2: Magnetic state of a single domain 2 μm APEB sensor with an applied field along the long axis. The MO sensitivity is set along the short axis of the sensor. The field values are given in the bottom section of the video.

Video 3: Example of escalator moving domains on patterned edge structures with AC field application along the horizontal axis with 0.25 mT amplitude and 21 Hz frequency. The MO sensitivity is set along the short axis of the structures.

Video 4: Example of escalator moving domains on another set of structures with AC field application along the horizontal axis with 0.35 mT amplitude and 21 Hz frequency. The MO sensitivity is set along the horizontal direction.

Video 5: The gradual motion of domains with AC field excitation with amplitude of 0.4 mT and frequency of 1 Hz. The field is applied along the short axis. The MO sensitivity is set along the horizontal direction.

Video 6: The gradual motion of domains with AC field excitation with amplitude of 0.4 mT and frequency of 21 Hz. The field is applied along the short axis. The MO sensitivity is set along the horizontal direction.

Video 7: The gradual motion of domains with AC field excitation with amplitude of 0.4 mT and frequency of 21 Hz. The field is applied along the short axis (15° tilted with the structure). The images are substracted from the beginning state and the images are 8x averaged. The MO sensitivity is set along the horizontal direction.

Video 8: Wave-like motion of domains with AC field excitation of 0.5 mT amplitude at 1 Hz. The field is applied vertically. The MO sensitivity is set along the horizontal direction.

Video 9: The change of the domain state with temperature during cooling. Note: the temperature evolution has been reversed in order to allow easier visualization of the change of the domain state. The MO sensitivity is set along the horizontal direction.

Video 10: Twitching of domains with the application of a heat pulse from the heating plate. The moment of the heater activation is denoted in the video. The MO sensitivity is set along the horizontal direction.

List of developed sensors

The list is intended to provide a short summary of all the sensors developed, researched and characterized in this work. The table below shows the sensors characterized using direct detection and MFC. The table has all the necessary information about each sensor and its figures of merit.

Name˝	Structure×	Type°	f_{res} (Hz)	Opt. bias (mT)*	Direct det. LOD (pT)	MFC det. LOD (pT)	Bandwidth (Hz) / SNR†
200	5x 90/110	PEB	851	+0.67 (-)	60	350	N.A.
201	5x 90/110	PEB	863	+0.72 (+)	60	250	N.A.
202	5x 90/110	PEB	872	+0.33 (-)	70	300	N.A.
203	5x 90/110	PEB	844	+0.33 (-)	20	100	N.A.
204	5x 90/110	APEB	862	-0.12 (-)	10	150	N.A.
205	10x 90/110	PEB	853	+0.22 (+)	30	150	N.A.
206	10x 90/110	PEB	862	+0.49 (+)	10	500	N.A.
207	10x 90/110	PEB	853	-0.13 (-)	15	150	N.A.
208	10x 90/110	PEB	837	-0.24 (-)	10	150	N.A.
209	20x 90/110	PEB	836	+0.36 (-)	15	300	N.A.
210	20x 90/110	PEB	855	+0.53 (-)	10	250	N.A.
211	20x 90/110	PEB	874	+0.4 (-)	15	300	N.A.
212	8x500	APEB	846	+0.36 (-)	10	280	N.A.
213	10x 90/110	APEB	845	+1.12 (+)	40	150	N.A.
214	20x 90/110	APEB	855	-1.05 (-)	15	90	N.A.
215	5x 90/110	APEB	826	-0.12 (-)	100	300	N.A.
216	5x 90/110	APEB	853	+0.14 (-)	100	150	N.A.
217	10x 90/110	APEB	843	-0.12 (-)	15	90	N.A.
218	10x 90/110	APEB	843	0.13 (+)	20	180	N.A.
219	20x 90/110	APEB	862	-1.17 (-)	20	160	N.A.
220	20x 90/110	APEB	849	-1.1 (-)	20	100	N.A.
221	2x500	APEB	871	+0.32 (-)	30	330	N.A.
222-cl	20x 90/110	APEB	846	-1.01 (-)	15	80	N.A.
222a_cl	20x 90/110	APEB	850	+1.08 (+)	15	110	N.A.

223	4x500	APEB	848	+0.36 (-)	12	280	N.A.
224	8x500	APEB	850	-0.38 (+)	12	330	N.A.
245-100	5x 90/110	PEB	762	-0.82 (-)	85	939	2.56 / 43
246-101	5x 90/110	PEB	825	0.39 (-)	92	433	1.74 / 51
250-102	5x 90/110	PEB	812	+0.52 (-)	428	1007	1.61 / 42
239-103	10x 90/110	PEB	798	+0.51 (-)	37	352	2.29 / 48
240-104	10x 90/110	PEB	832	+0.38 (-)	20	160	2.22 / 55
248-105	10x 90/110	PEB	813	-0.27 (+)	19	147	1.6 / 60
235-106	20x 90/110	PEB	822	+0.32 (+)	9	307	2.56 / 51
236-107	20x 90/110	PEB	820	-0.13 (-)	5	91	1.69 / 62
247-108	20x 90/110	PEB	802	-0.22 (-)	8	85	1.78 / 63
244-91	5x 90/110	APEB	837	+1.23 (+)	75	497	2.09 / 48
243-92	5x 90/110	APEB	887	+1.31 (+)	65	1050	2.00 / 48
251-93	5x 90/110	APEB	872	+1.21 (+)	138	518	2.93 / 46
241-94	10x 90/110	APEB	830	+1.15 (+)	28	540	1.6 / 51
242-95	10x 90/110	APEB	768	+1.21 (+)	88	571	1.89 / 48
249-96	10x 90/110	APEB	837	-1.19 (-)	43	357	3.58 / 50
237-97	20x 90/110	APEB	818	+1.12 (+)	15	167	1.45 / 55
238-98	20x 90/110	APEB	819	+1.06 (+)	16	179	1.7 / 52
252-109	20x 90/110	APEB	817	-0.99 (-)	17	491	1.96 / 48
253-110	10x 90/110	APEB/TK	804	0.79 (+)	30	197	1.98 / 54
252-112	5x 90/110	APEB	825	-1.13 (+)	75	525	2.22 / 47
255-113	5x 90/110	APEB	839	+1.11 (-)	64	548	2.71 / 49
258-114	5x 90/110	APEB	854	+1.10 (-)	102	410	1.99 / 51
250-115	10x 90/110	APEB	782	-1.10 (+)	41	290	1.7 / 52
254-116	10x 90/110	APEB	595	-1.17 (+)	124	464	6 / 50
257-117	10x 90/110	APEB	827	-1.09 (-)	35	315	2.75 / 50
251-118	20x 90/110	APEB	849	+0.94 (-)	17	229	2.06 / 58
253-119	20x 90/110	APEB	821	+1.03 (-)	23	310	3 / 52
256-120	20x 90/110	APEB	839	+0.97 (-)	20	151	1.75 / 58
260-clEB	20x 90/110	PEB	834	+0.20 (-)	17	137	2.97 / 58
Tilt30	20x 90/110	APEB/TK	833	+0.80 (-)	75	126	2.50 / 57
Tilt32	20x 90/110	APEB/TK	848	+0.75 (-)	102	579	2.15 / 48

Tilt4	**10x 90/110**	**APEB/TE**	**837**	**+0.86 (-)**	**65**	**377**	**3.59 / 59**
Tilt5	**10x 90/110**	**APEB/TE**	**821**	**-0.66 (+)**	**27**	**372**	**2.32 / 52**
Tilt10	**10x 90/110**	**APEB/TE**	**818**	**-0.47 (+)**	**10**	**500**	**2.38 / 49**
Tilt11	**10x 90/110**	**APEB/TE**	**782**	**-0.177 (+)**	**10**	**1902**	**2.52/ 40**

˝Name: electric characterization index-magnetic characterization index

° PEB – parallel EB, APEB – antiparallel EB, TK – tilted Ku, TE – tilted Ku/EB

× 90/110 - [90 nm FeCoSiB / 8 nm MnIr / 5nm Ta / 110 nm FeCoSiB / 8 nm MnIr], 500 – [500 nm FeCoSiB / 8 nm MnIr / 5nm Ta]

*** Sign of saturation field from which the optimal bias is set, is denoted by (-) and (+) symbols.**

† For MFC detection, bandwidth is measured at -3 dB

Scientific contributions

Publications

1. Antiparallel exchange biased multilayers for low magnetic noise magnetic field sensors; M. Jovičević Klug, L. Thormählen, V. Röbisch, S. D. Toxværd, M. Höft, R. Knöchel, E. Quandt, D. Meyners, J. McCord, Appl. Phys. Lett. 114, 192410 (2019).

2. Influence of magnetic domain wall orientation on Barkhausen Noise and magneto-mechanical behavior in electrical steel; F. Qiu, M. Jovičević Klug, G. Tian, P. Hu, and J. McCord, J. Phys. D. Appl. Phys. 52, 265001 (2019).

3. Noise Limits in Thin-Film Magnetoelectric Sensors with Magnetic Frequency Conversion; S. Salzer, V. Röbisch, M. Klug, P. Durdaut, J. McCord, D. Meyners, J. Reermann, M. Höft, R. Knöchel: , IEEE Sens. J. 18, (2018).

Conferences

Oral presentations

1. Extinction of Magnetic Noise Contributions through Magnetic Domain Stabilization in Magnetoelectric Composite Sensors, M. Jovičević Klug, L. Thormählen, S. D. Toxværd, V. Röbisch, M. Höft, E. Quandt, D. Meyners, J. McCord, Intelligent Materials 2019, Kiel, Germany, June 2019

2. Single Domain Stabilization with Antiparallel Exchange Bias – A Novel Concept for Low Noise Composite Magnetoelectric Sensors; M. Klug, V. Röbisch, S. Salzer, L. Thormählen, M. Höft, E. Quandt, D. Meyners, J. McCord, JEMS 2018, Mainz, Germany, September 2018

3. Magneto-Optical Investigations of Tailored Exchange Biased Magnetoelectric Composites for Biomagnetic Field Sensing; M. Klug, V. Röbisch, N. O. Urs, E. Quandt, D. Meyners, J. McCord, Intelligent Materials 2017, Kiel, Germany, June 2017

Posters

1. Magnetic Noise Extinction through Single Domain Stabilization with Antiparallel Exchange Bias in Magnetoelectric Composite Sensors; M. Jovičević Klug, L. Thormählen, S. D. Toxværd, V. Röbisch, D. Meyners, R. Knöchel, M. Höft, E. Quandt, J. McCord: , Planica, Slovenia, April 2019

2. Large STT-driven domain wall velocities in perpendicularly magnetized Mn4N ferrimagnetic thin films; T. Gushi, M. Klug et. al., JEMS 2018, Mainz, Germany, September 2018

3. Magnetostrictive Multilayers for Magnetoelectric Sensors; M. Klug, V. Röbisch, S. Salzer, F. Klingbeil, E. Quandt, D. Meyners, M. Höft, R. Knöchel, J. McCord, ESM 2017, Cargèse, France, October 2017

Bibliography

[1] S.-J. Cheng *et al.*, "Correlation of magnetostriction variation on magnetic loss and noise for power transformer," *J. Appl. Phys.*, vol. 117, no. 17, p. 17E716, May 2015.

[2] A. O. Watanabe, P. M. Raj, D. Wong, R. Mullapudi, and R. Tummala, "Multilayered Electromagnetic Interference Shielding Structures for Suppressing Magnetic Field Coupling," *J. Electron. Mater.*, vol. 47, no. 9, pp. 5243–5250, Sep. 2018.

[3] K. Nakamoto, S. Narumi, T. Kawabe, T. Kobayashi, and H. Fukui, "Shield-related signal instability in magnetoresistive heads," *J. Appl. Phys.*, vol. 85, no. 8, pp. 5846–5848, Apr. 1999.

[4] J. McCord, H. Zolla, and H. Grimm, "Influence of magnetic properties of shields on recording head instability parameters," *IEEE Trans. Magn.*, vol. 39, no. 5, pp. 2384–2386, Sep. 2003.

[5] C. Tsang and S. K. Decker, "The origin of Barkhausen noise in small permalloy magnetoresistive sensors," *J. Appl. Phys.*, vol. 52, no. 3, pp. 2465–2467, Mar. 1981.

[6] E. Puppin, E. Pinotti, and M. Brenna, "Barkhausen noise in variable thickness amorphous finemet films," *J. Appl. Phys.*, vol. 101, no. 6, p. 063903, Mar. 2007.

[7] M. Lambeck, "Barkhausen-Effekt und Nachwirkung in Ferromagnetika sowie analoge Erscheinungen in der Festkörperphysik," *de Gruyter*, 1971.

[8] S. Middelhoek, "Static Reversal Processes in Thin Ni-Fe Films," *IBM J. Res. Dev.*, vol. 6, no. 4, pp. 394–406, Oct. 1962.

[9] K. Kuijk, W. van Gestel, and F. Gorter, "The barber pole, a linear magnetoresistive head," *IEEE Trans. Magn.*, vol. 11, no. 5, pp. 1215–1217, Sep. 1975.

[10] J. McCord, A. Hubert, G. Schropfer, and U. Loreit, "Domain observation on magnetoresistive sensor elements," *IEEE Trans. Magn.*, vol. 32, no. 5, pp. 4806–4808, 1996.

[11] U. Dibbern, "Magnetoresistive Sensors," in *Sensors*, Weinheim, Germany: Wiley-VCH Verlag GmbH, 2008, pp. 341–380.

[12] C. Tsang, "Magnetics of small magnetoresistive sensors (invited)," *J. Appl. Phys.*, vol. 55, no. 6, pp. 2226–2231, Mar. 1984.

[13] E. Lage *et al.*, "Exchange biasing of magnetoelectric composites," *Nat. Mater.*, vol. 11, no. 6, pp. 523–529, Jun. 2012.

[14] J. C. Slonczewski, B. Petek, and B. E. Argyle, "Micromagnetics of laminated permalloy-films," *IEEE Trans. Magn.*, vol. 24, no. 3, p. 2045, 1988.

[15] I. G. Trindade *et al.*, "Soft Thin Films for Flux Concentrators," *IEEE Trans. Magn.*, vol. 45, no. 1, pp. 168–171, Jan. 2009.

[16] D. Viehland, M. Wuttig, J. McCord, and E. Quandt, "Magnetoelectric magnetic field sensors," *MRS Bull.*, vol. 43, no. 11, pp. 834–840, Nov. 2018.

[17] M. Bichurin, V. Petrov, V. Leontyev, and A. Saplev, "Two-range magnetoelectric sensor," *AIP Adv.*, vol. 7, no. 1, 2017.

[18] C. M. Leung, J. Li, D. Viehland, and X. Zhuang, "A review on applications of magnetoelectric composites: from heterostructural uncooled magnetic sensors, energy harvesters to highly efficient power converters," *J. Phys. D. Appl. Phys.*, vol. 51, no. 26, p. 263002, Jul. 2018.

[19] X. Zhuang *et al.*, "Tunable Magnetoelectric Bending Resonance for Sensing Static Magnetic Fields," *IEEE Sens. J.*, vol. 16, no. 3, pp. 662–669, Feb. 2016.

[20] E. Yarar *et al.*, "Inverse bilayer magnetoelectric thin film sensor," *Appl. Phys. Lett.*, vol. 109, no. 2, 2016.

[21] V. Röbisch *et al.*, "Exchange biased magnetoelectric composites for magnetic field sensor application by frequency conversion," *J. Appl. Phys.*, vol. 117, no. 17, pp. 1–5, May 2015.

[22] S. Zabel, C. Kirchhof, E. Yarar, D. Meyners, E. Quandt, and F. Faupel, "Phase modulated magnetoelectric delta-E effect sensor for sub-nano tesla magnetic fields," *Appl. Phys. Lett.*, vol. 107, no. 15, 2015.

[23] V. Röbisch *et al.*, "Pushing the detection limit of thin film magnetoelectric heterostructures," *J. Mater. Res.*, vol. 32, no. 6, pp. 1009–1019, 2017.

[24] N. O. Urs, I. Teliban, A. Piorra, R. Knöchel, E. Quandt, and J. McCord, "Origin of hysteretic magnetoelastic behavior in magnetoelectric 2-2 composites," *Appl. Phys. Lett.*, vol. 105, no. 20, pp. 2012–2017, 2014.

[25] S. Salzer *et al.*, "Noise limits in thin-film magnetoelectric sensors with magnetic frequency conversion," *IEEE Sens. J.*, vol. 18, no. 2, 2018.

[26] A. Hubert and R. Schäfer, *Magnetic Domains. The Analysis of Magnetic Microstructures*, 3rd ed. Springer, 2009.

[27] B. D. Cullity and C. D. Graham, *Introduction to magnetic materials*, 2nd ed., vol. 12, no. 3. John Wiley & Sons Inc., 2009.

[28] R. C. O'Handley, *Modern Magnetic Materials: Principles and Applications*. John Wiley & Sons Inc., 2000.

[29] A. Aharoni, "'Local' Demagnetization in a Rectangular Ferromagnetic Prism," *Phys. Status Solidi B*, vol. 229, no. 3, pp. 1413–1416, Feb. 2002.

[30] S. Chikazumi and T. Oomura, "On the Origin of Magnetic Anisotropy Induced by Magnetic Annealing," *J. Phys. Soc. Japan*, vol. 10, no. 10, pp. 842–849, Oct. 1955.

[31] S. Chikazumi, *Physics of Ferromagnetism*, 2nd ed. Oxford University Press, 2005.

[32] P. Bruno and C. Chappert, "Interlayer Exchange Coupling: RKKY Theory and Beyond," *Magn. Struct. Syst. Reduc. Dimens.*, pp. 389–399, 1993.

[33] P. Bruno, "Theory of interlayer magnetic coupling," *Phys. Rev. B*, vol. 52, no. 1, 1995.

[34] L. Néel, "Magnetisme-sur un nouveau mode de couplage entre les animantations de deux couches minces ferromagnetiques," *C. R. Acad. Sci*, vol. 255, pp. 1676–1681, 1962.

[35] J. C. S. Kools, W. Kula, D. Mauri, and T. Lin, "Effect of finite magnetic film thickness on Néel coupling in spin valves," *J. Appl. Phys.*, vol. 85, no. 8, pp. 4466–4468, Apr. 1999.

[36] T. R. Gao *et al.*, "Exchange bias, training effect, hysteretic behavior of angular dependence, and rotational hysteresis loss in NiFe/FeMn bilayer: Effect of antiferromagnet layer thickness," *J. Appl. Phys.*, vol. 105, no. 5, p. 053913, Mar. 2009.

[37] M. Kiwi, "Exchange bias theory," *J. Magn. Magn. Mater.*, vol. 234, no. 3, pp. 584–595, 2001.

[38] W. H. Meiklejohn and C. P. Bean, "New Magnetic Anisotropy," *Phys. Rev.*, vol. 102, no. 5, pp. 1413–1414, Jun. 1956.

[39] T. C. Schulthess and W. H. Butler, "Consequences of Spin-Flop Coupling in Exchange Biased Films," *Phys. Rev. Lett.*, vol. 81, no. 20, pp. 4516–4519, Nov. 1998.

[40] T. C. Schulthess and W. H. Butler, "Coupling mechanisms in exchange biased films (invited)," *J. Appl. Phys.*, vol. 85, no. 8, pp. 5510–5515, Apr. 1999.

[41] N. C. Koon, "Calculations of Exchange Bias in Thin Films with Ferromagnetic/Antiferromagnetic Interfaces," *Phys. Rev. Lett.*, vol. 78, no. 25, pp. 4865–4868, Jun. 1997.

[42] T. M. Hong, "Simple mechanism for a positive exchange bias," *Phys. Rev. B*, vol. 58, no. 1, pp. 97–100, Jul. 1998.

[43] S. Anandakumar, V. S. Rani, S. Oh, and C. Kim, "Positive and negative exchange bias in IrMn/NiFe bilayers," *Thin Solid Films*, vol. 519, no. 3, pp. 1020–1024, Nov. 2010.

[44] A. P. Malozemoff, "Random-field model of exchange anisotropy at rough ferromagnetic-antiferromagnetic interfaces," *Phys. Rev. B*, vol. 35, no. 7, pp. 3679–3682, Mar. 1987.

[45] M. Fähnle and J. Furthmüller, "The effect of external stress on the saturation magnetostriction constant of metallic glasses," *Phys. Status Solidi*, vol. 116, no. 2, pp. 819–825, Dec. 1989.

[46] G. Herzer, S. Flohrer, C. Polak, V. Gmbh, C. Kg, and D.- Hanau, "Effect of Stress Annealing on the Saturation Magnetostriction of Nanocrystalline Fe73.5Cu1Nb3Si15.5B7," *IEEE Trans. Magn.*, vol. 46, no. 2, pp. 341–344, 2010.

[47] N. A. Spaldin, *Magnetic Materials: Fundamentals and Applications*, 2nd ed. Cambridge: Cambridge University Press, 2011.

[48] N. A. Hill, "Why Are There so Few Magnetic Ferroelectrics?," *J. Phys. Chem. B*, vol. 104, no. 29, pp. 6694–6709, Jul. 2000.

[49] M. I. Bichurin, V. M. Petrov, and R. V. Petrov, "Direct and inverse magnetoelectric effect in layered composites in electromechanical resonance range: A review," *J. Magn. Magn. Mater.*, vol. 324, no. 21, pp. 3548–3550, Oct. 2012.

[50] Z. Chu, M. PourhosseiniAsl, and S. Dong, "Review of multi-layered magnetoelectric composite materials and devices applications," *J. Phys. D. Appl. Phys.*, vol. 51, no. 24, p. 243001, Jun. 2018.

[51] M. D. Mermelstein and A. Dandridge, "Low-frequency magnetic field detection with a magnetostrictive amorphous metal ribbon," *Appl. Phys. Lett.*, vol. 51, no. 7, pp. 545–547, Aug. 1987.

[52] Y. Wang *et al.*, "An extremely low equivalent magnetic noise magnetoelectric sensor," *Adv. Mater.*, vol. 23, no. 35, pp. 4111–4114, Sep. 2011.

[53] E. Yarar, V. Hrkac, C. Zamponi, A. Piorra, L. Kienle, and E. Quandt, "Low temperature aluminum nitride thin films for sensory applications," *AIP Adv.*, vol. 6, no. 7, p. 075115, Jul. 2016.

[54] K. C. Cheng, H. L. W. Chan, C. L. Choy, Q. R. Yin, H. S. Lu, and Z. W. Yin, "Piezoelectric coefficients of PMN-0.33PT single crystals," in *ISAF 2000. Proceedings of the 2000 12th IEEE International Symposium on Applications of Ferroelectrics (IEEE Cat. No.00CH37076)*, vol. 2, pp. 533–536.

[55] X. Jiang, F. Tang, J. T. Wang, and T.-P. Chen, "Growth and properties of PMN–PT single crystals," *Phys. C Supercond. its Appl.*, vol. 364–365, pp. 678–683, Nov. 2001.

[56] S. Zhao, S. J. Zhang, W. Liu, N. J. Donnelly, Z. Xu, and C. A. Randall, "Time dependent dc resistance degradation in lead-based perovskites: 0.7 Pb(Mg1/3Nb2/3)O3−0.3 PbTiO3," *J. Appl. Phys.*, vol. 105, no. 5, p. 053705, Mar. 2009.

[57] R. Jahns, H. Greve, E. Woltermann, E. Quandt, and R. Knöchel, "Sensitivity enhancement of magnetoelectric sensors through frequency-conversion," *Sensors Actuators, A Phys.*, vol. 183, pp. 16–21, Aug. 2012.

[58] M. Jovičević Klug *et al.*, "Antiparallel exchange biased multilayers for low magnetic noise magnetic field sensors," *Appl. Phys. Lett.*, vol. 114, no. 19, p. 192410, May 2019.

[59] F. N. Hooge, T. G. M. Kleinpenning, and L. K. J. Vandamme, "Experimental studies on 1/f noise," *Reports Prog. Phys.*, vol. 44, no. 5, pp. 479–532, May 1981.

[60] S. Salzer *et al.*, "Generalized Magnetic Frequency Conversion for Thin-Film Laminate Magnetoelectric Sensors," *IEEE Sens. J.*, vol. 17, no. 5, pp. 1373–1383, 2017.

[61] P. Hayes *et al.*, "Electrically modulated magnetoelectric AlN/FeCoSiB film composites for DC magnetic field sensing," *J. Phys. D. Appl. Phys.*, vol. 51, no. 35, p. 354002, Sep. 2018.

[62] P. Hayes *et al.*, "Converse Magnetoelectric Composite Resonator for Sensing Small Magnetic Fields," *Sci. Rep.*, 2019.

[63] S. Zabel *et al.*, "Multimode delta-E effect magnetic field sensors with adapted electrodes," *Appl. Phys. Lett.*, vol. 108, no. 22, p. 222401, May 2016.

[64] D. . Drung *et al.*, "Highly Sensitive and Easy-to-Use SQUID Sensors," *IEEE Trans. Appl. Supercond.*, vol. 17, no. 2, pp. 699–704, Jun. 2007.

[65] P. Brown *et al.*, "Magnetoresistive magnetometer for space science applications," *Meas. Sci. Technol.*, vol. 23, no. 2, p. 025902, Feb. 2012.

[66] Y.-S. Chiang, X. T. Trinh, and J.-T. Jeng, "Flat Bandwidth Expansion for Spin-Valve GMR Magnetic Field Sensors," *IEEE Trans. Magn.*, vol. 54, no. 11, pp. 1–4, Nov. 2018.

[67] S. H. Liou *et al.*, "Picotesla Magnetic Sensors for Low-Frequency Applications," *IEEE Trans. Magn.*, vol. 47, no. 10, pp. 3740–3743, Oct. 2011.

[68] M. Pannetier, C. Fermon, G. Le Goff, J. Simola, and E. Kerr, "Femtotesla magnetic field measurement with magnetoresistive sensors.," *Science*, vol. 304, no. 5677, pp. 1648–50, Jun. 2004.

[69] S. Ikeda *et al.*, "Tunnel magnetoresistance of 604% at 300K by suppression of Ta diffusion in CoFeB/MgO/CoFeB pseudo-spin-valves annealed at high temperature," *Appl. Phys. Lett.*, vol. 93, no. 8, p. 082508, Aug. 2008.

[70] F. Han, S. Harada, and I. Sasada, "Fluxgate and Search Coil Hybrid: A Low-Noise Wide-Band Magnetometer," *IEEE Trans. Magn.*, vol. 48, no. 11, pp. 3700–3703, Nov. 2012.

[71] P. Ripka, "Advances in fluxgate sensors," *Sensors Actuators A Phys.*, vol. 106, no. 1–3, pp. 8–14, Sep. 2003.

[72] H. Shi, Y. Wang, and J. Lin, "Optimized Design and Calibration of the Triaxis Induction Magnetometer with Crosstalk and Nonorthogonality Compensation," *J. Sensors*, vol. 2016, pp. 1–8, Aug. 2016.

[73] H. Karo and I. Sasada, "Magnetocardiogram measured by fundamental mode orthogonal fluxgate array," *J. Appl. Phys.*, vol. 117, no. 17, p. 17B322, May 2015.

[74] W. Happer, "Optical Pumping," *Rev. Mod. Phys.*, vol. 44, no. 2, pp. 169–249, Apr. 1972.

[75] E. Boto *et al.*, "A new generation of magnetoencephalography: Room temperature measurements using optically-pumped magnetometers," *Neuroimage*, vol. 149, pp. 404–414, Apr. 2017.

[76] T. H. Sander, J. Preusser, R. Mhaskar, J. Kitching, L. Trahms, and S. Knappe, "Magnetoencephalography with a chip-scale atomic magnetometer," *Biomed. Opt.*

Express, vol. 3, no. 5, p. 981, May 2012.

[77] E. Portalier, B. Dufay, S. Saez, and C. Dolabdjian, "Noise Behavior of High Sensitive GMI-Based Magnetometer Relative to Conditioning Parameters," *IEEE Trans. Magn.*, vol. 51, no. 1, pp. 1–4, Jan. 2015.

[78] G. L. S. Vilela, J. G. Monsalve, A. R. Rodrigues, A. Azevedo, and F. L. A. Machado, "Giant magnetoimpedance effect in a thin-film multilayer meander-like sensor," *J. Appl. Phys.*, vol. 121, no. 12, p. 124501, Mar. 2017.

[79] M. Pannetier-Lecoeur, L. Parkkonen, N. Sergeeva-Chollet, H. Polovy, C. Fermon, and C. Fowley, "Magnetocardiography with sensors based on giant magnetoresistance," *Appl. Phys. Lett.*, vol. 98, no. 15, p. 153705, Apr. 2011.

[80] J. Kerr, "On rotation of the plane of polarization by reflection from the pole of a magnet," *London, Edinburgh, Dublin Philos. Mag. J. Sci.*, vol. 3, no. 19, pp. 321–343, May 1877.

[81] C. C. Robinson, "Longitudinal Kerr Magneto-Optic Effect in Thin Films of Iron, Nickel, and Permalloy*," *J. Opt. Soc. Am.*, vol. 53, no. 6, p. 681, Jun. 1963.

[82] M. Schlenker and Y. Souche, *Magnetism*. New York, NY: Springer New York, 2005.

[83] A. Hubert and G. Traeger, "Magneto-optical sensitivity functions of thin-film systems," *J. Magn. Magn. Mater.*, vol. 124, no. 1–2, pp. 185–202, Jun. 1993.

[84] J. McCord, "Progress in magnetic domain observation by advanced magneto-optical microscopy," *J. Phys. D. Appl. Phys.*, vol. 48, no. 33, p. 333001, Aug. 2015.

[85] S. D. Bader, "SMOKE," *J. Magn. Magn. Mater.*, vol. 100, no. 1–3, pp. 440–454, Nov. 1991.

[86] Hamamatsu Photonics K.K., "ORCA-Flash4.0 V3, Digital CMOS Camera, C13440-20CU / C13440-20CU0, Instruction manual," 2018. [Online]. Available: https://www.hamamatsu.com/sp/sys/en/manual/C13440-20CU_IM_En.pdf. [Accessed: 09-Feb-2019].

[87] B. Mozooni, T. von Hofe, and J. McCord, "Picosecond wide-field magneto-optical imaging of magnetization dynamics of amorphous film elements," *Phys. Rev. B*, vol. 90, no. 5, p. 9, Aug. 2014.

[88] R. B. Holländer, C. Müller, M. Lohmann, B. Mozooni, and J. McCord, "Component selection in time-resolved magneto-optical wide-field imaging for the investigation of magnetic microstructures," *J. Magn. Magn. Mater.*, vol. 432, pp. 283–290, Jun. 2017.

[89] CAVITAR Ltd, "CAVILUX® Smart UHS for Ultra High-Speed Illumination." [Online]. Available: https://www.cavitar.com/cavilux-laser-illumination-products/cavilux-smart-uhs/#cavilux-smart-system-featurescfac-1a24. [Accessed: 10-Feb-2019].

[90] E. C. Stoner and E. P. Wohlfarth, "A Mechanism of Magnetic Hysteresis in Heterogeneous Alloys," *Philos. Trans. R. Soc. A Math. Phys. Eng. Sci.*, vol. 240, no. 826, pp. 599–642, May 1948.

[91] R. Jahns *et al.*, "Microelectromechanical magnetic field sensor based on ?? e effect," *Appl. Phys. Lett.*, vol. 105, no. 5, 2014.

[92] G. Bertotti, *Hysteresis in Magnetism*. London: Academic Press Limited, 1998.

[93] H. Barkhausen, *Das Problem der Schwingungserzeugung mit besonderer Berücksichtigung schneller elektrischer Schwingungen*. Leipzig: S. Hirzel, 1907.

[94] H. Barkhausen, "Zwei mit Hilfe der neuen Verstärker entdeckte Erscheinungen," *Phys. Zeitschrift*, vol. 20, pp. 401–403, 1919.

[95] J.-P. Tetienne *et al.*, "Nanoscale imaging and control of domain-wall hopping with a nitrogen-vacancy center microscope.," *Science*, vol. 344, no. 6190, pp. 1366–9, Jun. 2014.

[96] A. J. Moses, H. V. Patel, and P. Williams, "AC Barkhausen noise in electrical steels: Influence of sensing technique on interpretation of measurements," *J. Electr. Eng.*, vol. 57, no. 8, pp. 3–8, 2006.

[97] A. A. Samimi *et al.*, "Correlation Between AC Core Loss and Surface Magnetic Barkhausen Noise in Electric Motor Steel," *J. Nondestruct. Eval.*, vol. 33, no. 4, pp. 663–669, Dec. 2014.

[98] T. Wang *et al.*, "Magnetic design evolution in perpendicular magnetic recording media as revealed by resonant small angle x-ray scattering," *Appl. Phys. Lett.*, vol. 103, no. 11, p. 112403, Sep. 2013.

[99] E. Lage *et al.*, "Magnetic domain control and voltage response of exchange biased magnetoelectric composites," *Appl. Phys. Lett.*, vol. 104, no. 13, pp. 2012–2016, Mar. 2014.

[100] D. Meyners, J. Puchalla, S. Dokupil, M. Lohndorf, and E. Quandt, "Magnetoelectronical Sensors for Mechanical Measurements," in *ECS Transactions*, 2007, vol. 3, no. 25, pp. 223–233.

[101] A. Ludwig and E. Quandt, "Optimization of the ΔE effect in thin films and multilayers by magnetic field annealing," *IEEE Trans. Magn.*, vol. 38, no. 5, pp. 2829–2831, Sep. 2002.

[102] J. McCord, "Irregular domain patterns in structured magnetic thick films," *J. Appl. Phys.*, vol. 95, no. 11, pp. 6855–6857, Jun. 2004.

[103] J. McCord, R. Schäfer, M. Frommberger, S. Glasmachers, and E. Quandt, "Stress-induced remagnetization in magnetostrictive films," *J. Appl. Phys.*, vol. 95, no. 11 II, pp. 6861–6863, Jun. 2004.

[104] M. Rührig and A. Hubert, "Domain wall observations in magnetic multilayers," *J. Magn. Magn. Mater.*, vol. 121, no. 1–3, pp. 330–335, Mar. 1993.

[105] M. Rührig *et al.*, "Domain Observations on Fe-Cr-Fe Layered Structnres. Evidence for a Biquadratic Coupling Effect," *Phys. Status Solidi*, vol. 125, no. 2, pp. 635–656, Jun. 1991.

[106] J. McCord and J. Westwood, "Domain formation in Fe–N multilayers," *J. Appl.*

Phys., vol. 87, no. 9, pp. 6502–6504, May 2000.

[107] M. Labrune and J. Miltat, "Wall structures in ferro/antiferromagnetic exchange-coupled bilayers: A numerical micromagnetic approach," *J. Magn. Magn. Mater.*, vol. 151, no. 1–2, pp. 231–245, Nov. 1995.

[108] H. Niedoba, L. J. Heyderman, H. O. Gupta, I. B. Puchalska, and A. Hubert, "Micromagnetics of two-layer laminated films with superimposed domains," *J. Appl. Phys.*, vol. 69, no. 8, pp. 5865–5867, Apr. 1991.

[109] V. Hrkac *et al.*, "Amorphous FeCoSiB for exchange bias coupled and decoupled magnetoelectric multilayer systems: Real-structure and magnetic properties," *J. Appl. Phys.*, vol. 116, no. 13, p. 134302, Oct. 2014.

[110] J. McCord, C. Hamann, R. Schäfer, L. Schultz, and R. Mattheis, "Nonlinear exchange coupling and magnetic domain asymmetry in ferromagnetic/IrMn thin films," *Phys. Rev. B*, vol. 78, no. 9, p. 094419, Sep. 2008.

[111] J. McCord, R. Mattheis, and D. Elefant, "Dynamic magnetic anisotropy at the onset of exchange bias: The Ni Fe / Ir Mn ferromagnet/antiferromagnet system," *Phys. Rev. B*, vol. 70, no. 9, p. 094420, Sep. 2004.

[112] M. D. Stiles and R. D. McMichael, "Temperature dependence of exchange bias in polycrystalline ferromagnet-antiferromagnet bilayers," *Phys. Rev. B*, vol. 60, no. 18, pp. 12950–12956, Nov. 1999.

[113] A. Hoffmann, "The Origin for Training Effects in Exchange Bias Systems: Frustration and Multiple Anisotropy Axes at the Interface," in *INTERMAG 2006 - IEEE International Magnetics Conference*, 2006, pp. 582–582.

[114] C. Binek, "Training of the exchange-bias effect: A simple analytic approach," *Phys. Rev. B*, vol. 70, no. 1, p. 014421, Jul. 2004.

[115] A. Kohn, A. Kovács, R. Fan, G. J. McIntyre, R. C. C. Ward, and J. P. Goff, "The antiferromagnetic structures of IrMn3 and their influence on exchange-bias," *Sci. Rep.*, vol. 3, no. 1, p. 2412, Dec. 2013.

[116] S. R. Hartshorn, *Structural Adhesives: Chemistry and Technology*, 1st editio. New York, NY: Plenum Press, 1986.

[117] J. W. Gooch, *Biocompatible Polymeric Material and Tourniquets for Wounds*. Heidelberg: Springer, 2010.

[118] M. K. Al-Munajed, P. H. Gordon, and J. F. Mccabe, "The Use of a Cyanoacrylate Adhesive for Bonding Orthodontic Brackets: an ex-vivo study," *J. Orthod.*, vol. 27, no. 3, pp. 255–260, Sep. 2000.

[119] N. O. Urs *et al.*, "Advanced magneto-optical microscopy: Imaging from picoseconds to centimeters - Imaging spin waves and temperature distributions (invited)," *AIP Adv.*, vol. 6, no. 5, p. 055605, May 2016.

[120] R. Jahns, H. Greve, E. Woltermann, E. Quandt, and R. H. Knochel, "Noise performance of magnetometers with resonant thin-film magnetoelectric sensors,"

IEEE Trans. Instrum. Meas., vol. 60, no. 8, pp. 2995–3001, Aug. 2011.

[121] P. Durdaut *et al.*, "Thermal-Mechanical Noise in Resonant Thin-Film Magnetoelectric Sensors," *IEEE Sens. J.*, vol. 17, no. 8, pp. 2338–2348, Apr. 2017.

[122] J. Reermann *et al.*, "Evaluation of magnetoelectric sensor systems for cardiological applications," *Measurement*, vol. 116, pp. 230–238, Feb. 2018.

[123] J. Reermann, E. Elzenheimer, and G. Schmidt, "Real-time Biomagnetic Signal Processing for Uncooled Magnetometers in Cardiology," *IEEE Sens. J.*, pp. 1–1, 2019.

[124] P. Hayes *et al.*, "Converse Magnetoelectric Resonator Composite for Sensing Small Magnetic Fields," *Sci. Rep.*, vol. xx, no. xx (submitted), 2019.

[125] C. Binek, X. Chen, A. Hochstrat, and W. Kleemann, "Exchange bias in Fe0.6Zn0.4F2/Fe heterostructures," *J. Magn. Magn. Mater.*, vol. 240, no. 1–3, pp. 257–260, Feb. 2002.

[126] K. Takenaka, A. D. Setyawan, Y. Zhang, P. Sharma, N. Nishiyama, and A. Makino, "Production of Nanocrystalline (Fe, Co)-Si-B-P-Cu Alloy with Excellent Soft Magnetic Properties for Commercial Applications," *Mater. Trans.*, vol. 56, no. 3, pp. 372–376, Mar. 2015.

[127] F. Kong *et al.*, "High Bs Fe84−xSi4B8P4Cux (x=0-1.5) nanocrystalline alloys with excellent magnetic softness," *J. Appl. Phys.*, vol. 109, no. 7, p. 07A303, Apr. 2011.